UNIVERSITÉ DE LORRAINE | BIBLIOTHÈQUES UNIVERSITAIRES

AVERTISSEMENT
DROIT D'AUTEUR

Ce document est le fruit d'un long travail approuvé par le jury de soutenance et mis à disposition de l'ensemble de la communauté universitaire élargie.

Il est soumis à la propriété intellectuelle de l'auteur. Ceci implique une obligation de citation et de référencement lors de l'utilisation de ce document. Toute contrefaçon, plagiat ou reproduction illicite encourt une poursuite pénale.

Contact bibliothèque : ddoc-theses-contact@univ-lorraine.fr
(Cette adresse ne permet pas de contacter les auteurs)

Code de la Propriété Intellectuelle. articles L 122. 4
Code de la Propriété Intellectuelle. articles L 335.2- L 335.10

UNIVERSITÉ DE LORRAINE
34 COURS LÉOPOLD — CS 25233
54052 NANCY CEDEX
TÉL : 03 54 50 54 00
CONTACT@UNIV-LORRAINE.FR
WWW.UNIV-LORRAINE.FR

Université de Lorraine

École doctorale SIReNa

Centre de **R**echerches **P**étrographiques et **G**éochimiques

Thèse de Doctorat

Présentée et soutenue publiquement le 28 mars 2025 pour l'obtention du titre de

DOCTEUR DE l'UNIVERSITE DE LORRAINE

(mention Géosciences)

par **Etienne LARGE**

Paléo-taux de dénudation en Afrique Tropicale

Paleo-denudation rates of Tropical Africa

Membres du jury

Directeurs de thèse

Pr. Julien Charreau – Professeur – CRPG / Université de Lorraine – Nancy
Dr. Pierre-Henri Blard – Directeur de Recherche – CRPG / CNRS – Nancy

Rapporteuses

Dr. Marina Rabineau – Directrice de Recherche – Géo-Océan / CNRS – Plouzané –

Présidente du jury

Pr. Taylor Schildgen – Professeure – GFZ / University of Potsdam – Potsdam

Examinateurs

Dr. Delphine Rouby – Chargée de Recherche – GET / Université Toulouse 3 – Toulouse
Dr. Alexander Whittaker – Maître de conférences – Imperial College – London
Dr. Jérôme Van der Woerd – Chargé de Recherche – ITES / CNRS – Strasbourg

Invités

Dr. Sophie Hage – Docteure – GEOPS / Université Paris Saclay – Orsay
Dr. Samuel Toucanne – Chargé de Recherche – Géo-Océan / CNRS - Plouzané

English Abstract

Denudation, the collective action of physical erosion and chemical weathering, controls the evolution of the Earth's surface, together with climate and tectonics. These three processes are linked by several feedback loops, constantly acting on one another. In the context of climate change, understanding how climate affects denudation is of the upmost importance, especially since a debate has been ongoing over the past 30 years on the effect of Cenozoic cooling and Quaternary climate cycles on denudation rates. Most of the studies invested in solving this debate have concentrated on tectonically active or previously glaciated regions. The effect of tectonic activity on denudation can be difficult to quantify, and it is a complication if one wants to study the effect of climate on denudation. Glaciers, although controlled by climate, have a non-linear effect on denudation. Furthermore, most studies are concentrated in the northern hemisphere, leaving a knowledge gap in the tropical areas. In this PhD, I studied the effect of Quaternary climatic cycles on paleo-denudation rates of Tropical, unglaciated, and tectonically quiescent regions.

To do so, I measured *in-situ* ^{10}Be in turbidites of cores located offshore SW Madagascar and Gabon. Turbidites are the deposits of turbidity currents, which bring terrigenous sediments from continental margins to deep sea depocenters. Because they are distal archives, the sediment transport time from continental erosion to deep sea deposition may be large and has only seldom been quantified. A large transfer time (10^5-10^6 a) could lead to discrepancies in the paleo-denudation rates we measure and to wrongful association of measured paleo-denudation rates to known climatic events. By dating different materials both marine and terrigenous in origin of the cores studied, I can constrain the depositional ages of turbidites and more importantly quantify continental transport and marine storage durations. I find ages of submarine storage of 7 to 14 ka, and durations of continental transport from 9 to 15 ka. I insist on the very large and low relief catchment in which these durations were obtained and conclude that these are within the resolution of ^{10}Be, thus not affecting denudation rates measured.

In the main trunk of this work, I show that paleo denudation rates of the Ogowé catchment (Gabon), and of Madagascar have not varied significantly since the mid-Pleistocene, although the Mid-Pleistocene Transition may have had an effect on the Ogowé paleo-denudation rates. These results highlight the limited effect of Quaternary climate over denudation in Tropical regions. I successfully show that Quaternary climate cannot be the main, or the only factor controlling denudation. From this work, and publications of the last two decades, it is becoming clear that denudation cannot be considered as a global process and can only be tackled in a regional perspective. In the tropics, shorter variations of climate such as migrations of the Inter Tropical Convergence Zone, may control climatic variations, although this interpretation is purely speculative as ^{10}Be does not possess the resolution to investigate such high frequency variations and the appropriate paleoclimatic data are missing in this region.

Finally, I show, from new ^{10}Be data, and a review of previously published ^{10}Be, thermochronology and planation surface data, that Madagascar has been in a landscape steady-state over the Cenozoic, with denudation rates following mantle-driven tectonic activity.

Overall, my PhD has shown that turbidites are effective tools to quantify continental processes in the past, but more efforts need to be made to constrain and understand them. Quaternary climate does not control tropical denudation, but large-wavelength mantle-related uplift may. The Mid-Pleistocene Transition may have had an effect on Late Cenozoic denudation rates. Tropical regions crucially lack data, whether it be geomorphological or paleoclimatic. Filling this gap may be key to understand the Earth as a whole.

Abstract Français

La dénudation (érosion physique + altération chimique), contrôle avec le climat et la tectonique, l'évolution de la surface de la Terre. Ces trois processus sont liés par des boucles de rétroaction, agissant constamment les uns sur les autres. Dans le contexte du changement climatique, il est primordial de comprendre comment le climat contrôle la dénudation, d'autant qu'un débat est en cours depuis 30 ans sur l'effet du refroidissement Cénozoïque et des cycles climatiques Quaternaires sur les taux de dénudation.

Les études travaillant sur ce débat se sont concentrées sur des régions tectoniquement actives ou anciennement englacées. L'effet de la tectonique sur la dénudation complique l'étude de l'effet du climat sur la dénudation. Les glaciers, bien que contrôlés par le climat, ont un effet non linéaire sur la dénudation. En outre, la plupart des études se concentrent sur les hautes latitudes, et les zones tropicales restent peu contraintes. Dans ce travail de thèse, j'ai étudié l'effet des cycles climatiques Quaternaires sur les paléo-taux de dénudation de régions tropicales, non englacées et tectoniquement quiescentes.

Pour ce faire, j'ai mesuré le ^{10}Be *in-situ* dans les turbidites de carottes situées au large du Gabon et de Madagascar. Les turbidites sont des sédiments terrigènes transportés des marges continentales vers les dépocentres sous-marins. Étant des archives distales, le temps de transport entre la source et le dépôt peut être important et n'a été que rarement quantifié. Un temps de transfert de 10^5 à 10^6 a pourrait entraîner des erreurs dans les paléo-taux de dénudation mesurés et une association erronée de ces résultats à des événements climatiques connus. En datant différents matériaux d'origine marine et terrigène des carottes étudiées, j'ai pu contraindre les âges de dépôt des turbidites et quantifier les durées de transport continental, et de stockage marin. J'obtiens des âges de stockage sous-marin de 7 à 14 ka, et des durées de transport continental de 9 à 15 ka. Ces durées sont obtenues pour un bassin versant de très grande taille et de faible relief et sont donc maximales. Elles sont néanmoins inférieures à la résolution du ^{10}Be et n'affectent donc pas les taux de dénudation mesurés.

La partie principale de ce travail montre que les paléo-taux de dénudation de l'Ogowé (Gabon) et de Madagascar n'ont pas varié de manière significative depuis le milieu du Pléistocène. La transition mi-Pléistocène a cependant pu avoir un effet sur les paléo-taux de dénudation du bassin de l'Ogowé. Ces résultats montrent l'effet limité du climat Quaternaire sur la dénudation des régions tropicales. Le climat Quaternaire ne peut donc pas être le principal, ou le seul facteur contrôlant la dénudation. D'après ce travail et les publications des deux dernières décennies, il devient clair que la dénudation ne peut pas être considérée comme un processus global et qu'elle ne peut être abordée que dans un cadre régional. Dans les tropiques, des variations plus courtes du climat, telles que les migrations de la zone de convergence intertropicale, peuvent contrôler les variations climatiques, bien que cette interprétation soit spéculative car le ^{10}Be ne possède pas la résolution nécessaire pour étudier des variations à ces fréquences et que les données paléoclimatiques manquent dans cette région.

Je montre enfin à partir de données nouvelles et précédemment publiées que Madagascar a connu au cours du Cénozoïque un état d'équilibre topographique, avec des taux de dénudation suivant l'activité tectonique induite par le manteau.

Dans l'ensemble, ma thèse démontre que les turbidites sont des outils efficaces pour quantifier les processus continentaux, mais que des efforts supplémentaires sont nécessaires pour mieux les contraindre. Le climat Quaternaire ne contrôle pas la dénudation tropicale, même si la transition mi-Pléistocène a pu avoir un effet sur cette dernière. Les régions tropicales manquent cruellement de données, qu'elles soient géomorphologiques ou paléoclimatiques. Combler cette lacune peut s'avérer essentiel pour comprendre le système Terre.

Remerciements

I thank the members of my jury, Taylor Schildgen, Marina Rabineau, Delphine Rouby, Alex Whittaker, Jérôme Van der Woerd, Samuel Toucanne and Sophie Hage for their lecture of my manuscript, and their detailed and constructive comments. I also thank them for the exciting and interesting discussion that followed the defense of this manuscript and all the comments, remarks, propositions, ideas, and very positive critics.

Ce manuscrit est le résultat de plus de trois ans de travail et bien que mon nom figure en haut du document, je ne peux raisonnablement m'attribuer tous les mérites tant ce travail a été le fruit de collaborations riches, d'entraides, de discussions, de rencontres. En arrivant à Nancy, je dois dire que j'étais quelque peu effrayé, si loin des montagnes, pour commencer un projet lui aussi effrayant. Je me suis très vite rendu compte que venir à Nancy avait été une excellente décision tant ces trois années ont été riches en apprentissages et en rencontres. Remercier individuellement, comme ils.elles le méritent toutes les personnes qui m'ont soutenu.es, accompagné.es, avec qui j'ai partagé des moments de vie durant ces trois années demanderait un manuscrit supplémentaire. Alors je tiens à dire un énorme merci global à toutes les personnes que j'ai rencontré durant ces trois années à Nancy ou ailleurs. **MERCI**

En premier lieu, je tiens à remercier mes deux formidables directeurs, Julien Charreau et Pierre-Henri Blard, de m'avoir accordé leur confiance pour me lancer dans ce projet en 2021. Cette confiance s'est ressentie tout au long de ce travail de thèse, je les remercie du fond du cœur pour leur bienveillance à mon égard, leur aide précieuse tant scientifique qu'humaine. On m'avait prévenu avant le début de cette thèse que la direction était responsable de 50% du bon déroulé d'une thèse, je sais maintenant que c'est vrai, et je ne pense pas que j'aurai pu mieux tomber. J'espère avoir la chance de pouvoir continuer à travailler encore longtemps avec eux.

Je me dois également de remercier comme il se doit toute l'équipe du CRPG qui est également grandement responsable du bon déroulé de cette thèse, ainsi que de souvenirs précieux. Merci à Catherine Zimmerman et Aimeryc Schumacher pour leur patience et leur aide précieuse, merci de vous être démené.es pour répondre à mes nombreuses sollicitations malgré votre emploi du temps déjà surchargé. Merci également à Marie Protin pour son aide précieuse, sa bienveillance et son savoir profond qu'elle partage sans retenue. Merci à Abdallah pour son sourire et sa disponibilité, merci à Pierre pour son aide précieuse, sur le vélo mais pas que ! Et merci à tous.tes les autres qui se démènent pour se rendre disponible pour les étudiants, vous êtes nombreux.ses au CRPG et ce formidable labo ne serait pas ce qu'il est sans vous.

Le CRPG, de par sa taille, permet également une ambiance de famille qui permet aux jeunes étudiants insécures de discuter avec des chercheur.euses parfois intimidant.es, surtout de par leur C.V. souvent impressionnants. Merci à vous d'avoir accordé un peu de temps pour répondre à des questions, parfois un peu idiotes d'un jeune doctorant stressé.

En dehors du CRPG, ce travail de thèse a joui de nombreuses collaborations qui ont permis d'aborder des points de vue multiples. La collaboration scientifique est selon moi un des plus beaux aspects de ce métier et j'ai eu la chance d'en avoir un aperçu privilégié. Merci à Germain Bayon, Samuel Toucanne, Bernard Dennielou et Gwennaël Jouet pour leur accueil chaleureux à l'Ifremer, leur bienveillance, la chaleur et la qualité de leurs discussions. Merci à Régis Braucher, Laetitia Léanni, Karim Keddadouche et Georges Aumaître pour leur accueil chaleureux au CEREGE, leur patience dans les explications sur le protocole complexe d'extraction des nucléides cosmogéniques et de leur mesure sur le formidable appareil qu'est ASTER. Merci à Eduardo Garzanti pour de nombreux échanges, toujours passionnants et chaleureux. Merci à Sébastien Carretier, Vincent Regard et Rémi Bossis pour la semaine de terrain passionnante au Cap Vert. Merci aussi à Sébastien et Vincent pour tous les échanges qui ont eu lieu par la suite.

Enfin, pour revenir au CRPG qui a été ma maison pendant ces trois années et demie, merci à toutes les personnes qui font de ce lieu ce qu'il est, et qui m'ont permis de venir à bout de ce travail, non en tant que personnels de la recherche scientifique mais en temps qu'amis. Merci à Simon et David qui m'ont accueilli au sein de leur groupe d'amis. Merci à Lydé, Guillaume, Julien, PH, Pierre, qui m'ont prouvé que la hiérarchie doctorants/chercheurs n'était pas une norme obligatoire et qu'elle n'empêchait pas l'amitié.

Et puis, les mots ne sont pas suffisants pour remercier toute l'équipe des doctorants.es/postdoctorants.es du CRPG. Merci infiniments à vous, Alex, Mara, Pauline, Sumit, Qasid, Melissa, Nico, Waël, Blandine, Julie, Gab, Thomas, Chloé, Mahaud, Hugo, Arno, Clarisse, Mathieu, Louis, Belen. Merci à vous pour le soutien continue, les discussion (de géologie ou d'autre chose !), pour les longues soirées au Malta ou ailleurs, pour les weekends, les confs, les aventures. La bienveillance et le soutien entre (post)doctorants fait beaucoup pour l'ambiance, la qualité de travail et de vie dans ce labo, je vous fais confiance pour faire perdurer cet esprit merveilleux.

Un merci tout particulier à Nico, le merveilleux breton avec qui j'ai eu la chance de partager le bureau. Les derniers moments de rédaction mais aussi beaucoup de moments de ces trois années (dont j'ai des souvenirs flous pour certains), ont été mythiques grâce à toi.

Merci à Marie, amie fidèle parmi toutes. Merci d'avoir été là tout au long de cette thèse, pour les bons moments comme pour les plus difficiles. Ton énergie, ta gentillesse, ta bienveillance rendent tout plus facile, je chéris ton amitié qui, j'en suis sûr survivra à ce manuscrit.

Merci à ma famille pour leur soutien indéfectible tout au long de ce parcours. Vous êtes et restez mon socle et ma boussole, je vous aime.

Merci à Camille qui m'a soutenu lors des indécisions de début de thèse, qui m'a poussé à poursuivre ce projet et qui m'a accompagné dans ses débuts. J'espère du fond du cœur pouvoir continuer à te compter parmi mes ami.es.

A Léa, moi aussi je t'aime.

RESUME ETENDU **1**

CHAPTER 1. INTRODUCTION **6**

1.1. Motivations and main objectives 6
1.2. State of the art 7
1.2.1. Quaternary climate and denudation *7*
1.2.2. In-situ cosmogenic nuclides *12*
1.3. Material 18
1.4. Summary of the chapters of this manuscript 22
1.4.1. Summary of Chapter 1 ..... *22*
1.4.2. Summary of Chapter 2 ..... *22*
1.4.3. Summary of Chapter 3 ..... *22*
1.4.4. Summary of Chapter 4 ..... *23*
1.4.5. Summary of Chapter 5 ..... *23*
1.4.6. Summary of Chapter 6 ..... *24*
Supplementary Information 25

CHAPTER 2. METHODS **29**

2.1. Cosmogenic nuclides 29
2.1.1. ^{10}Be denudation rates *30*
2.1.2. ^{26}Al/^{10}Be burial dating *31*
2.1.3. ^{10}Be and ^{26}Al extraction protocol *33*
2.2. Sample dating and transfer times 36
..... 39
2.3. Low-Temperature-Thermochronology 39
2.3.1. AFT *40*
2.3.2. (U-Th)/He (AHe) *40*
2.4. Neodymium isotopes 41

CHAPTER 3. SOURCE-TO-SINK TRANSPORT DURATION OF TURBIDITE SANDS FROM CONTINENTAL EROSIONAL, TO DEEP MARINE DEPOSITIONAL ENVIRONMENTS **44**

Authors 44
Abstract 44
3.1. Introduction 45
3.2. The Ogowe turbiditic system 46
3.3. Method 48
3.3.1. General approach *48*
3.3.1. Biostratigraphic age models *48*
3.3.2. Sample treatment for ^{14}C analyses *51*
3.4. Material 51
3.5. Results 55
3.5.1. Age models *55*
3.5.2. Low-Resolution sampling *56*
3.5.3. High-Resolution sampling *61*
..... 66
3.6. Discussion 66
3.6.1. Storage and transport durations *66*
3.6.2. Variability of ages *67*
3.6.3. Implications *68*
3.7. Conclusions 69

CHAPTER 4. LATE CENOZOIC PALEO-DENUDATION RATES IN THE TROPICAL OGOWE DRAINAGE 73

Abstract 73
4.1. Introduction 73
4.2. The Ogowe drainage system 74
4.1. Material and Methods 76

4.1.1. Studied cores and borehole cuttings ... 76
4.1.2. Absolute age of turbidite sediments ... 78
4.1.3. ^{10}Be paleo-denudation rates ... 78
4.1.4. ^{26}Al/^{10}Be ratios ... 79
4.1.5. Cosmogenic nuclide sampling and treatment ... 80
4.2. Results ... 81
4.2.1. Age of turbiditic material ... 81
4.2.1. ^{26}Al/^{10}Be burial ages ... 83
4.2.2. Paleo-denudation rates of the Ogowé drainage ... 87
4.3. Discussion ... 89
4.3.1. Implications of ^{26}Al/^{10}Be ages ... 89
4.3.2. Late Cenozoic evolution of denudation ... 92
4.4. Conclusions ... 94
Supplementary Information ... 95

CHAPTER 5. NEAR STEADY DENUDATION RATES DURING THE LATE PLEISTOCENE IN THE TROPICS 99

Authors ... 99
Key points ... 99
Abstract ... 99
Plain Language Summary ... 100
Key words ... 100
5.1. Introduction ... 100
5.2. Study Area ... 103
5.2.1. Physiography of Madagascar ... 103
5.2.2. Geologic domains of Madagascar ... 105
5.2.3. Tectonic activity of Madagascar ... 106
5.2.4. Climate ... 106
5.2.5. Modern denudation rates of Madagascar ... 107
5.2.6. Sampling location and material used ... 107
5.3. Methods ... 108
5.3.1. Chronostratigraphy of core MOZ4-CS24 ... 108
5.3.2. Geochemical analysis ... 108
5.3.3. Heavy minerals ... 111
5.3.4. Cosmogenic radionuclide denudation rates ... 112
5.3.5. Comparison of calculated denudation rates with the climatic cycle ($\partial^{18}0$) ... 114
5.4. Results ... 118
5.4.1. Age model of core MOZ4-CS24 ... 118
5.4.2. Provenance analysis ... 118
5.4.3. ^{10}Be concentrations and paleo-denudation rates ... 119
5.4.4. Denudation rates vs. climate and $\partial^{18}O$ variations ... 120
5.5. Discussion ... 122
5.5.1. Steadiness of denudation rates ... 122
5.5.2. Effect of sediment mixing and lateritic cover on cosmogenic nuclide concentrations ... 123
5.5.3. Duration of sediment transport duration from source to sink ... 126
5.5.4. Source evolution and impact of geology ... 130
5.5.5. Why are denudation rates not impacted by climate in Madagascar ? ... 133
5.6. Conclusion and perspectives ... 135
Supplementary Information ... 137

CHAPTER 6. LANDSCAPE STEADY STATE IN AN ANOROGENIC TROPICAL REGION? ... 147

Authors ... 147
Abstract ... 147
6.1. Introduction ... 148
6.2. Geodynamic history and geological setting of Madagascar ... 150
6.3. ^{10}Be denudation rates ... 151
6.3.1. Material and methods ... 151

6.3.2. Results *151*
6.4. Low-Temperature-Thermochronology 153
6.4.1. Methods *153*
6.4.2. Material and results *154*
6.5. Discussion 156
6.5.1. Spatial distribution of recent denudation (10-100ka) derived from cosmogenic nuclides *156*
6.5.2. Denudation history across the island *158*
6.5.3. Temporal and spatial distribution of uplift *160*
6.5.4. Implication for Meso-Cenozoic landscape equilibrium *162*
6.6. Conclusions 165
Supplementary Information 167
CONCLUSIONS AND PERSPECTIVES 181
REFERENCES 186

Résumé étendu

This first section, in French, is a shorter version of the introduction (Chp. 1) of this work. It is a mandatory section for acceptance of this manuscript by the doctoral school.

Motivations de l'étude

La dénudation correspond à l'action conjointe de l'altération chimique et de l'érosion physique. Elle est l'un des trois processus principaux qui contrôlent la forme et l'évolution de la surface de la Terre, les deux autres étant la tectonique et le climat. Ces trois processus sont liés par un nombre de boucles de rétroaction, interagissant en permanence les uns avec les autres. Les variations du climat influencent l'évolution des taux de dénudation à travers le control de la précipitation (e.g., Fuller et al., 2009; Moon et al., 2011), de la température, ainsi que du couvert végétal (e.g., Acosta et al., 2015; Olen et al., 2016). Les variations de dénudation ont à leur tour un effet sur l'évolution du climat, à travers l'altération des silicates (Berner et al., 1983), la mise à nue de minéraux « frais », plus faciles à altérer (Caves Rugenstein et al., 2019), ou encore l'enfouissement du carbone organique (Galy et al., 2007). La tectonique, comprise ici comme les mouvements verticaux de la surface terrestre dus aux mouvements relatifs des plaques, influence le climat à travers la formation de barrières orographiques ou de creux topographiques (Hay, 1996), ainsi que via l'enfouissement des carbonates au niveau des zones de subduction (Clift and Vannucchi, 2004; Galvez and Pubellier, 2019) mais aussi du dégazage terrestre de CO_2 via l'activité volcanique (Burton et al., 2013; Delmelle et al., 2015). Le climat influence ensuite la tectonique via le contrôle de la dénudation. La formation des chaînes de montagnes quant à elle, créé une situation de déséquilibre qui, de concert avec des effets orographiques susmentionnés,

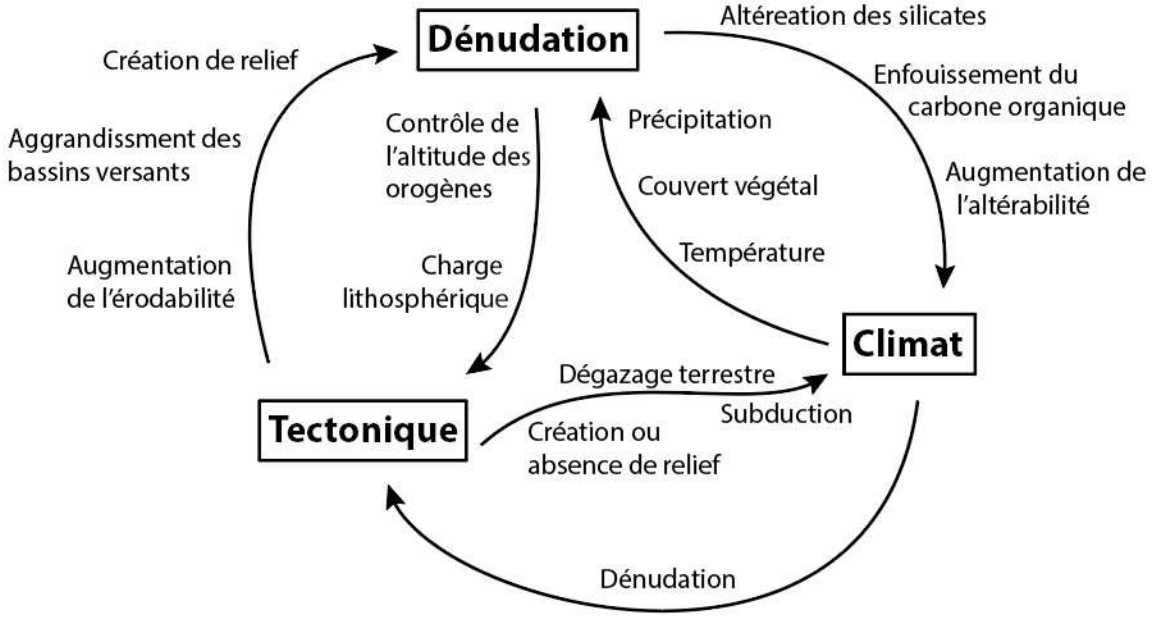

Liens et boucles de rétroaction existant entre tectonique, dénudation et climat. Figure adaptée de Willett et al. (2006).

l'augmentation des pentes, et les risques de glissements de terrain dus aux séismes, mènent à une augmentation des taux de dénudation. La dénudation, à son tour, en contrôlant les altitudes des reliefs et en influençant la charge lithosphérique qui pèse sur le manteau, agit sur les processus tectoniques via le rebond isostatique (Dahlen and Suppe, 1988).

Dans le contexte actuel du réchauffement climatique, et des bouleversements climatiques profonds qui affectent notre habitat (GIEC, Calvin et al., 2023), évaluer et prédire l'évolution future de la surface terrestre, en réponse à ces bouleversements est primordial. Ainsi, l'étude et la quantification des interactions entre dénudation et climat, ainsi que leur effet sur l'évolution de la surface terrestre dans le passé est l'une des clefs essentielles à notre adaptation aux changements profond de notre habitat. Le climat Quaternaire (i.e., 2.5 Ma) a subi des cycles entre périodes glaciaires et interglaciaires d'amplitude similaire au réchauffement actuel (Zachos et al., 2001), bien que le changement climatique actuel se dénote par sa rapidité, et surtout son origine. Le Quaternaire correspond donc à un laboratoire naturel exceptionnel pour comprendre, prédire, et tenter de quantifier les bouleversements à venir. C'est pourquoi dans ce travail, nous proposons de quantifier l'évolution des variations de dénudations Quaternaire, et de vérifier l'effet de la cyclicité climatique sur ces dernières.

Où et comment ?

Des études ont suggéré une accélération globale des taux de dénudation durant la période Quaternaire (e.g., Hay et al., 1988; Zhang et al., 2001), dont l'origine pourrait être l'incapacité de la surface terrestre à atteindre un équilibre dans un climat en constante variation, selon une hypothèse avancée par Peter Molnar (2004). En effet, un model numérique d'évolution de terrain a par la suite démontré que la variation cyclique du climat pouvait mener à un pic de dénudation (Godard et al., 2013). Afin de confirmer ou d'infirmer cette hypothèse, de nombreuses études ont reconstruis des paléo-taux de dénudation, avec l'objectif de vérifier la véracité de cette accélération, et d'étudier son origine. Notamment, une condition qui doit être vérifiée pour que cette hypothèse soit validée est l'ubiquité de l'augmentation des taux de dénudation. Différentes méthodes ont été employées pour analyser l'évolution des taux de dénudation dans le passé: i) la reconstruction de budget sédimentaire dans des bassins marins (Hay et al., 1988) ou continentaux (Kuhlemann et al., 2002) ; ii) l'estimation de l'érosion glaciaire (Hallet, 1996) ; iii) l'utilisation de proxys géochimiques (Willenbring and von Blanckenburg, 2010) ; iv) l'emploi de la thermochronologie (Herman et al., 2013). Pour chacune de ces méthodes, des faiblesses et de potentiels biais ont été avancés, respectivement : i) l'effet Sadler (Sadler, 1981) ou les variations de dépocentre ; ii) le biais potentiel dû au relargage sédimentaire lors de la déglaciation (Koppes and Hallet, 2006) ainsi que l'effet fortement non linéaire de l'érosion glaciaire (Mariotti et al., 2021a) ; iii) la nécessité d'indépendance des proxys utilisés ainsi que la bonne contrainte des temps d'intégration (von Blanckenburg and Bouchez, 2014) ; iv) l'impossibilité, intrinsèque à la thermochronologie, de mesurer des taux de dénudation faibles sur des objets jeunes (Willenbring and

Jerolmack, 2016), ainsi que la possibilité de biais dus à un contexte géologique mal pris en compte (Schildgen et al., 2018).

L'un des objectifs de ce travail de thèse étant de reconstruire des paléo-taux de dénudation, une méthode n'étant pas affectée par ces différents biais a été choisie, celle des nucléides cosmogéniques et plus particulièrement la mesure du ^{10}Be *in-situ*. Cette méthode permettant de reconstruire des taux de dénudation intégrés sur l'entièreté d'un bassin versant (Brown et al., 1995) a l'avantage de ne pas être affectée par un changement de dépocentre ou un enregistrement sédimentaire incomplet. De plus, le ^{10}Be est couramment utilisé dans la mesure de taux de dénudation récents (i.e., 1-100ka) (e.g., Granger et al., 1996; Portenga and Bierman, 2011) et peut être appliqué a des enregistrements sédimentaires afin de reconstruire des paléo-taux de dénudation (e.g., Balco and Stone, 2005; Charreau et al., 2011; Mariotti et al., 2021; Schaller et al., 2016). A l'échelle du Quaternaire les reconstructions sont nombreuses, dans des contextes géologiques variés (e.g., Fisher et al., 2023; Fuller et al., 2009; Grischott et al., 2017; Hidy et al., 2014; Mariotti et al., 2021; Marshall et al., 2017; Puchol et al., 2017; Schaller et al., 2002), mais rares sont les études ayant une résolution suffisante pour investiguer l'effet des variations climatiques Quaternaires sur les taux de dénudation (Fisher et al., 2023; Mariotti et al., 2021; Marshall et al., 2017). De plus, ces reconstructions de paléo-taux de dénudation utilisant le ^{10}Be sont réalisées dans des zones tectoniquement actives (e.g., Gonzalez et al., 2016) ou précédemment englacées (Grischott et al., 2017; Madella et al., 2018; Mariotti et al., 2021) ce qui complique l'analyse de l'effet du climat sur la dénudation. Enfin, la nécessité d'ubiquité de l'augmentation de la dénudation, et le manque considérable de données dans l'Hémisphère Sud, et plus particulièrement dans les zones tropicales en fait donc des zones d'ombres sur ce sujet. L'objectif principal de cette thèse est donc de mesurer, grâce aux nucléides cosmogéniques, des paléo-taux de dénudation en Afrique tropicale, plus précisément à Madagascar et au Gabon. Les enregistrements sédimentaires choisis pour cette étude sont des carottes sédimentaires marines affectés par des turbidites, des dépôts marins profonds issus de courants de turbidités (i.e., glissement sous-marins).

La question principale qui mène ce manuscrit est la suivante :

Comment les taux de dénudation Pléistocène de zones tropicales, tectoniquement quiescentes et affectées par aucun processus glaciaire, réagissent-ils à la cyclicité climatique Quaternaire ?

Déroulé de ce manuscrit

Les chapitres 1 et 2 de ce manuscrit sont consacrés respectivement à l'introduction, qui présente l'état de l'art, et à la présentation des méthodes. À la suite de cela, le chapitre 3 traite la quantification de temps transferts sédimentaires afin de mieux dater et comprendre l'histoire de nos échantillons. Les chapitres 4 et 5 présentent les deux études de paléo-taux de dénudation, réalisés respectivement au Gabon et à Madagascar. Enfin, le chapitre 6 pose la question de la stabilité du relief malgache au cours

des 100 derniers millions d'années, et du contrôle de la tectonique sur la dénudation Cénozoïque de cette île.

La conclusion principale de ce travail de thèse est l'absence de contrôle climatique sur les taux de dénudation tropicaux, à l'échelle de résolution de la dizaine de millier d'années. Il apparaît qu'a cette résolution, les paléo-taux de dénudation tropicaux sont stables depuis au moins 900 ka et qu'ils ne soient donc pas affectés par les cycles climatiques Quaternaires. La Transition mi-Pléistocène a cependant pu avoir un effet sur les paléo-taux de dénudation du bassin de l'Ogowé. Des variations de plus grande fréquence ne sont pas exclues, par exemple, dus à des variations d'intensité et de durée des moussons, mais la résolution de notre méthode ne nous permet pas de les enregistrer. Il ressort également de cette étude que l'utilisation des turbidites permet la reconstruction de processus continentaux passés, mais que des efforts restent à être entrepris concernant leur datation et la compréhension de leur mise en place.

Diversifier les études en zone tropicales, en étoffant surtout les enregistrements paléoclimatiques de ces dernières, permettra de préciser les conclusions de ce manuscrit et de mieux comprendre le système Terre dans son ensemble.

Chapter 1. Introduction

1.1. Motivations and main objectives

Denudation is the joint action of chemical weathering and physical erosion. It is one of the three main processes controlling the shape and evolution of the Earth's surface, the other two being tectonics and climate. These three processes are linked by a number of feedback loops, constantly interacting with each other at various timescales (Figure 1.1, Willett et al., 2006). Climate variations control denudation rates through the modulation of precipitation (e.g., Fuller et al., 2009; Moon et al., 2011), temperature, and vegetation cover (e.g., Acosta et al., 2015; Olen et al., 2016). Variations in denudation in turn influence climate evolution through the weathering of silicates (Berner et al., 1983), the exposure of "fresh" minerals that are easier to weather (Caves Rugenstein et al., 2019), or the burial of organic carbon (Galy et al., 2007), these processes acting as CO_2 pumps at geological timescales. Tectonics, understood here as the vertical movements of the Earth's surface due to relative plate movements, influences climate through the formation of basins and orographic barriers (Hay, 1996), as well as via carbon burial in subduction zones (Clift and Vannucchi, 2004; Galvez and Pubellier, 2019) but also terrestrial CO_2 degassing through volcanic activity (Burton et al., 2013; Delmelle et al., 2015). Climate then influences tectonics by its impact over denudation. Furthermore, tectonic movements induce the creation of reliefs, creating a situation of imbalance which, together with increased slopes, risk of

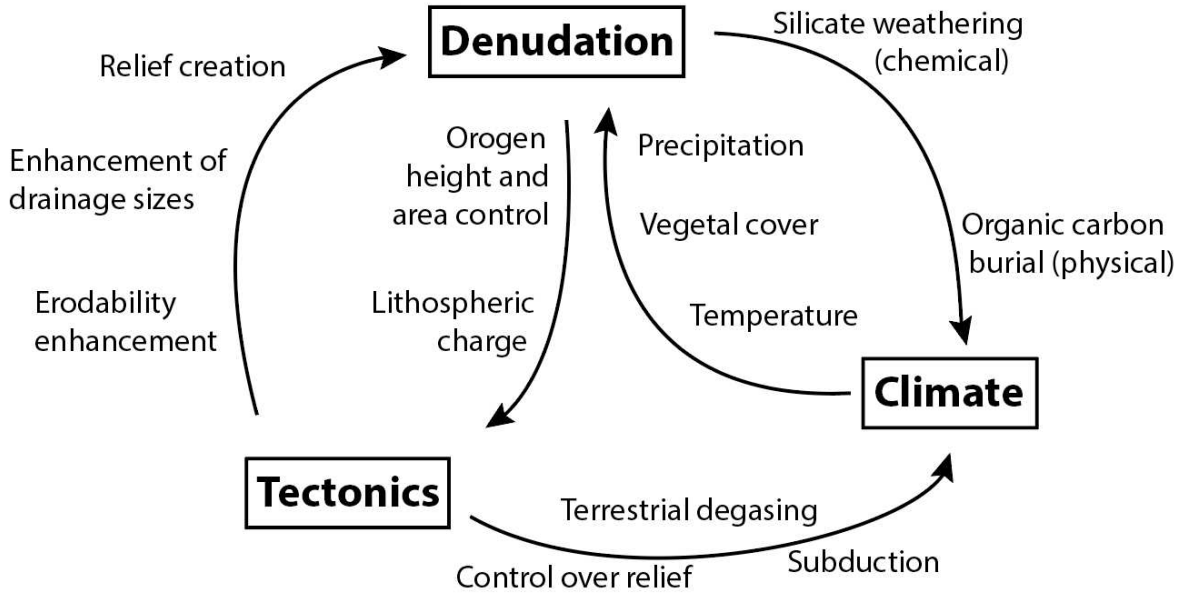

Figure 1.1: Relationships and feedback loops between tectonics, denudation, and climate. Modified from Willet et al. (2006).

landslides due to earthquakes (e.g., Malamud et al., 2004), and previously mentioned orographic effects, lead to an increase in denudation rates. Denudation, in turn, by controlling altitudes and redistributing the lithospheric load on the mantle, acts on tectonic processes via isostatic rebound (Dahlen and Suppe, 1988).

In the current context of global warming, and of the profound climatic upheavals affecting our habitat (IPCC, Calvin et al., 2023), assessing and predicting the future evolution of the Earth's surface in response to these changes is of the upmost importance. In Geosciences, we have a strange way of answering questions about the future, we investigate the past. Studying and quantifying the interactions between paleo-denudation and climate, and their effect on the past evolution of the Earth's surface, is indeed one of the keys to our adaptation to profound changes affecting our habitat in the future.

The Quaternary (i.e., 2.5 Ma) climate was affected by cyclic variations from glacial to interglacial periods (Figure 1.2, Zachos et al., 2001). Although the rapidity and origin of modern global changes is unprecedented, these variations had amplitudes comparable to the current warming. This period therefore represents an exceptional natural laboratory for understanding, predicting, and attempting to quantify future disruptions. In this work, we aim to quantify the evolution of Quaternary denudation variations in Tropical regions, and to investigate if and how the contemporary climatic cyclicity affected them.

1.2. State of the art

1.2.1. Quaternary climate and denudation

The normalized ratio of $^{18}O/^{16}O$, noted $\delta^{18}O$, is a tracer of the Earth's global temperature and of the ice sheets volume (e.g., Lisiecki and Raymo, 2005). This tracer indicates a long term cooling event since the Paleocene-Eocene Thermal maximum, ~57 Ma (Kennett and Stott, 1991; Koch et al., 1992; Zachos et al., 2001), punctuated by fast high amplitude drops in temperature, notably the one that occurred since the Late Pliocene (~3.5 Ma) (Figure 1.2, Zachos et al., 2001), which was associated to the emergence of the Isthmus of Panama (Haug and Tiedemann, 1998) and led to the appearance of the Quaternary period. The record presented in Figure 1.2 also shows the initiation and intensification with time of the Quaternary climatic cycles since 2.56 Ma, with the alternance of long (40 ka to 80 ka) glacial periods, separated by shorter (< 20 ka) interglacial warm episodes (Figure 1.2, Maslin et al., 1996; Zachos et al., 2001). These cycles changed in frequency from 40 ka to 100 ka cycles between 0.7 Ma and 1.2 Ma, during a transition period known as the Mid-Pleistocene Transition (MPT, Berends et al., 2021).

As mentioned in section 1.1., complex interactions exist between climate and denudation, such that deciphering which process controls the others can be difficult. The cause of the Late Cenozoic global cooling is a long-lasting question in Geosciences, especially since Molnar and England (1990), set the cat among the pigeons by linking Himalayan and Alpine uplifts to the Late Cenozoic cooling through

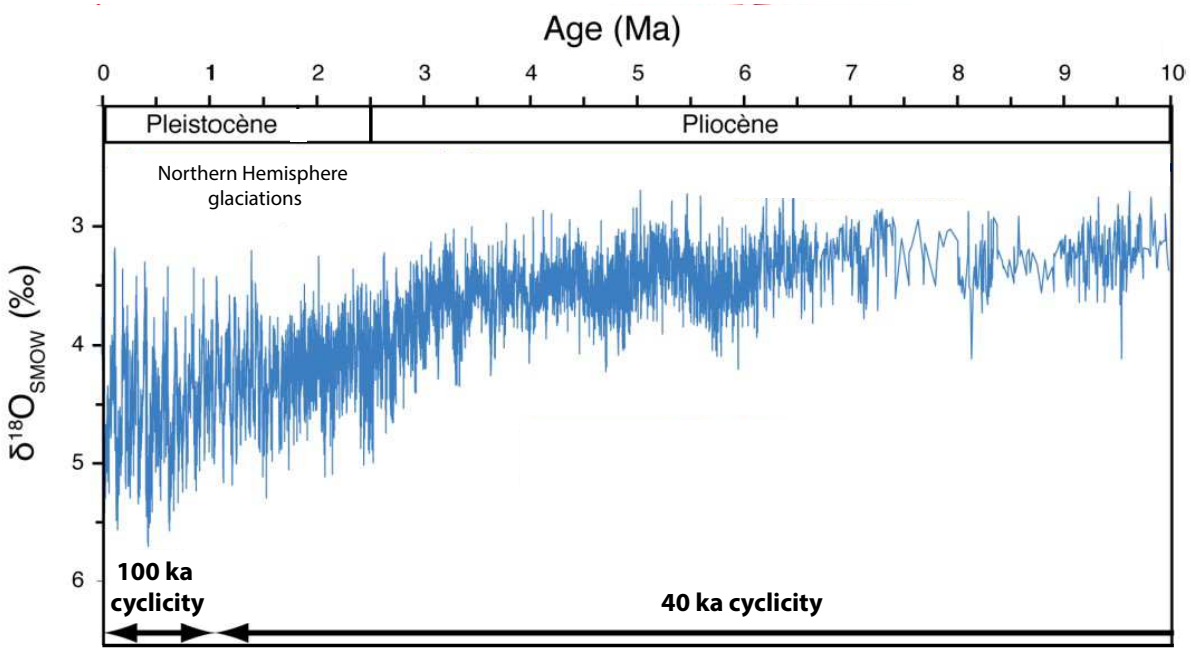

Figure 1.2 : Benthic $\delta^{18}O$ compilation throughout the Plio-Pleistocene showing global cooling and the initiation of the Quaternary climatic cycles. Figure from Zachos et al. (2001).

denudation. They postulated that the cooling could in fact have been responsible for these high elevation ranges by increasing erosion rates, thus creating deeply incised valleys that lower mean elevations and allow for an increase in height of the higher peaks through isostatic rebound. Two years later, Raymo and Ruddiman (1992) answered by acknowledging the link between Cenozoic uplift and climate, but insisting on the primary control of uplift on climate and erosion, and not the contrary.

In Plio-Pleistocene times, the increased global cooling has also been proposed to have led to increased sedimentation rates. Hay et al. (1988) report a global two-fold increase in terrigenous sedimentation rates in the last 5 Ma, a result consistent with reconstructions of continental sedimentary budgets (Kuhlemann et al., 2002). However, these interpretations may have been affected by possible bias, such as depocenter variations, poorly constrained basin geometries and stratal discontinuities (Métivier, 2002; Willenbring and von Blanckenburg, 2010), or by the Sadler effect (Sadler, 1981). This latter effect postulates that sedimentation rates measured over short timescales (i.e., 1 Ma) will be artificially high due to better completeness of the sedimentary record. Conversely, the longer the timescale considered, the greater the possibility for gaps and basin inversions (i.e., closure and uplift of a basin leading to the transformation of a low relief, sedimentary deposition area, to an area where sediments are eroded) to affect the sedimentary record. Furthermore, sedimentary budget of marine basins based on seismic reconstructions yielded contradictory results (Clift, 2006).

Nevertheless, some authors postulated that the global acceleration of sedimentation rates over the Pleistocene was a reality (Figure 1.3, Molnar, 2004; Zhang et al., 2001). Along with the observation of a global increase in sediment granulometry, this led them to propose that only a global forcing such as climate could lead to the Pleistocene sedimentation increase. Zhang et al. (2001) and later Molnar (2004) proposed that the Plio-Pleistocene cooling, associated with the initiation of the Quaternary

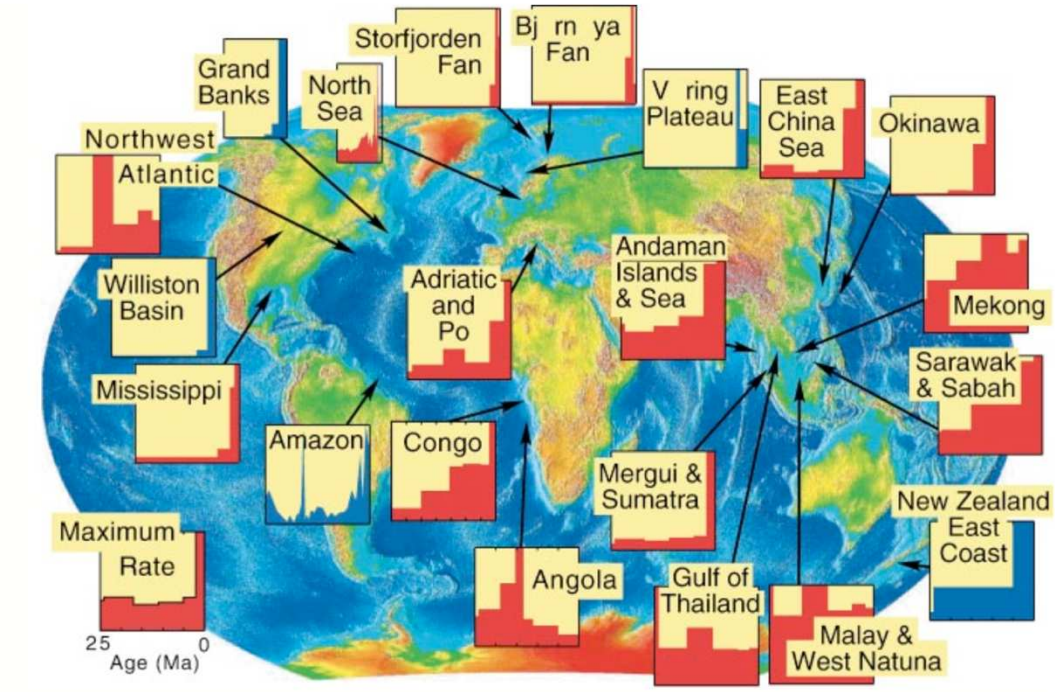

Figure 1.3 : World compilation of average sedimentation rates since 25 Ma. Figure from Molnar (2004).

glacial/interglacial cycles created a transition from a period of relatively stable climate to a period of frequent and large amplitude changes which forbids Earth's surface response to reach a new equilibrium. Indeed, a landscape evolution model subsequently demonstrated that cyclical climate variations could lead to a peak in denudation (Godard et al., 2013). To confirm or refute this hypothesis, numerous studies have reconstructed paleo-denudation rates, with the aim of verifying the veracity of this denudation acceleration and investigating its origin. The ubiquity of the increase in denudation rates, or at least the spatial homogeneity of the control of Quaternary climatic cycles on Quaternary denudation rates must be verified for this hypothesis to be validated.

Estimation of glacial erosion (Hallet, 1996) suggested increased denudation during glacial periods due to the greater efficiency of glacial over fluvial erosion. The subglacial storage of sediments is however difficult to constrain and may lead to different results (Koppes and Hallet, 2006). It has also been shown that the effect of glaciers on denudation rates is non-linear, with possible tipping points (Mariotti et al., 2021a).

A global 1D inversion of thermochronological data showed an up to four-fold increase in erosion rates between the 4-6 Ma and 0-2 Ma periods (Figure 1.4, Herman et al., 2013). It was however suggested that a large part of the results from this global inversion where affected by spatial gradients associated to local geology of the sampled areas, and not a climatic signal (Figure 1.5, Schildgen et al., 2018). Moreover, the intrinsic impossibility of thermochronology to measure low denudation rates on young objects (Willenbring and Jerolmack, 2016), also limits this approach.

Geochemical proxies, and more specifically meteoric $^{10}Be/^{9}Be$ ratios (Willenbring and von Blanckenburg, 2010) were also used as tracers of chemical weathering. Applied to core sediments from

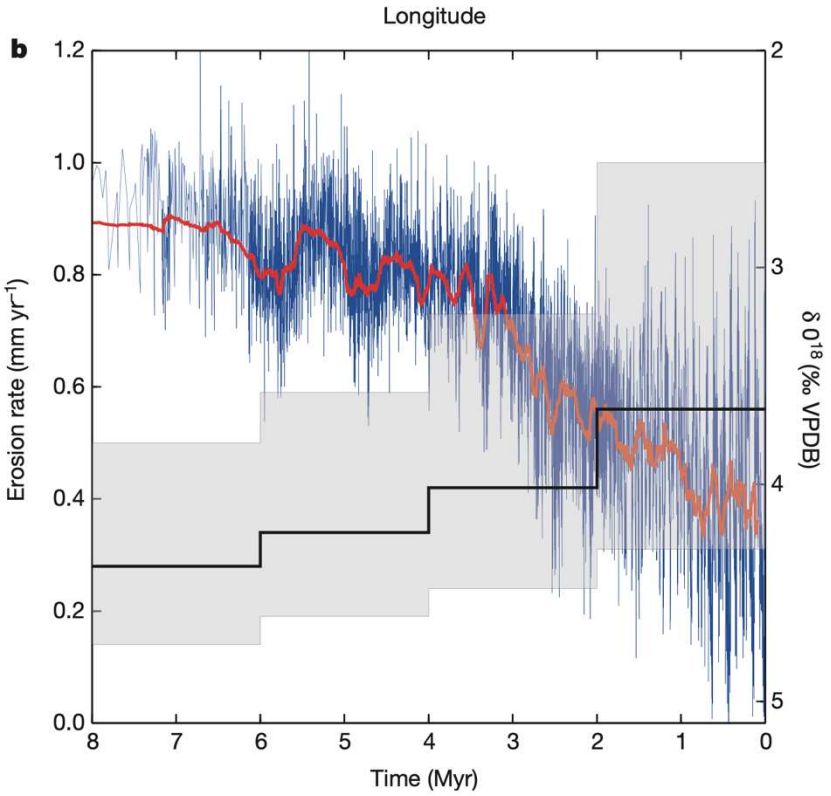

Figure 1.4 : Global 1D inversion of thermochronological data (grey line) and $\delta^{18}O$ records (blue line) show inverse evolutions. Figure from Herman et al. (2013).

the Pacific and the Arctic oceans, as well as to hydrogenous ferromanganese crusts of the Pacific and Atlantic oceans, this proxy suggests constant weathering rates since the Mid-Miocene, 12 Ma (Figure 1.6). The integration time of the oceanic $^{10}Be/^{9}Be$ ratio has however since been debated (von Blanckenburg and Bouchez, 2014), and the effect of pH on Be isotopes, as well as the blindness of this method to basaltic or carbonate weathering could lead to uncertainties (Willenbring and Jerolmack, 2016). Moreover, physical erosion may not be captured by this method, the covariance of physical erosion and chemical weathering being subject to debate (Norton and Schlunegger, 2017).

To this day, there is no consensus about the effect of Quaternary climatic cycles on denudation rates and this stems largely from the uncertainties and biases arising from the methods employed to answer such a question. In this work, we use terrestrial cosmogenic nuclides, a method for which extensive literature already exists, and of which I will summarize the main concepts in the following section.

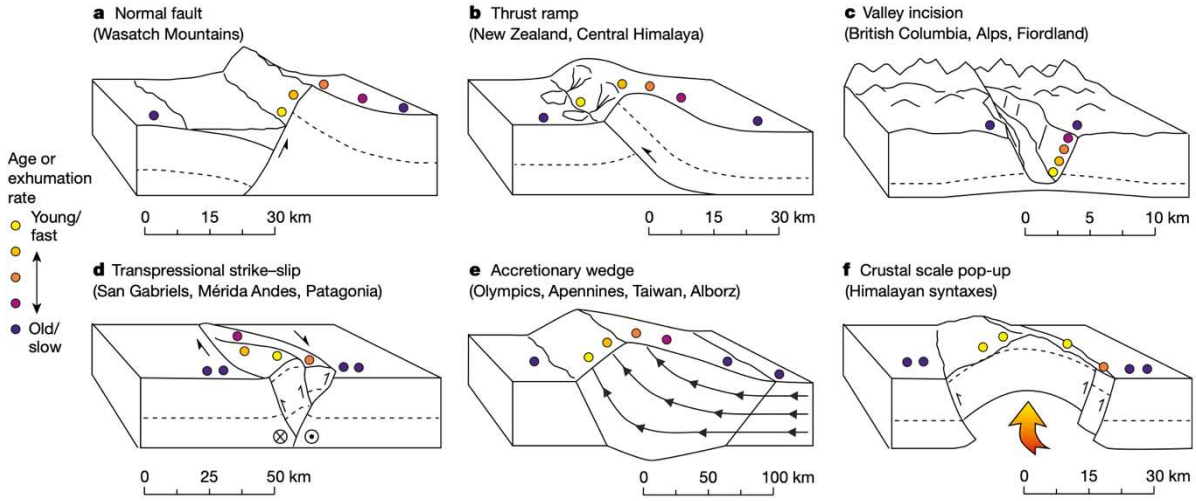

Figure 1.5 : Sketches of areas where spatial variability in thermochronological data shows geological rather than temporal gradients. Figure from Schildgen et al. (2018).

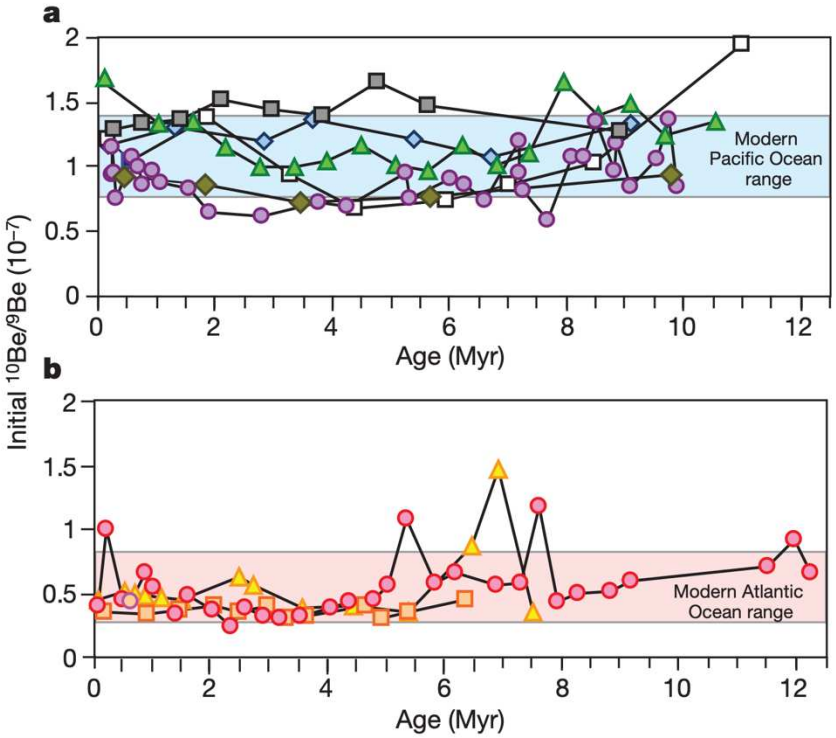

Figure 1.6 : $^{10}Be/^{9}Be$ ratios of marine cores (purple and pink circles for Pacific and Arctic oceans, respectively) and hydrogenous ferromanganese crusts (all other symbols). This figure was taken from Willenbring and von Blanckenburg, (2010).

1.2.2. In-situ cosmogenic nuclides

To pursue the main objective of this thesis, the reconstruction of paleo-denudation rates, we used *in-situ* produced cosmogenic isotopes, and notably *in-situ* ^{10}Be measured in quartz grains, a method that is not affected by the main biases presented above. This method, which enables the calculation of denudation rates integrated over an entire watershed, has the advantage of not being affected by changes in depocenter or an incomplete sedimentary record. Brown et al. (1995), published the first study using ^{10}Be on quartz grains to calculate denudation rates over a catchment of the island of Puerto Rico. They discussed the various effects of cosmogenic production rates, bioturbation, quartz availability, weathering, sediment storage or episodic mass wasting, on their measurements. Following this initial publication, ^{10}Be has been commonly used to determine recent (i.e., 1-100 ka) denudation rates (e.g., Granger et al., 1996; Portenga and Bierman, 2011). It has also later been applied to sedimentary records to reconstruct paleo-denudation rates (e.g., Balco and Stone, 2005; Puchol et al., 2017; Schaller et al., 2016).

In total, and apart from any work which would have been published in early 2025, 29 studies have used cosmogenic nuclides to reconstruct Late Cenozoic paleo-denudation rates. These publications are compiled and displayed on a map in Figure 1.7.. A first striking observation is the concentration of these studies in the Northern Hemisphere, with only 5 studies located in the Southern Hemisphere (Bekaddour et al., 2014; Fisher et al., 2023; Madella et al., 2018; Pingel et al., 2019; Val et al., 2016), all in the Andes. Only one study explores paleo-denudation rates on the African continent, in Kenya (Garcin et al., 2017). All other studies are located either in the USA (Balco and Stone, 2005; Fuller et al., 2009; Hidy et al., 2014; Marshall et al., 2017; Mason and Romans, 2018; Oskin et al., 2017), Europe (Cyr and Granger, 2008; Grischott et al., 2017; Grischott et al., 2017; Haeuselmann et al., 2007; Mariotti et al., 2021; Schaller et al., 2016, 2004, 2002), Tian Shan (Charreau et al., 2023, 2011; Grin et al., 2018; Puchol et al., 2017) or the Himalayan range (Charreau et al., 2021; Kapannusch et al., 2020; Lenard et al., 2020; Mandal et al., 2021). Such clusters of localities may lead to over-representation of some regions and potential bias in establishing global conclusions from this dataset.

These studies concentrate on a variety of timescales, from 1-100 ka (e.g., Balco and Stone, 2005; Charreau et al., 2023; Fuller et al., 2009; Grin et al., 2018; Grischott et al., 2017; Mariotti et al., 2021), to 1-10 Ma (e.g., Charreau et al., 2011; Madella et al., 2018; Mason and Romans, 2018; Pingel et al., 2019). However, only a few have sufficient resolution to investigate the impact of Quaternary climatic cycles and of the interglacial versus glacial periods on denudation (Fisher et al., 2023; Mandal et al., 2021; Mariotti et al., 2021; Mason and Romans, 2018; Oskin et al., 2017).

Figure 1.7 : (following page) Map of all ^{10}Be paleo-denudation rates studies with references. Locations are given in parentheses after the authors and dates.

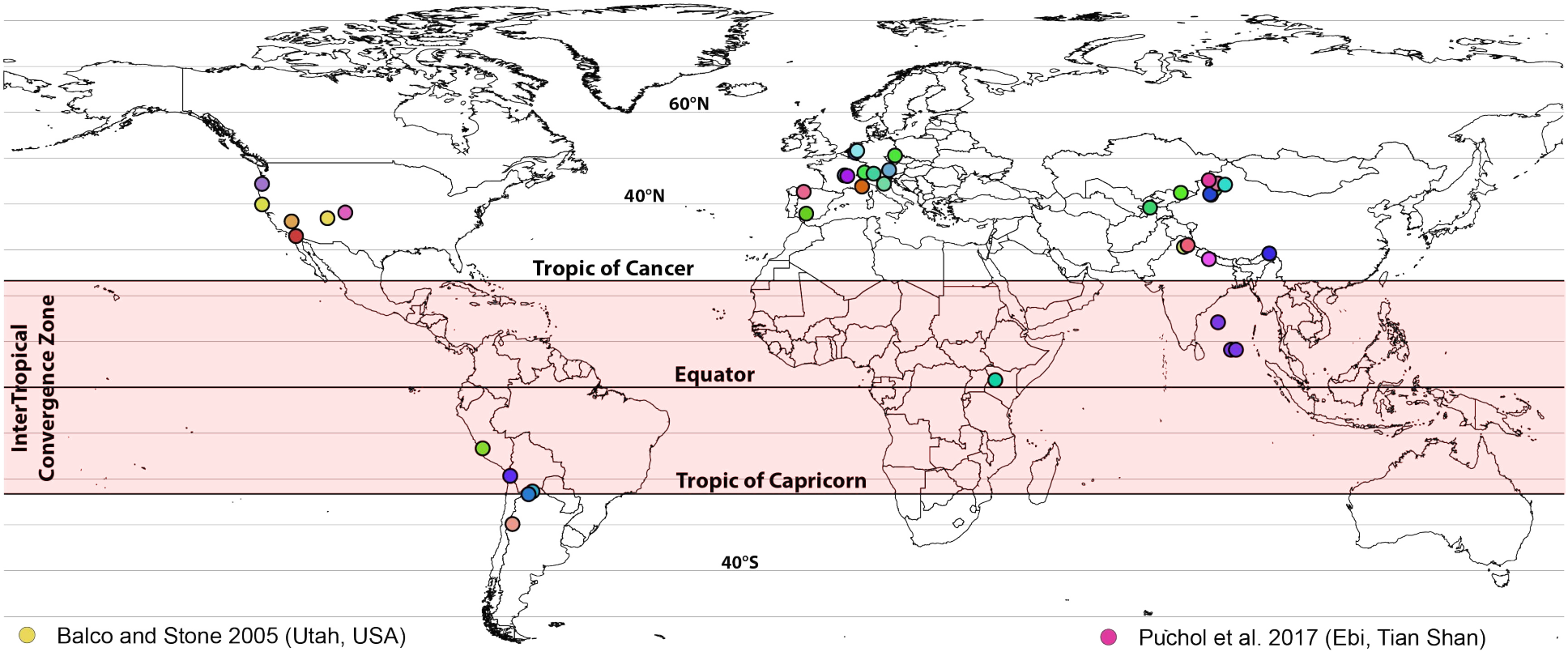

- Balco and Stone 2005 (Utah, USA)
- Bekaddour et al. 2014 (Peru)
- Charreau et al. 2011 (Kuitun, Tian Shan)
- Charreau et al. 2021 (Surai, C. Himalaya)
- Charreau et al. 2023 (Bayanbulak, Tian Shan)
- Charreau et al. 2023 (Kuitun, Tian Shan)
- Charreau et al. 2023 (Yaha, Tian Shan)
- Cyr and Granger 2008 (Appenines, Italy)
- Fisher et al. 2023 (Rio Iruya, Andes)
- Fuller et al. 2009 (California, USA)
- Garcin et al. 2017 (Kenya)
- Grin et al. 2018 (Tian Shan)
- Grischott et al. 2016 (Alps)
- Grischott et al. 2017 (Alps)
- Haeuselmann et al. 2007 (Switzerland)
- Hidy et al. 2014 (Texas, USA)
- Kapannusch et al. 2020 (NW Himalaya)
- Kudriavtseva et al. 2023 (N Pamir - Tian Shan)
- Lenard et al. 2020 (Bengal Fan)
- Madella et al. 2018 (Andes)
- Mandal et al. 2021 (W. Himalaya)
- Mariotti et al. 2021 (Var, France)
- Marshall et al. 2016 (Oregon, USA)
- Masons & Romans 2018 (California, USA)
- Oskin et al. 2017 (California, USA)
- Pingel et al. 2019 (Argentina)
- Puchol et al. 2017 (Ebi, Tian Shan)
- Puchol et al. 2017 (Jingu, Tian Shan)
- Puchol et al. 2017 (Kuitun, Tian Shan)
- Puchol et al. 2017 (Yaha, Tian SHan)
- Refsnider et al. 2010 (USA)
- Schaller et al. 2002 (Allier)
- Schaller et al. 2002 (Dore, France)
- Schaller et al. 2002 (Meuse, Netherlands)
- Schaller et al. 2004 (Meuse, Netherlands)
- Schaller et al. 2016 (Allier, France)
- Schaller et al. 2016 (Esla, Spain)
- Schaller et al. 2016 (Guadalquivir, Spain)
- Schaller et al. 2016 (Vltava, Czechia)
- Val et al. 2016 (Argentina)

The conclusions of these publications are heterogeneous: (i) some studies indicate long-term steady denudation rates over the Plio-Pleistocene transition (Grischott et al., 2017; Lenard et al., 2020; Madella et al., 2018; Oskin et al., 2017), while (ii) others identified a climatic forcing on denudation (Bekaddour et al., 2014; Charreau et al., 2011; Fisher et al., 2023; Fuller et al., 2009; Garcin et al., 2017; Grischott et al., 2017a; Haeuselmann et al., 2007; Hidy et al., 2014; Kapannusch et al., 2020; Mariotti et al., 2021; Marshall et al., 2017; Mason and Romans, 2018; Refsnider, 2010; M. Schaller et al., 2002) or (iii) a tectonic control (Balco and Stone, 2005; Charreau et al., 2023; Grin et al., 2018; Mandal et al., 2021; Pingel et al., 2019; Puchol et al., 2017; Val et al., 2016).

These datasets are difficult to compare due to the differences between their tectono-climatic settings, and the fact that the studied material varies from river terrace samples (e.g., Schaller et al., 2004) to cave deposits (e.g., Haeuselmann et al., 2007) or marine sedimentary cores (Lenard et al., 2020; Mariotti et al., 2021). Nevertheless, if we compare these different datasets at the first order, there is not a single homogeneous pattern among these denudation rates records. There is a significant regional variability, and this is true no matter the time scale considered, whether it be the Late Pleistocene (Figure 1.8), or the Plio-Pleistocene (Figure 1.9). All comparisons are shown in supplementary information.

The near exclusivity of the Northern Hemisphere as study areas is of concern, for the several reasons discussed above, but it is not the only concern. The tectono-climatic settings of these studies might even further affect the results and interpretations. As shown in section 1.1 of this chapter, the feedback processes between tectonics, climate and denudation are complex. One might then wonder if investigating a potential climatic signal over denudation in a geological setting controlled by tectonics is the easiest way to do it. Moreover, although glaciers are considered as a climatic forcing as they are controlled by temperature and precipitation, I present in section 1.2.1, the potential biases that could arise from landscapes affected by glacial processes (e.g., Mariotti et al., 2021). The ^{10}Be paleo-denudation rate reconstructions presented above are concentrated in regions which are either tectonically active, or have been affected, to some extent, by Quaternary glaciations. These contexts complicate the signal of climate over denudation, which is the forcing we investigate in this work.

In the present PhD manuscript, we have chosen to bring our brick to the long-lasting debate of the control of Quaternary climate over denudation, by studying the Tropics, an area that was up to now free of paleo-denudation records. At low latitudes, the effect of the Quaternary climate cyclicity is poorly understood, making these regions a cornerstone to answer Molnar's theory. For this work, two tropical regions were selected: SW Madagascar and the Ogowé catchment in Gabon, W Africa. These 2 settings are suited given the availability of well dated continuous sedimentary marine archives over the Quaternary, the presence of denudation rates data in the modern watersheds, and the absence of tectonic or glacial activity during the Quaternary. In the following sections I will present the material used for this paleo-denudation rate reconstruction, and rapidly present the different chapters and the logic behind their order.

This review of the literature has brought me to the main question that this work attempts to answer:

How do Pleistocene denudation rates of Tropical, tectonically quiescent, unglaciated regions react to Quaternary climatic cycles?

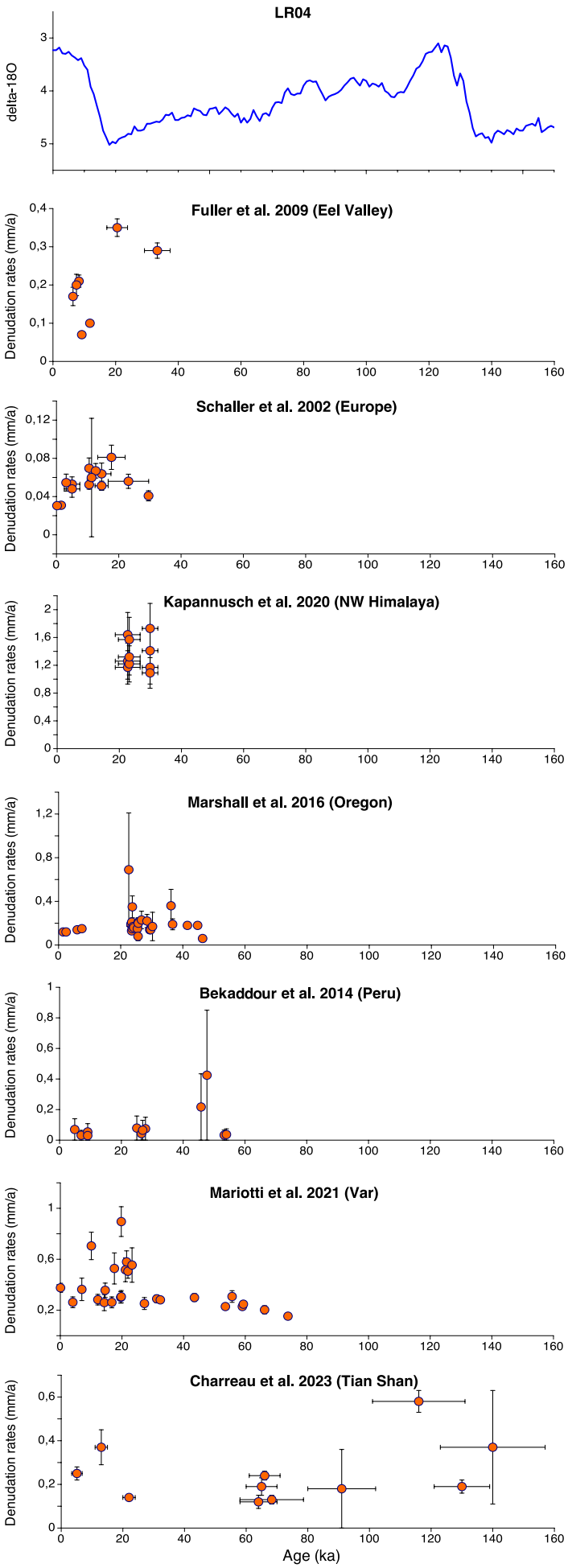

Figure 1.8 : Compilation of ^{10}Be paleo-denudation rates from 0 to 160 ka

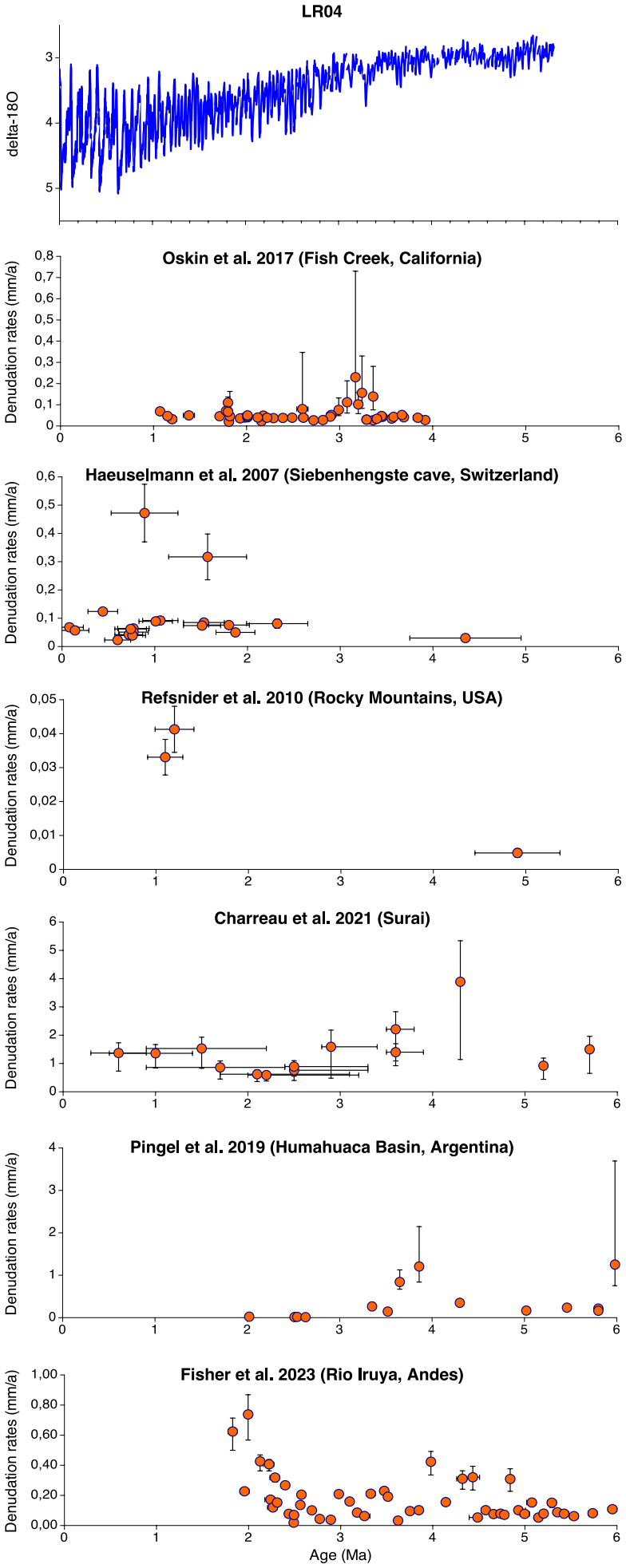

Figure 1.9 : Compilation of ^{10}Be paleo-denudation rates from 0 to 6 Ma.

1.3. Material

The different samples used for this work are presented in detail at the beginning of every chapter. Overall, samples from 4 marine sedimentary cores, 15 modern riverbeds, and cuttings from one drilling were used for this work.

In Madagascar, one 26 m long marine sedimentary core, MOZ4-CS24, recovered ~150 km from the coast at 3090 m depth was used (Figure 1.10). It records sediments over the past 900 ka. To compare this sedimentary record to modern denudation rates, 14 modern river sands of SW Madagascar were also analyzed for ^{10}Be.

In Gabon, three marine sedimentary cores were used, KC13, KC10 and KC11 recovered at 2852 m, 3148 m, and 3372 m depths, respectively (Figure 1.10). These cores record Late Pleistocene sediments brought to the Ogowé submarine sedimentary system from proximal (KC13) to distal (KC11) locations. To compare values obtained in these cores with values on land, we relied on a recently published study (Regard et al., 2025), which presents a dataset of modern ^{10}Be denudation rates for the Ogowé continental catchment, and on a sample of the Ogowé riverbed sand collected close to the outlet. Additionally, we used cuttings from a drilling performed by Total ~30 km offshore of the mouth of the Ogowé river (Torpille Marine, TM, Figure 1.10). These cuttings were poorly dated but were suspected to record sediments as old as the Miocene, allowing us to compare denudation rates of this catchment before and after the MPT.

The sedimentary logs of the 4 cores are presented in fFigure 1.11 and Figure 1.12. These cores are composed of hemipelagic sediments, resulting from the decanting of material present in the water

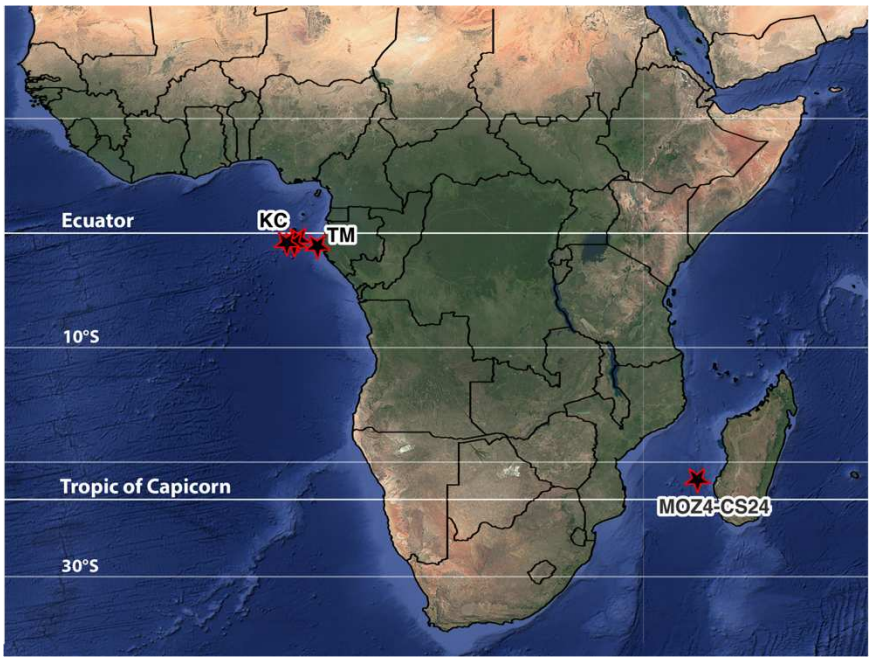

Figure 1.10: Location of the paleo archives used in this work.

column and of very small granulometry (<50µm), in which turbidites, corresponding to coarser terrigenous sediments

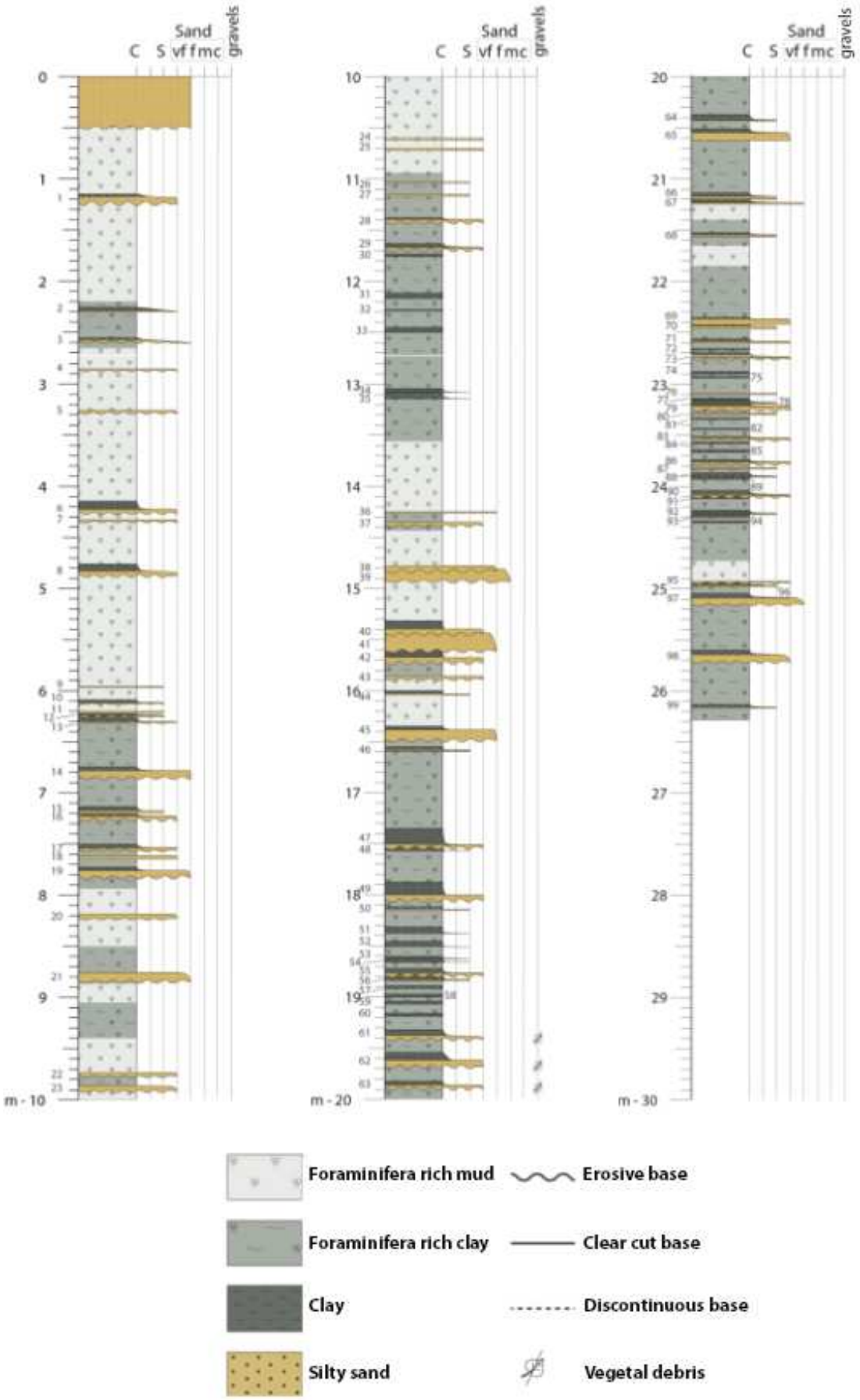

Figure 1.11: Stratigraphic log of core MOZ4-CS24, showing the hemipelagic layers (clays and muds), intercalated by turbidite deposits (silty sands). This figure was made by Léa Faubert during her internship at Ifremer.

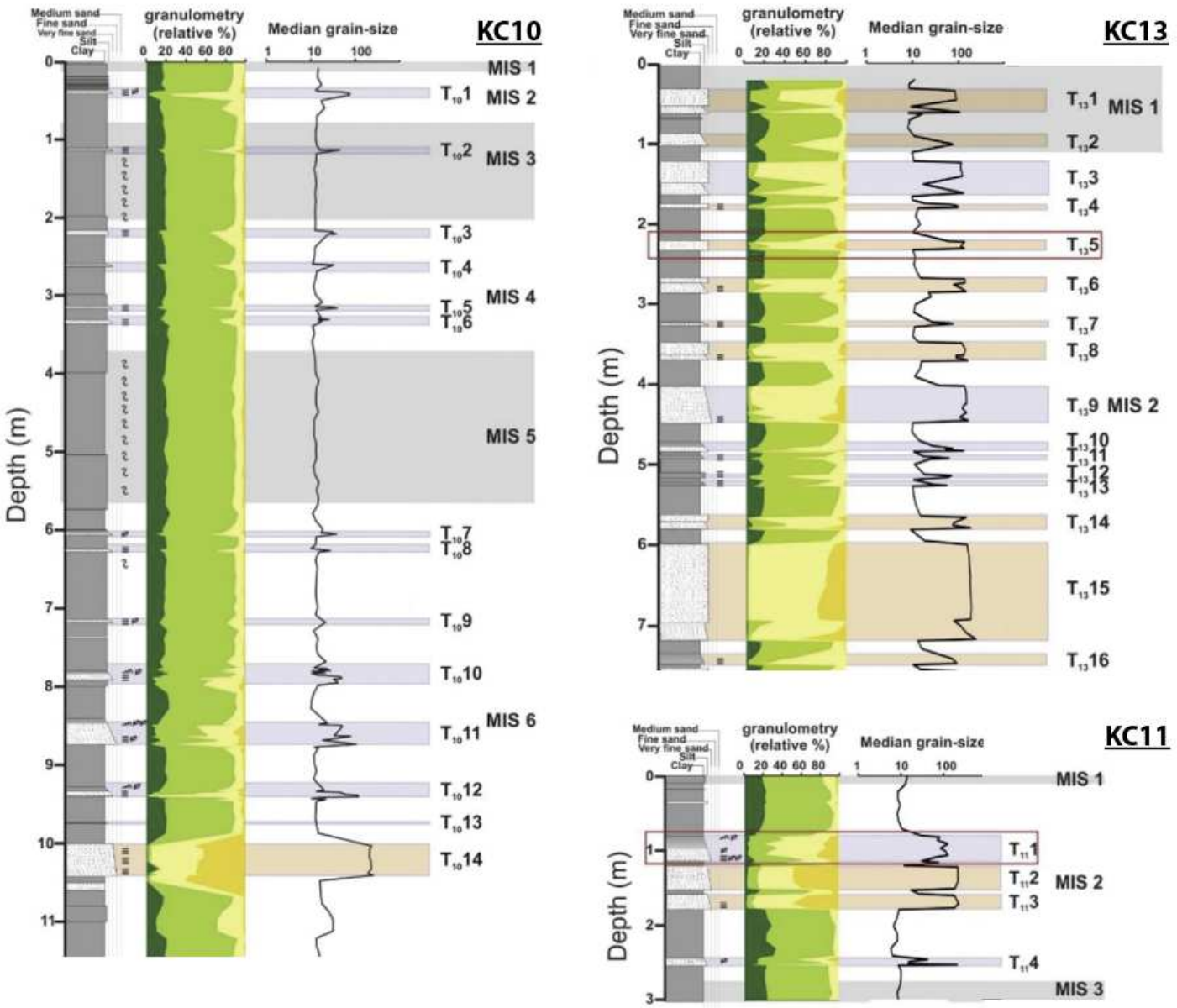

Figure 1.12: Stratigraphic log with corresponding Marine Isotope Stages of cores KC10, KC11 and KC13. All turbidites are shown by blue/grey or orange rectangles. Figure modified from Mignard et al. (2017).

(50-250µm) are intercalated. Turbidites are the deposits issued from turbidity flows, submarine landslides that carry terrigenous material derived from continental erosion to great depths. Because measurements of *in-situ* ^{10}Be are done on quartz grains, we are interested in the presence of this mineral. Fortunately, quartz is a difficult mineral to alter, and its relative concentration in sediments increases with distance from the source. Turbidites are therefore generally rich in quartz, enabling us to measure *in-situ* ^{10}Be and reconstruct paleo-denudation rates.

Further descriptions of the samples are given in the material parts of every chapter and the treatment applied to the samples before measurement is presented in Chapter 2 of this manuscript.

1.4. Summary of the chapters of this manuscript

In this following section, I will present summaries of the different chapters composing this manuscript. The objective here is not to create duplicates of the abstracts present at the beginning of chapters 3, 4, 5 and 6, but rather to justify the choice of the orders of the chapters, and to explain to the readers, what they may expect in each chapter.

1.4.1. Summary of 0

In this first chapter, I have presented the main objectives of this work, and explained why they are relevant to research and society. I have presented the scientific debate in which this work is rooted and the precedent efforts that have been made to solve this debate. Cosmogenic nuclides, the method chosen to reconstruct paleo-denudation rates, is a well-known method on which a number of publications rest upon. I have presented the 29 publications which used this method to reconstruct paleo-denudation rates and demonstrated why the present study complements these past efforts, by investigating the response of denudation rates to Quaternary climatic fluctuations of an area never investigated before, which I have shown to be a cornerstone of Molnar's theory. Finally, I have rapidly presented the material that were used to answer our main question: **How do Pleistocene denudation rates of Tropical, tectonically quiescent, unglaciated regions react to Quaternary climatic cycles?**

1.4.2. Summary of Chapter 2

In the second chapter of this manuscript, I present the different methods used to answer the above question. Cosmogenic nuclides, particularly, take up the main part of the second chapter. The historic discoveries that have led to the applications used today are presented. The core of this chapter is focused on denudation rates measurements, the main application I used during my PhD. Burial dating is also addressed as this method was used to constrain transport time and sediment burial ages in 0.
Radiocarbon dating, and especially the way it was used to quantify sediment transfer times from continental erosional to marine depositional environments is also presented. Finally, εNd and Low Temperature Thermochronology are introduced briefly, as these methods were used to constrain sediment sources, and Cenozoic denudation rates, respectively.

1.4.3. Summary of 0

0 is the first chapter to be constructed as a scientific article, with the objective of a submission in a peer-reviewed journal in early 2026. It presents a side-project which has occupied a significant place in the timeline of my PhD and yielded interesting results.

Because I mainly used in this project very distal sediment records (i.e., marine sedimentary cores), the question of transport duration from continental environments to marine basins is important. First, significant burial or long-term exposure (i.e., 100ka) during transport might significantly impact the measurement of cosmogenic nuclides (see Chapter 2). Second, because my objective is to correlate paleo-denudation rates to climatic events, a significant uncertainty on the age of erosion of the sediments studied is of concern. Historically, the age of turbidites correspond to their time of deposition. We have developed a method, based on ^{14}C dating of continental and marine elements present in the turbidites and in the hemipelagic layers surrounding it. This original approach allowed us to quantify the time of transfer from the continent to the deep sea. This method will be further presented in Chapter 2.

In 0, we apply this method to our sedimentary records of the Ogowé system and find mean transport durations from the continent to the deep sea of 12.9 ± 0.2 ka. In the future, and before publication of this work, a second area will be studied, the Var sedimentary system, which has the advantage of presenting steep slopes and a good connectivity between the continental and submarine sedimentary systems. A pilot study has already shown transfer times of less than 1 ka in this area.

1.4.4. Summary of 0

0 is the second chapter to be constructed as a scientific article, with the objective of a submission in a peer-reviewed journal, in 2026. It presents the first ^{10}Be paleo-denudation rate reconstruction of the Ogowé sedimentary system.

In 0, results for turbidites of cores KC10, KC11 and KC13, and cuttings of the Torpille Marine (TM) drilling are presented. The results of 0 are used to constrain the transport time of sediments from the continent to the deep sea. Additionally, $^{26}Al/^{10}Be$ burial ages (see Chapter 2 for the method) were calculated to constrain possible storage of sediments and to verify the age model of the TM cuttings. Overall, our results show near-steady denudation since the Pliocene, although the Mid-Pleistocene Transition may have had an effect on the paleo-denudation rates. The rates obtained are consistent with modern denudation of the Ogowé catchment.

1.4.5. Summary of 0

0 is the third chapter to be constructed as a scientific article and corresponds to the first submission of this thesis work to a peer reviewed journal, the Journal of Geophysical Research, Earth Surface. It has been published in 2025. This published version is presented in this manuscript. This chapter presents the first ^{10}Be paleo-denudation rate reconstruction of Madagascar.

0 extends 0, by applying the same method to a different region. The main objective is to reconstruct paleo-denudation rates of SW Madagascar over the past 900 ka. Modern denudation rates of 5 of the main rivers draining SW Madagascar are also presented, to compare paleo and modern denudation rates.

To constrains the sediment sources, we also use εNd and Heavy Minerals. Our results show that over the past 900 ka, sediment sources have not varied significantly, and any changes are uncorrelated to climatic signals. Paleo-denudation rates of SW Madagascar are consistent with modern denudation of the island and have not varied significantly since Late Pleistocene.

1.4.6. Summary of 0

0 is the fourth, and last chapter to be constructed as a scientific article, with the objective of a submission in a peer-reviewed journal in 2026. It presents new ^{10}Be data of modern river sands of SW Madagascar, along with a review of denudation and uplift rates over Madagascar in the Cenozoic.

In 0, we have investigated the steadiness of the landscape of Madagascar. In this chapter, we present 9 new ^{10}Be catchment denudation rates of SW Madagascar that are used to complete the existing dataset of 104 datapoints on the island. This gives us a general overview of the spatial distribution of modern denudation in Madagascar. We also compile published Low Temperature Thermochronology data which we use to calculate long term paleo-denudation rates throughout the Cenozoic. Finally, we use a published landscape evolution model which uses previous work on planation surfaces to reconstruct the spatial distribution of uplift of the island. We compare these datasets and conclude on a long-term steady state of the landscape, with a tectonic control of Cenozoic denudation rates in Madagascar.

Supplementary Information

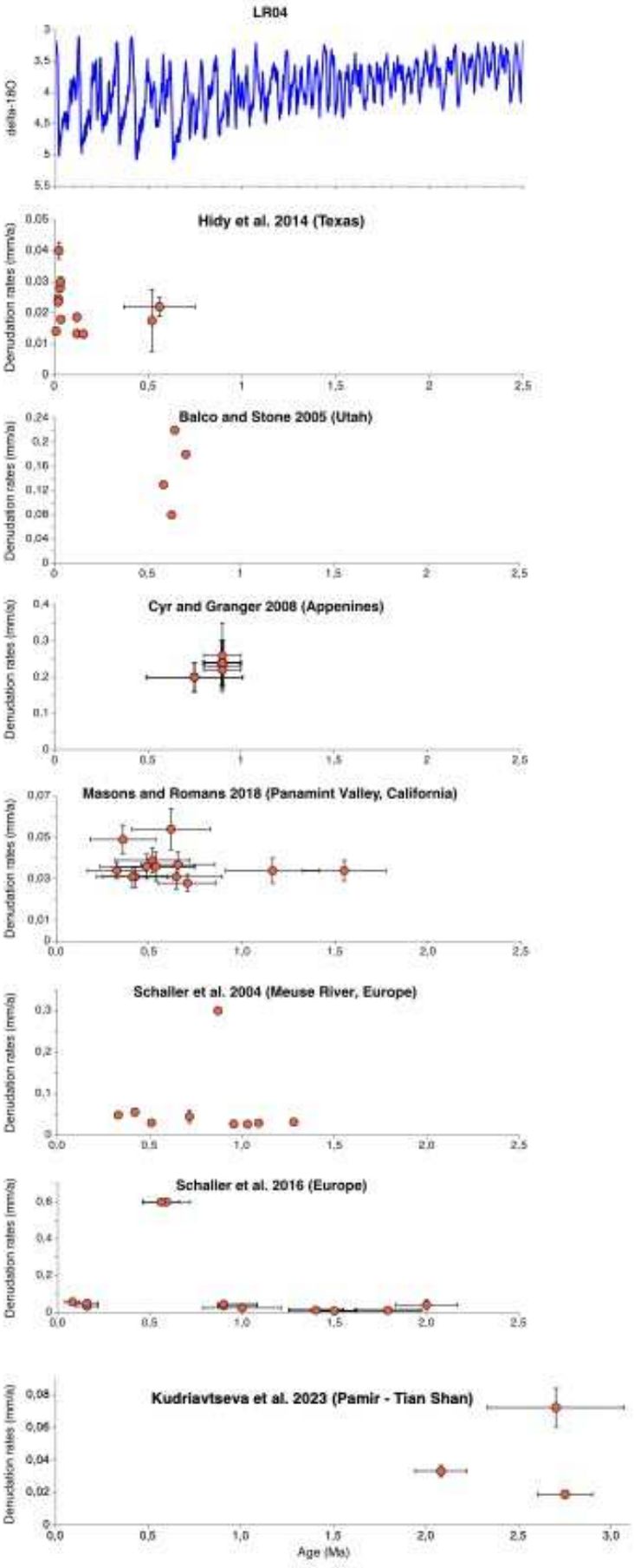

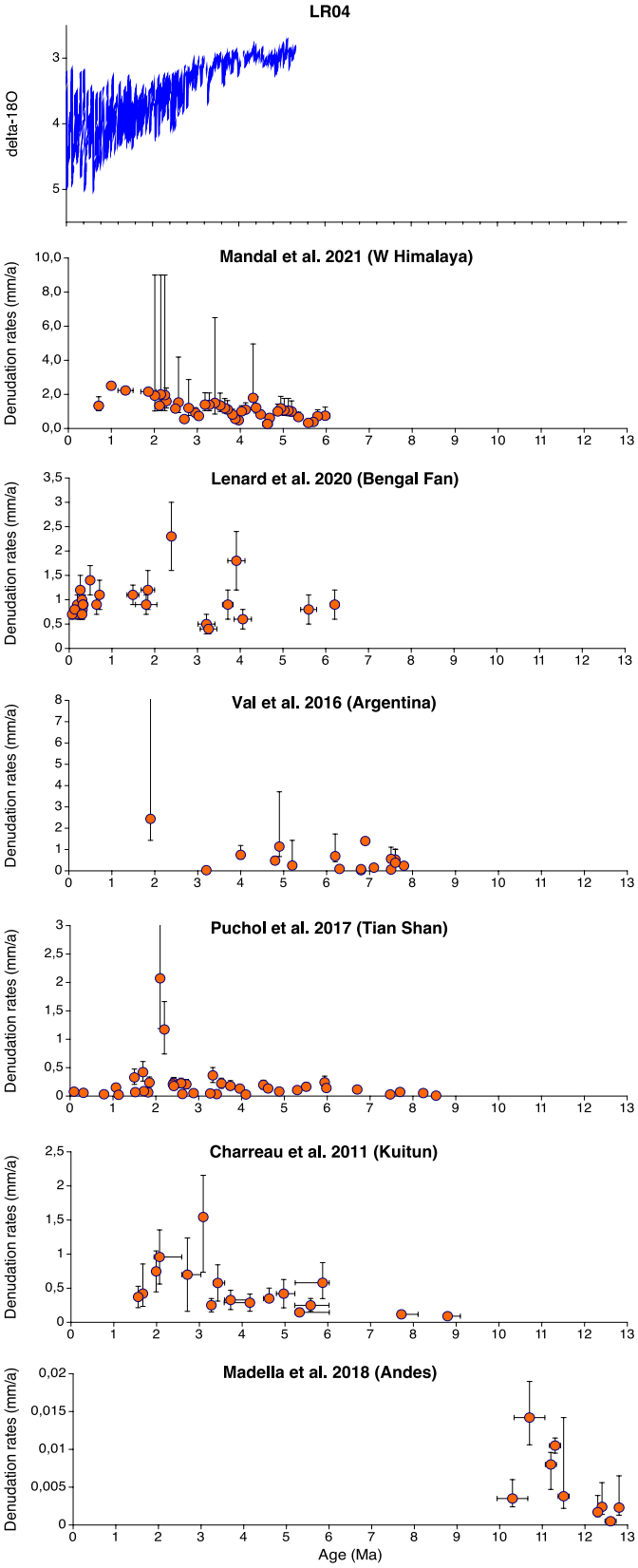
LR04
delta-18O
Mandal et al. 2021 (W Himalaya)
Lenard et al. 2020 (Bengal Fan)
Val et al. 2016 (Argentina)
Puchol et al. 2017 (Tian Shan)
Charreau et al. 2011 (Kuitun)
Madella et al. 2018 (Andes)
Denudation rates (mm/a)
Age (Ma)

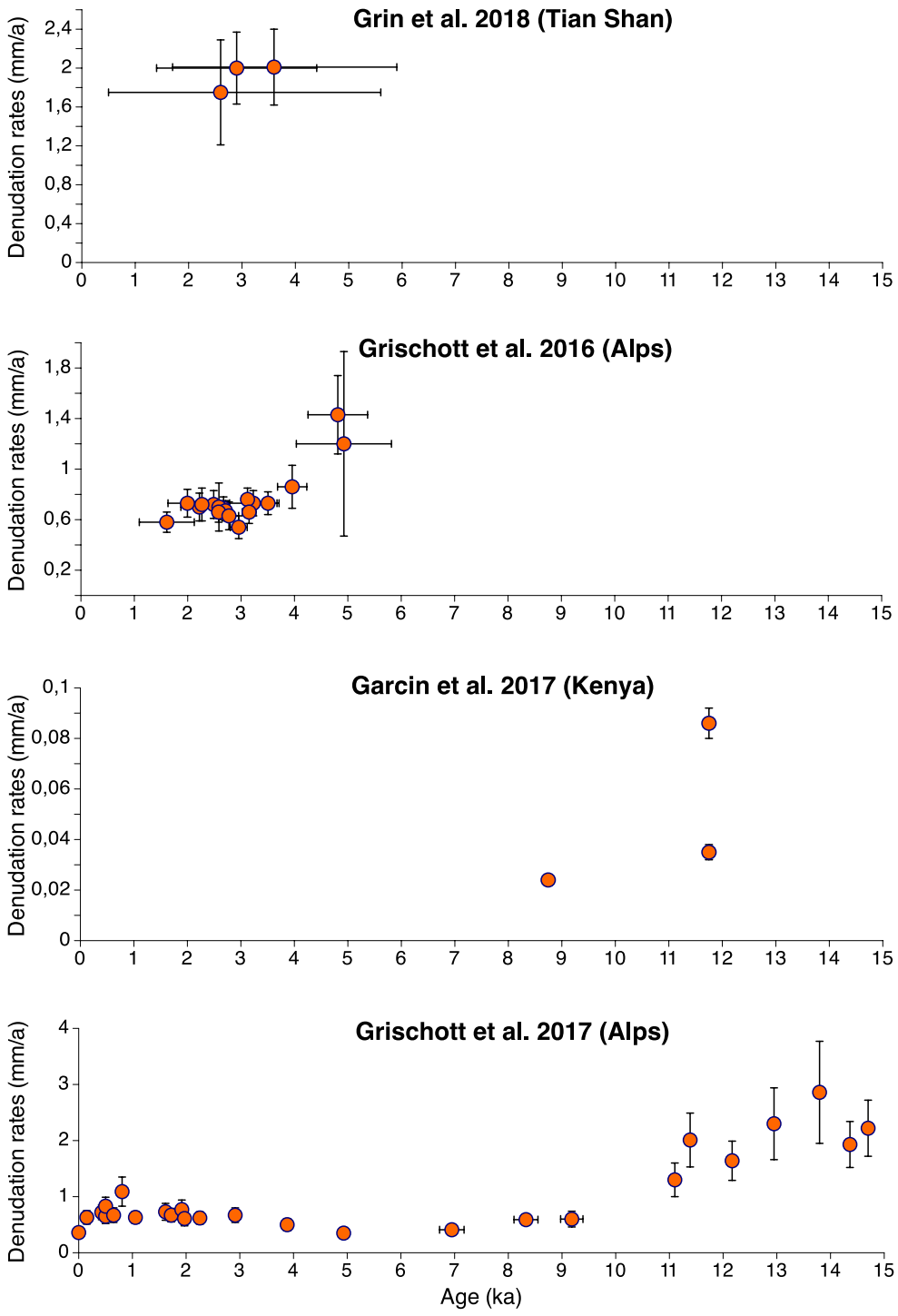
Grin et al. 2018 (Tian Shan)
Grischott et al. 2016 (Alps)
Garcin et al. 2017 (Kenya)
Grischott et al. 2017 (Alps)
Denudation rates (mm/a)
Age (ka)

Chapter 2. Methods

In this Chapter, the different methods used during this PhD are presented. Cosmogenic nuclides, and particularly ^{10}Be denudation and ^{26}Al/^{10}Be burial are presented first, followed by turbidite transfer time estimations with ^{14}C. Finally, two other methods, Low Temperature Thermochronology and εNd are presented.

2.1. Cosmogenic nuclides

Cosmic rays are high energy particles (1GeV < E < 10^{10}GeV) which originate from supernovae explosions, and are composed of protons (87%), α-particles (12%) and heavier nuclei (1%) (Dunai, 2010). When they reach the Earth's atmosphere, they interact with it creating secondary cosmic rays, mainly consisting in neutrons and muons (Figure 2.1). An electromagnetic component also exists but is not relevant to Earth Science and will thus not be tackled in this work. This secondary cosmic radiation creates new nuclides in the Earth's atmosphere (called atmospheric cosmogenic nuclides) and within certain mineral matrices (called *in-situ* cosmogenic nuclides). It is only the latter that we used and in which we are interested in this work.

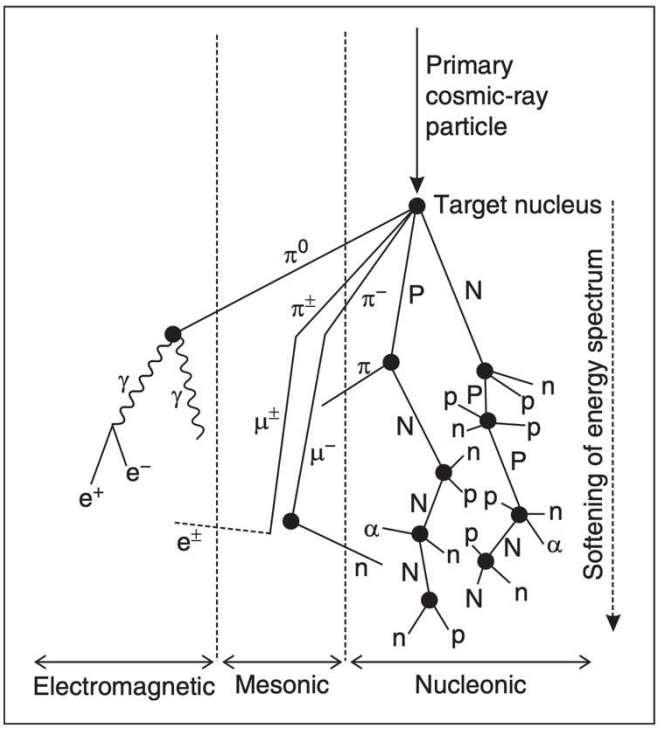

Figure 2.1: Interaction between primary cosmic rays and the atmosphere creating the three components of the secondary cosmic radiation. Figure is from Dunai (2010).

The existence of cosmic rays was first suggested by the pioneer work of Domenico Pacini (Carlson and De Angelis, 2011), and then confirmed and demonstrated by the work of Victor Hess (1912) after he observed an altitudinal increase of radiations during a near-total eclipse of the sun with an electroscope on a hot air balloon. Since the origin of this radiation could not be the solar wind, he concluded on a different origin of these cosmic rays. Following this discovery, Willard Libby was the first to propose radiocarbon dating as the first application of atmospheric cosmogenic nuclide by dating wood samples of an Egyptian tomb of which the age was well constrained. This development led him to receive a Nobel Prize (Libby and Johnson, 1955). Years later, Devendra Lal (1991) published the equations to describe the evolution of *in-situ* cosmogenic nuclides within geological surfaces. In this publication, Lal also constrained the production rates of *in-situ* ^{10}Be and ^{26}Al and the methodology to use these nuclides. As the trajectories and the flux of cosmic particles are attenuated by the Earth's magnetic field and by the atmosphere, cosmogenic nuclide production rates are highly dependent on latitude and altitude (Lal, 1991; Stone, 2000). Neutrons and muons also have penetration depths that depend largely on the density of the medium they penetrate and are subject to exponential attenuation in matter. Spallation reactions from fast neutrons is the dominant mechanism of cosmogenic nuclide production at the Earth's surface. However, at depth, this reaction is quickly attenuated and decay following an exponential factor every 60 cm under the ground. Thus, the longer a mineral has spent in the 60 cm below the surface (low denudation rates), the higher its cosmogenic nuclide concentration. Nuclide concentrations are therefore inversely proportional to denudation rates (Brown et al., 1995).

By using two different nuclides with different production rates and radioactive half-lives, burial dating is also possible (Lal and Arnold, 1985). Finally, *in-situ* cosmogenic nuclide concentrations can also be used for surface exposure dating, the concentration of these nuclides being directly related to the time during which production occurred as long as erosion can be independently constrained or neglected. In the following sections, I will present the two former methods, as exposure dating was not used in my work.

2.1.1. ^{10}Be denudation rates

The *in-situ* cosmogenic nuclide concentration (N) as a function of depth (z) and time (t) is given by:

$$N(z,t) = N_0\, e^{-\lambda t} + \frac{P_0}{\lambda + \mu\varepsilon}\, e^{-\mu z}\,(1 - e^{-(\lambda+\mu\varepsilon)t})$$

With N_0 the inherited initial concentration, λ (1/a) the decay constant of the considered nuclide ($\lambda = \ln(2) / t_{1/2}$; $t_{1/2}$ the half-life), $\mu = \rho/\Lambda$ (ρ the density in g/cm^3 and Λ the attenuation length in g/cm^2), ε the denudation rate (cm/a) and P_0 the production rate (at/g/a) at the surface (z = 0).

If we consider the following assumptions:

- The soil surface is a fixed Euler referential (z = 0);
- There is no inherited concentration ($N_0 = 0$);

- The surface has been subject to constant erosion ε for a long time, such as $t > \lambda+\mu\varepsilon$;
- Erosion rates are sufficiently high to assume that $\lambda << \mu\varepsilon$;

Then the equation simplifies into:

$$\varepsilon = \frac{P_0}{N\mu}$$

and permits to compute denudation rates.

This measured denudation is averaged over an integration time, which corresponds to the time during which the nuclide is produced within the mineral matrix. In the case of ^{10}Be, most of its production in quartz takes place within the upper 60 cm below the surface, over the time the mineral took to cross these 60 cm during soil denudation. For example, for a denudation rate of 100 mm/ka, the integration time is 6 ka (600mm x 1ka / 100mm).

Denudation can be integrated to entire catchments by measuring ^{10}Be concentrations in quartz grains sampled in active (and ancient) river sands, at the outlet of the considered catchment. This method was first proposed by Brown et al. (1995) in Porto Rico. They were the first to demonstrate that cosmogenic nuclides measured in river sands have the property to integrate the mean denudation rate ε_{mean} of the catchment:

$$\varepsilon_{mean} = \frac{P_{mean}}{N_{mean} \times \mu}$$

with P_{mean} the mean production rate of the catchment and N_{mean} the mean concentration of ^{10}Be of the sediments produced by erosion. This method has been largely used in the Earth Science community since this original publication and the principles behind it have been thoroughly tested and approved (e.g., Granger et al., 1996; Portenga and Bierman, 2011; Regard et al., 2025).

This method can also be applied to sedimentary records (e.g., Balco and Stone, 2005; Mariotti et al., 2021; Puchol et al., 2017) to reconstruct paleo-denudation rates. In this case, several assumptions and corrections must be made:

- The age of deposition t_d of the sedimentary archive must be constrained in order to correct for radioactive decay ($N = N_{measured}\, e^{-\lambda td}$);
- The paleo-catchment has not significantly evolved since erosion of the sampled sediments, in terms of size, latitude and altitude;
- Production during transport and burial of the sediments can be estimated or neglected.

2.1.2. ^{26}Al/^{10}Be burial dating

In 2006, Granger presented a review and history of dating techniques using the ^{26}Al/^{10}Be ratio, of which the following paragraph is a summary. The principle behind the use of two cosmogenic nuclides is based on the fact that the two nuclides employed (^{26}Al and ^{10}Be) have different half-lives (0.7 Ma and 1.38

Ma, respectively). Assuming a secular initial equilibrium, the concentration of the two nuclides will decay at different rates through time, thus creating a geochronometer.

The first use of cosmogenic nuclides as a "burial" geochronometer was the estimation of the terrestrial age of meteorites (e.g., Arnold, 1961; Honda et al., 1961). Terrestrial detection of cosmogenic nuclides came later and was laborious at first (Hampel et al., 1975; Tanaka et al., 1968) because of their very low concentration in the terrestrial material. Novel developments and applications of Accelerator Mass Spectrometry (AMS) techniques (Brown, 1984), allowed the first detection of *in-situ* produced cosmogenic nuclides (Yiou et al., 1984) and led Lal and Arnold (1985) to point out the suitability of quartz for ^{26}Al and ^{10}Be measurements and to theorize for the first time the possibility of burial dating with the ^{26}Al/^{10}Be ratio. A year later, Klein et al. (1986) measured *in-situ* ^{26}Al/^{10}Be ratios in Libyan desert glass and concluded that its use for exposure and burial dating was possible. They showed that all possible measurements fell within a given range limited by a maximum ratio, bounded by the production rate ratio, and a minimum ratio controlled by the steady state erosion rate, both being modulated by the half-lives of ^{26}Al and ^{10}Be. These limits were put in the form of a graph later modified (Lal, 1991; Nishiizumi et al., 1991), giving birth to what is now commonly referred to as the "banana plot", because of the banana-shaped area representing the "erosional island", within which all samples exposed at the surface should theoretically belong, whatever the denudation rate (Figure 2.2).

The lower bound curve of the banana plot, which gives the graph its name, is the area in which are located and locked all the samples affected by steady-state denudation. Samples located on the top-most limit of this graph are on the contrary unaffected by erosion (Figure 2.2). The samples plotted on this

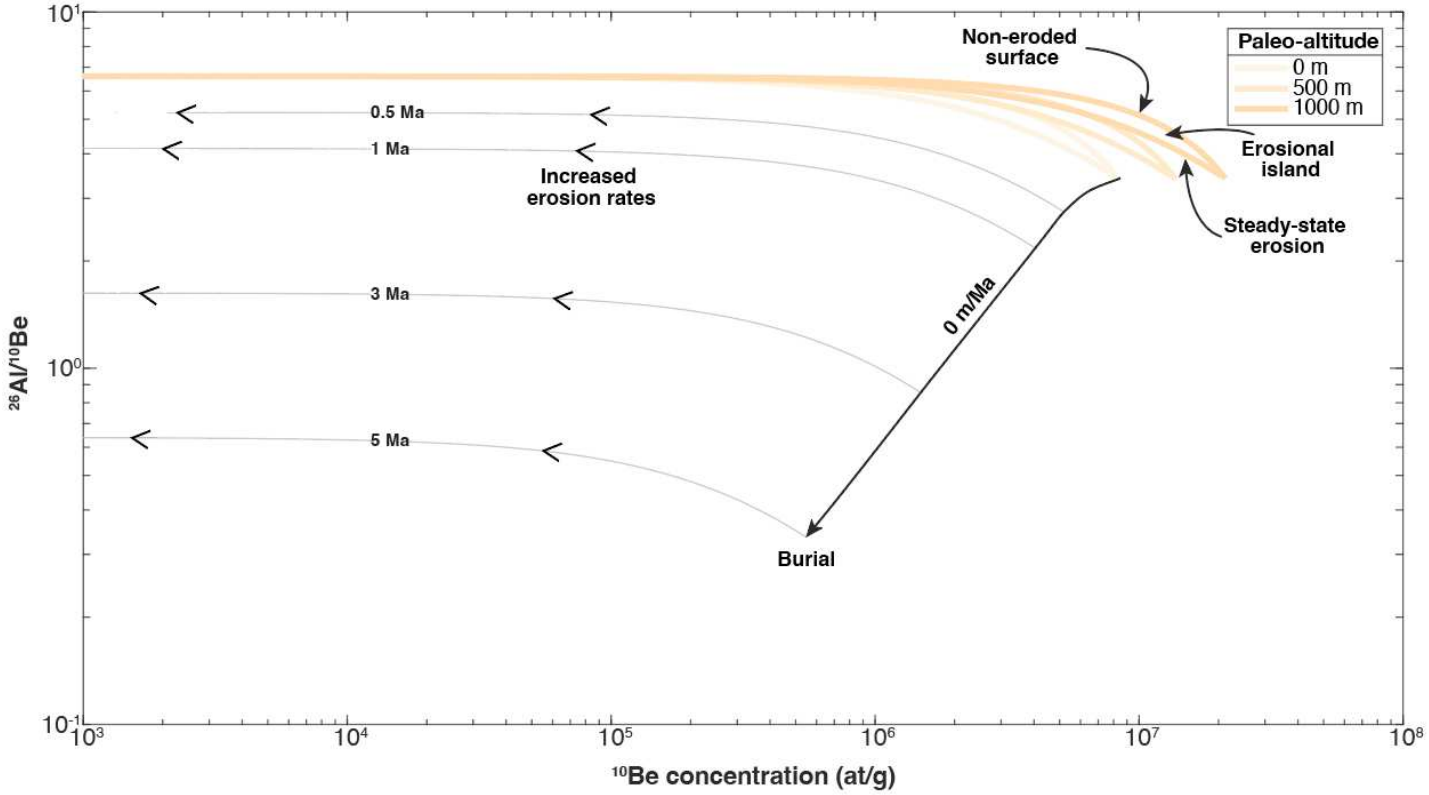

Figure 2.2: Example of a banana plot and its significance.

graph, however, display uncertainties that makes it impossible to determine a single exposure-erosion scenario.

Below this "banana", to the left, is the so called "authorized area". This corresponds to the allowed range defined by Klein et al. (1986). All other regions are forbidden. Data points belonging to these areas either suggest an analytical issue or an altitudinal (or depth of exposure) change (for points that are located on the right forbidden part) during the exposure history of the sample (Blard et al., 2019a). The lower positions, corresponding to lower $^{26}Al/^{10}Be$ ratios, are samples that have been affected by burial from cosmic rays, over durations that are long enough to have induced a significant radioactive decay, thereby decreasing both the ^{10}Be concentration and the $^{26}Al/^{10}Be$ ratio. Within the authorized area, samples located to the right of this area, with higher ^{10}Be concentrations correspond to samples affected by slow pre-burial denudation rates, whereas the further we move towards the left, the lower the ^{10}Be concentrations and thus the higher the corresponding pre-burial denudation rates (Figure 2.2).

At the surface, the concentrations of each nuclide with time C(t), is controlled by production rates P, radioactive decay constant λ, density ρ, erosion rate ε, and attenuation length Λ (Lal, 1991):

$$C(t) = \frac{P}{\lambda + {\rho\varepsilon}/{\Lambda}} \times \left(1 - e^{-\left(\lambda + {\rho\varepsilon}/{\Lambda}\right)t}\right)$$

with a production ratio at the surface (P_{10}/P_{26}) of ca. 6.6.

When elements are buried, the evolution of the concentrations of ^{26}Al and ^{10}Be are linked by:

$$\frac{\lambda_{26} - \lambda_{10}}{f} = \frac{P_{26}}{N_{26}} e^{-\lambda_{26} \times t} - \frac{P_{10}}{N_{10}} e^{-\lambda_{10} \times t}$$

with t, the duration of burial and f the geographic correction factor (Blard et al., 2019a).

To measure burial ages with this method, samples need to be first exposed, so that their initial concentrations fall within the erosional island or banana (Figure 2.2), and their burial must be sufficiently rapid and deep so that negligeable production of nuclides occur during burial. Note that the production ratios can also allow to reconstruct paleo-altitudes of basins (Blard et al., 2019a) which is also shown in Figure 2.2. Higher altitude basins will shift the banana plot towards the right.

2.1.3. ^{10}Be and ^{26}Al extraction protocol

The process of extracting cosmogenic nuclides from detrital sediments is long and typically requires weeks of intense lab work. It starts by crushing samples to obtain individual grains. In this work, because samples used were all sands (marine cores or alluvial), this step was not necessary. In the case of ^{10}Be and ^{26}Al analysis, the measurements are done in quartz grains, which are typically concentrated in the 100-800 µm granulometric fraction. Sediments are thus sieved to isolate the required fraction. In our case, since we processed relatively distal marine sediments, we were obliged to select much finer fractions, leading to the selection of the 50-250 µm range, permitting to get as much material as possible. Once sieved, sediments are processed through a Frantz magnetic separator to remove the non-magnetic

fraction (Rosenblum, 1958). Then, quartz grains are concentrated, by acid attacks. Several rounds of a mixture of concentrated 1/3 HCl (typically 36% weight proportion) + 2/3 H_2SiF_6 (typically 41% weight proportion) are used to dissolve all grains but quartz. This step is repeated until the acidic solution is clear. Samples are then checked under the binocular to verify the purity of the quartz. These first steps of the protocol are presented in Figure 2.3.

After this step the quartz is decontaminated from atmospheric cosmogenic nuclides by 3 steps of etching to remove a total of 30% of each grain, following Brown et al. (1991), using the ad hoc amount of concentrated HF (48%). A new clean lab was opened at CRPG in 2023, in which the chemical extraction of cosmogenic nuclides is now routinely done. Quartz decontamination is the first step of the protocol to be done in the clean lab (Figure 2.3). Decontaminated quartz samples are then spiked with solutions of known ^{9}Be and ^{27}Al concentrations and having low $^{10}Be/^{9}Be$ and $^{26}Al/^{27}Al$ ratios (10^{-16} and $< 5\ 10^{-16}$, respectively), before being digested in HF. Once quartz grains are totally dissolved (after a few days), a solution aliquot (few mL) is sampled for ^{9}Be and ^{27}Al measurements, as these can be naturally present in some sediments. HF-rich solution samples are then evaporated (at 110°C) and redissolved in HCl. Samples are then passed through an anion exchange column (Dowex 1x8 resin), evaporated and redissolved in HCl before being precipitated at pH = 8, at which Be and Al are both precipitated. After HCl conversion, samples are passed in a cationic exchange column (Dowex 50Wx8 resin) during which Be and Al are separated. Both Be and Al fractions undergo a new chloride conversion before being precipitated again at pH = 8. All samples are then oxidized at 700°C for 1 hour. Finally, samples are loaded in cathodes with adding of niobium powder for Be samples and silver powder for Al samples (same volume as the sample is added) and sent to the AMS ASTER facility in CEREGE (Aix-en-Provence) for measurements of the $^{10}Be/^{9}Be$ and $^{26}Al/^{27}Al$ ratios.

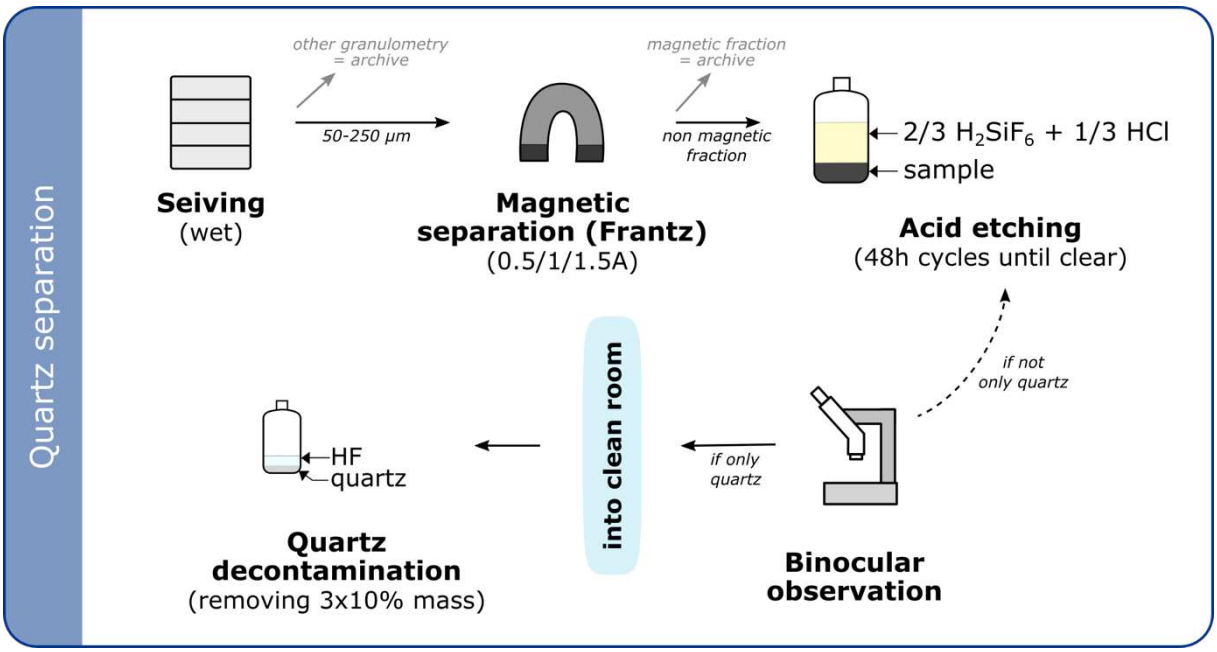

Figure 2.3: First steps of Quartz concentration before chemical separation of ^{10}Be and ^{26}Al. Personal communication from Marie Protin.

At the beginning of my PhD, increasing concerns arose on the loss of Al during this protocol, notably with measurement of two sand samples from active bars of the Isère River, sampled north of Romans-sur-Isère, close to the Alps, which yielded $^{26}Al/^{10}Be$ ratios of 1 ± 0.3 and 1.2 ± 0.4. These results being inconsistent with the regional geological context, we deduced a problem with the chemical extraction protocol, that might have led to an underestimation of the ^{26}Al concentration. Together with the lab manager Marie Protin, we designed a series of tests to check this potential issue. For this, aliquots collected at different steps of the protocol during one of my series (Figure 2.4) confirmed a loss of Al during the chemistry and enabled us to identify the key steps where the loss happened, namely, evaporation after first dissolution in HF and precipitations. The study of previously published work (Corbett et al., 2016; Hunt et al., 2008; Merchel et al., 2019) along with supplementary tests, allowed us to elaborate a new protocol for the extraction of ^{10}Be and ^{26}Al which is presented in Figure 2.5. These tests, along with the elaboration of the new protocol was mainly undertaken by Marie Protin (research engineer at CRPG). The main differences with the previous CRPG protocol are the addition of a fluoride breaking step with 6M HCl, as fluorides tend to trap Al resulting in a big loss, and the washing of the final precipitate which was not routinely done at CRPG before. This washing limits the possibility of Al hydroxide to be carried away when heated afterwards, by removing NH_4Cl. Additionally, it was found useful to leave the precipitate sit for at least 2h before centrifugation as it limits the loss of Al in the supernatant (Merchel et al., 2019).

This evolution of protocol has led to the production of very clean blanks (10^{-16}) and measurements of standards (UVM-A and Cronus-A, Corbett et al., 2019; Jull et al., 2015) within expected concentrations. This will further be addressed in 0 of this manuscript.

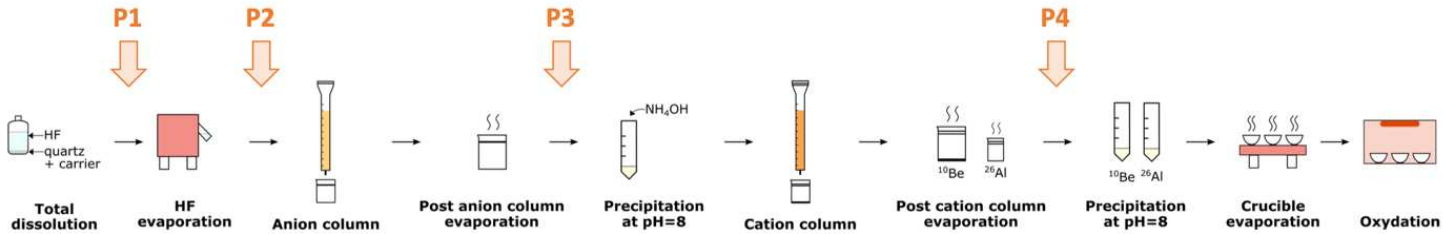

Figure 2.4: Steps at which aliquots were sampled to measure ^{27}Al and ^{9}Be concentrations and check for potential loss. Personal communication from Marie Protin.

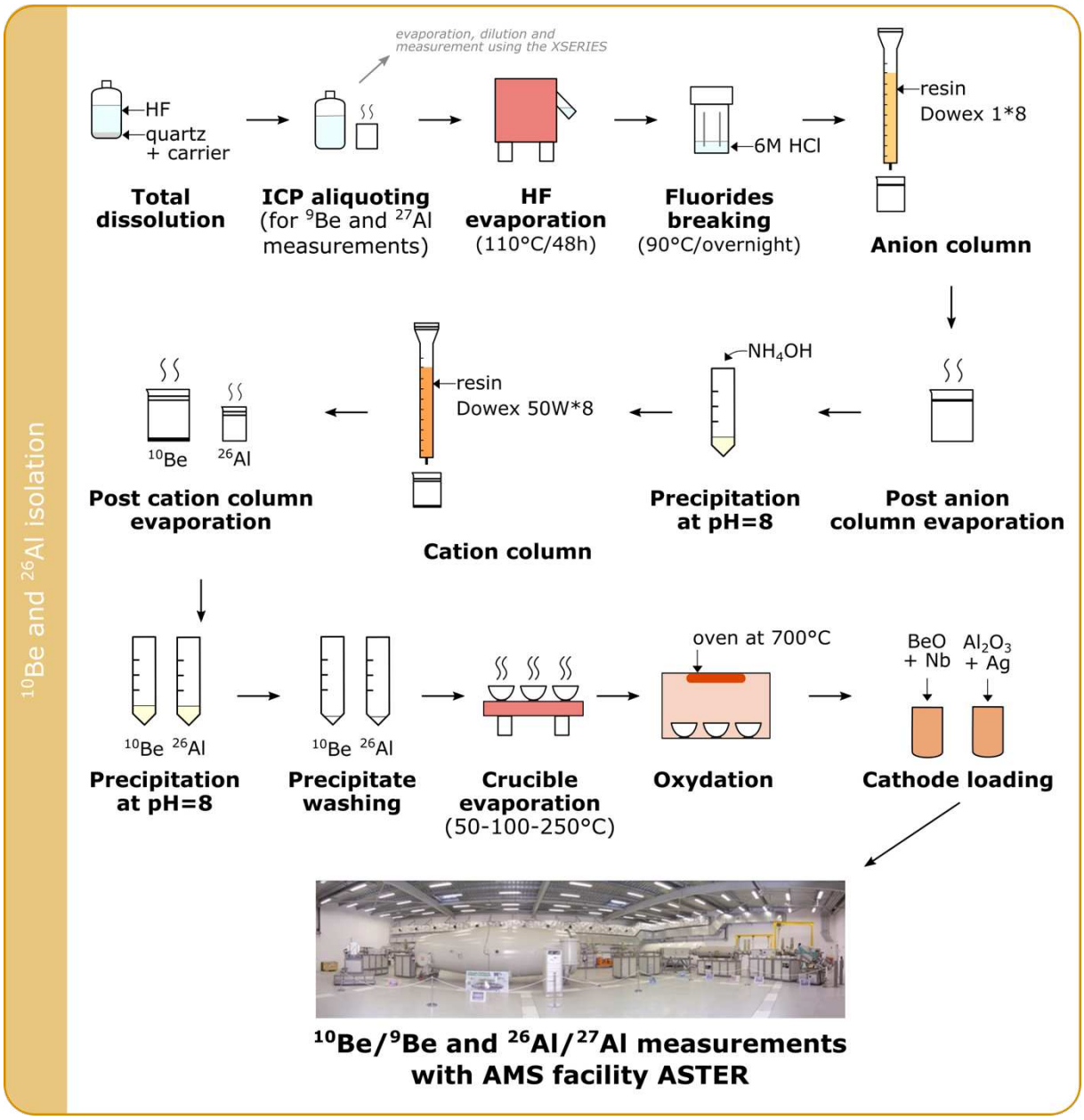

Figure 2.5: Steps of the actualized protocol of CRPG for ^{10}Be and ^{26}Al extraction. Personal communication from Marie Protin.

2.2. Sample dating and transfer times

To reconstruct a history of the variations of denudation as accurate and precise as possible, it is essential to constrain the ages of the analyzed sediments. However, we need to distinguish between the age of sediment deposition in the distal submarine domain and the age of erosion. In the case of turbidites, only the age of deposition is known as they are considered as records of instantaneous events when dating cores (i.e., only the hemipelagic deposition is dated, and intercalated turbidites are considered instantaneous). In this work, we are interested in the age of erosion of the sediments transported by the turbidity currents. However, a significant transport time (i.e., 10-100 ka) could lead to the association

of denudation variations to the wrong climatic events. Questioning the age of the material used is the third chapter of this thesis.

To calculate the age of the sediments transported by turbidity flows, and their total transport time, certain elements contained in these sediments were dated by ^{14}C. Foraminifera, microscopic organisms (10-500 µm) with a carbonate exoskeleton, represent a non negligeable proportion of hemipelagic sediments, that are dominated by clays and silty fractions. As turbidity currents are highly erosive, foraminifera are also transported during these events, incorporated into the flow as it erodes the seabed in its path. Turbidites are largely composed of terrigenous material, and thus also potentially carry plant debris (leaf debris, twigs). The difference between radiocarbon ages of these plant debris, referred to here as turbiditic (TVD in this manuscript), and the hemipelagic foraminifera (referred in this manuscript as HPF) gives us the total transport time from the erosional continental environment to the deep marine environment of deposition (ΔT_{trans}, Figure 2.6). The difference between radiocarbon ages of turbiditic foraminifera (i.e. foraminifera contained in turbidite deposits, referred to as TPF in this manuscript) and the hemipelagic foraminifera (HPF), gives us the average marine storage time upstream of the turbidite deposition site, before remobilization by the turbidity current (ΔT_{stor}, Figure 2.6). Finally, the ^{14}C ages of the hemipelagic foraminifera (HPF) directly above and below the turbidite in the core give us minimum and maximum deposition ages, respectively (T1, Figure 2.6), the minimum age being the most accurate, since the hemipelagic sediments below the turbidite deposit were certainly affected by erosion during the latter's deposition. The difference between ΔT_{trans} and ΔT_{stor} also yields an estimate of the duration of continental transport of sediments, ΔT_{cont} (Figure 2.6).

These different objects, contained within the turbiditic and hemipelagic deposits, were all picked with a small wet brush under the binocular. Examples of the picked samples are given in Figure 2.7. In interval 91-92 cm of core KC11, I found what appeared to be wood resin, that I sampled for ^{14}C analysis. The vegetal debris were picked based on the absence of recrystallisation on them and the fact that they were complete (what looked like entire twigs or leaf pieces). Finally, in all the samples, the same type of foraminifera was found, corresponding to the globigerina family. These were found both in turbidites and hemipelagites, although the ratios varied from one sample to the other. The foraminifera were picked based on their absence of fracture (complete shells) and recrystallization. Coarser samples were also selected as they are easier to pick.

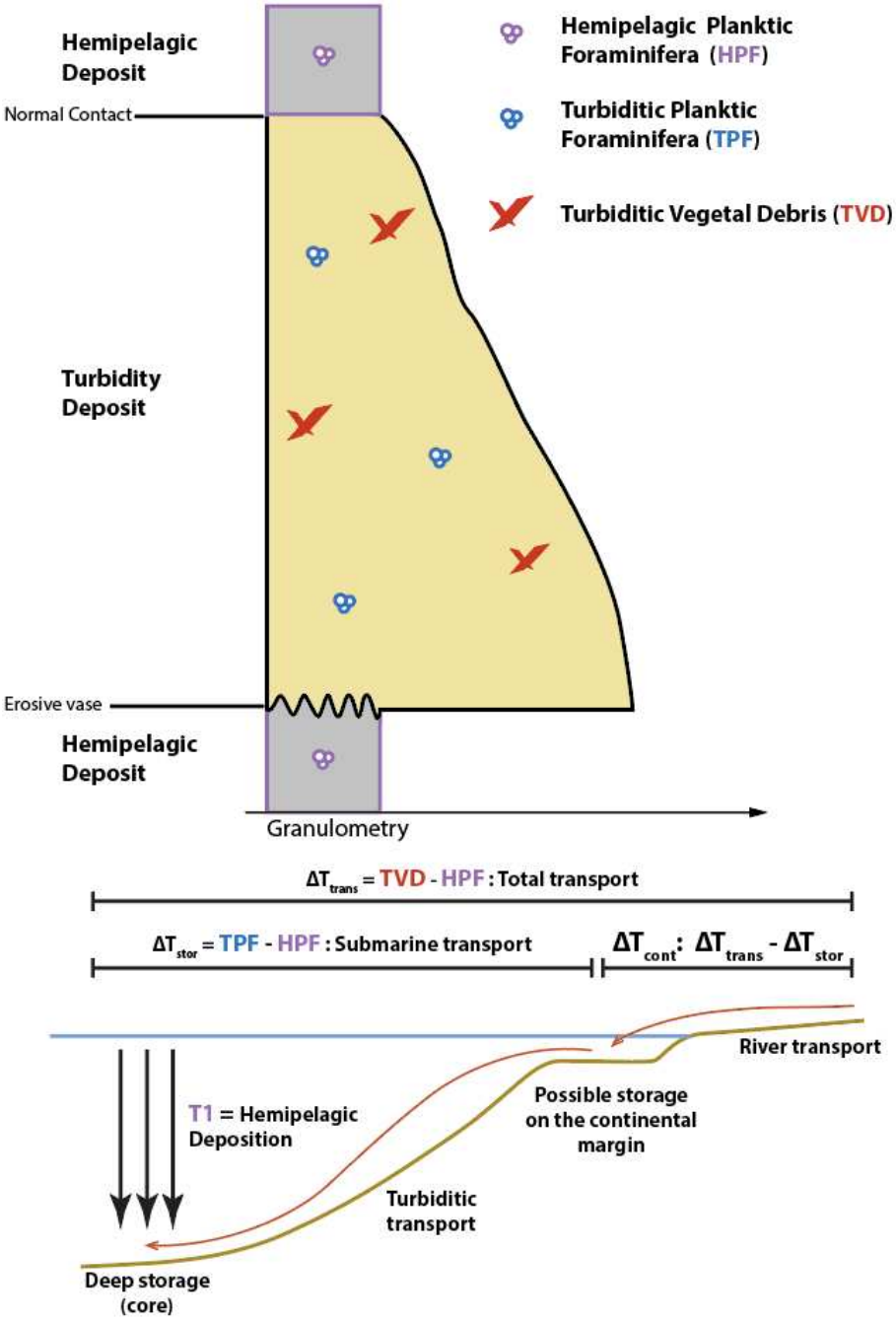

Figure 2.6 : Sedimentary transport by turbidity currents and implication of the ages of the different types of material they carry.

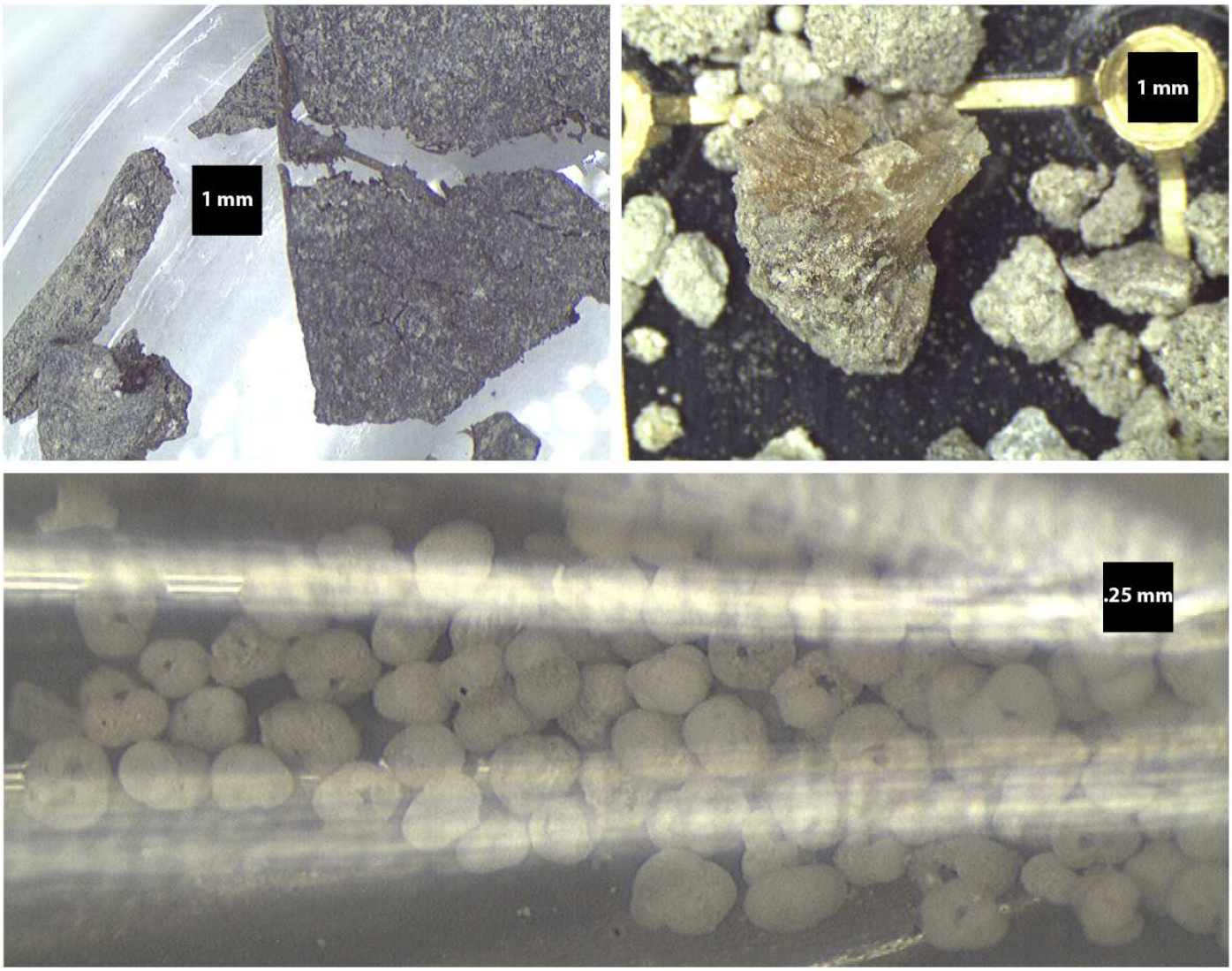

Figure 2.7: Different types of material picked for radiocarbon dating. Top left picture shows plant debris, picked in sample KC11 124-130 cm. On the top right picture are what we believe to be wood resins, found in sample KC11 91-92 cm. The bottom picture shows the type of foraminifera picked in all samples.

2.3. Low-Temperature-Thermochronology

A thermochronometer is defined by a radioactive couple enclosed in a crystalline system whose closure (i.e., the conservation of daughter element) is dependent on temperature, thus enabling the measurement of the system's cooling process rather than its crystallization. Low-temperature thermochronometers (LTT) are typically employed to ascertain the time-temperature history of the subsurface (< 5 km depth) and to infer the nature of exhumation and burial events, considering a stable geothermal gradient. Several LTT exist but I will present in the following only the two presented in this manuscript, Apatite Fission Tracks (AFT, age and length) and (U-Th)/He method on Apatites (or AHe). Donelick et al. (2005) justify the use of apatite by several reasons: (i) apatite minerals are relatively abundant but mostly

ubiquitous on Earth; (ii) their physical properties make them resistant to surface processes and easy to separate from other minerals; (iii) they contain appropriate major and minor chemical elements; (iv) they are naturally rich in uranium and thorium, the former being responsibe for AFTs, and both of them being responsible for (U-Th)/He (see below); (v) they retain fission tracks (FT) and He above a certain temperature (see below) with great success; (vi) spontaneous fission of ^{238}U, and diffusion of He can be experimentally reproduced in apatites using induced fission of ^{235}U, and ^{3}He implentation, respectively.

2.3.1. AFT

Apatite Fission Track (AFT) analysis is a long-known thermochronometric method, based on spontaneous nuclear fission of ^{238}U in apatite grains (e.g., Donelick et al., 2005; Laslett et al., 1987; Price and Walker, 1963; Tagami and O'Sullivan, 2005), which damages the mineral lattice, creating a fission track (FT) of about 16 µm length (e.g. Donelick et al., 2005; Tagami and O'Sullivan, 2005) which is visble when the mineral is etched by acid. These tracks are annealed or shortened with increasing temperature and time (e.g., Carlson et al., 1999; Green et al., 1986, 1985). In apatites, the range of temperatures where these tracks are generally annealed known as the partial annealing zone (PAZ), generally span from ~60°C to 110°C, (Carlson, 1990; Corrigan, 1993; Fitzgerald and Malusà, 2019; Gleadow et al., 1986; Ketcham et al., 1999; Laslett et al., 1987). The number of FT (relative to the ^{238}U content), and their length distribution provides insight both on the time since the mineral passed the PAZ as well as the time the mineral spent within the PAZ, respectively.

Intrinsic cristalline controling factors of annealing are (i) orientation of the FT with respect to the mineral lattice and (ii) chemical composition of the mineral. These controling factors are defined by etching of the FTs and measurement of their width (Barbarand et al., 2003; Ketcham et al., 2007). The exploitation and interpretation of AFT results are done thanks to FT annealing models that integrate all parameters (i.e., time, temperature, cristalline structure, FT length,…). For apatites, the recognized model is Ketcham et al. (2007).

2.3.2. (U-Th)/He (AHe)

Helium (He) is produced within mineral matrices by the radioactive decay of ^{238}U, ^{235}U, ^{232}Th and ^{147}Sm producing respectively 8, 7, 6 and 1 α particles, each particle corresponding to a He nucleus. When the α particle is emitted, it interacts with its surroundings, incorporating two electrons and thus creating a ^{4}He atom. Because Sm contributes very little to the He production compared to other elements, and because its effect was discovered later, this method is typically referred to as (U-Th)/He, or AHe when the measurement is done on an apatite grain. Note that for every two million ^{238}U atoms that experience α-decay, only one will experience spontaneous fission, making the (U-Th)/He thermochronometer, theoretically much more sensible. In the same way that AFT are annealed at temperatures within and

above the PAZ, He is diffused out of the mineral lattice of apatite above a certain temperature range known as the Partial Retention Zone (PRZ). The diffusion of He in mineral lattices is however complex, depending on the mineral lattice type, composition and defects (Farley, 2000; Shuster et al., 2006). To model the diffusion of He in apatite, two main models exist (Flowers et al., 2009; Gautheron et al., 2009) and are currently used to interpret AHe results.

2.4. Neodymium isotopes

In 0, because of the widespread catchment feeding sediments to the deep depocenter, and the several rivers draining that catchment, we wanted to verify that major changes in sources, that could control the variations of denudation rates, did not affect our sediment record. Nd isotopes, or more exactly, variations in the abundance of the radiogenic isotope ^{143}Nd, formed by the decay of ^{147}Sm, normalized to the abundance of the non-radiogenic isotope ^{144}Nd are commonly used in source studies. Unlike stable isotope tracers, abundances of the radiogenic isotope ^{143}Nd are not directly affected by weathering processes, making Nd isotopes a particularly robust tool for source tracing (e.g., Bayon et al., 2015; Garzanti et al., 2022b). Furthermore, because of the very long half-life of ^{147}Sm (~106 Ga), the ^{143}Nd/^{144}Nd ratios of the sediment sources can be viewed as essentially constant over 1 Ma periods.

Variations in Nd isotopic composition are often expressed in εNd units, which represent the deviation, in parts per 10^4, of the measured ^{143}Nd/^{144}Nd ratio from the assumed value of a chondritic uniformed reservoir (CHUR, $^{143}Nd/^{144}Nd_{CHUR}$ = 0.51263 Bouvier et al., 2008) :

$$\varepsilon_{Nd} = \left[\left\{\frac{(^{143}Nd/^{144}Nd)_{sample}}{(^{143}Nd/^{144}Nd)_{CHUR}}\right\} - 1\right] \times 10^4$$

Because Nd is more incompatible than Sm, it will more likely be incorporated in magma resulting in lower Sm/Nd ratios in the Earth's continents, compared to the mantle (Figure 2.8, Goldstein and Hemming, 2003). Source regions with different Sm/Nd ratios will thus develop different ^{143}Nd/^{144}Nd ratios, and thus different εNd values, over time.

Further details are given on the extraction protocol for εNd measurements in Chapter 5 of this manuscript. In this same chapter, we also use heavy minerals and present the methodology involved. Because this part of the study was done By Eduardo Garzanti's team in Milan, and not by me, it is not mentioned in this Chapter.

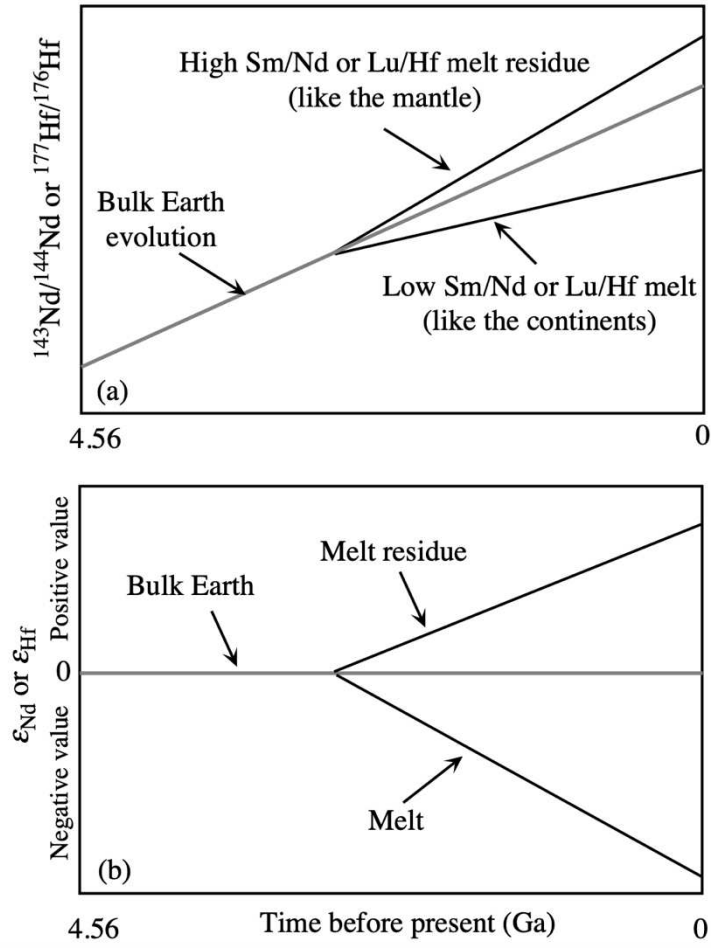

Figure 2.8: Evolution from a bulk Earth ratio of εNd and εHf (not used in this work) with time. Figure from Goldstein an Hemming (2003)

Chapter 3. Source-to-sink transport duration of turbidite sands from continental erosional, to deep marine depositional environments

Authors

Etienne Large[1] ; Sophie Hage[2] ; Bernard Dennielou[3] ; Julien Charreau[1] ; Samuel Toucanne[3] ; Pierre-Henri Blard[1]

[1]Centre de Recherches Pétrographiques et Géochimiques, Nancy, France
[2]GEOPS, Univ Paris-Saclay, Orsay, France
[3]Univ Brest, Ifremer, Géo-Océan, Plouzané, France

Abstract

Turbidity currents are the final link of the sedimentary source-to-sink chain as they transport continental sediments to deep sea depocenters through underwater land-sliding events. Their triggers are numerous: floods, storms, earthquakes, or simple destabilization of continental slope sediments due to overload. Turbidite sediments generally originate from widespread drainages, making them ideal targets for geological reconstructions integrated over large areas, and are thus key sedimentary archives to track past large-scale continental processes.

To interpret the information contained within turbidites, it is however crucial to correctly constrain their age of deposition, keeping in mind that the age of formation of the deposited material may be much older. In most studies, turbidites are considered as instantaneous deposits and dated using foraminifera of the hemipelagic layers bracketing the deposit, but the age of the sediments they transport is rarely constrained.

In this work, we bring new constraints on the age of the material remobilized by turbidity currents by using 29 ^{14}C ages in both foraminifera and vegetal debris contained in turbidites from three different cores of the Ogowé turbiditic system, western Africa. Two of these turbidites from two different cores are also investigated at higher resolution with 12 foraminifera samples and 34 vegetal debris samples (~1 sample every 2 cm vs. 1 sample/turbidite for the rest of the cores). The radiocarbon ages measured in the turbidites, when compared to the depositional ages of under- and overlying hemipelagic layers provide quantitative information on the total transportation time from the source to the depositional

environments, including both the duration of transport on land, and the potential storage of the sediments onshore and offshore (on the continental margin).

Our results shed new light on the transport from the continent to marine depositional environments of turbidite sediments (12.9 ± 0.2 ka), on the residence time of sediments on the continental slopes or margins (9.6 ± 0.2 ka), and on the depositional sequences and mechanisms of turbidites, in the Ogowé sedimentary system.

3.1. Introduction

Turbidity currents are submarine landslides that remobilize distal sediments. The deposits they create are called turbidites and are easily recognizable as the coarser terrigenous fraction in marine sedimentary cores as well as by their depositional sequence (Bouma, 1964). They are useful archives, as they are the final product of the sedimentary source-to-sink chain, transporting sediments created by continental surface processes over large catchments, to deep depocenters (e.g., Vandekerkhove et al., 2020). Their ubiquity is both temporal and spatial.

Three main processes trigger turbidity currents (Piper and Normark, 2009): slope failure of deltaic slopes or canyon flanks (e.g., Clare et al., 2016), hyperpycnal flows (i.e., sediment-rich, flood-type river flows triggering turbidites, Mulder and Syvitski, 1995) and dilute river plumes with low sediment concentrations typically of 1 kg/m^3 (Parsons et al., 2001), but that can be as low as 0.07 kg/m^3 (Hage et al., 2019).

These archives have been used in the past to constrain seismic (e.g., Gutiérrez-Pastor et al., 2013; Shiki et al., 2000) or paleoclimatic (Vandekerkhove et al., 2020; Wilhelm et al., 2013; Zhang et al., 2014) events. These studies have however concentrated only on the triggers of the turbidites at very recent timescales (Holocene). To use the sediments within these archives as records of continental processes, quantifying the length of transport duration from the source to the final deposition in the deep ocean basin is crucial. Because turbidity currents can be erosive, the sediments they carry may be eroded, transported and deposited on the canyon floor several times (e.g., Ruffell et al., 2024). Yet, to accurately interpret our ^{10}Be concentration records and calculate paleo-denudation rates (00) it is important to constrain this lag time between the depositional ages and the denudation time.

Unfortunately, few studies have dated turbidites accurately enough to constrain the lag time between continental erosion and deep-sea burial, especially in tropical, low denudation settings. In Monterey Bay, Stevens et al. (2014) used Optically Simulated Luminescence (OSL) to date the timing of sediment entry into the canyon head and ^{14}C ages of benthic foraminifera to constrain the depositional age of hemipelagic sediments that bound the sand horizons. They demonstrated relatively rapid, decadal-to-millennial-scale lag time between the entry of sediment into the canyon and deposition in the deep-sea fan. Nakamura et al. (1990) dated organic fractions in 1 to 3 m thick turbidites recovered from Suruga

Bay (Japan), yielding radiocarbon ages between 270 ± 80 to 2270 ± 90 a BP, also suggesting rapid transport (< 2360 a) despite the lack of direct age constraints on the deposition of immediately succeeding and underlying hemipelagic deposits. These two studies where however done in regions with geological settings fundamentally different from the tropical, low relief, tectonically quiescent landscapes investigated in this work. Mignard (2017) explored the source-to-sink transport time of turbidite deposits in the Ogooué deep-sea fan on the West African equatorial margin, using 7 radiocarbon ages obtained on vegetal debris found within the turbidites that they compared to the age of turbidite deposition. They found lag times between the ages found in the turbidites and associated hemipelagic layers ranging between 0.01 to 14.33 ka, with a mean of 6.33 ka. These data, while interesting, remain too few to be robust.

In this chapter, to better quantify the duration of continental transport and marine storage before turbiditic mobilization we significantly increase the amount of data by measuring 36 new radiocarbon ages on different objects of turbidites (both foraminifera and vegetal debris) and of their surrounding hemipelagites (foraminifera). We also analyze 2 turbidites at cm-scale resolution with 39 new radiocarbon ages of vegetal debris and planktic foraminifera partitioned between them. Based on these new radiocarbon data we (1) refine the depositional age models of the cores and (2) constrain the duration of both sediment transport on the continent and sediment storage on the continental shelf. These two durations are estimated by calculating the difference between the depositional ages of the hemipelagic layers and the ages of foraminifera and vegetal debris measured in the turbidites, respectively. We show that the distribution of ages with depth can be highly non-linear and give us information on the processes leading to turbidity currents both onshore and offshore.

3.2. The Ogowé turbiditic system

The Ogowé river which drains sediments over ~2.15 10^5 km^2 covering most of Gabon has a mean annual discharge of > 4.3 10^3 m^3/s and is prolonged in the Atlantic Ocean by a well-developed turbiditic system. Although the precise bathymetry of this area is unavailable as it was collected by the French military, it was largely described by Mignard et al, (2019) and is presented in Figure 3.1.. The system is composed of several canyons with relatively steep slopes (~2.4°) incising the continental margin NW of the Ogowé river mouth (Mignard et al., 2019). These canyons are connected to channel-levee systems and an intermediate depocenter where slopes decrease (0.9° and 0.3°, respectively), before merging SE of São Tomé into a distal valley (Figure 3.1) where slopes increase (0.6°) (Mignard et al., 2019). Sediments are then conveyed through this distal valley and into a distal lobe, separated in an upper and lower lobe (0.2°), connected by a corridor (0.3°) (Mignard et al., 2019). This submarine sedimentary system crosses the end of the Cameroon Hot Line between the São Tomé et Principe and Annobòn Paleogene to

Neogene volcanic islands (Nkono et al., 2014) which constitute another source of sediments, easily separated due to their volcanic nature and thus not considered in this work (Mignard et al., 2019).

On land, the Ogowé region is located directly south of the area of influence of the African monsoon. Consequently, in terms of Köppen-Geiger classification, the region is considered as an Equatorial winter dry area, with the northernmost part of the country summer dry (Kottek et al., 2006). Mean precipitations are of 1.5 to 2 m/a but can reach 2.7 m/a in the NW (e.g., in Libreville). The climate is supposed wet and tropical since the Neogene (Séranne and Anka, 2005). Modern Gabon is moreover largely covered by a relatively well-preserved rainforest.

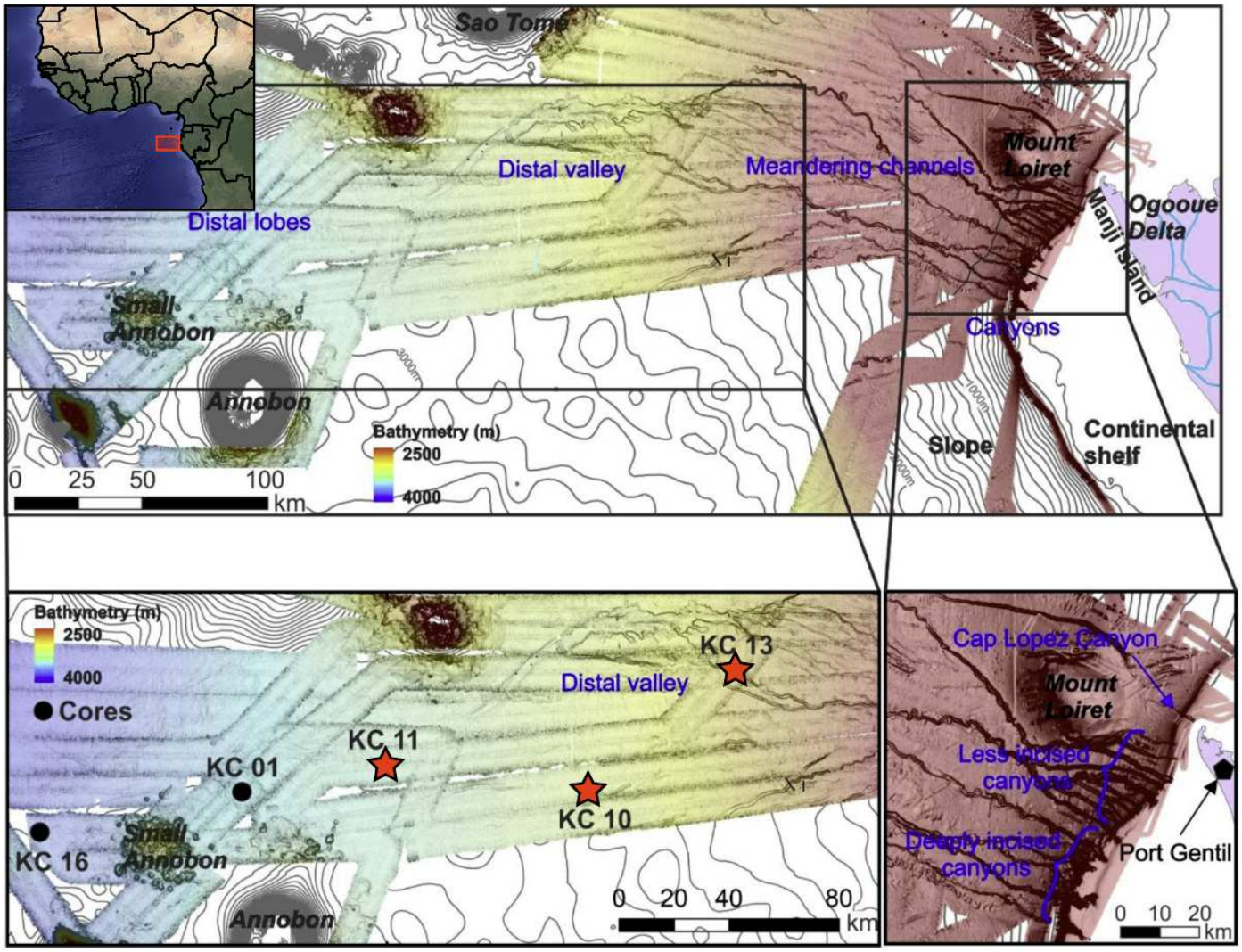

Figure 3.1: Bathymetry of the Ogowé turbiditic system, showing the succession between canyons, meandering channels, a distal valley, and distal lobes. The location of this system is shown in the top left inset. Location of the cores used in this work are shown by red stars in the bottom map. Figure modified from Mignard et al. (2017).

3.3. Method

3.3.1. General approach

The method used in this chapter is described in Chapter 2 of this manuscript. We use ^{14}C to date different objects: Hemipelagic Planktic Foraminifera (HPF), Turbiditic Planktic Foraminifera (TPF) and Turbiditic Vegetal Debris (TVD). The HPF ages bracketing the turbidite yield maximum (HPF sampled below the turbidite) and minimum (HPF sampled above the turbidite) ages of deposition. The difference between TPF ages and these deposition ages yield an estimation of the submarine storage duration of sediments on the continental margin before turbiditic remobilization (ΔT_{stor}, Figure 3.2). Similarly, the difference in ages between the TVD and the depositional ages provide an estimation of the total duration of sediment transfer (ΔT_{trans}, Figure 3.2). These differences between TPF and TVD and the maximum and minimum depositional ages yield minimal and maximum durations, respectively. The difference between ΔT_{trans} and ΔT_{stor} yield an estimate of the duration of sediment transfer on the continent (ΔT_{cont}). The depositional ages of the hemipelagic layers were constrained either by direct dating of the HPF when available or by refining the age models determined by Mignard et al. using peak correlation (see below).

3.3.1. Biostratigraphic age models

The age models for cores KC10, KC11 and KC13 were previously established by Mignard et al. (2017). They first obtained the age of KC10 by peak correlation of the benthic $\delta^{18}O$ record measured on this core to the LR04 (Lisiecki and Raymo, 2005), using the Analyseries program (Paillard et al., 1996). Then, Mignard et al. (2017) constrained depositional ages of cores KC11 and KC13 by correlating these two cores to KC10, taken as reference, using XRF measurements of the Ca+Sr/Ti+Al ratio. For this present work, I refine the age models of KC10 and KC11 based on new ^{14}C ages done on bulk planktic foraminifera of the hemipelagic layers (4 in KC10 and 1 in KC11,
). The ^{14}C ages were used as pointers along with graphical identification of peaks, and the ages were interpolated linearly between each pointer (Sup. Info. 3.1) using the interpolation tool on the Gnumeric software (http://www.gnumeric.org).

Sample	^{14}C counts	Weight µgC	^{14}C Age a	Marine 20 calBP
KC10 34-35	82 896	966	14376 ± 81	16690 ± 330
KC10 48-49	66 806	638	15779 ± 62	18390 ± 267
KC10 112-114	26 933	867	23689 ± 205	27189 ± 464
KC10 122-123	21 101	940	26356 ± 278	29787 ± 450
KC11 186-191	1 233	102	28562 ± 369	32091 ± 931
KC13 64-67	118 822	913	11545 ± 67	12961 ± 218
KC13 96-99	110 874	844	11899 ± 69	13334 ± 233

compiles the radiocarbon ages used to calibrate these age models. We also tried the same approach on KC13, but the correlation was unsatisfying due to the large number of turbidites recorded in the core and in which

Sample	^{14}C counts	Weight µgC	^{14}C Age a	Marine 20 calBP
KC10 34-35	82 896	966	14376 ± 81	16690 ± 330
KC10 48-49	66 806	638	15779 ± 62	18390 ± 267
KC10 112-114	26 933	867	23689 ± 205	27189 ± 464
KC10 122-123	21 101	940	26356 ± 278	29787 ± 450
KC11 186-191	1 233	102	28562 ± 369	32091 ± 931
KC13 64-67	118 822	913	11545 ± 67	12961 ± 218
KC13 96-99	110 874	844	11899 ± 69	13334 ± 233

Ca+Sr/Ti+Al ratios are not measured, leading to hiatuses in the correlation curves. Furthermore, nearly all turbidites in core KC13 were dated using ^{14}C, yielding nonlinear results with depth (see below). To obtain ages of the turbidites in which no radiocarbon ages were available, we used the same interpolation tool in Gnumeric (http://www.gnumeric.org) and used the dated turbidites as pointers.

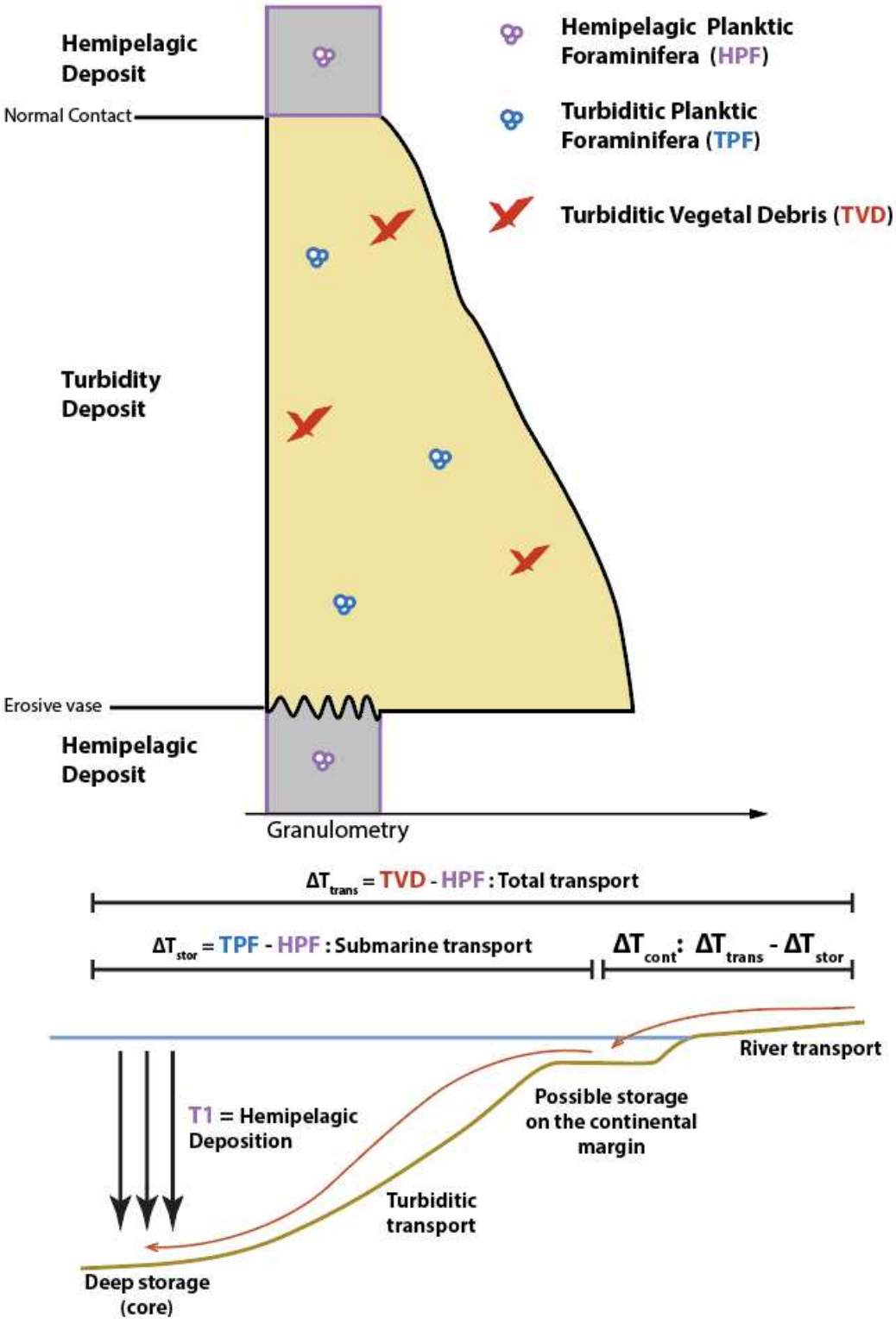

Figure 3.2: Implication of the ages of the different material picked for ^{14}C dating.

3.3.2. Sample treatment for ^{14}C analyses

Each interval sampled was dry sieved with 100 µm, 250 µm and 500 µm sieves before being put on a picking tray and picked with a wet brush under a binocular. In each interval, all the material (HPF, or TPF and TVD) available was taken. I picked objects based on their cleanness (absence of recrystallization or smaller particles sticking to them), completeness (absence of fracture, preserved foraminifera, twigs or leaf residue) and size. I selected the coarser fraction preferentially as they were easier to pick and allowed a huge time gain, especially considering the elevated number of samples picked. For the foraminifera, only the planktic were identified and picked. These were mostly of the Globigerina family, but samples were not mono species. The benthic foraminifera were discarded as their radiocarbon ages are affected by higher uncertainties due to longer marine reservoir effects (e.g., Lippold et al., 2024).

Picked samples were sent to the Alfred Wegener Institute and measured on a MICADAS Accelerated Mass Spectrometer as graphite targets, following standard procedure (Mollenhauer et al., 2021). The obtained radiocarbon ages were then calibrated using the Oxcal v4.4 online software (https://c14.arch.ox.ac.uk/oxcal/OxCal.html) (Bronk Ramsey, 2009). For foraminifera, the Marine 20 calibration curve (Heaton et al., 2020) was applied with a reservoir age ΔR of -106 ± 63 (Soulet et al., 2023). For vegetal debris, the IntCal 20 calibration curve was used (Reimer et al., 2020).

3.4. Material

We used for this study 3 Küllenberg-type cores, KC10, KC11 and KC13 (Figure 3.1Figure 3.3), drilled as part of the MOCOSED 2010 cruise on the R/V "Pourquoi Pas?" by the SHOM (Service Hydrographique et Océanographique de la Marine https://www.shom.fr) (Division Plans De DMI-SHOM, 2010) in the Ogowé turbiditic system. KC10 was sampled at 3148m depth, in a disconnected channel, believed to be currently inactive, KC11 at 3372m depth, at the outlet of the distal valley, where four main channels merge. KC13 was sampled at 2852m depth, on the levee of one of the active channels, about 1km from the channel axis (Mignard et al., 2017) (Figure 3.1) .

Radiocarbon ages were measured in core KC10 from planktic foraminifera of 4 hemipelagic intervals (HPF) surrounding 2 turbidites in which planktic foraminifera where also picked (TPF). In core KC11, planktic foraminifera (HPF) from 1 hemipelagic interval were picked, while both planktic foraminifera (TPF) and vegetal debris (TVD) where picked in 4 turbidite intervals. Finally, in core KC13, planktic foraminifera (HPF) were picked in 2 hemipelagic intervals, whereas both TPF and TVD were picked in 6 turbidites, TVD only were picked in 1, and TPF only were picked in 5 (Figure 3.3,

Sample	^{14}C counts	Weight	^{14}C Age	Marine 20

and Table 3.2).

		µgC	a	calBP
KC10 34-35	82 896	966	14376 ± 81	16690 ± 330
KC10 48-49	66 806	638	15779 ± 62	18390 ± 267
KC10 112-114	26 933	867	23689 ± 205	27189 ± 464
KC10 122-123	21 101	940	26356 ± 278	29787 ± 450
KC11 186-191	1 233	102	28562 ± 369	32091 ± 931
KC13 64-67	118 822	913	11545 ± 67	12961 ± 218
KC13 96-99	110 874	844	11899 ± 69	13334 ± 233

Additionally, to investigate the evolution of ages within single turbidites, we did a high-resolution sampling (i.e., 1 sample every ~2 cm) of the topmost turbidites of cores KC11 (KC11-T1, 84-117 cm)

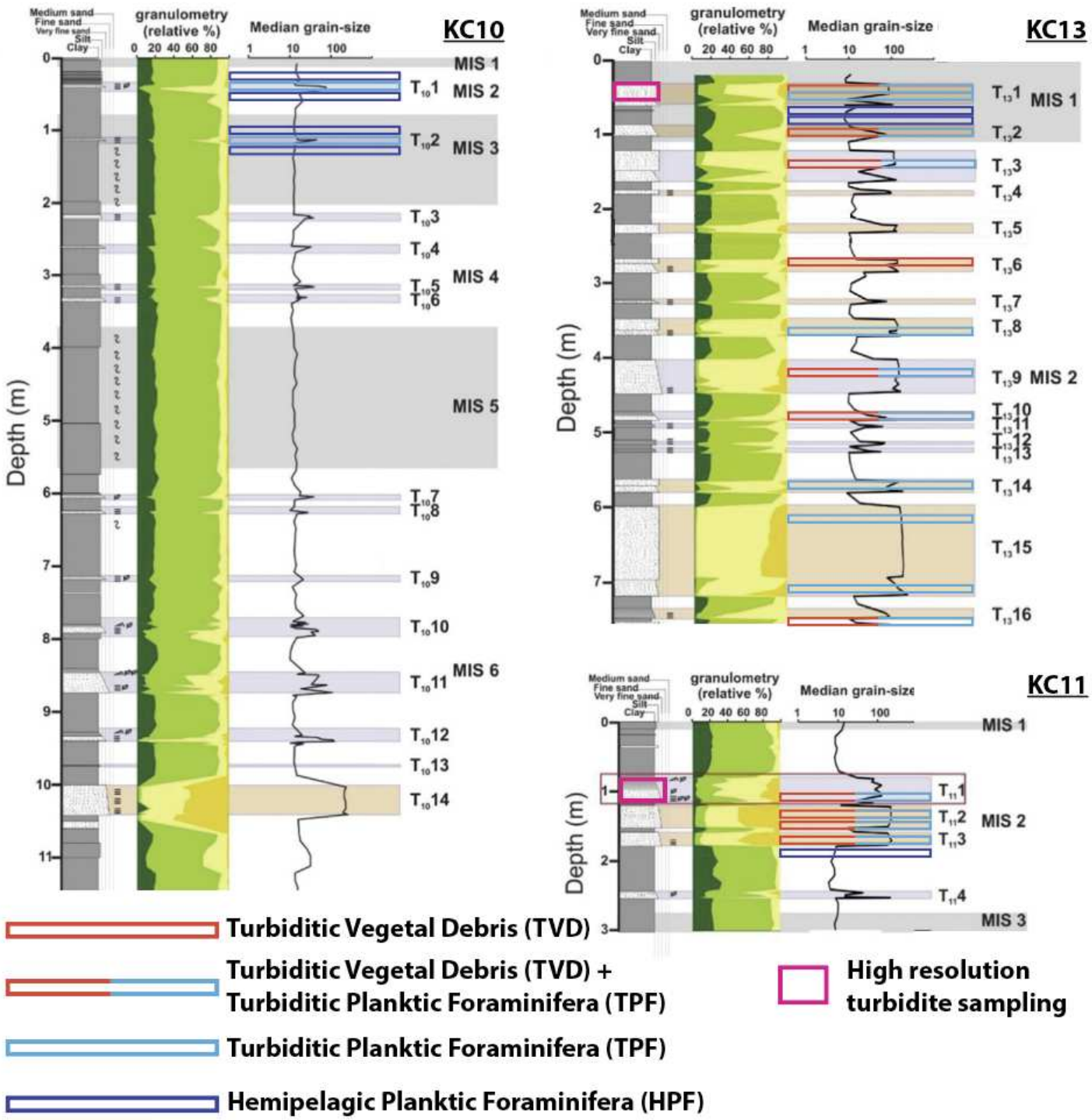

Figure 3.3: Description of the granulometry and median grain size for the three cores considered in this work. Turbidites are shown by light grey colors and coarser granulometry. The samples turbidite and hemipelagite intervals are shown by colored rectangles for Turbiditic Vegetal Debris (TVD), Turbiditic Planktic Foraminifera (TPF) and Hemipelagic Planktic Foraminifera (HPF) picked within them. The two high resolution cores presented in Figure 3.4 are also shown in pink. Figure modified from Mignard et al. (2017).

and KC13 (KC13-T1, 33-60 cm) (Figure 3.3Figure 3.4). These two turbidites were largely sampled for previous analysis, leading to gaps in the records. Sedimentary observations of these two turbidites, and associated logs were done in Brest by Sophie Hage and Bernard Dennielou.

KC11-T1 is ~33 cm thick and presents a fining upwards sequence from < 125 µm massive, dark medium sand at its bottom, to < 62 µm silty sand at its top. It is massive from 117 cm to 110 cm, from 100 cm to 90 cm, and from 87 cm to 84 cm and affected by laminae from 109 cm to 102 cm and from 88 to 87 cm. A concretion, corresponding to the pyritization of a burrow was found at about 97 cm. In this turbidite, 21 intervals were sampled (Figure 3.4, Table 3.2). In 2 hemipelagic intervals above and under the turbidite, both planktic foraminifera (HPF) and, more surprisingly, vegetal debris were picked (see discussion). Within the turbidite, in the 19 intervals sampled, both TPF and TVD were picked in 6

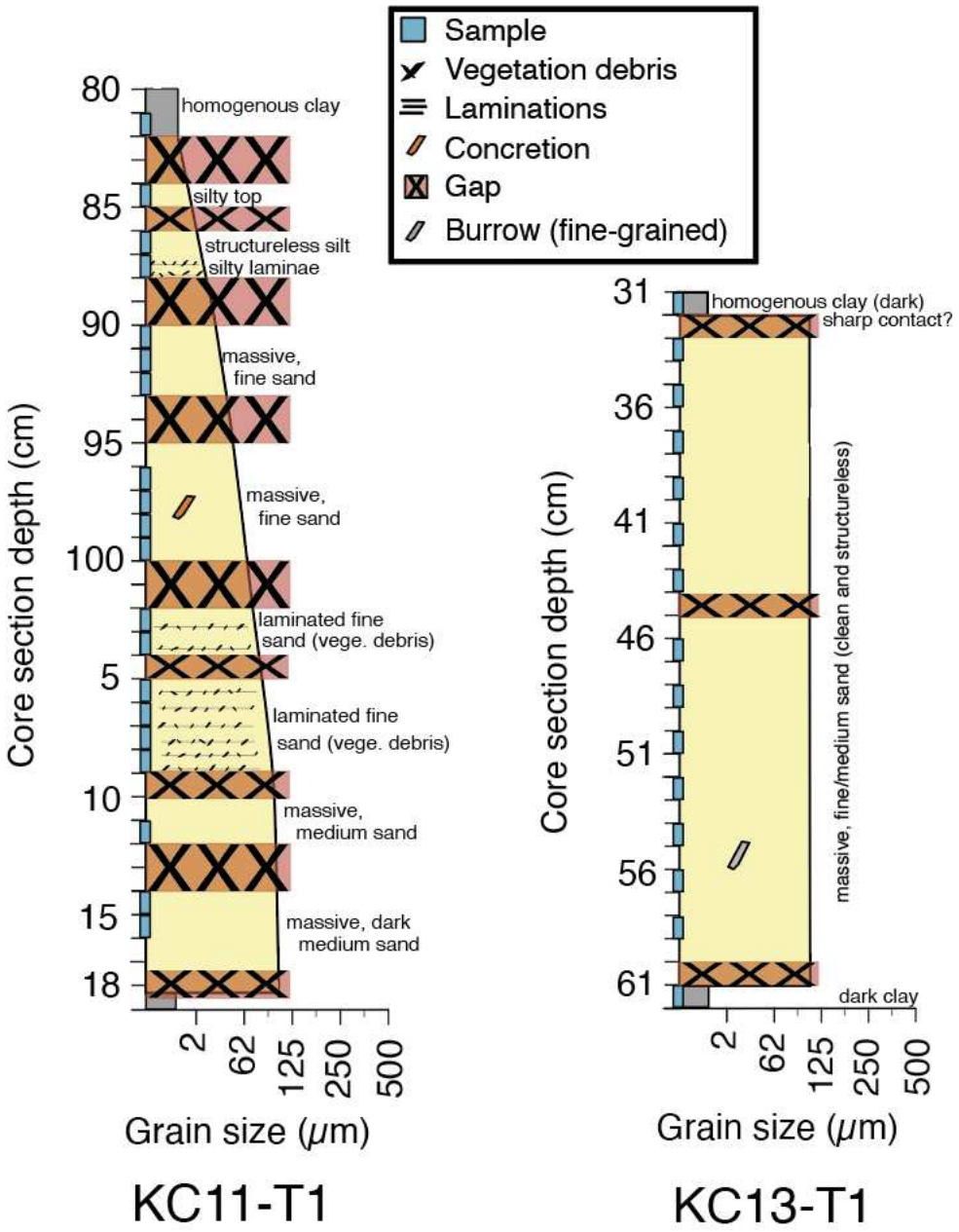

Figure 3.4: Stratigraphic logs of the two topmost turbidites of cores KC11 (KC11-T1) and KC13 (KC13-T1). Values of grain size shown in this figure where evaluated with a naked eye. More precise values of granulometry are given in All results of the high-resolution sampling are given in Table 3.3 and shown in ***Erreur ! Référence non valide***

intervals, and only TVD in the 13 remaining. This picking strategy was motivated mainly by financial and time questions, as picking takes time and ^{14}C measurements on the MICADAS is expensive (~330 € / sample). All intervals however contained TPF in the 250-500 µm fraction in varying completeness and cleanness.

The TVD were mostly picked in the 250-500 µm fraction from 92 cm to 98 cm (with a few > 500 µm). Below 98 cm, the TVD were much coarser (> 500 µm with several intervals where TVD were picked without the need of a binocular, i.e., cm scale). I also picked what was believed to be tree resin in 1 sample and vegetal debris in two different fractions (>500 µm and 250-500 µm) in 2 samples (Table 3.3).

KC13-T1 is ~27 cm thick and much more massive than KC11-T1 (Figure 3.4). It is composed of structureless medium to fine sand (~100 µm) from bottom to top. A fine-grained burrow was found at ~55 cm. Two hemipelagic layers were sampled above and below the turbidite, respectively. Both HPF and vegetal debris were picked in these samples. Within the turbidite, 13 intervals were sampled. However, because of very limited amounts of vegetal debris found in most samples, and of their very fine granulometry (250-500 µm) the TVD from 7 intervals were grouped into 3 larger intervals in order to have sufficient mass for ^{14}C measurements (41-44 cm corresponds to 41-42 cm + 43-44 cm, 50-55 cm to 50-51 cm + 52-53 cm + 54-55 cm, and 56-59 cm to 56-57 cm + 58-59 cm). In total TVD were picked in 9 samples (counting the three grouped ones). TPF were picked in one of these intervals (37-38 cm), and in 3 additional intervals, 2 of which correspond to part of the grouped intervals (43-44 cm and 58-59 cm) (Table 3.3).

Laser granulometry was also carried out by Bernard Dennielou in Ifremer, using a Malvern MasterSizer 3000. This method is based on the principle of diffraction and scattering of a beam by particles at a specific angle correlated to the size of each grain. There are a number of limitations to this principle, particularly with regard to particle geometry. Scattering is optimal when the particle is spherical, but admits a bias when grains have more irregular or elongated shapes, as in the case of clays or carbonates (Eshel et al., 2004; Konert and Vandenberghe, 1997). From this analysis, done on 1 cm intervals throughout both turbidites (excluding the gaps where no material was available), the D10, D50 and D90 were calculated, corresponding to the first, fifth and ninth deciles respectively. Results are shown in All results of the high-resolution sampling are given in Table 3.3 and shown in **Erreur ! Référence non valide pour un signet.** (KC13-T1) and Figure 3.11 (KC11-T1).Figure 3.11.

3.5. Results

3.5.1. Age models

Figure 3.5 shows the age models of cores KC10 and KC11, which are dated from 8 ka to 192 ka and from 3 ka to 38 ka, respectively. These values are consistent with the age models created by Mignard et

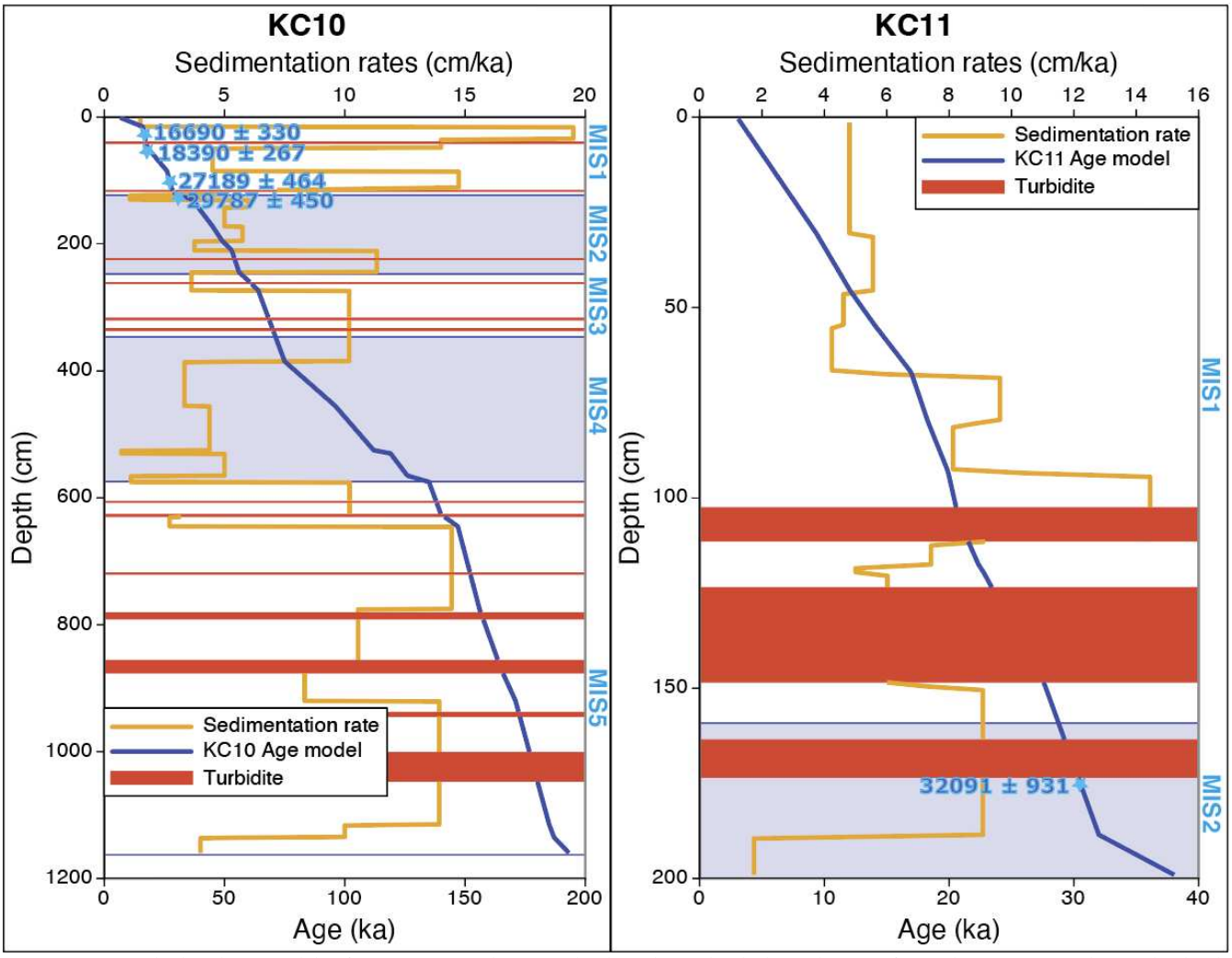

Figure 3.5: Recalculated age models of cores KC10 and KC11. Blue line shows depth-dependent age for each core. Orange line is the depth-dependent sedimentation rate. Red rectangles indicate turbidites. Blue stars with associated ages show bulk planktic foraminifera radiocarbon ages (Marine 20 calBP) used to calibrate age models. Marine Isotope Stages are shown to the right of each graph.

al. (2017). The $\delta^{18}O$ data of core KC10 correlates well with the LR04 (Sup. Info. 3.1) and we consider the age model to be robust. The correlation of core KC11 data, however, is less robust and we were not able to build an age model with the data available.

Sedimentation rates for both cores show strong variations with up to fourfold increases, ranging from 2 cm/ka to 20 cm/ka. Furthermore, sedimentation rates tend to be higher during interglacial periods with mean rates of 10 cm/ka, 8 cm/ka and 12 cm/ka for MIS1, MIS3 and MIS5, respectively, while lower rates of 6 cm/ka and 5 cm/ka are recorded for MIS2 and MIS4, respectively (Figure 3.5).

3.5.2. Low-Resolution sampling

Results of the low-resolution sampling are given in

Sample	^{14C} counts	Weight µgC	^{14C} Age a	Marine 20 calBP

KC10 34-35	82 896	966	14376 ± 81	16690 ± 330
KC10 48-49	66 806	638	15779 ± 62	18390 ± 267
KC10 112-114	26 933	867	23689 ± 205	27189 ± 464
KC10 122-123	21 101	940	26356 ± 278	29787 ± 450
KC11 186-191	1 233	102	28562 ± 369	32091 ± 931
KC13 64-67	118 822	913	11545 ± 67	12961 ± 218
KC13 96-99	110 874	844	11899 ± 69	13334 ± 233

Table 3.2, and in Figure 3.6. In terms of ages, HPF samples from core KC10 range from 16.7 ± 0.3 ka at 35 cm depth, to 29.8 ± 0.5 ka at 123 cm depth. In core KC11, the only HPF sample yields an age of 32.1 ± 0.9 ka (191 cm depth) while HPF ages of core KC13 are of 13 ± 0.2 and 13.3 ± 0.2 ka at 67 and 99 cm depths, respectively.

For the turbiditic intervals, the 2 TPF of core KC10 yield values of 22.3 ± 0.3 ka and 31.6 ± 0.4 ka, at 43 cm and 117 cm depth respectively (Table 3.2, Figure 3.6). The marine storage durations, ΔT_{stor} (Figure 3.2) are thus of 3.9 ± 0.02 ka and 5.6 ± 0.05 ka, and 1.8 ± 0.06 ka and 4.4 ± 0.08 ka, for turbidites sampled at 40-43 cm and 116-117 cm intervals, respectively (Figure 3.7).

In core KC11, TPF ages range from 25.7 ± 0.3 ka at 147 cm depth, to 40.2 ± 0.8 ka at 170 cm depth. TPF ages decrease with depth on the three topmost turbidites before increasing for the bottom most turbidite. In terms of TVD, ages increase with depth from 27.6 ± 0.2 ka at 110 cm depth, to 46.9 ± 0.9 ka at 172 cm depth. ΔT_{stor} values range from -1.8 ± 0.3 ka and 2.3 ± 0.3 ka, to 10.3 ± 0.6 ka to 11.3 ± 0.6 ka for the 140-147 cm and 103-110 cm intervals respectively (Figure 3.7). The total transport durations ΔT_{trans} are of 2.1 ± 0.4 ka and 6.3 ± 0.4 ka (124-130 cm interval) to 16.5 ± 0.9 ka and 17.6 ± 0.9 ka (164-172 cm interval). These values lead to continental transport estimations of ΔT_{cont} of -4.2 ± 0.4 ka to 8.6 ± 0.1 ka for 103-110 cm and 140-147 cm intervals, respectively, with a mean of 3.1 ± 0.2 ka.

In core KC13, TPF ages range from 11.8 ± 0.5 ka at 107 cm depth, to 25.1 ± 0.4 ka at 626 cm depth (Figure 3.6). In this core as well, these ages are highly nonlinear with depth. Ages decrease with depth until 107 cm, then increase at 149 cm before remaining relatively stable between 19 ± 0.3 ka and 19.8 ± 0.3 ka, until 484 cm depth. At the bottom of the core TPF ages increase until 626 cm depth (25.1 ± 0.4 ka) before decreasing again until 763 cm (20.4 ± 0.3 ka). The TVD ages of core KC13 also vary significantly with depth, ranging from 19.3 ± 0.2 ka at 484 cm depth to 36.5 ± 2.5 ka at 763 cm depth (Figure 3.6). For the intervals where both TPF and TVD were picked the TVD ages are always older, with age differences ranging from 0.3 ± 0.1 ka at 484 cm depth, to 16.1 ± 2.2 ka at 763 cm depth. Note that for interval 38-43 cm, two TPF samples were picked independently, yielding ages of 20.3 ± 0.3 ka and 17 ± 0.3 ka. The discrepancy among these values shows that some variability exists within the samples, although these ages are consistent with each other, within uncertainties. However, in core KC13, because we have no constraints on the hemipelagic ages, we cannot calculate ΔT_{stor}, ΔT_{trans}, or ΔT_{cont} durations.

Table 3.1: Radiocarbon and calibrated ages of the hemipelagic samples for each core. Reservoir age is ΔR = -106 ± 63 (Soulet et al., 2023).

Sample	^{14}C counts	Weight µgC	^{14}C Age a	Marine 20 calBP
KC10 34-35	82 896	966	14376 ± 81	16690 ± 330
KC10 48-49	66 806	638	15779 ± 62	18390 ± 267
KC10 112-114	26 933	867	23689 ± 205	27189 ± 464
KC10 122-123	21 101	940	26356 ± 278	29787 ± 450
KC11 186-191	1 233	102	28562 ± 369	32091 ± 931
KC13 64-67	118 822	913	11545 ± 67	12961 ± 218
KC13 96-99	110 874	844	11899 ± 69	13334 ± 233

Table 3.2: Radiocarbon and calibrated ages of both TPF (Turbiditic Planktic Foraminifera) and TVD (Turbiditic Vegetal Debris) of cores KC10, KC11 and KC13. For the Marine 20 calibration curve reservoir age is ΔR = -106 ± 63 (Soulet et al. 2023).

Sample	Target	^{14}C counts	Weight	^{14}C Age	Marine 20	IntCal 20
			µgC	a	calBP	calBP
KC10 40-43	TPF	20241	598	19102 ± 69	22287 ± 284	
KC10 116-117	TPF	6383	642	28283 ± 144	31568 ± 387	
KC11 103-110	TPF	9592	712	28424 ± 197	31832 ± 642	
KC11 103-110	TVD	35237	956	23382 ± 51		27628 ± 196
KC11 124-130	TPF	14668	799	24927 ± 135	28331 ± 418	
KC11 124-130	TVD	27905	957	25368 ± 58		29677 ± 353
KC11 140-147	TPF	20449	750	22265 ± 102	25726 ± 294	
KC11 140-147	TVD	13700	568	29744 ± 91		34353 ± 214
KC11 164-172	TPF	4086	777	35977 ± 474	40189 ± 817	
KC11 164-172	TVD	2987	461	44350 ± 376		46873 ± 923
KC13 38-43	TPF	24321	626	17474 ± 62	20317 ± 308	
KC13 38-43	TPF	51659	731	14639 ± 52	17030 ± 292	
KC13 38-43	TVD	41017	985	16519 ± 47		20102 ± 228
KC13 48-52	TPF	4627	72	13787 ± 129	15948 ± 431	
KC13 103-107	TPF	6925	77	10532 ± 104	11788 ± 454	
KC13 103-107	TVD	2936	59	17989 ± 267		21815 ± 715
KC13 142-149	TPF	40277	791	16638 ± 61	19282 ± 304	
KC13 142-149	TVD	16711	299	24291 ± 454		28746 ± 999
KC13 278-283	TVD	48021	823	17173 ± 44		20793 ± 214
KC13 360-366	TPF	42182	788	16372 ± 59	19012 ± 282	
KC13 430-436	TPF	44491	569	17085 ± 45	19847 ± 302	
KC13 430-436	TVD	18665	982	22886 ± 70		27356 ± 216
KC13 480-484	TPF	36826	708	16334 ± 61	18962 ± 274	
KC13 480-484	TVD	41396	984	15891 ± 46		19311 ± 203
KC13 565-573	TPF	25363	775	20548 ± 86	23876 ± 315	
KC13 612-626	TPF	22193	777	21601 ± 96	25090 ± 381	
KC13 710-716	TPF	28446	753	19370 ± 78	22588 ± 291	
KC13 756-763	TPF	35468	716	17549 ± 66	20420 ± 307	
KC13 756-763	TVD	8918	335	31149 ± 1060		36529 ± 2546

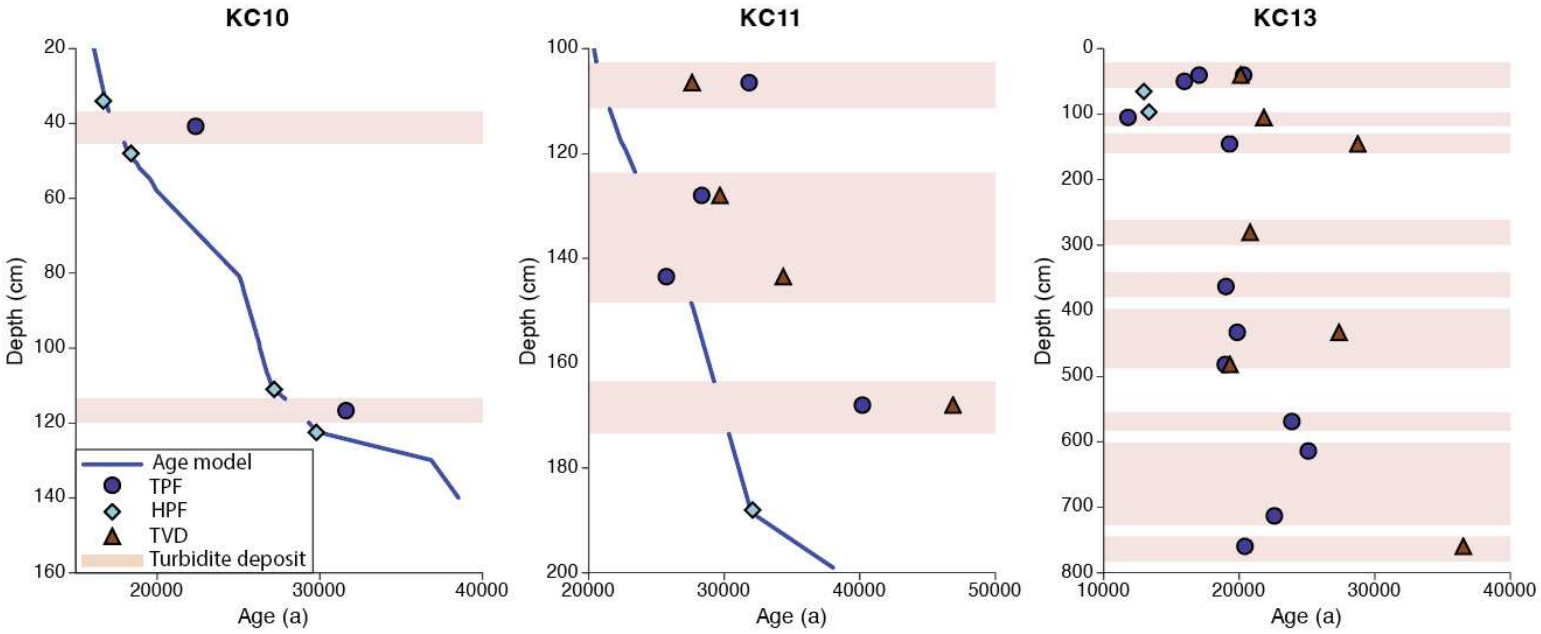

Figure 3.6: Results of calibrated radiocarbon ages with depth for cores KC10, KC11 and KC13.Ages given are Turbiditic Planktic Foraminifera (TPF), Hemipelagic Planktic Foraminifera (HPF) and Turbiditic Vegetal Debris (TVD).

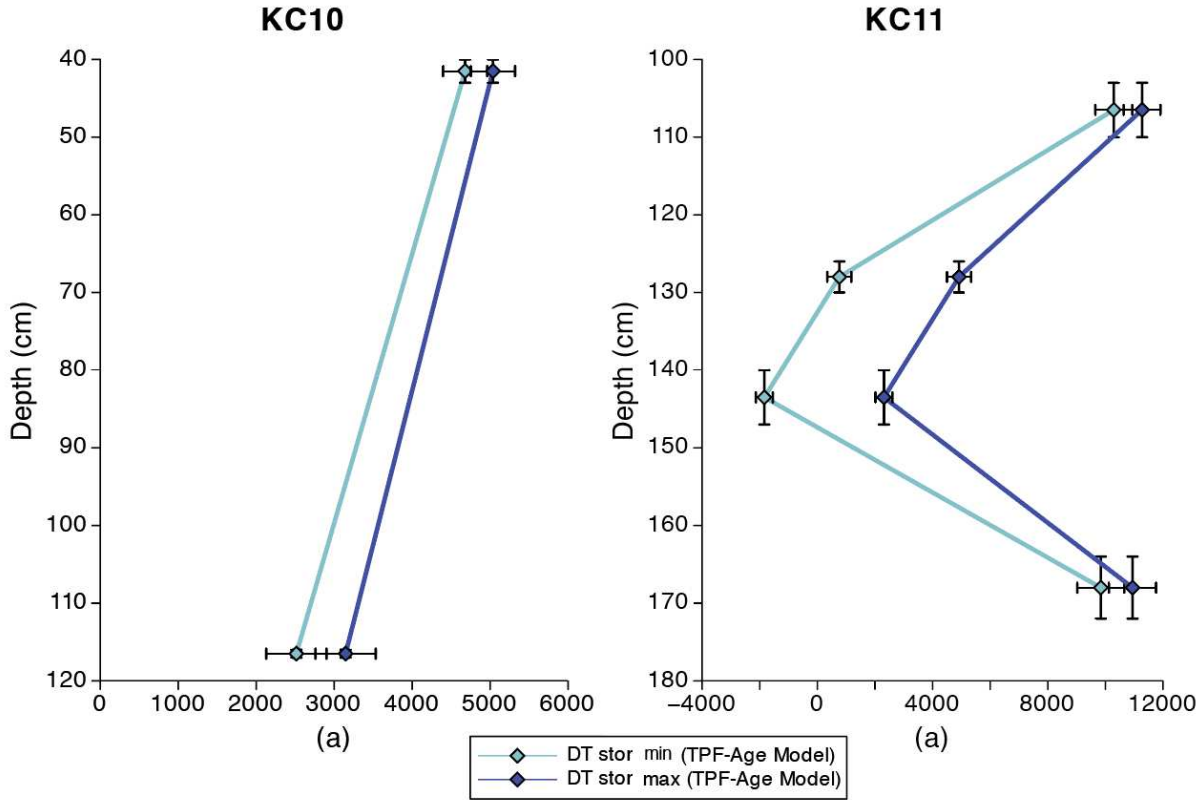

Figure 3.7: ΔT_{stor} (TPF-HPF) for turbidites of cores KC10 and KC13.

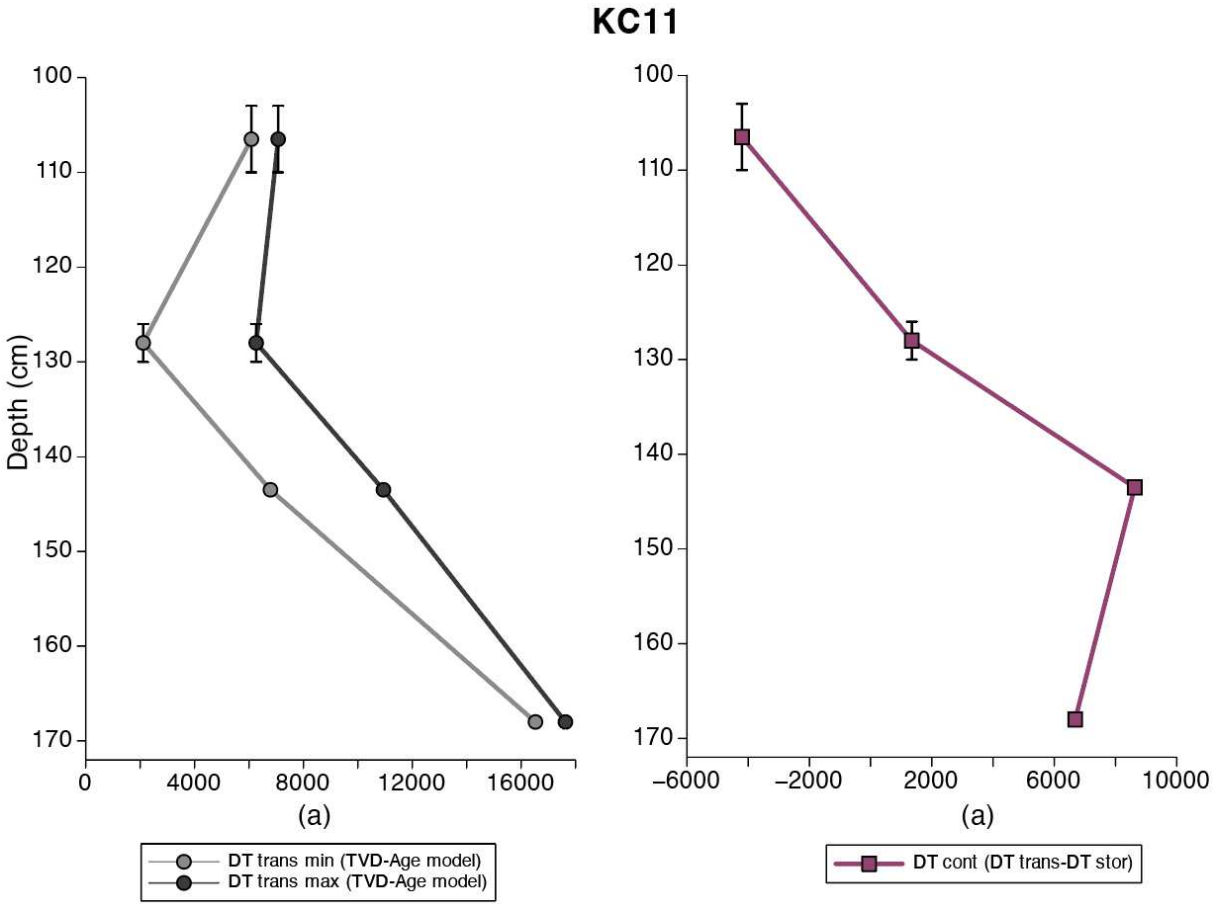

Figure 3.8:ΔT_{trans} and ΔT_{cont} for core KC13

3.5.3. High-Resolution sampling

All results of the high-resolution sampling are given in Table 3.3 and shown in **Erreur ! Référence non valide pour un signet.** (KC13-T1) and Figure 3.11 (KC11-T1).

3.5.3.1. KC13-T1

The age of deposition of turbidite KC13-T1 is constrained by the two HPF dated directly above and below it, yielding maximum and minimum ages of deposition of 17.1 ± 0.3 ka (61-62 cm) and 11.3 ± 0.3 ka (31-32 cm), respectively. The vegetal debris of these two intervals (noted VD in Table 3.3) yield ages of 26.5 ± 0.6 ka and 32.3 ± 1.3 ka and for the 61-62 cm and 31-32 cm, respectively. Note that the VD at 31-32 cm is the second oldest of the turbidite, that it is affected by the largest uncertainty, and that it is the only sample to be > 500 µm in terms of granulometry (Table 3.3). Within the turbidite, ages of the TPF do not vary significantly with ages ranging from 21.7 ± 0.4 ka (58-59 cm) to 22.9 ± 0.4 ka (50-51 cm), with a mean of 22.1 ± 0.4 ka. TVD ages, however, are more dispersed, ranging from 23.7 ± 0.3 ka (39-40 cm) to 34.5 ± 0.2 ka (50-55 cm), with a mean of 28.7 ± 0.5 ka.

Table 3.3: Radiocarbon and calibrated ages of the Turbiditic Vegetal Debris (TVD) and Turbiditic Planktic Foraminifera (TPF) sampled at high resolution in the two topmost turbidites of cores KC11 and KC13. Errors are 1 sigma.

Core	Object	Interval	^{14}C counts	^{14}C Age	Weight	Fraction	Marine 20	IntCal 20
		cm		age (y)	µgC	µm	CalBP	CalBP
KC11	VD	81-82	9 720	26985 ± 91	997	>500		31165 ± 131
	HPF	81-82	50 562	17845 ± 50	803	250-500	20746 ± 288	
	TVD	84-85	16 257	26826 ± 131	698	>500		31074 ± 163
	TVD	86-87	11 232	29850 ± 184	629	>500		34423 ± 335
	TVD	87-88	13 099	26541 ± 79	976	>500		30939 ± 191
	TVD	90-91	11 827	26157 ± 83	796	>500		30530 ± 320
	TVD	91-92	11 989	28239 ± 89	501	>250		32491 ± 519
	TPF	91-92	13 628	30104 ± 144	785	250-500	33908 ± 366	
	TVD	92-93	12 960	27697 ± 85	489	>250		31683 ± 294
	TVD	96-97	775	30153 ± 696	73	>250		34778 ± 1442
	Resin	97-98	44 289	14811 ± 50	337			18114 ± 138
	TVD	97-98	907	28261 ± 571	79	>250		32683 ± 1381
	TPF	97-98	10 242	31335 ± 169	744	250-500	35010 ± 424	
	TVD	98-99	13 365	26757 ± 79	996	>500		31060 ± 121
	TVD	99-100	13 553	26629 ± 78	990	>500		30992 ± 147
	TVD	102-103	11 320	29306 ± 93	512	>500		34013 ± 304
	TPF	102-103	14 395	28745 ± 128	778	250-500	32242 ± 528	
	TVD	103-104	18 566	23405 ± 66	990	>500		27642 ± 203
	TVD	103-104	9 646	30369 ± 197	630	250-500		34888 ± 417
	TVD	105-106	9 046	31936 ± 232	751	>500		36464 ± 519
	TVD	106-107	21 120	24184 ± 65	994	>500		28464 ± 304
	TVD	107-108	16 171	26649 ± 76	986	>500		31004 ± 140
	TPF	107-108	10 219	30654 ± 159	800	250-500	34400 ± 358	
	TVD	108-109	10 362	30448 ± 101	993	>500		34940 ± 332
	TVD	111-112	15 030	27170 ± 80	995	>500		31332 ± 225
	TVD	114-115	21 803	24293 ± 64	997	>500		28612 ± 262
	TVD	115-116	19 697	24959 ± 68	983	>500		29407 ± 312
	TVD	115-116	10 000	30842 ± 104	877	250-500		35223 ± 402
	VD	120-121	6 305	35206 ± 149	989	>500		40455 ± 457
	HPF	120-121	20 352	27269 ± 277	964	250-500	30628 ± 523	
KC13	VD	31-32	814	27375 ± 543	126	>500		32317 ± 1251
	HPF	31-32	118 951	10185 ± 44	991	250-500	11320 ± 265	
	TVD	33-34	1 706	22442 ± 314	108	>250		26710 ± 672
	TVD	35-36	13 392	26061 ± 124	427	>250		30459 ± 359
	TVD	37-38	1 329	24894 ± 398	89	>250		29275 ± 834
	TPF	37-38	42 803	18741 ± 104	913	>250	21877 ± 382	
	TVD	39-40	39 751	19690 ± 47	998	>250		23751 ± 314
	TVD	41-44	1 427	24094 ± 368	50	>250		28451 ± 714
	TPF	43-44	40 514	18728 ± 104	888	>250	21858 ± 377	
	TVD	46-47	10 614	27034 ± 141	322	>250		31287 ± 251
	TVD	48-49	1 566	23769 ± 351	60	>250		28097 ± 723
	TPF	50-51	36 931	19669 ± 115	889	>250	22868 ± 380	
	TVD	50-55	9 960	29909 ± 100	503	>250		34450 ± 223
	TVD	56-59	2 100	21288 ± 275	81	>250		25714 ± 583
	TPF	58-59	44 643	18563 ± 102	904	>250	21689 ± 387	
	VD	61-62	1 828	21944 ± 298	130	>250		26464 ± 619
	HPF	61-62	74 969	14730 ± 40	550	>250	17130 ± 270	

Minimum and maximum ΔT_{stor} range from 4.6 ± 0.1 ka and 10.4 ± 0.1 ka (58-59 cm) to 5.7 ± 0.1 ka and 11.5 ± 0.1 ka (50-51 cm) (Figure 3.10). Minimum and maximum ΔT_{trans} range from 6.6 ± 0.04 ka and 12.4 ± 0.05 ka (39-40 cm) to 17.3 ± 0.3 ka and 23.1 ± 0.04 ka (50-55 cm), respectively. In intervals where both TPF and TVD were sampled, the continental transport duration ΔT_{cont} ranges from 4.0 ± 0.1 (56-59 cm) to 7.4 ± 0.5 ka (37-38 cm) (Figure 3.10). Mean ΔT_{cont} is of 6.4 ± 0.2 ka.

The D50 granulometry is constant throughout the turbidite. D90 increases from 125 µm to 275 µm (32-38 cm), then remains between 225 µm and 300 µm until 52 cm where it drops to 175 before increasing again to 350 µm at 64 cm (All results of the high-resolution sampling are given in Table 3.3 and shown in **Erreur ! Référence non valide pour un signet.** (KC13-T1) and Figure 3.11 (KC11-T1).).

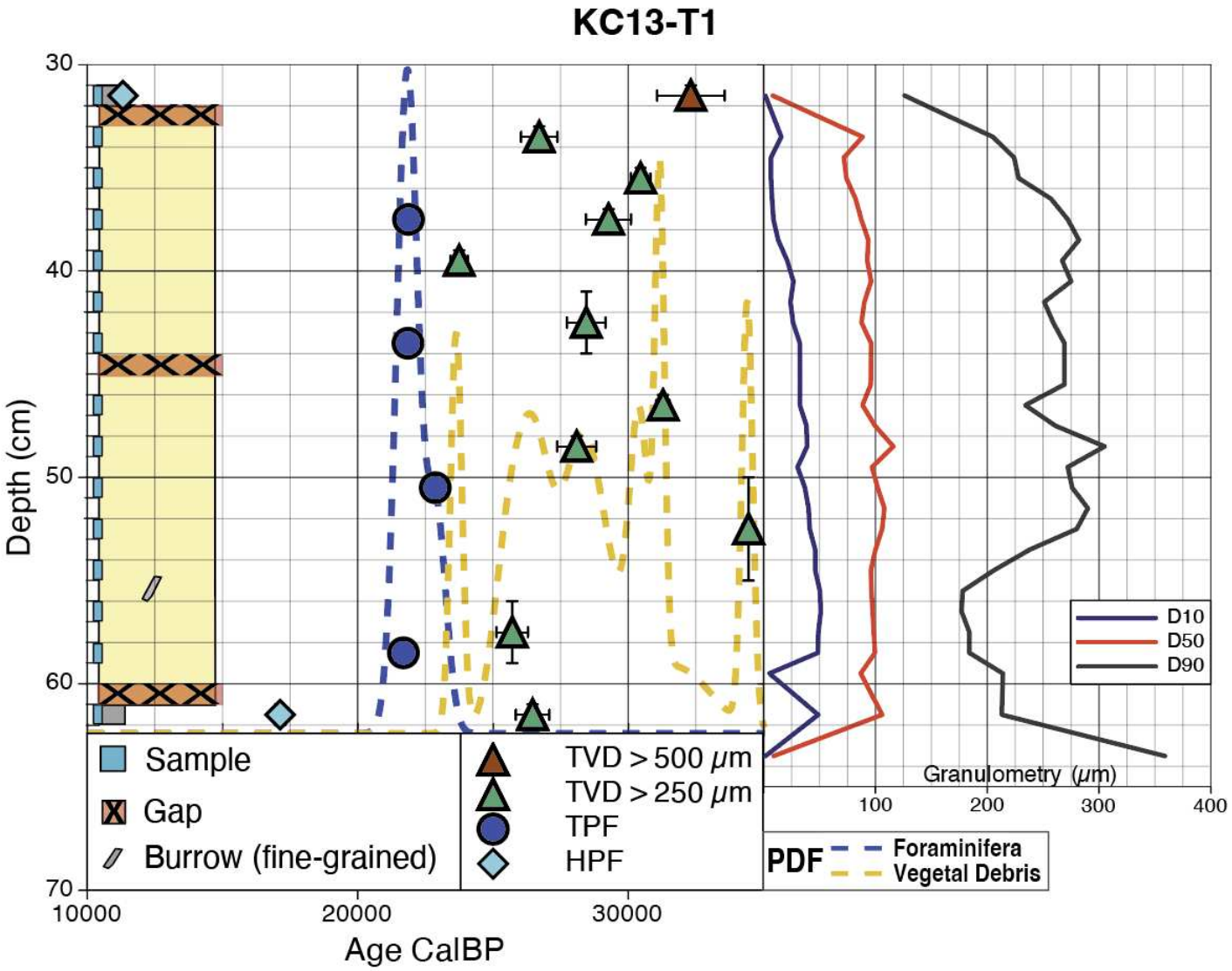

Figure 3.9: Age distribution of different objects within the topmost turbidite of core KC13. On the right is the stratigraphic log of said turbidite. All relevant information is given in the legends. Blue and yellow dashed lines are Probability Density Functions for TPF and TVD ages, respectively.

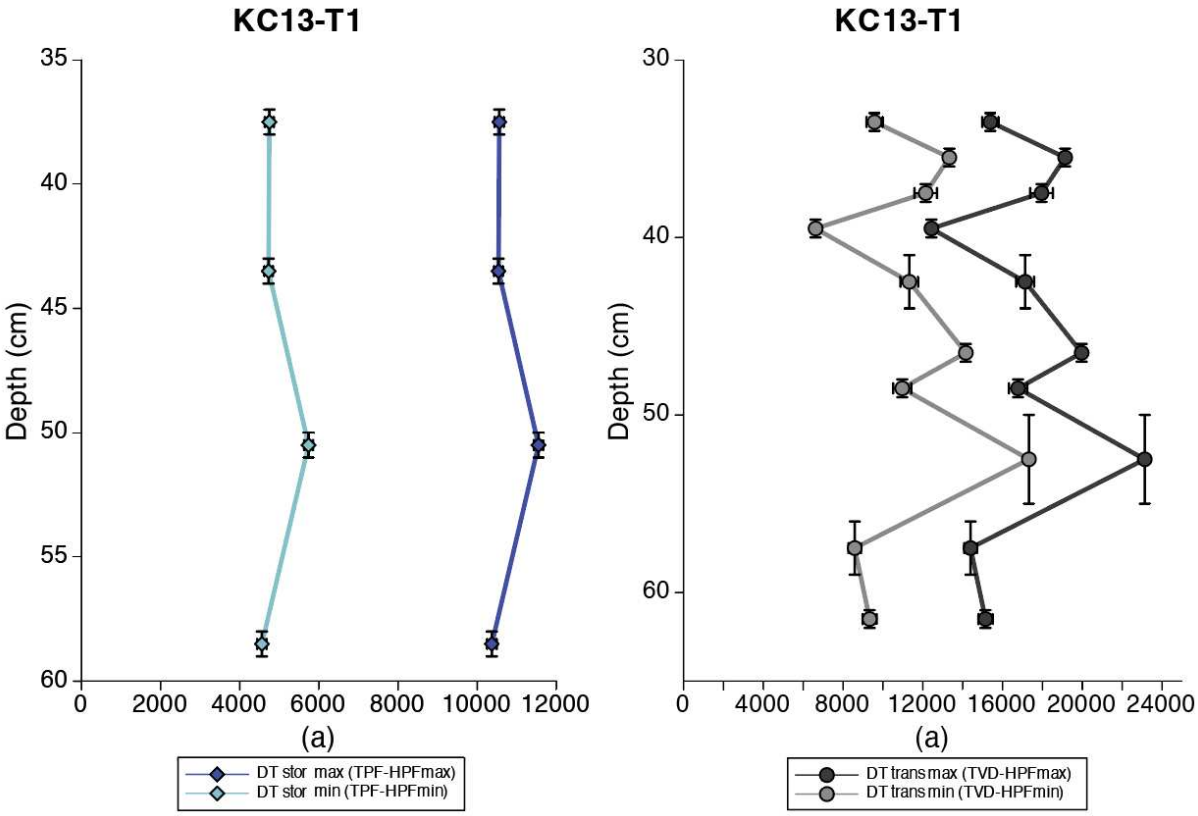

Figure 3.10: ΔT_{stor} and ΔT_{trans} for turbidite KC13-T1

3.5.3.2. KC11-T1

In turbidite KC11-T1, the age of deposition from the HPF, ranges from 20.7 ± 0.3 ka (81-82 cm) to 30.6 ± 0.5 ka (120-121 cm) (Figure 3.11, Table 3.3). Vegetal debris picked in the hemipelagic layers yield ages of 31.2 ± 0.1 ka (81-82 cm) and 40.5 ± 0.5 ka (120-121 cm).

Within the turbidite, ages of the TPF and TVD range from 32.2 ± 0.5 ka to 35 ± 0.4 ka and from 27.6 ± 203 ka (103-104 cm) to 36.4 ± 0.5 ka (105-106 cm), respectively. The TVD for which the > 500 µm and 150-500 µm fractions were picked yield ages of 27.6 ± 0.2 ka and 34.9 ± 0.4 ka (103-104 cm), and 29.4 ± 0.3 ka and 35.2 ± 0.4 ka (115-116 cm), respectively. However, intervals where the > 250 µm, and > 500 µm TVD were picked are comparable with means of 32.9 ± 0.9 ka and 31.4 ± 0.3 ka, respectively, consistent with the total mean of the TVD samples of 32 ± 0.4 ka.

The minimum and maximum ΔT_{stor} durations range from 1.6 ± 0.01 ka and 11.5 ± 0.2 ka (102-103 cm) to 4.4 ± 0.1 ka and 14.3 ± 0.1 ka (97-98 cm), respectively (Figure 3.12). The minimum and maximum ΔT_{trans} range from -3.0 ± 0.3 ka and 6.9 ± 0.1 ka (103-104 cm) to 5.8 ± 0.01 ka and 15.7 ± 0.2 ka (105-106 cm) (Figure 3.12). The resin picked yields an inconsistent age as it is 2.6 ± 0.2 ka younger than the minimum depositional age. In the turbidite intervals where both TVD and TPF where picked, the TPF are older for 3 out of 4 intervals (only older TVD is for interval 102-103 cm, ΔT_{cont} = 1.7 ± 0.2

ka) meaning ΔT_{cont} is negative. The mean absolute age difference between TVD and TPF is of 1.2 ± 0.2 ka.

The evolution of granulometry with depth presents more variation in this turbidite than in KC13-T1. The first decile (D10, Figure 3.11) does not vary much, remaining under 30 µm throughout the layer although the overall grain size is coarser below ~100 cm. The fifth decile (D50) also presents a fining upward sequence with the bottom part of the turbidite presenting grain sizes of up to 200 µm, while above ~100 cm, grain sizes are concentrated around 100 µm. This fining upward sequence is mostly visible in the ninth decile however (D90), with grain sizes above ~100 cm ranging from 250 µm to 300 µm, whereas below ~100 cm, grain sizes increase significantly, reaching > 1 mm from 108 cm down to 117 cm (Figure 3.11).

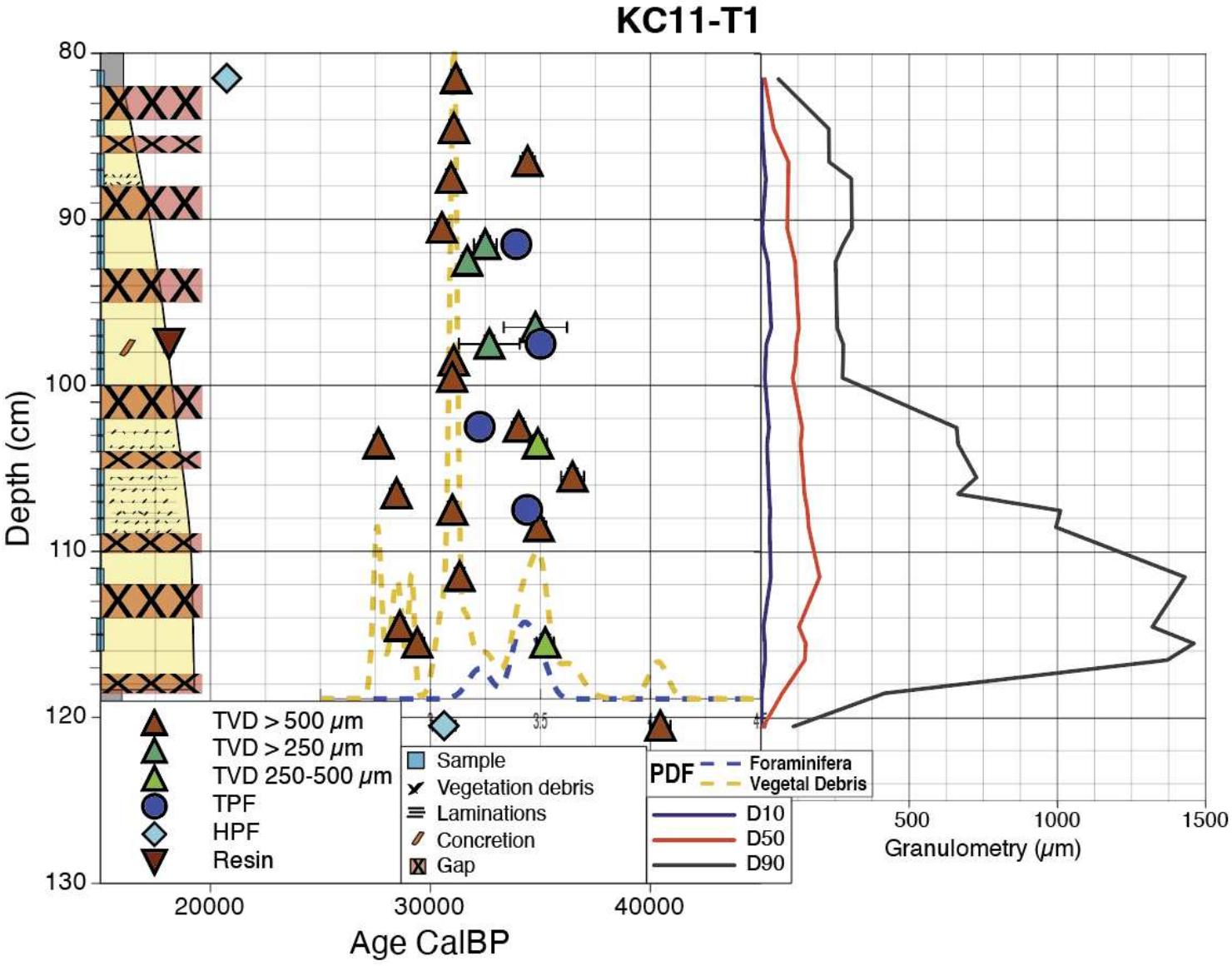

Figure 3.11: Age distribution of the different objects dated and their granulometry in the topmost turbidite of core KC11. On the right is the stratigraphic log for this turbidite. All relevant information is given in the legends. Blue and yellow dashed lines are Probability Density Functions for TPF and TVD ages, respectively.

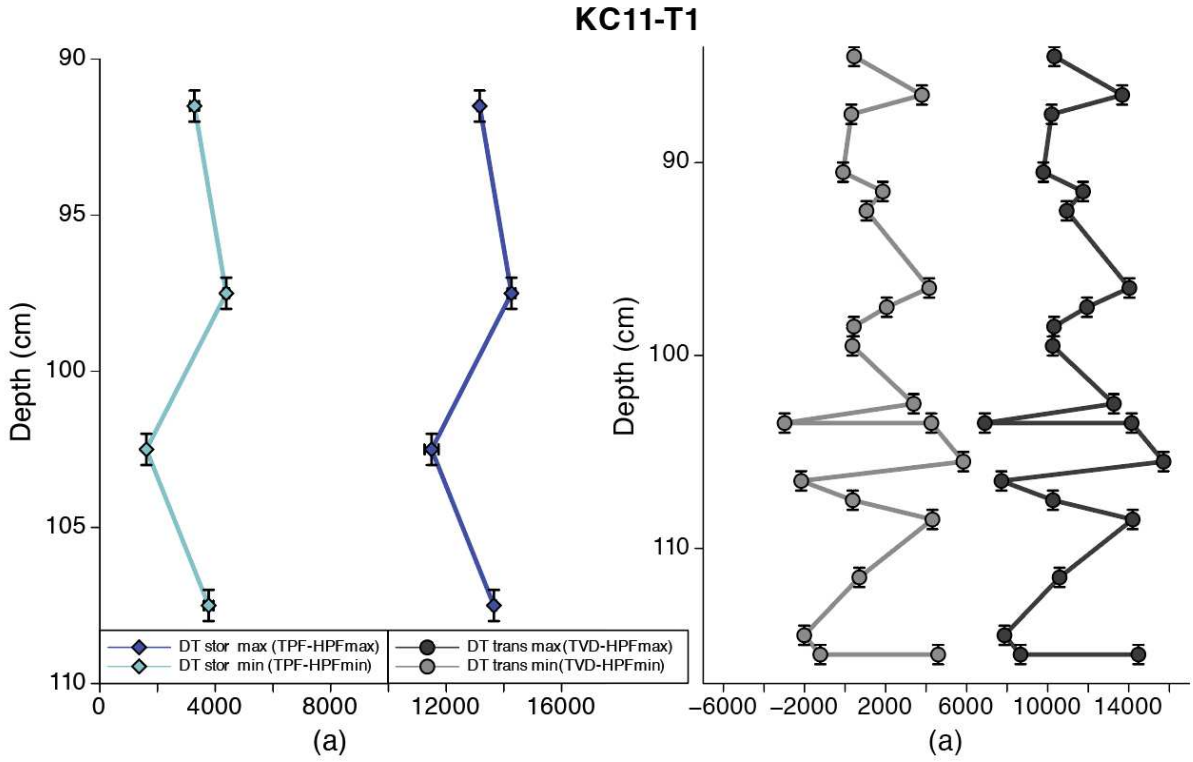

Figure 3.12: ΔT_{stor} and ΔT_{trans} for turbidite KC11-T1

3.6. Discussion

3.6.1. Storage and transport durations

Because the hemipelagic layers located below turbidite deposits are often affected by erosion, and the hemipelagic layers above turbidite deposits correspond to the recovery of decantation of the marine material after the turbiditic flow has settled, the age directly above the turbidite deposit is often considered closer to its depositional age.

For turbidites that are bracketed by HPF ages, if we extrapolate sedimentation rates derived from the age models, we can calculate the amount of hemipelagic sediments that have been eroded by the turbidity flow, at the location of its deposition. This yields values of 24 cm (14 cm/ka sedimentation rate), 26 cm, 58 cm, and 95 cm (10 cm/ka sedimentation rate) for turbidites KC10 40-43, KC10 116-117, KC13-T1 and KC11-T1, respectively. These values are maximum estimates of erosion, as they encompass both the erosion and the hiatus created by the time needed for hemipelagic sediments to settle and start decanting again, after the turbidite deposition.

This implies that our maximum estimations of sediment transfer and storage durations (ΔT_{stor} and ΔT_{trans}) are probably more realistic. Consequently, the turbidity sediments of core KC10 were stored upslope of deposition (ΔT_{stor}) for a mean duration of 5.0 ± 0.1 ka (Figure 3.7). The mean storage duration (ΔT_{stor})

of the sediments of core KC11 is 6.8 ± 0.5 ka, and their mean transport ΔT_{trans} is 12.0 ± 0.7 ka (Figure 3.7). For the high resolution KC13-T1 turbidite, the mean duration values are ΔT_{stor} = 10.8 ± 0.1 ka and ΔT_{trans} = 17.1 ± 0.3 ka (Figure 3.10). In the KC11-T1 turbidite, the mean storage duration, ΔT_{stor} is 13.1 ± 0.1 ka and the mean transport duration ΔT_{trans} is 11.3 ± 0.2 ka (Figure 3.12).

These results allow to quantify mean sediment storage in the Ogowé turbiditic system of 9.6 ± 0.2 ka, and mean transport, from the continent to deep depocenters of 12.9 ± 0.2 ka. These values lead to an estimate of the duration of continental transport of 3.2 ± 0.2 ka.

3.6.2. Variability of ages

Some discrepancies and stratigraphic evolution should be noted. In core KC13 the age of the HPF at 96-99cm (13.3 ± 0.2 ka,

) is 1.5 ka older than the underlying TPF (103-107 cm, 11.8 ± 0.5 ka). It is possible that this older HPF sampled above was not deposited after turbidite emplacement but was in fact remobilized upslope by the turbidite and

Sample	^{14C} counts	Weight µgC	^{14C} Age a	Marine 20 calBP
KC10 34-35	82 896	966	14376 ± 81	16690 ± 330
KC10 48-49	66 806	638	15779 ± 62	18390 ± 267
KC10 112-114	26 933	867	23689 ± 205	27189 ± 464
KC10 122-123	21 101	940	26356 ± 278	29787 ± 450
KC11 186-191	1 233	102	28562 ± 369	32091 ± 931
KC13 64-67	118 822	913	11545 ± 67	12961 ± 218
KC13 96-99	110 874	844	11899 ± 69	13334 ± 233

deposited during the final stage of decantation of the current. Since burrows were found in the sediments of these cores (Figure 3.4), bioturbation and sediment mixing could also explain this anomalous inverse age.

The relationship with depth of the TPF and TVD ages and of the continental transport duration ΔT_{cont}, also give us information on the connectivity of the rivers to the turbiditic systems. A first observation is the younger ages in the topmost turbidite of core KC11 (KC11-T1, Table 3.3) of the TVD, compared to the TPF for 3 out of the 4 investigated intervals (negative ΔT_{cont} for intervals 91-92 cm, 97-98 cm and 107-108 cm). Low resolution sampling of this turbidite (KC11 103-110 cm, Table 3.2) yields similar results, with a negative continental transport duration estimate (ΔT_{cont}) of -4.2 ± 0.4 ka.

These values indicate periods where the storage of marine sediments was more important than the transport of continental sediments. This could indicate a period where the Ogowé river was better connected to the canyons incising the continental margin (Figure 3.1). It would be consistent with the Marine Isotope Stage (MIS) 3 age of the sediments recorded by KC11, which corresponds to a sea-level low stand (Siddall et al., 2008). The vegetal debris would thus have been brought directly from the continent to the deep sea, while the foraminifera would be stored before remobilization.

Another explanation could be the variations of marine storage before remobilization by the turbidity current. In cores KC10 and KC11, ΔT_{stor} decreases with depth possibly controlled by differences in erosive power of the turbidity currents due to their sizes. A small event will have less erosive power, thus incorporating only the topmost part of the seafloor. A larger event, however, will erode much deeper into the canyon floor, remobilizing much older sediments. This interpretation is consistent with the granulometry and the thickness of the turbidites (Mignard et al., 2017, Figure 3.3). We thus argue that our study of the distribution of ages within these deposits gives us insight on the nature of the flow that created them.

The variations of marine storage could also be explained by variability in the source region of initiation of the turbidity flow. At high resolution (KC11-T1 and KC13-T1), the uniformity of the TPF ages, show a rather uniformity of the source of this turbidity current. This implies that both these turbidites were most certainly deposited in single events, and the sediments remobilized by the turbidity flow were constrained to a limited area. The variability of the TVD ages, however, tend to indicate variability in continental material source and duration of transport.

In core KC13, the variability with depth of the different TPF and TVD ages are somewhat chaotic, which could also be explained by variations in sources of the turbidity flow initiation. The location of the core, on the levee of an active channel, ~1 km from the channel axis may also play a role. The frequency of the turbidity flows affecting this area are important, as shown by the high number of turbidite deposits recorded (Figure 3.3). Depending on the size of the turbidity current, the turbidite deposited does not sample the same part of the flow. In a large event, the lower, coarser layers of the turbidity flow can reach the levee, whereas in a small event, only the top finer layers would. This could explain the high variability of the ages with depth. The granulometry and aspect of the KC13-T1 turbidite agrees well with deposition of the upper layers of a turbidity flow, as the material deposited is fine and homogenous.

3.6.3. Implications

Most of the publications using turbidites as archives of continental processes, study mainly the processes that initiated them, and correlate these to climatic or tectonic events (e.g., Gutiérrez-Pastor et al., 2013; Mulder and Syvitski, 1995; Vandekerkhove et al., 2020; Wilhelm et al., 2013; Zhang et al., 2014). Our results show that it is possible to constrain the duration of transport and storage of the sediments contained within these turbidites, which opens the possibility to use them as sedimentary archives for continental processes at almost any temporal and spatial scale. To do so, one would however need to correct between the transport duration of vegetal debris and lithic material. This was not undertaken in this study although the test of different granulometries for TVD of the KC11-T1 turbidite, yield mean transport durations ΔT_{trans} of 10.6 ± 0.1 ka and 12.9 ± 0.5 ka for the coarse (>500 µm) and fine (250-500 µm) fractions. These results tend to indicate that finer objects have seen longer transport histories and

give a first estimate of the transposition of the durations presented in this work to lithic grains, although additional work is needed to better constrain this issue.

We find much longer durations of sediment storage (9.6 ± 0.2 ka), and transport (12.9 ± 0.2 ka) than the previous work. Nakamura et al. (1990) and Stevens et al. (2014) found transport durations of 2.36 ka and decadal to centennial marine transport of sediments, in the Suruga and Monterrey bays, respectively. The much more distal location of our sedimentary archives, together with the low-relief landscape of the continental Ogowé catchment may in part be responsible for these differences. Additional investigations, in diverse climatic, topographic, and tectonic settings would allow to better address these questions, and fully resolve interrogations surrounding turbidite deposits as archives of continental processes.

Finally, in the context of this PhD manuscript, our objective was to test the effect of this transport duration on our ^{10}Be denudation rates. Since the denudation rates we measure are low, they integrate over several 10 ka (see Chapter 200). This means that 12.9 ± 0.2 ka of total transport will be below the resolution of the method, therefore not affecting our measurements. Moreover, because the half-life of ^{10}Be is 1.38 Ma, and our samples have high concentrations of ^{10}Be (due to low denudation rates, see Chapter 2), radioactive decay during the 9.6 ± 0.2 ka of marine storage should not significantly affect our paleo-denudation rate calculations.

As a future perspective of this work, we will investigate the ages of the different material contained within turbidites of the Var sedimentary system, SW France. This system presents high relief and no continental margin and should thus yield different results. These two regions will allow us to create end members to study turbiditic systems of different regions of the Earth.

3.7. Conclusions

This study has successfully constrained transport durations of turbidite sediments. In a low relief, slowly eroding catchment such as the Ogowé, sediment storage before turbidity remobilization reaches 9.6 ± 0.2 ka. The total duration of transport from the continent to the marine depositional environment is also quantified at 12.9 ± 0.2 ka. This leads to an estimate of continental transport in this region of 3.2 ± 0.2 ka.

We have also shown that the study of the distribution of ages within turbidite deposits give us information on the nature and the size of the turbidity current that led to its deposition, and insight on the organization of the sedimentary system upslope of the turbidite deposit. Information on river connectivity or the area from which turbidity flow originate can be extracted from thorough studies of turbidite sediments.

This study shows that turbidites are effectively powerful tools to study and quantify continental processes across scales. Further work to understand and constrain them will be necessary, and we are

already working on constraining a region with different settings, the Var basin. We have presented here an efficient method for studying these distal deposits.

Supplementary Information

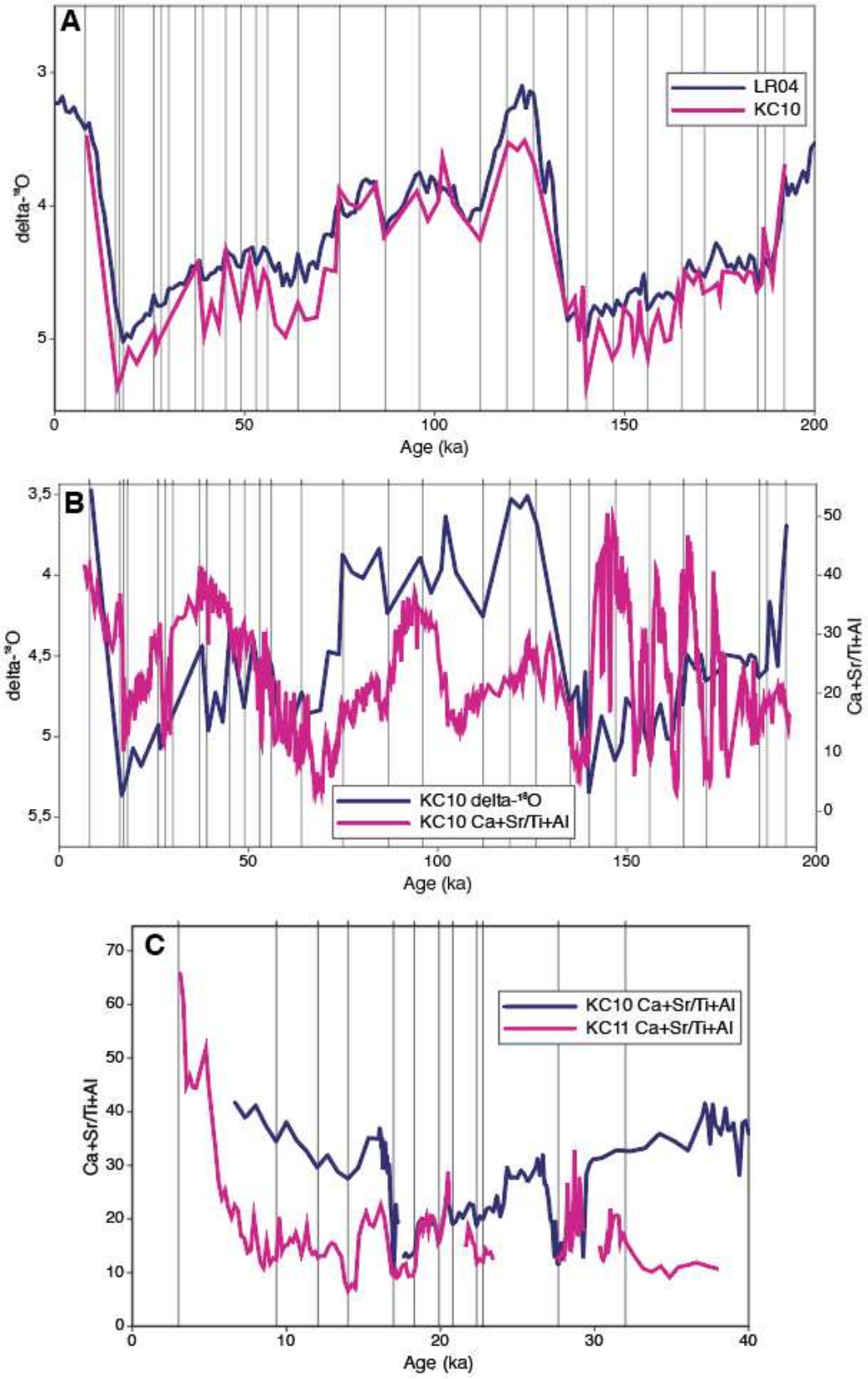

Sup. Info. 3.1: Building steps of the age models for cores KC10 and KC11. In all plots, dark blue data is the reference to which the pink curve is correlated. A/ Correlation between $\delta^{18}O$ data of the LR04 curve (Lisiecki and Raymo, 2004) and of the KC10 core. B/ Correlation between $\delta^{18}O$ data and Ca+Sr/Ti+Al ratios of the KC10 core. C/ Correlation between Ca+Sr/Ti+Al ratios of the KC10 and KC11 cores.

Chapter 4. Late Cenozoic paleo-denudation rates in the Tropical Ogowé drainage

Abstract

The impact of Quaternary glaciations on denudation rates has long been debated. The instability of Quaternary climatic fluctuations was proposed to be a driver of higher denudation rates since the Pleistocene, but this hypothesis has yet to be proven. Most denudation rate reconstructions have focused on areas either tectonically active or glaciated, or both, leading to difficulty in constraining the impact and the modalities of climate cyclicity on denudation. Deciphering the respective roles of climate and tectonic on denudation can be challenging, and glacial erosion appears to be non-linear. Furthermore, these studies have focused mainly on the Northern Hemisphere or high latitude regions. If real, a global increase of denudation involving common forcings and mechanisms implies that all other regions should be equally impacted. However, a large gap in data and knowledge exists in low latitude Tropical regions. Therefore, tectonic-free Tropical regions are key to better understand the impact of climate on denudation independently from the role of glaciers.

In this work, we propose to quantify paleo-denudation rates of the Ogowé catchment (Gabon) over Plio-Pleistocene times by measuring ^{10}Be in quartz grains collected from turbidite samples of three cores and cuttings from one borehole collected 30 km to 200 km offshore the mouth of the Ogowé river. To better constrain transport times of these sediments and quantify their ages of burial, we also use radiocarbon ages of vegetal debris contained in the turbidites (Chapter 3) as well as $^{26}Al/^{10}Be$ ratios.

Our results show lower denudation rates in the Late Pliocene than in the Pleistocene, although the variations do not seem to follow glacial/interglacial cyclicity. We conclude that the Mid Pleistocene Transition may have had an effect on paleo-denudation rates of the Ogowé region. Furthermore, although since the Pleistocene denudation rates do not follow glacial/interglacial cyclicity, we conclude that either the Quaternary climatic cycles did not affect local tropical climate of the Ogowé region, or denudation rates remain unaffected by climatic variability, at the scales of 10 ka to 100 ka.

4.1. Introduction

In the following work, for the reasons already exposed in 0 of this thesis manuscript, we study a tropical region where Quaternary sedimentary archives are available: the Ogowé drainage basin. This region has the advantage that the modern basin has been thoroughly studied by Regard et al. (2025) who quantified

modern denudation rates using *in-situ* ^{10}Be. We reconstruct paleo-denudation rates of the Ogowé basin using terrestrial cosmogenic nuclides measured from turbidites of 3 marine sedimentary cores (KC10, KC11 and KC13), and cuttings from 1 borehole (Torpille Marine, TM). The three cores were collected in the Ogowé deep sea fan and record sediments at high resolution (i.e., 10-20 cm/ka) over the past 200 ka (Mignard et al., 2017). The borehole was drilled ~30km from the mouth of the Ogowé river and although its age model is affected by great uncertainties, it permits to document Pliocene paleo-denudation rates, before the Mid Pleistocene Transition (MPT, Berends et al., 2021). For 2 of the marine sedimentary cores (KC10 and KC11), we refine the age models using the interpolation tool on the Gnumeric software (http://www.gnumeric.org) and constraining the model by peak correlation and new ^{14}C ages (see Chapter 3). In addition, cosmogenic ^{26}Al was also measured whenever possible, in order to use the ^{26}Al/^{10}Be ratio as an additional constraint on the burial and sediment transport history of these sediments.

4.2. The Ogowé drainage system

On land, the Ogowé river drains an area of ~2.15 10^5 km^2 with an annual discharge of ~4.3 10^3 m^3/s at Lambaréné (Figure 4.1). This catchment occupies the near totality of Gabon, reaching Cameroon in the North, Equatorial Guinea in the NW, and the Republic of Congo in the NE, East and SW (Figure 4.1). The Ogowé region is located directly south of the area of influence of the African monsoon. Consequently, in terms of Köppen-Geiger classification, the region is considered in an Equatorial (or Tropical) savannah climate with dry winters, and a summer dry northernmost part of the country (Figure 4.1) (Kottek et al., 2006). Mean annual precipitations are of 1.5 to 2 m but can reach 3 m in the NW (e.g., in Libreville). Gabon climate is supposed to be wet and tropical since the Neogene (Séranne and Anka, 2005).

The geology of the catchment is mainly composed of felsic and metamorphic crystalline basement corresponding to the Archean Congo Craton that is locally affected by mafic intrusions (Thiéblemont et al., 2009) (Figure 4.2). This crustal domain is dominated by granites and granitoids (Regard et al., 2025). Along the western coast, sedimentary successions record the Atlantic Rifting (Mbina Mounguengui et al., 2002) while in the SE, the upstream Ogowé erodes the Batéké plateau composed of quarzitic Cenozoic sandstone whose origin is unclear (Seranne et al., 2008). Downstream, the Paleoproterozoic sediments of the Francevillian basins are mainly composed of sandstones and conglomerates (Weber et al., 2016). The emplacement of these sedimentary units is accompanied by intracrustal and compressive volcanism (Thiéblemont et al., 2014).

These lithologies of the Congo craton are as old as Archean ages (Thiéblemont et al., 2018) and very stable. The last major geodynamic event affecting this region was the Late Mesozoic break-up of

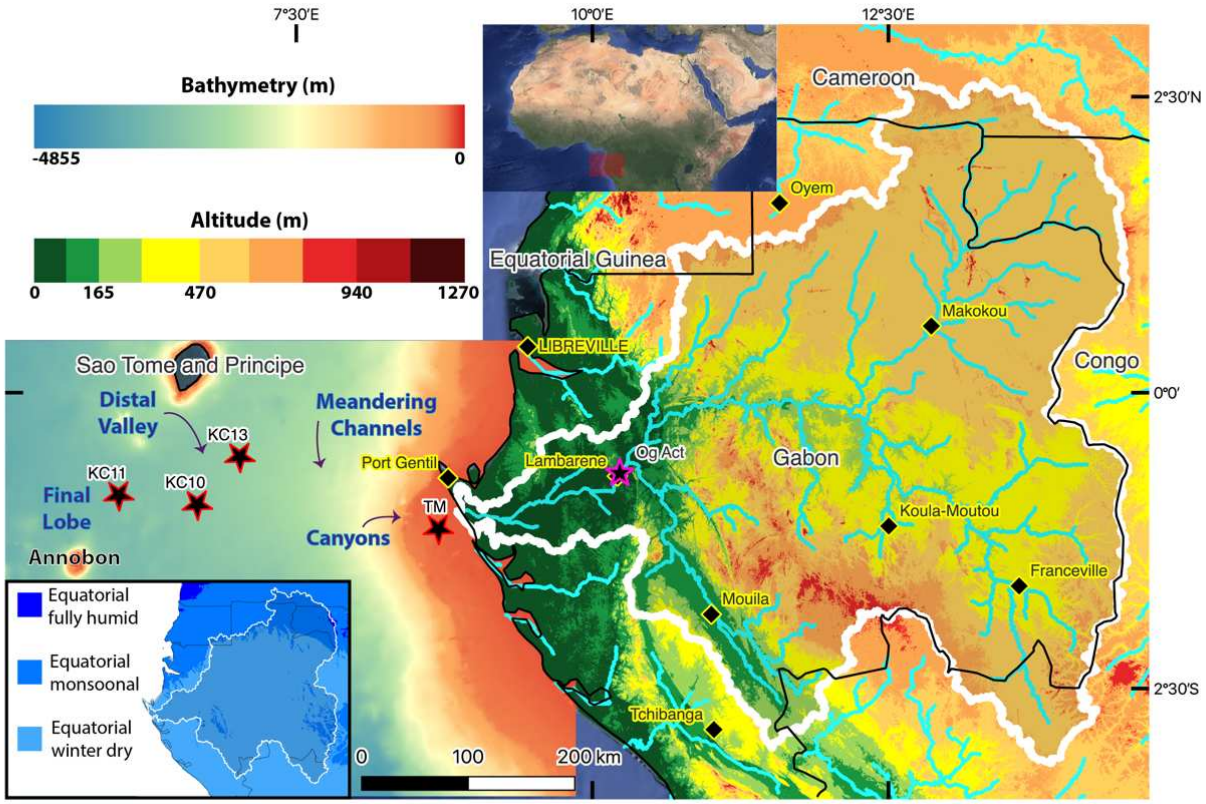

Figure 4.1: General map of the Ogowé sedimentary system. Top middle inset shows general position on the African continent. Bottom right inset shows the climatic zones in terms of Köppen-Geiger (Kottek et al., 2006). Thick white line is the contour of the Ogowé drainage. Black and yellow diamonds are cities. Red stars indicate position of cores. Pink star is the position of the river sand sample.

Gondwana and opening of the Atlantic ocean (Binks and Fairhead, 1992), recorded along the Gabonmargin (Dupré et al., 2007). More recently the Ogowé region was affected by the African superplume with two phases of uplift inferred from inverse modelling of velocity profiles in the Oligocene and in the Pliocene (Al-Hajri et al., 2009). Uplift of up to 500m is also observed since the late Miocene along the Atlantic coast from the mapping of planation surfaces (Guillocheau et al., 2015). The Ogowé sedimentary system is prolonged in the Atlantic Ocean by a well-developed turbiditic system, channeling the terrestrial sediments from the continental margin to deep-sea depocenters. The detailed bathymetry of this area was described by Mignard et al, (2019) (shown in Chapter 3), but the raw data were unfortunately unavailable for this work. This system is composed of several canyons with relatively steep slopes (~2.4°) incising the continental margin NW of the Ogowé river mouth (Mignard et al., 2019). These canyons are downstream connected to channel-levee systems and an intermediate depocenter where slopes decrease (0.9° and 0.3°, respectively), before merging SE of São Tomé into a distal valley where slopes increase (0.6°) (Mignard et al., 2019). Sediments are then conveyed through this distal valley and into a distal lobe, separated in an upper and lower lobe (0.2°), connected by a corridor (0.3°) (Mignard et al., 2019). This submarine sedimentary system crosses the end of the Cameroon Hot Line between the São Tomé et Principe and Annobòn volcanic islands, which constitute

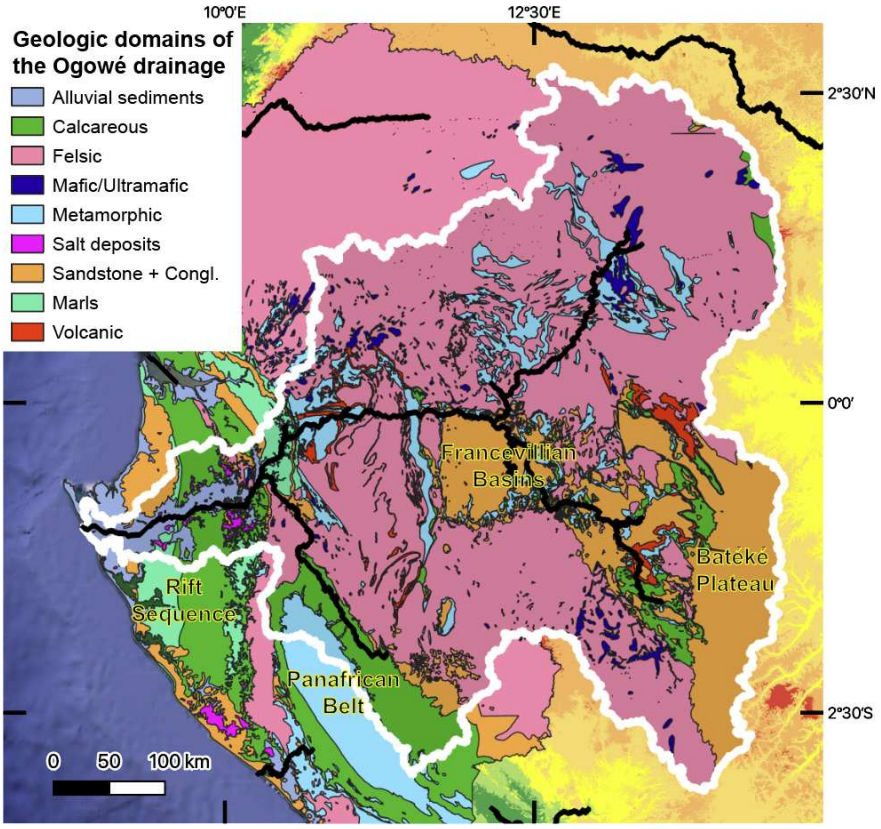

Figure 4.2: Geologic domains of the Ogowé drainage. Thick white line is the limits of the Ogowé catchment. Black lines are rivers. Geological mapping is from Thiéblemont et al. (2009)

another source of sediments. Due to their volcanic nature, they are however very easy to identify and distinguish from the cratonic sediments brought by the Ogowé river, on which this work is focused (Mignard et al., 2019). This volcanic area may however have been responsible for uplift affecting the system (Nkono et al., 2014), although km-scale uplift would have been localized on the volcanic islands and concentrated in the Miocene (Meyers et al., 1998). Modern meter-scale uplift is difficult to disentangle from eustatic variations (Barfod and Fitton, 2014).

Modern denudation rates of the Ogowé catchment range from 3.1 ± 0.2 mm/ka in the NE to 21.8 ± 1.8 mm/ka in the SE, with a denudation rate of 14.6 ± 1.2 mm/ka measured close to the outlet (Regard et al., 2025)

4.1. Material and Methods

4.1.1. Studied cores and borehole cuttings

For this work, we rely on 3 Küllenberg-type cores, KC10, KC11 and KC13 (Figure 4.3), drilled in the Ogowé turbiditic system during the MOCOSED 2010 cruise on the R/V "Pourquoi Pas?" by the SHOM (Service Hydrographique et Océanographique de la Marine. https://www.shom.fr) (Division Plans De DMI-SHOM, 2010). KC10 was sampled at 3148 m depth, in a disconnected channel, believed to be currently inactive, KC11 at 3372m depth, at the outlet of the distal valley, where four main channels

merge and KC13 at 2852m depth, on the levee of one of the active channels, about 1km from the channel axis (Mignard et al., 2017). These cores are composed of hemipelagic sediments intercalated with turbiditic deposits of various thicknesses and at various frequencies (Figure 4.3, see Mignard, 2017 for a thorough study of these cores). Hemipelagic samples are typically silts (D50 < 62 µm), while turbidites are composed of fine to coarse sand (typically, D50 of 100 µm) (Mignard, 2017) (Figure 4.3).

In addition, we were able to access well cuttings from a borehole, Torpille Marine (TM), drilled by Total in 1968 about 30 km offshore from the mouth of Ogowé river. These cuttings correspond to medium to fine continental sand.

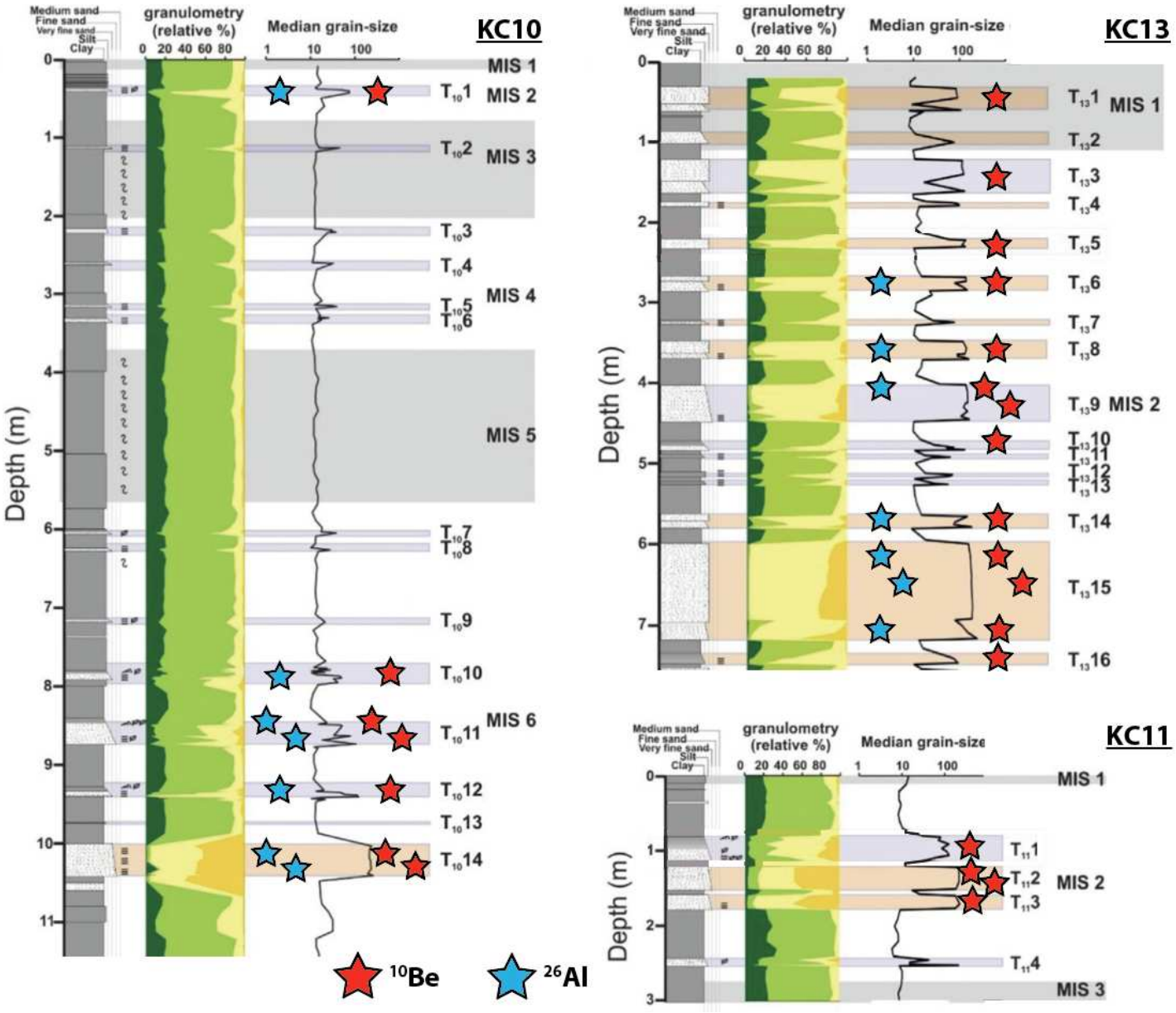

Figure 4.3: Stratigraphic log with corresponding Marine Isotope Stages of cores KC10, KC11 and KC13. All turbidites are shown by blue/grey or orange rectangles. Blue and red stars indicate intervals where ^{26}Al and ^{10}Be were measured, respectively. Figure modified from Mignard et al. (2017).

4.1.2. Absolute age of turbidite sediments

Turbididites are typically considered as instantaneous events and are thus generally dated considering the associated depositional ages of the underlying and overlying hemipelagic layers. However, turbidites consist of remobilized sediment (see Chapter 3) and because we are interested in this work in the erosion age on the continent, we must correct the depositional ages by the time of transport from continental erosional to marine depositional regions. This lag time correction is necessary to yield the absolute age of sediments, i.e., the timing of the continental denudation (see Chapter 3). The absolute ages of studied sediment of the turbidite sampled for cosmogenic nuclide analysis were therefore constrained based, whenever possible, on the numerous ^{14}C measurements that we made on Turbiditic Vegetal Debris (TVD, see Chapter 3), Turbiditic or Hemipelagic Planktic Foraminifera (TPF or HPF, see Chapter 3), or both, depending on the availability of material.

We choose to use the TVD ages for our ^{10}Be samples, when available, as we expect these to be the closest to an erosional age. For some samples these ages were not available, and we hence use turbiditic foraminifera ages and add an uncertainty of 8 ka to account for possible storage on the continental margin (see Chapter 3). If only the modelled age (see Chapter 3) is available, we add an uncertainty of 10ka to account for both the uncertainty on the age model and for possible time lapse between the time of erosion and the time of deposition. For turbidites of the KC13 core, as no age model was done, turbidites which are not dated with ^{14}C are dated by linear interpolation between the closest overlying and underlying dated turbidite using the Gnumeric software (http://www.gnumeric.org).

Since material of the TM probe does not originate from a core, but corresponds to cuttings, the age model of these sediments is affected by large uncertainties, as only the transitions between certain stratigraphic intervals were dated from a Palynological and Micropaleontological analysis, first done in 1968 and revised in 1997 by Total (Sup. Info. 4.1Sup. Info. 4.2). With constraints on the maximum (4.37 Ma at 570 m depth) and minimum (3.6 Ma at 206 m depth) ages of the N'Tchengué formation, we were able to calculate an age model by extrapolation, considering a constant sedimentation rate within this interval, and a different constant sedimentation between 206 m depth and the surface. For each sample, uncertainties are considered as the age difference between the samples located directly above and below it, yielding an age range for each sample.

4.1.3. ^{10}Be paleo-denudation rates

We calculate paleo-denudation rates by measuring ^{10}Be concentrations in quartz grains of the turbiditic samples and solving equation 1 (Chapter 2 and e.g., Brown et al., 1995; Puchol et al., 2017). To do so, we calculated the average production rates of the Ogowé basin. Production of cosmogenic nuclides is highly dependent on altitude and latitude (Lal, 1991; Stone, 2000), as the Earth's atmosphere and magnetic field are efficient shields against cosmic particles. We must hence work under the assumption

that altitude and latitude have not varied significantly over Late Cenozoic, a reasonable hypothesis, as tectonic activity is limited during that period.

As we measure ^{10}Be in quartz grains, we consider only quartz-bearing lithologies for production rate calculations. Quartz-bearing lithologies (i.e., alluvial sediments, felsic lithologies, sand, sandstone and sedimentary coarse-grained, Figure 4.1) were isolated from a vectorized version of the geological map of Gabon (Thiéblemont et al., 2009) using ArcGIS. These lithologies represent 77.3 % of the entire Ogowé drainage leading to a reasonable assumption that our turbidite-derived ^{10}Be denudation rates are representative of the Ogowé drainage denudation. We used the Basinga ArcGIS toolbox (Charreau et al., 2019) to calculate the production rates of quartz bearing lithologies of the Ogowé basin. This area yields production rates of 2.7515 at/g/a, 0.037733 at/g/a and 0.012135 at/g/a for neutrons, fast muons, and slow muons, respectively.

4.1.4. ^{26}Al/^{10}Be ratios

The surficial production ratio of ^{26}Al/^{10}Be in quartz is ca. 6.6 (Borchers et al., 2016). When the grains are buried, they are shielded from cosmic rays and hence the ratio decreases with time, due to the difference in half-life of ^{26}Al (0.7 Ma) and ^{10}Be (1.38 Ma). The ratio measured in sediment may therefore represent a burial age assuming the initial surface ratio was preserved during erosion and sediment transport before deposition. The method is largely presented in the introduction chapter of this manuscript and in the literature (e.g., Braucher et al., 2011; Granger and Muzikar, 2001). However, in large watersheds, sediments may also have been stored and buried for a significant time (up to 1 Ma) during their transportation modifying the initial ^{26}Al/^{10}Be ratio (e.g., Wittmann et al., 2011). The measured values in sediments may therefore represent an "apparent" burial age and include both the time since sediments were buried but also the duration of transport. This method may therefore provide constraints on the depositional ages and durations of sediment transport, which is critical to interpret ^{10}Be concentration and reconstruct paleo-denudation rates (e.g., Charreau et al., 2023; Mariotti et al., 2021; Puchol et al., 2017, see also Chp.5 of this manuscript).

In this study, whenever possible, we analyzed ^{26}Al/^{10}Be ratios with two goals. For cores KC10, KC11 and KC13, the very young ages (i.e., < 200 ka) of the cores, place them under the resolution limit of the ^{26}Al/^{10}Be method, which begins to be consistent at about 500 ka of burial (i.e., the necessary time for the ratio to decrease sufficiently to be below the "production banana"). Therefore, the aim of measuring ^{26}Al/^{10}Be ratios in these three cores was only to investigate the existence of a possible transport delay. Second, for cuttings of the TM probing, the older ages make them more appropriate for ^{26}Al/^{10}Be burial dating. For this set of samples, the aim was therefore to provide additional control on the age of deposition (in addition to biostratigraphy).

In all cases, we calculate burial ages using the Matlab code from Blard et al. (2019) which is based on the equations described by Granger and Muzikar (2001), taking into account the elevation of the

watershed (Blard et al., 2019a). The mean altitude of the catchment, 447 m and its mean latitude of 1° are considered in this calculation. Importantly, the modern river sediments sampled at Lambaréné, close to the outlet of the Ogowé River, yield measured $^{26}Al/^{10}Be$ ratios of 5.3 and not 6.6. Hence, it is highly possible that sediments, at their time of deposition within the Ogowé turbiditic system had already experienced burial (of < 1 Ma) during their continental journey. We thus calculated burial ages using initial ratios of 6.6 and 5.3 and compared the results.

4.1.5. Cosmogenic nuclide sampling and treatment

For our study, we measured ^{10}Be and ^{26}Al in 7 turbiditic samples of core KC10. In core KC11, 4 turbiditic samples were analyzed for ^{10}Be and ^{26}Al. Thirteen turbiditic samples of core KC13 were processed for ^{10}Be and ^{26}Al measurements. Unfortunately, the 4 ^{26}Al samples of core KC11 and 5 of the 13 ^{26}Al samples of core KC13 have not yet been analyzed in CEREGE (where the Accelerated Mass Spectrometer necessary for these measurements is located, see Chapter 2). Moreover, one of the samples of core KC13 (KC13 222-228) could not be measured on the AMS due to the absence of current. Therefore, in the present version of this work, only 7 ratios for core KC13 and none for core KC11 are presented (Figure 4.3). Measured samples were selected according to their granulometry (50-250 µm) and their mass (typical masses of 10^1-10^2 g of turbidite sand).

In cores KC10 and KC13, we chose to test the consistency of ^{10}Be and ^{26}Al values with varying grain fractions. We thus separated the 50-100 µm and 100-250 µm fractions for 3 samples of KC10 and 2 samples of KC13, chosen depending on their mass (i.e., > 100g of turbidite sand). Some of the thicker turbidites (i.e., > ~20cm) were also sampled twice, at two different intervals, to check for potential variations of the ^{10}Be concentrations within single turbidity deposit (Figure 4.3, Table 4.1Table 4.3).

We sampled 12 of the TM cuttings from 144 m to 385 m depths selected for their availability, their coarseness (typically D50 > 100 µm) and their masses (typically > 50 g) for ^{10}Be and ^{26}Al analysis.

To compare modern and paleo-denudation rates, we also processed a modern river sand sample, collected by Vincent Regard during a field campaign close to the mouth of the Ogowé river, and measured both its ^{10}Be and ^{26}Al concentrations. This sample comes in complement to the widespread dataset from Regard et al. (2025), allowing a very good understanding of the spatial distribution of denudation within the modern Ogowé catchment.

For cosmogenic nuclide extraction the followed protocol has been largely described in the introduction chapter of this manuscript and modified from (Kohl and Nishiizumi, 1992). Samples were sieved using 50 µm, 100 µm and 250µm sieves for samples for which we wanted to test the granulometry, and only 50 µm and 250 µm for the rest. Non-magnetic minerals were then isolated using a Frantz magnetic separator following Rosenblum (1958), before quartz purification using 3 to 7 rounds of a concentrated 2/3 H_2SiF_6 + 1/3 HCl solution. Quartz grains were etched using calculated amounts of concentrated HF to eliminate atmospheric contamination by dissolving a total of 30 % of the quartz mass, in three

successive steps (Brown et al., 1991). Chromatographic column chemistry was then done, first with an anionic resin DOWEX 1x8 and HCl 10.2 mol/L, then with a cationic resin DOWEX 50Wx8 with HCl 1 mol/L to extract BeO and with HCl 4.5 mol/L to extract Al_2O_3.

Samples were prepared in different batches. Batch 3 (Table 4.1Table 4.3) was processed at CEREGE (Aix-en-Provence) with their home carriers having ^{9}Be and ^{27}Al concentration of 3025 ± 9 and 1000 ppm, respectively. The last 5 batches were treated in the clean lab of CRPG (batches 5_6 and 8_9_10 of Table 4.1Table 4.3) with the spike developed at CRPG with a ^{9}Be concentration of 2129 ± 13 ppm and an Al standard with ^{27}Al concentrations of 1003 ± 4 µg/ml. $^{10}Be/^{9}Be$ and $^{26}Al/^{27}Al$ ratios were then measured at the ASTER facility in CEREGE, Aix-en-Provence (France). The Accelerated Mass Spectrometer (AMS) was calibrated using the STD-11 in-house standard (Braucher et al., 2015), with a certified $^{10}Be/^{9}Be$ ratio of 1.191 ± 1.298 10^{-13}, similar to KNSTD07 standardization (Nishiizumi et al., 2007) and SM-AL-11 internal standard with a certified $^{26}Al/^{27}Al$ ratio of 7.401 ± 0.064 10^{-12} (Merchel and Bremser, 2004).

Mean analytical $^{10}Be/^{9}Be$ blank ratios are of 5.0 ± 1.1 10^{-16}. However, the blank is higher for batch 3 (22 ± 3.8 10^{-16}, Table 4.2) than for batches 6_7 and 8_9_10 (means of 3.6 ± 1.4 10^{-16} and 7.2 ± 1.8 10^{-16}, respectively, Table 4.2). This discrepancy can be explained both by the low $^{10}Be/^{9}Be$ carrier developed at CRPG (initial $^{10}Be/^{9}Be$ ratio of 1.0 x 10^{-16}, Blard et al., in prep.) and the fact that the samples were processed in a clean lab at CRPG. ^{10}Be blank corrections represent less than 10 % (mean of 3 %) of the analyzed samples and their contribution to the total ^{10}Be uncertainty is lower than 20% (mean of 13 %). The $^{26}Al/^{27}Al$ blanks of all batches yielded either no counts or only 1 count (Table 4.4), leading to 0 correction or to $^{26}Al/^{27}Al$ blank ratios < 5 10^{-16}, with a 100% uncertainty associated with this ratio. However, there is a high level of confidence in these measured blanks, since their AMS measurements yielded high ^{27}Al current, indicating that there was no issue with the Al chemical processing, but rather an absence of ^{26}Al to measure, indicating very low-level blanks. Such clean blanks could also suggest a possible loss of Al during sample chemistry, a problem largely explained in the introduction chapter of this manuscript and that we avoided by important improvements of the CRPG ^{26}Al extraction protocol, with the work of Marie Protin. ^{26}Al blank corrections represent less than 2 % (Batch 8_9_10) of the analyzed samples and their contribution to the total ^{26}Al uncertainty is lower than 20 % (batch 8_9_10).

4.2. Results

4.2.1. Age of turbiditic material

The maximum and minimum depositional ages obtained for the youngest turbidite deposit (KC10 40-43) were of 15.8 ± 0.1 ka and 14.4 ± 0.1 ka, respectively, while they are 26.4 ± 0.3 ka and 23.7 ± 0.2 ka, respectively for the oldest turbiditic deposit (KC10 116-117) (

, see Chapter 3). Turbidite $T_{10}1$ (40-43 cm) yielded a TPF age of 22.3 ± 0.3 ka (Table 4.1, see Chapter 3). Because this age is a TPF age, we add 8 ka to the 1 sigma uncertainty to account for the uncertainty associated to possible continental transport duration.

Sample	^{14}C counts	Weight µgC	^{14}C Age a	Marine 20 calBP
KC10 34-35	82 896	966	14376 ± 81	16690 ± 330
KC10 48-49	66 806	638	15779 ± 62	18390 ± 267
KC10 112-114	26 933	867	23689 ± 205	27189 ± 464
KC10 122-123	21 101	940	26356 ± 278	29787 ± 450
KC11 186-191	1 233	102	28562 ± 369	32091 ± 931
KC13 64-67	118 822	913	11545 ± 67	12961 ± 218
KC13 96-99	110 874	844	11899 ± 69	13334 ± 233

In core KC11, TVD ages of the four intervals analyzed yield ages from 27.6 ± 0.2 ka ($T_{11}1$, 103-110 cm, see Chapter 3) to 46.9 ± 0.9 ka ($T_{11}3$, 164-172 cm, see Chapter 3), increasing with depth. Notice that turbidite $T_{11}2$ yields contrasting ages from 29.7 ± 0.4 ka (124-130 cm) to 34.4 ± 0. 2 ka (140-147 cm), although these results are consistent with the study presented in chapter 3. These TVD ages are the ones used to calculate and interpret ^{10}Be denudation rates.

For turbidites of core KC13, ages vary from 19 ± 0.3 ka (360-366 cm) to 36.5 ± 2.5 ka (756-763 cm) (Table 4.1, see Chapter 3). Ages are highly non-linear with depth. The turbidites in which no TVD or TPF were dated were constrained by interpolation between dated turbidites. The uncertainty on this interpolation is reflected by the 10 ka error associated to these ages. Note that turbidites sampled at different intervals ($T_{13}9$ and $T_{13}15$, Table 4.1) yield results which are consistent, within 1 sigma.

Because of the limited temporal range (0.5 cm to 199 cm with a 3 ka to 38 ka age range) of core KC11, it is difficult to observe significant variations between turbidite occurrence, sedimentation rate and Marine Isotope Stage (MIS). Core KC10 on the other hand, presents a much longer record (1 cm to 1159 cm with a 6 ka to 193 ka age range), ranging from MIS1 to the MIS5-MIS6 transition (Figure 4.3). It is noteworthy that turbidites preferentially occur in interglacial periods s(n = 14) with only 2 turbidites occurring during MIS2 and none during MIS4. For a further description and interpretation of turbidite ages, see chapter 3.

Cuttings of the TM probe yield biostratigraphic ages ranging from 1026.7 ± 126.7 ka to 2633.3 ± 63.3 ka. These ages could be challenged due to the method used to calculate them (see section 4.1.2). Nevertheless, the sedimentation rate calculated for the N'Tchengué formation is of 15 cm/ka, a value consistent with our findings on cores KC10 and KC11, and consistent with previously published values (e.g.. Mignard et al.. 2017).

4.2.1. $^{26}Al/^{10}Be$ burial ages

The $^{26}Al/^{10}Be$ ratios obtained are presented in Table 4.3. For core KC10, ratios range from 2.5 ± 0.5 (941-944, 50-100 μm) to 5.7 ± 1.3 (788-791, 50-100 μm) with a weighted mean of 4.7 ± 0.4 (MSWD 1; p 0.39). In core KC13, ratios are of 4.8 ± 0.4 (680-690, 100-250 μm) to 6.0 ± 0.5 (360-366) with a weighted mean of 5.5 ± 0.3 (MSWD 0.77; p 0.63) and the TM cuttings yield ratios of 0.9 ± 0.2 (252) to 1.9 ± 0.4 (376) with a weighted mean of 1 ± 0.1 (MSWD 0.42; p 0.91).

Two standards where analyzed to check reproducibility, Cronus-A (Jull et al., 2015) and UVM-A (Corbett et al., 2019). Results of these measurements are given in Table 4.5 and Table 4.6 and show results which are within uncertainties of expected values for both ^{10}Be and ^{26}Al.

Table 4.1: Complete ^{10}Be results. Errors are 1 sigma. TVD are Turbiditic Vegetal debris and TPF are Turbiditic Planktic Foraminifera.

Batch	Sample name	Turbidite	Granulometric range	$^{10}Be/^{9}Be$	Total count ^{10}Be	Mass of Quartz	^{9}Be	10Be	Age	Datation type	10Be corrected	Denudation rates	Integration time
			µm	10^{-15}		g	10^{19} at	10^{4} at/g	ka		10^{4} at/g	mm/ka	ka
6_7	KC10 40-43	T_{10} 1	50-250	43 ± 1.8	665	10.7	2.9	11.6 ± 0.5	22.3 ± 8.3	TPF	11.7 ± 0.5	17.3 ± 3.7	34.7
3	KC10 788-791	T_{10} 10	50-100	7.4 ± 0.8	79	1.5	3.1	10.5 ± 1.8	160 ± 10	Age Model	11.3 ± 2	18.5 ± 5	32.4
3	KC10 788-791	T_{10} 10	100-250	6 ± 0.6	120	1.1	3.1	16.7 ± 1.9	160 ± 10	Age Model	18.1 ± 2	11.3 ± 2.6	53.1
8_9_10	KC10 858-860	T_{10} 11	50-250	55.7 ± 1.9	1214	13.5	3	12.1 ± 0.4	165 ± 10	Age Model	13.1 ± 0.4	15.4 ± 3.2	39
8_9_10	KC10 873-876	T_{10} 11	50-250	72.9 ± 2.3	1199	16.5	3	13 ± 0.4	165 ± 10	Age Model	14.1 ± 0.5	14.4 ± 2.9	41.7
3	KC10 941-944	T_{10} 12	50-100	11.6 ± 0.7	261	1.6	3.1	22.6 ± 1.6	172 ± 10	Age Model	24.6 ± 1.7	8.3 ± 1.8	72.3
3	KC10941-944	T_{10} 12	100-250	10 ± 0.6	247	2	3.1	15.5 ± 1.2	172 ± 10	Age Model	16.9 ± 1.3	12.1 ± 2.6	49.6
3	KC10 1020-1024	T_{10} 14	50-100	7 ± 0.6	152	1.4	3.1	15 ± 1.6	180 ± 10	Age Model	16.4 ± 1.7	12.4 ± 2.9	48.4
3	KC10 1020-1024	T_{10} 14	100-250	20.1 ± 1.4	257	5	3.1	12.4 ± 0.9	180 ± 10	Age Model	13.6 ± 1	15 ± 3.2	40
8_9_10	KC10 1036-1040	T_{10} 14	50-250	51.6 ± 2.4	506	13.3	3	11.4 ± 0.5	180 ± 10	Age Model	12.5 ± 0.6	16.3 ± 3.4	36.8
8_9_10	KC11 103-110	T_{11} 1	50-250	77.7 ± 2.7	1209	16.8	3	13.5 ± 0.5	27.6 ± 0.2	TVD	13.7 ± 0.5	14.7 ± 3	40.8
8_9_10	KC11 124-130	T_{11} 2	50-250	82.1 ± 2.6	1196	18	2.9	13.2 ± 0.4	29.7 ± 0.4	TVD	13.4 ± 0.4	15.2 ± 3.1	39.5
8_9_10	KC11 140-147	T_{11} 2	50-250	92.1 ± 2.9	1203	19.8	2.9	13.6 ± 0.4	34.4 ± 0.2	TVD	13.9 ± 0.4	14.6 ± 3	41.1
8_9_10	KC11 164-172	T_{11} 3	50-250	97.1 ± 3.1	1213	19.6	2.9	14.5 ±0.5	46.9 ± 0.9	TVD	14.8 ± 0.5	13.7 ± 2.8	43.8
8_9_10	KC13 38-43	T_{13} 1	50-250	3.9 ± 0.4	107	0.8	2.9	11.7 ± 1.6	20.1 ± 0.2	TVD	11.8 ± 1.6	17.5 ± 4.3	34.3
8_9_10	KC13 142-149	T_{13} 3	50-250	73.7 ± 2.6	1131	17.6	2.9	12.2 ± 0.4	28.7 ± 1	TVD	12.4 ± 0.4	16.4 ± 3.3	36.6
3	KC13 222-228	T_{13} 5	50-100	28.7 ± 1	882	9.1	3.1	9.6 ± 0.4	23.9 ± 10	Age Model	9.7 ± 0.4	20.7 ± 4.3	29
8_9_10	KC13 278-283	T_{13} 6	50-250	43.6 ± 1.6	915	10.8	2.9	11.7 ± 0.4	20.8 ± 0.2	TVD	11.9 ± 0.4	17.1 ± 3.5	35.1
8_9_10	KC13 360-366	T_{13} 8	50-250	95.1 ± 6.5	304	19.4	2.9	13.9 ±1	19 ± 8.3	TPF	14.1 ± 1	14.5 ± 3.1	41.4
3	KC13 404-410	T_{13} 9	50-100	28.1 ± 1.2	702	6.8	3.1	12.8 ± 0.6	24.3 ± 10	Age Model	12.9 ± 0.6	15.7 ± 3.2	38.2
3	KC13 404-410	T_{13} 9	100-250	31 ± 1.2	782	7.1	3.1	13.4 ± 0.5	24.3 ± 10	Age Model	13.6 ± 0.5	15 ± 3.1	40
8_9_10	KC13 430-436	T_{13} 9	50-250	77.8 ± 2.4	1212	17.6	2.9	12.9 ± 0.4	27.4 ± 0.2	TVD	13 ± 0.4	15.5 ± 3.2	38.7
8_9_10	KC13 480-484	T_{13} 10	50-250	59.6 ± 1.9	1210	13.5	2.9	12.8 ± 0.4	19.3 ± 0.2	TVD	12.9 ± 0.4	15.6 ± 3.2	38.5
8_9_10	KC13 565-573	T_{13} 14	50-250	86.0 ± 3	1218	18.9	2.9	13.2 ± 0.5	23.9 ± 8.3	TPF	13.3 ± 0.5	15.1 ± 3.1	39.7

8_9_10	KC13 612-626	T_{13} 15	50-250	74.1 ± 2.3	1212	15.4	3	14.1 ± 0.4	25.1 ± 8.4	TPF	14.2 ± 2.9	14.2 ± 2.9	42.3
3	KC13 680-690	T_{13} 15	50-100	25.3 ± 1.9	331	6.5	3.1	12 ± 0.9	23.3 ± 10	Age Model	12.2 ± 3.6	16.8 ± 3.6	35.7
3	KC13 680-690	T_{13} 15	100-250	24 ± 1.1	588	5.5	3.1	13.5 ± 0.7	23.3 ± 10	Age Model	13.7 ± 3.1	14.8 ± 3.1	40.5
8_9_10	KC13 710-716	T_{13} 15	50-250	89.2 ± 3	1190	19.8	3.0	13.2 ± 0.4	22.6 ± 8.3	TPF	13.4 ± 3.1	15.1 ± 3.1	39.7
8_9_10	KC13 756-763	T_{13} 16	50-250	54.9 ± 1.7	1196	11.8	2.9	13.4 ± 0.4	36.5 ± 2.5	TVD	13.6 ± 3.1	14.9 ± 3.1	40.3
8_9_10	TM144		50-250	39.6 ± 1.3	1058	19.2	2.9	5.9 ± 0.2	2516.5 ± 384.5	Age Model	9.4 ± 0.5	21.6 ± 4.5	27.8
8_9_10	TM166		50-250	38.8 ± 1.3	972	18.7	2.9	5.9 ± 0.2	2901 ± 419.4	Age Model	10.1 ± 0.5	20.1 ± 4.2	29.9
8_9_10	TM190		50-250	30.2 ± 1.2	745	19.3	2.9	4.4 ± 0.2	3320.4 ± 279.6	Age Model	8.3 ± 0.5	24.3 ± 5	24.7
8_9_10	TM252		50-250	25 ± 1	661	19.3	3	3.7 ± 0.2	3697.3 ± 16.9	Age Model	8.9 ± 0.5	22.7 ± 4.7	26.4
8_9_10	TM260		50-250	23.8 ± 1	590	18.5	2.9	3.6 ± 0.2	3714.2 ± 16.9	Age Model	8.9 ± 0.5	22.6 ± 4.8	26.5
8_9_10	TM268		50-250	23.6 ± 1.1	541	17.9	2.9	3.7 ± 0.2	3731.2 ± 10.6	Age Model	9.5 ± 0.6	21.4 ± 4.6	28
8_9_10	TM295		50-250	22.1 ± 1	526	16.5	2.9	3.8 ± 0.2	3788.3 ± 48.7	Age Model	10.7 ± 0.6	19 ± 4	31.6
8_9_10	TM338		50-250	17.1 ± 0.9	427	18.1	2.9	2.6 ± 0.1	3879.2 ± 42.3	Age Model	8.7 ± 0.6	23.1 ± 4.9	26
8_9_10	TM358		50-250	17.6 ± 0.9	433	18.6	2.9	2.7 ± 0.1	3921.5 ± 16.9	Age Model	9.5 ± 0.6	21.2 ± 4.5	28.3
8_9_10	TM366		50-250	17.2 ± 0.9	417	17.3	2.9	2.8 ± 0.1	3938.5 ± 21.2	Age Model	10.2 ± 0.7	19.8 ± 4.3	30.3
8_9_10	TM376		50-250	9.7 ± 0.7	218	8.6	3	3.1 ± 0.2	3959.6 ± 19	Age Model	11.9 ± 1	17 ± 3.7	35.3
8_9_10	TM385		50-250	16.2 ± 0.8	393	12.7	3	3.6 ± 0.2	3978.7 ± 21.2	Age Model	14.4 ± 1	14.2 ± 3	42.3
3	Og Act		50-250	85.8 ± 2.9	1228	21.62	2.96 E+19	11.5 ± 0.4				17.5 ± 3.6	34.3

Table 4.2: ^{10}Be blanks

	^{10}Be/^{9}Be	^{10}Be count	^{9}Be
	10^{-16}		10^{19} at
Batch 3	22.0 ± 3.8	40	3.0
Batch 6_7	4.0 ± 1.4	8	3.0
	4.0 ± 1.4	9	3.0
	1.7 ± 1.3	2	2.9
	6.0 ± 1.8	13	3.7
Batch 8_9_10	8.9 ± 2.3	24	2.9
	4.6 ± 1.5	12	3.0
	10.1 ± 2.1	25	2.9
	7.8 ± 1.7	21	2.9

For core KC10, ^{26}Al/^{10}Be burial ages range from 0.48 ± 0.13 Ma (873-876) to 1.91 ± 0.35 Ma (941-944, 50-100 µm), and 16 ± 131 ka (873-876) to 1.47 ± 0.36 Ma (941-944, 50-100 µm) for pre-burial ratios of 6.6 and 5.3 ratios, respectively. For core KC13, the minimum and maximum ages for initial ratios of 6.6 and 5.3 are of 0.18 ± 0.19 Ma (360-366) and 0.65 ± 0.15 Ma (680-690, 100-250 µm), and -0.29 ± 0.19 Ma (360-366) and 0.20 ± 0.19 Ma (680-690, 100-250 µm), respectively. Burial ages of the TM cuttings are much older than that of the cores, ranging from 2630 ± 220 ka (166) to 4220 ± 385 ka (252) and 2170 ± 223 ka (166) to 3770 ± 390 ka (252) for initial ratios of 6.6 and 5.3, respectively.

As explained above, the chemistry protocols where different for batch 3 and batches 6_7 and 8_9_10. Although no sample was processed following both protocols for comparison, the latter batches typically yield lower burial ages. Cuttings of the TM probing were all treated using the P2 protocol.

Tests done for different granulometric fractions (50-100 µm and 100-250 µm) all yield comparable results, within uncertainties, except for sample KC10 941-944. The treatment using protocol P1, as well as the low masses of quartz analyzed (1.6 g and 2 g for the 50-100 µm and 100-250 µm fractions, respectively, Table 4.1) could be responsible for this discrepancy, although it should be noted that, considering the associated high uncertainties, these two values are statistically compatible.

Turbidites in which several layers were analyzed also yield consistent burial ages within uncertainties.

All these ages are significantly older than the age models or radiocarbon ages presented above, if we use the 6.6 initial ratio. Using the 5.3 initial ratio, however, burial ages are much closer to radiocarbon or modelled ages, for cores KC10, KC11 and KC13. The negative burial ages show that for certain samples, the 5.3 initial ratio is probably underestimated. However, it is worth noting that our ^{26}Al/^{10}Be ages are close to the detection limit of this method (ca. 500 ka), and we can thus use this statistical agreement between radiocarbon, modelled, and ^{26}Al/^{10}Be ages to confirm that the pre-deposition ratio is closer to 5.3 than 6.6.

In cuttings of the TM probe however, burial ages are much older than the modelled ages, indicating, as expected from the little constraints on the age model (see section 3.5.1), that the age model is probably underestimated.

4.2.2. Paleo-denudation rates of the Ogowé drainage

The complete ^{10}Be data is presented in Table 4.1. The ^{10}Be concentrations, corrected from radioactive decay based on the ages of turbidites determined above, range from 8.4 ± 0.6 10^4 at/g (TM 338) to 24.6 ± 1.7 10^4 at/g (KC10 941-944 50-100µm) with mean weighted value of 12.1 ± 1.7 10^4 at/g (MSWD 14; p 0, using the isoplotr online tool http://isoplotr.es.ucl.ac.uk (Vermeesch, 2018); values of MSWD >> 1 and of p << 0.05 are considered over-dispersed with respect to the uncertainties). All standards measured are within expected results within uncertainty (Corbett et al., 2019; Jull et al., 2015, Table 4.5). In terms of calculated denudation rates, our results range from 8.3 ± 1.8 mm/ka (KC10 941-944 50-100µm) to 24.2 ± 5 mm/ka (TM 338) with a weighted mean of 15.9 ± 1.1 mm/ka (MSWD 0.7; p 0.92). Denudation rates calculated from the turbidites of core KC10 range from 8.3 ± 1.8 mm/ka (941-944 50-100µm) to 18.5 ± 5 mm/ka (788-791 50-100µm) with a weighted mean of 12.6 ± 1.8 mm/ka (MSWD 1.4; p 0.2). For core KC11, the range is of 13.7 ± 2.8 mm/ka (164-172) to 15.2 ± 3.1 mm/ka (124-130) with a weighted mean of 14.5 ± 2.9mm/ka (MSWD 0.05; p 0.99), and for core KC13, from 14.2 ± 2.9 mm/ka (612-626) to 20.7 ± 4.3 mm/ka (222-228) with a weighted mean of 15.6 ± 1.7 mm/ka (MSWD 0.18; p 1). For cutting samples of the TM probe, the range is from 15 ± 3.2 mm/ka (TM385) to 24.2 ± 5 mm/ka (TM338), with a weighted mean 20.1 ± 2.5 mm/ka (MSWD 0.44; p 0.94). These ages are consistent with the modern denudation rate of the Ogowé drainage of 17.5 ± 3.6 mm/ka (Regard et al., 2025).

Samples measured for different granulometries (50-100 µm and 100-250 µm) all yield consistent results within error bars, except for KC10 788-791, for which denudation of the 50-100 µm fraction is higher. These denudation rates are however within the same order of magnitude (18.5 ± 5 mm/ka and 11.3 ± 2.6 mm/ka for the 50-100 µm and 100-250 µm, respectively), and the small inconsistency could be related to the very small masses of quartz analyzed (~1g), leading to low levels of ^{10}Be counts on the AMS (79 and 120 for 50-100 µm and 100-250 µm, respectively) or possibly the sampling of a heterogeneous signal. Different layers of single turbidites are also consistent with one another. Turbidite $T_{10}11$ yields denudation rates of 15.4 ± 3.2 mm/ka (858-860 cm) and 14.4 ± 2.9 mm/ka (873-876 cm). The same is true for turbidites $T_{10}14$ (15.5 ± 3.2 mm/ka at 1020-1024 cm and 16.3 ± 3.4 mm/ka at 1036-1040 cm) $T_{11}2$ (15.2 ± 3.1 mm/ka and 14.6 ± 3 mm/ka at 124-130 cm and 140-147 cm, respectively) $T_{13}9$ (15 ± 3.1 mm/ka and 15.5 ± 3.2 mm/ka at 404-410 cm and 430-436 cm, respectively) and $T_{13}15$

Table 4.3: (Next page) ^{26}Al results and burial ages. All uncertainties are 1 sigma.

Batch	Sample	Turbidite	Granulo. range µm	$^{26}Al/^{27}Al$ 10^{-14}	Total counts ^{26}Al	Mass Quartz g	^{27}Al 10^{19} at	^{26}Al 10^{4}at/g	$^{26}Al/^{10}Be$	Burial (Ri = 6.6) ka	Burial (Ri = 5.3)
6_7	KC10 40-43	T_{10} 1	50-250	10.7 ± 1.1	92	10.7	3.3	36.7 ± 3.4	3.2 ± 0.3	1510 ± 208	1060 ± 211
3	KC10 788-791	T_{10} 10	50-100	2.4 ± 0.3	54	1.5	3.9	59.5 ± 8.4	5.7 ± 1.3	996 ± 367	539 ± 373
3	KC10 788-791	T_{10} 10	100-250	2.2 ± 0.5	18	1.1	3.6	70.9 ± 17.3	4.2 ± 1.1	927 ± 551	481 ± 549
8_9_10	KC10 858-860	T_{10} 11	50-250	12.4 ± 1.1	197	13.5	6.5	59 ± 5.0	4.9 ± 0.4	598 ±189	136 ± 193
8_9_10	KC10 873-876	T_{10} 11	50-250	17.1 ± 0.9	406	16.5	6.5	67.1 ± 3.6	5.2 ± 0.3	476 ±127	16 ± 131
3	KC10 941-944	T_{10} 12	50-100	2.2 ± 0.3	39	1.6	4.3	57.6 ± 9.6	2.5 ± 0.5	1910 352	1470 ± 357
3	KC10 941-944	T_{10} 12	100-250	3.2 ± 0.4	62	2	4.1	66.6 ± 8.7	4.3 ± 0.6	860 ± 300	403 ± 304
3	KC10 1020-1024	T_{10} 14	50-100	2.2 ± 0.3	47	1.4	3.7	54.4 ± 8.3	3.6 ± 0.7	1230 ± 366	770 ± 367
3	KC10 1020-1024	T_{10} 14	100-250	5.9 ± 0.6	109	5	4.3	50.7 ± 5.6	4.1 ± 0.5	971 ± 270	517 ± 271
8_9_10	KC10 1036-1040	T_{10} 14	50-250	13.4 ± 0.9	251	13.3	5.4	54 ± 3.6	4.7 ± 0.4	668 ± 168	206 ± 170
8_9_10	KC13 278-283	T_{13} 6	50-250	8.0 ± 0.6	177	10.8	8.2	60.6 ± 4.6	5.2 ± 0.4	487 ± 176	25 ± 179
8_9_10	KC13 360-366	T_{13} 8	50-250	16.9 ± 1.0	322	19.4	9.5	82.9 ± 4.7	6 ± 0.5	179 ± 185	-286 ± 186
3	KC13 404-410	T_{13} 9	50-100	9.4 ± 0.8	146	6.8	5.1	70.4 ± 5.9	5.5 ± 0.5	345 ± 195	-113 ± 199
3	KC13 404-410	T_{13} 9	100-250	11.2 ± 0.8	218	7.1	4.7	75.1 ± 5.2	5.6 ± 0.4	311 ± 163	-151 ± 165
8_9_10	KC13 565-573	T_{13} 14	50-250	18.5 ± 1.0	380	18.9	7.5	73.6 ± 3.9	5.6 ± 0.4	310 ± 130	-149 ± 132
8_9_10	KC13 612-626	T_{13} 15	50-250	17.8 ± 0.9	414	15.4	7	80.1 ± 4.0	5.7 ± 0.3	272 ± 123	-190 ± 124
3	KC13 680-690	T_{13} 15	50-100	8.1 ± 0.8	112	6.5	4.8	60.4 ± 6.3	5 ± 0.7	536 ± 269	83 ± 273
3	KC13 680-690	T_{13} 15	100-250	7.6 ± 0.6	178	5.5	4.6	64.1 ± 4.9	4.8 ± 0.4	649 ± 185	195 ± 189
8_9_10	KC13 710-716	T_{13} 15	50-250	18.8 ± 0.9	445	19.8	8.1	77.1 ± 3.8	5.8 ± 0.3	228 ± 123	-238 ± 127
8_9_10	TM 144		50-250	4.5 ± 0.6	81	19.2	4.2	9.9 ± 1.3	1.7 ± 0.2	2900 ± 284	2450 ± 294
8_9_10	TM 166		50-250	4.9 ± 0.5	113	18.7	4.3	11.1 ± 1.1	1.9 ± 0.2	2630 ± 220	2170 ± 223
8_9_10	TM 190		50-250	2.2 ± 0.3	50	19.3	4.3	4.8 ± 0.7	1.1 ± 0.2	3800 ± 322	3340 ± 323
8_9_10	TM 252		50-250	1.6 ± 0.3	37	19.3	4.2	3.3 ± 0.6	0.9 ± 0.2	4220 ± 385	3770 ± 390
8_9_10	TM 260		50-250	1.5 ± 0.3	35	18.5	4.2	3.4 ± 0.6	0.9 ± 0.2	4130 ± 401	3660 ± 389
8_9_10	TM 268		50-250	1.5 ± 0.3	37	17.9	4.1	3.4 ± 0.6	0.9 ± 0.2	4220 ± 390	3770 ± 394
8_9_10	TM 295		50-250	1.6 ± 0.3	34	16.5	4.2	3.8 ± 0.8	1 ± 0.2	3990 ± 436	3540 ± 431
8_9_10	TM 338		50-250	1.1 ± 0.2	26	18.1	4.4	2.7 ± 0.6	1 ± 0.2	4000 ± 444	3530 ± 448
8_9_10	TM 358		50-250	1.2 ± 0.2	27	18.6	4.7	2.9 ± 0.6	1.1 ± 0.2	3840 ± 431	3380 ± 442
8_9_10	TM 366		50-250	1.1 ± 0.3	21	17.3	4.5	2.8 ± 0.7	1 ± 0.2	4000 ± 511	3530 ± 512
8_9_10	TM 376		50-250	1.2 ± 0.2	26	8.6	4.5	6.0 ± 1.3	1.9 ± 0.4	2650 ± 497	2200 ± 496
8_9_10	TM 385		50-250	1.5 ± 0.3	29	12.7	4.8	5.3 ± 1.2	1.5 ± 0.3	3210 ± 467	2760 ± 473
3	Og Act		50-250	18.1 ± 1.1	342	21,62	7.3	61.3 ± 3.7	5.3 ± 0.4	429 ± 144	-37 ± 144

	$^{26}Al/^{27}Al$ 10^{-16}	^{26}Al counts	^{27}Al 10^{19} at
Batch 3	5.4 ± 5.4	1	4
Batch 6_7	0	0	3.9
	0	0	3.9
	Invalid	0	4.1
	0	0	4.1
Batch 8_9	3.9 ± 3.9	1	4.3
	0	0	4

Table 4.4: Aluminum blanks obtained for different batches

Batch	Standard	$^{26}Al/^{27}Al$ 10^{-13}	^{26}Al counts	Mass Quartz	^{27}Al 10^{19} at	^{26}Al 10^{7} at/g
3	Cronus A	38.2 ± 1.4	1256	1.0	3.6	14.1 ± 0.5
8_9	UVM-A	4.3 ± 0.2	732			
	UVM-A	4.3 ± 0.2	569			

Table 4.5: Results for Al standards.

Table 4.6: ^{10}Be standards for each batch

Batch	Standard	$^{10}Be/^{9}Be$ 10^{-14}	^{10}Be count	Mass of Quartz g	^{9}Be 10^{19} at	10Be 10^{6} at/g
3	Cronus A	106.6 ± 2.1	8225	1.0	3.1	33.4 ± 0.7
6_7	Cronus A	138.1 ± 2.3	9688	1.2	3.0	33.7 ± 0.6
8_9_10	UVM-A	14.5 ± 0.6	934			
	UVM-A	14.9 ± 0.5	1262			

(14.2 ± 2.9 mm/ka, 14.8 ± 3.1 mm/ka and 15.1 ± 3.1 mm/ka at 612-626 cm, 680-690 cm and 710-716 cm, respectively).

4.3. Discussion

4.3.1. Implications of $^{26}Al/^{10}Be$ ages

Figure 4.4 compiles the results of $^{26}Al/^{10}Be$ burial ratios and compares them to the age models (TM and KC10) or the ^{14}C ages (KC13). In the lower part of the figure are presented the residues of each age, showing the subtraction of the calculated burial age and the age model (or ^{14}C) at the same depth.

In cores KC10 and KC13, burial ages are consistent with the modelled or radiocarbon ages, within uncertainties, this consistency being better considering an initial ratio of 5.3 (rather than 6.6). This indicates that no significant (i.e., >100 ka) storage occurred within the basin in the past 200 ka. Uncertainties on the $^{26}Al/^{10}Be$ ratios are often higher than the burial ages themselves, but this was expected considering the ages of the sediments are below the resolution of this method (< 500 ka). This means that if there had been a significant storage over a duration longer than 500 ka, the $^{26}Al/^{10}Be$ ratio should have detected it.

The results for the TM cuttings in the other hand, fall beyond the detection limit of the method. Our $^{26}Al/^{10}Be$ results are relatively consistent with the age model for the TM cuttings. We acknowledge that the age model could be challenged as we have no way of verifying that sedimentation rates of the Upper Pleistocene to Holocene were constant throughout the Plio-Pleistocene and the micro-paleontological study done by Total in 1968 is not well constrained. Furthermore, because these samples are well cuttings, there are poor constraints on their real depth within the sediment pile. It is thus necessary to reconsider the age model proposed in section 4.4.1. We consider the possibility that all samples above 206m depth could have any age between 0 and 3.6 ± 0.4 Ma (burial age of TM 252, Table 4.3), and all samples from 206 m to 385 m depths could have any age between 3.6 and 4.37 ± 0.4 Ma (burial age of TM 268, Table 4.3), as shown by the two red boxes in Figure 4.4A. Despite large uncertainties, this data

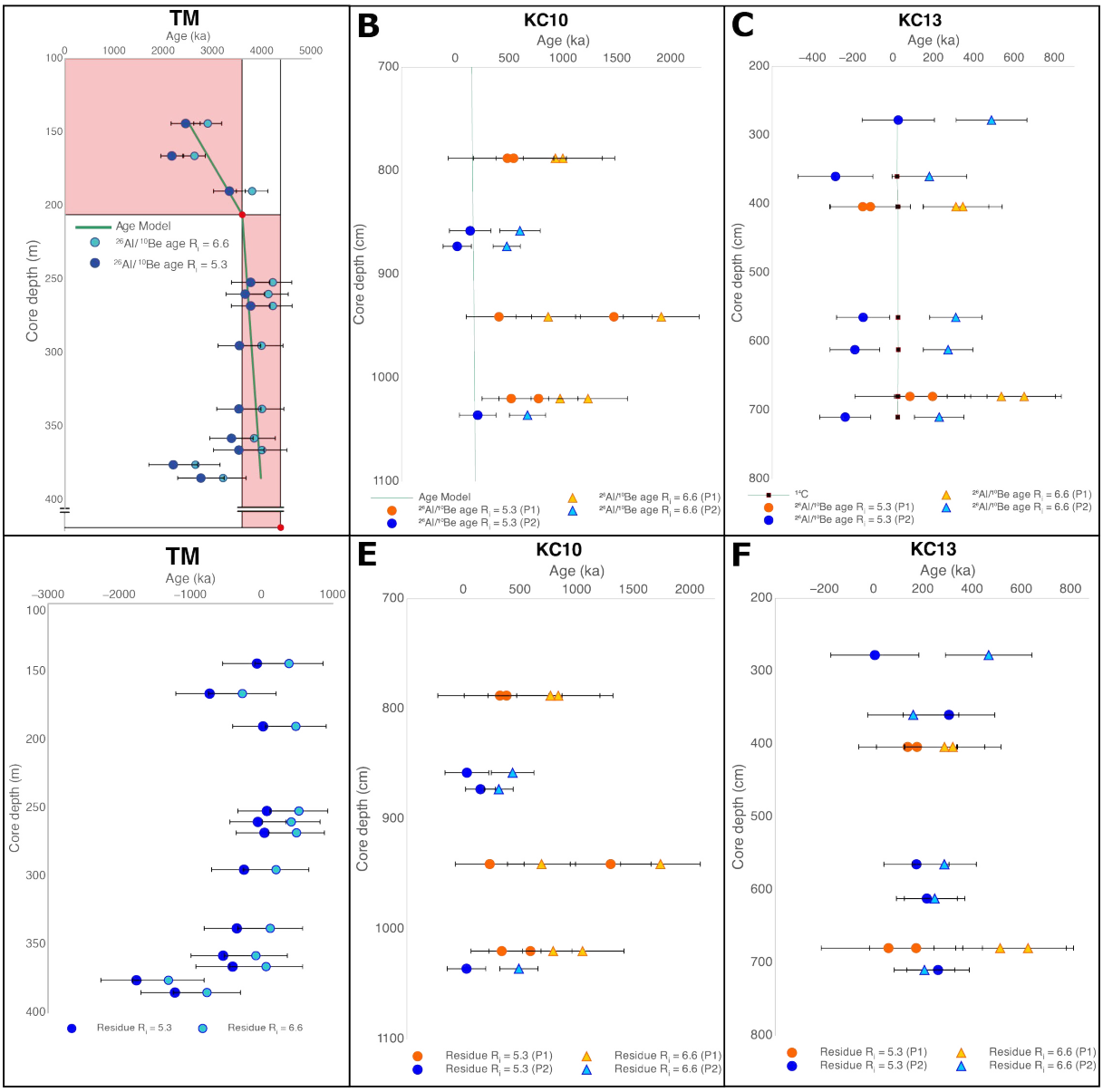

Figure 4.4: Comparison of age models and $^{26}Al/^{10}Be$ ages (A-C) and residues with depth of said comparison (D-F). Triangles represent calculations done with initial ratio of 6.6, circles with initial ratio of 5.3. Blue shows results from the new protocol, orange from the old protocol. In A, the red shaded area represents the age possibilities from the constrains existing on the age model. Notice that core depth is given in m in A and D and in cm in all the other insets.

places strong control on the age at the bottom of the studied samples. Furthermore, as will be described in part 4.5.2 of this manuscript, precise absolute ages are not compulsory for our study at this Ma time scale.

Another important uncertainty on the burial ages is the initial ratio. As presented in Figure 4.4, a change of initial ratio (R_i) from 6.6 to 5.3, changes the burial ages substantially (by about 500 ka), and the 5.3 ratio yields ages that are more consistent with independent age constrains. Unfortunately, we have little control on this initial ratio, and in the present work, we can barely do better than using the ratio of 5.3 ± 0.4 (Table 4.3) measured in the modern Ogowé sediments.

From our results, two interpretations are possible. The first is to consider that the age model is consistent, and that the $^{26}Al/^{10}Be$ ages reveal burial within the continental catchment or the marine turbiditic system of several Ma. As exposed above, it is difficult to trust the age model from only one dated depth, poorly constrained in 1968. Furthermore, as tackled in Chapter 3 of this manuscript, both continental transport durations and marine storage are not larger than a few 10 ka, in the Ogowé sedimentary system. This is true for the Holocene, and there is no reason why continental transport durations should decrease by 2 orders of magnitude over the Pliocene. These observations hence tend to indicate that the depleted initial ratio of 5.3 is not due to storage during transport of Quaternary sediments, but more probably to the incorporation of sedimentary Cenozoic rocks that have already experienced burial cycles (Francevilian basins + Bateke plateaus).

Our $^{26}Al/^{10}Be$ data from the TM cuttings also suggest a very high sedimentation rates from 350 m to 200 m depth. These high sedimentation rates are not completely unrealistic, especially if we consider that during that time, continental storage may have also slightly increased, leading to this increasing upward age trend. As said above, variations in the initial ratio may also have varied with time, which would also affect our burial ages.

Finally, only the two lowermost samples (TM276 and TM385) yield $^{26}Al/^{10}Be$ ages younger than the age model and than all ages above them. We consider the possibility that these samples were re-exposed after burial and hence treat them as outliers.

Overall, even though $^{26}Al/^{10}Be$ are often difficult to interpret, and even though some uncertainties remain on the efficiency of the chemistry protocol for ^{26}Al extraction, our results bring constraints on the ages of the TM cuttings, or at least show us that a linear age model is incorrect. In the context of this PhD, these difficult results have also led to significant efforts, mainly undertaken by Marie Protin, to understand when, how and why we could lose Al during the chemical extraction protocol, efforts that have led to the development of a new protocol and to significant improvements in our understanding of the ^{26}Al behavior. These developments have been presented in chapter 2 of this manuscript.

4.3.2. Late Cenozoic evolution of denudation

Denudation rates of MIS 2 and MIS4 are relatively constant (Figure 4.5) and consistent with values of modern denudation rates of the Ogowé drainage (Regard et al., 2025). This consistency of long term glacial with modern interglacial denudation rates indicates very little control of climate over denudation, although given the integration durations, modern denudation rates cannot be strictly ascribed to interglacial periods. This is well represented by the results of the KC10 core (Figure 4.5), which record denudation rates between 150 and 200 ka, integrating over a maximum duration of ca. 70 ka (941-944 cm, Table 4.1). These results record denudation rates over both interglacial and glacial periods but are consistent with denudation rates of the KC11 and KC13 cores, integrating only over a glacial period. Moreover, the good agreement between the KC cores and the TM cuttings indicates a long term Plio-Pleistocene stability of denudation of the Ogowé drainage (Figure 4.6), although the MPT seems to have had an effect on the Ogowé paleo-denudation rates.

Strong uncertainties on the ages of the TM cuttings leads to different possible values of denudation, as the ages of the sample will influence the radioactive decay calculations, and thus calculated denudation rates. Figure 4.6 shows denudation rates of the KC cores, and of the TM cuttings, calculated with ages

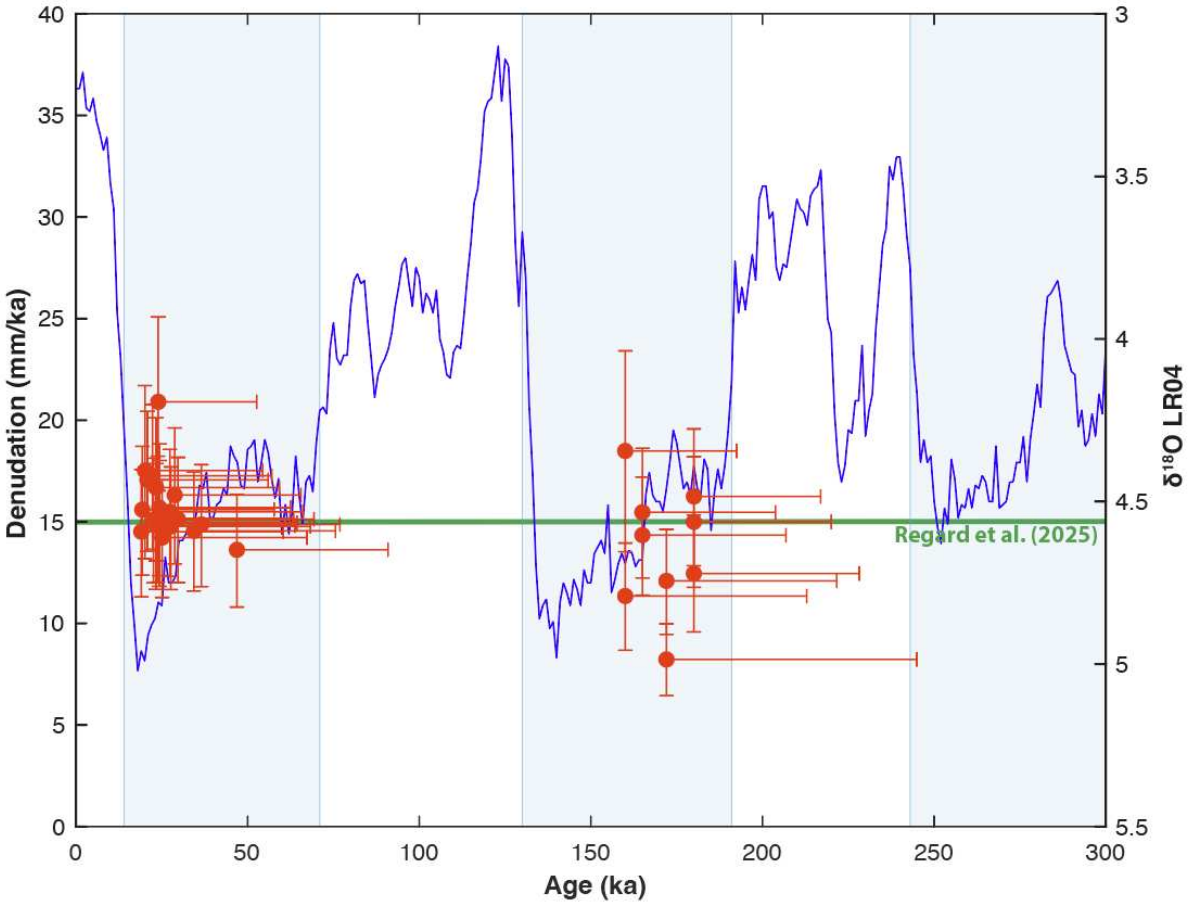

Figure 4.5: ^{10}Be paleo-denudation rates of the Ogowé catchment from cores KC10, KC11 and KC13. Blue line is the LR04 $\delta^{18}O$ curve (Lisiecki and Raymo, 2004). Red points show denudation values. Uncertainties on denudation rates are 1 sigma. The negative age uncertainties are integration times (Table 4.1, see Chp. 2 for explanation). Green line show the mean modern denudation rates of the Ogowé catchment from Regard et al., (2025).

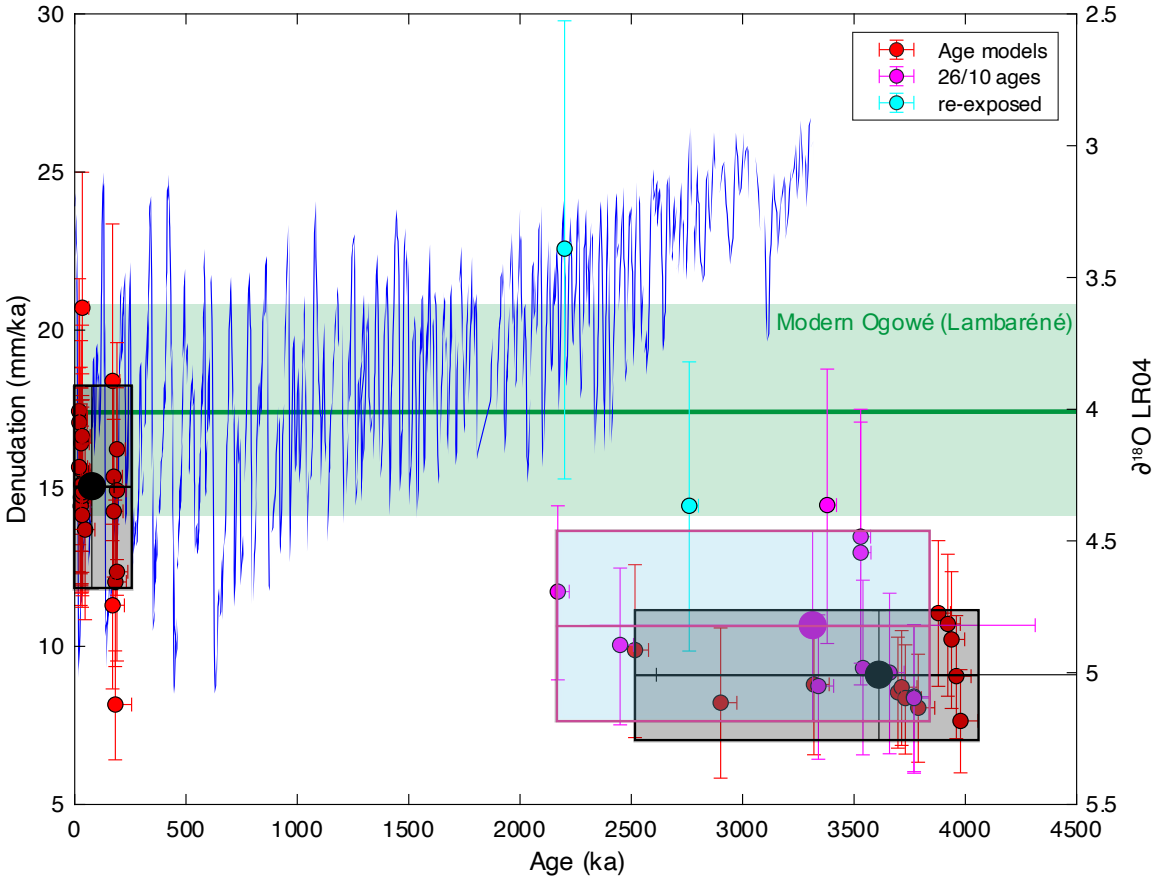

Figure 4.6: ^{10}Be denudation rates for cores KC10, KC11, KC13, and for the cuttings of the TM probing. Blue curve is the LR04 $\delta^{18}O$ compilation (Lisiecki et Raymo, 2004). Positive age uncertainties are the integration rates associated to each denudation rate. Black rectangles indicate mean denudation rates. Red points are denudation rates calculated with the ages from the age models. Magenta points are the denudation rates calculated with the ^{26}Al/^{10}Be ages.

of the age model (in red) and ages of the ^{26}Al/^{10}Be data (in magenta). Mean values of paleo-denudation rates calculated using the age model and the ^{26}Al/^{10}Be ages remain within uncertainty of one another.

We test all the values of denudation rates we can obtain with the different possible ages for the TM cuttings (Sup. Info. 4.3). The variation in calculated denudation rates, due to the variations in radioactive corrections remain limited, with maximum variations by a factor of 2.7 (TM 252, comparison of modelled age of 1.75 ± 0.12 Ma with ^{26}Al/^{10}Be age of 3.77 ± 0.39 Ma, initial ratio of 5.3). A threefold increase in calculated denudation is not negligeable and could affect our interpretation. We however consider it to be reasonable, as the maximum ages (3.7 Ma) are extremes and are most certainly far from reality. Overall, Sup. Info. 4.3 shows that the uncertainty on the TM cutting ages should not significantly impact our denudation rates results and associated interpretations.

Because of the strong uncertainty on ages of the TM cuttings and of the long integration times (Figure 4.6), it is difficult to associate any denudation value to specific climatic period (e.g., glacial/interglacial periods). Although we do not have the resolution to resolve the effect of single climatic cycles before ~1 Ma, our results tend to show that the initiation of the northern Hemisphere glaciations and the Mid Pleistocene Transition may have had an effect on denudation rates of Gabon. Other controls such as

tectonics (Regard et al., 2025) or migrations of the ITCZ leading to rapid short-lived climate fluctuations associated to monsoons could control denudation of these regions but high-resolution long-term paleoclimatic data lacks to resolve this hypothesis.
Our results imply that the hypothesis of Peter Molnar (2004), which states that the constantly oscillating Quaternary climate may have led to increased denudation is not verified in this tropical setting.

4.4. Conclusions

This work has successfully shown that denudation rates of the Ogowé region have remained steady, at least since the Pliocene, with only a possible effect of the MPT. Our results indicate that Quaternary climatic cycles do not control denudation of this Tropical region. This leads to 2 possible interpretations. Either the Quaternary climatic cycles had no effect on the climate evolution of the Ogowé catchment, or there were changes in the climatic signal of this region, but they had no impact on the denudation rates. Unfortunately, the absence of paleoclimatic reconstruction in this region makes it impossible to validate or discard one or the other interpretation.

Supplementary Information

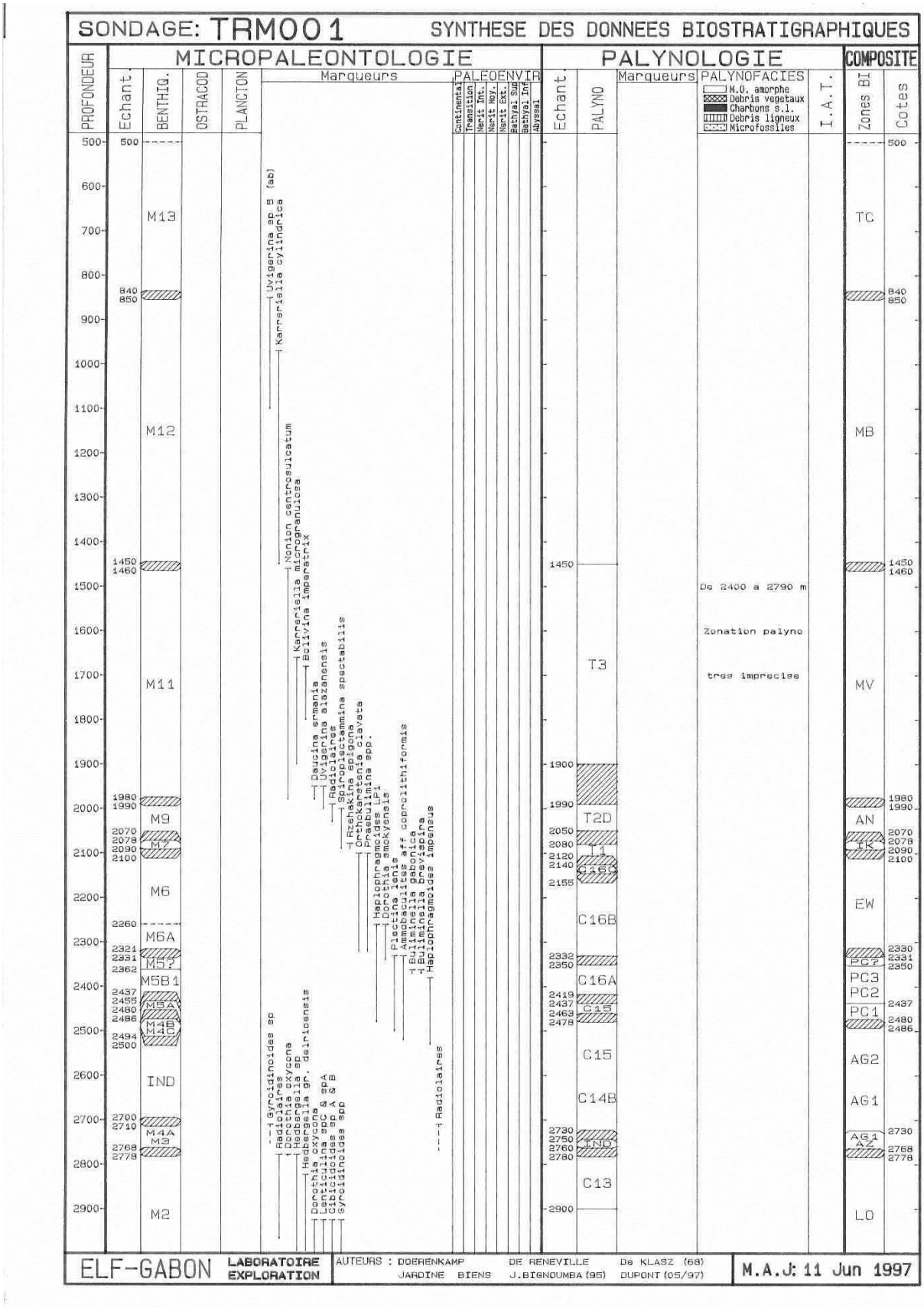

Sup. Info. 4.1: Updated version of the micropalentological analysis of the TM probing (1997). Authors are given at the bottom. Rapport interne Totalenergies.

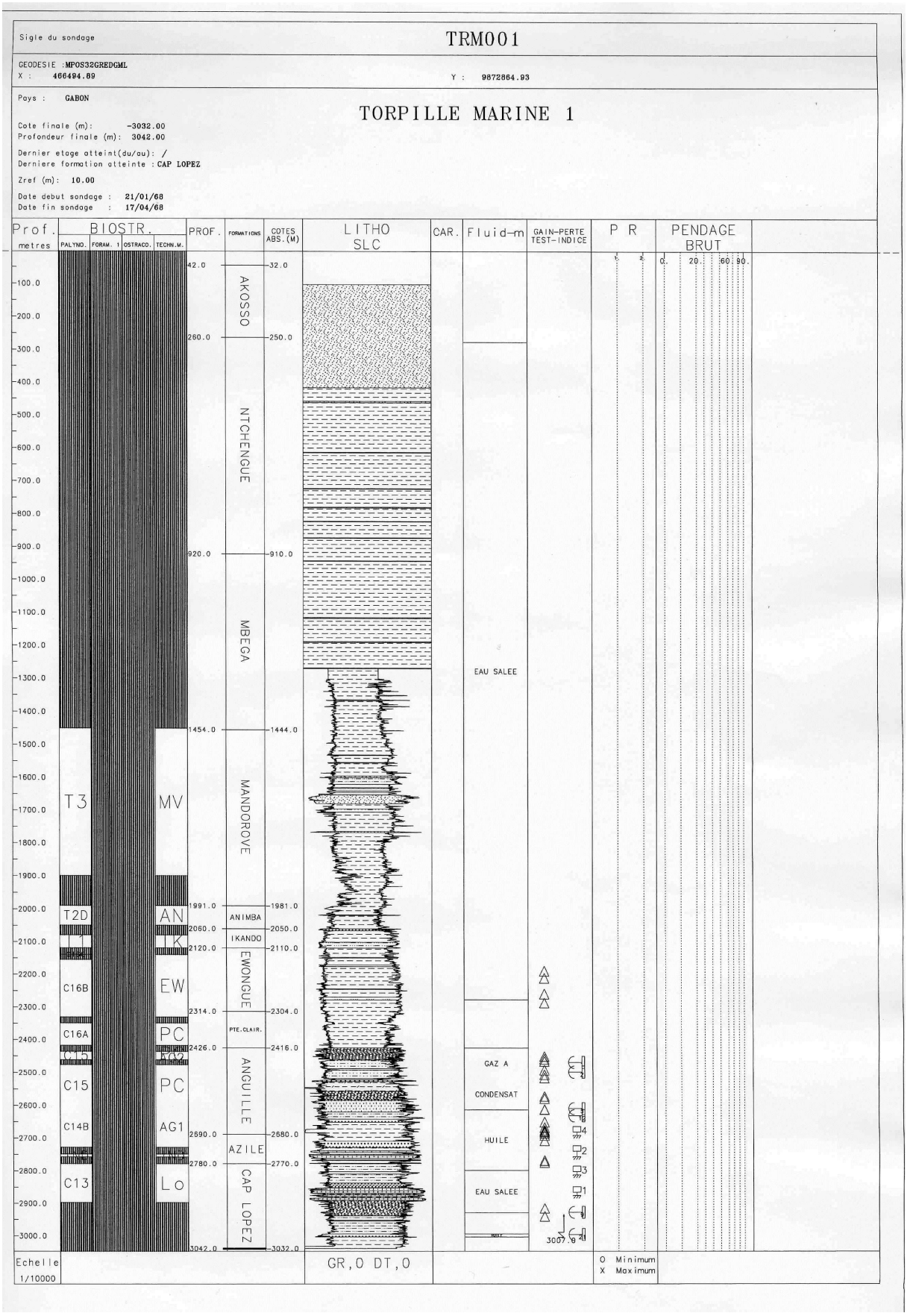

Sup. Info. 4.2: Original log description of the Torpille Marine Probing. 1968, Rapport interne Totalenergies.

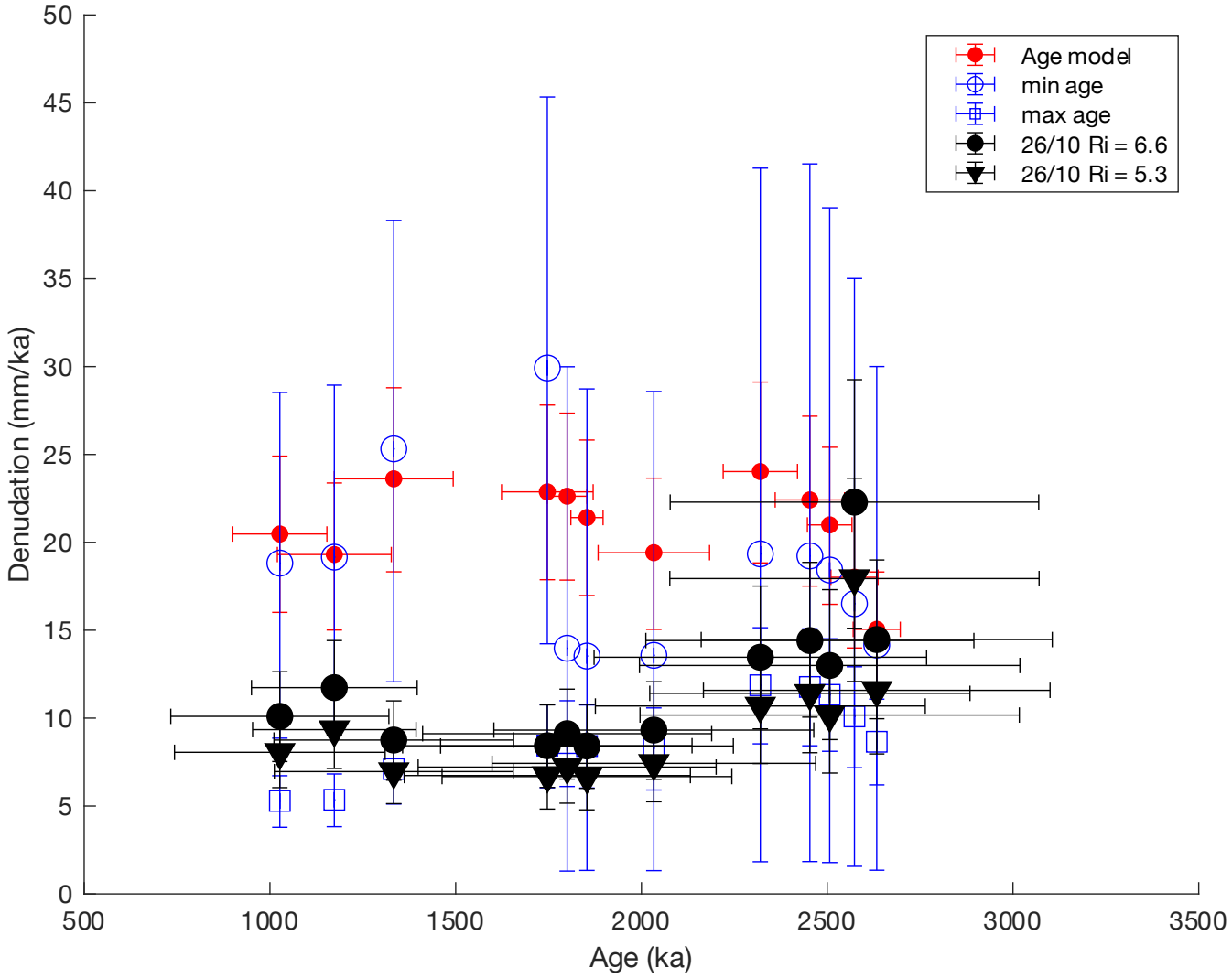

Sup. Info. 4.3: Tests of the effect of different ages of the TM cuttings on calculated denudation rates. All values are plotted for ages of the age model, but the denudation rates associated were calculated using different ages for radioactive decay calculation. Min age is 0 and 1.8 Ma (minimum age possible of the age model). Max age is 3.8 ± 0.4 Ma (maximum age of the $^{26}Al/^{10}Be$ ratio). Black circles and triangles correspond to the ages of the $^{26}Al/^{10}Be$ ratios for initial ratios of 6.6 and 5.3, respectively.

Chapter 5. Near steady denudation rates during the late Pleistocene in the tropics

This chapter is published in the Journal of Geophysical Research, Earth Science (https://doi.org/10.1029/ 2024JF008147)

Authors

Etienne Large[1], Julien Charreau[1], Pierre-Henri Blard[1], Germain Bayon[2], Eduardo Garzanti[3], Bernard Dennielou[2], Gwenaël Jouet[2], Alfred Andriamamonjy[4], Amos Fety Michel Rakotondrazafy[4], Aimeryc Shcumacher[1], Laurie Reisberg[1], Natalia Vazquez Riveiros[2], Jacques Giraudeau[5]

[1]CNRS/Université de Lorraine, UMR 7358 CRPG, 54500 Vandoeuvre-lès-Nancy, France

[2]CNRS/Université de Bretagne Occidentale/Ifremer, UMR 6538 Géo-Océan, 29280 Plouzané, France

[3]Università degli Studi di Milano-Bicocca/DISAT, 20126 Milano, Italy

[4]Université d'Antananarivo/Département des Sciences de La Terre, 101 Antananarivo, Madagascar

[5]CNRS/Université de Bordeaux, UMR 5805 EPOC, 33615 Pessac, France

Key points

- Paleo-denudation rates of SW Madagascar have remained within the range of modern values (i.e., 20 mm/ka), throughout the past 900 ka.
- Denudation is unaffected by Quaternary climatic cyclicity in Madagascar. Monsoon-type climatic variations could control tropical denudation.
- Turbidites are extremely promising tools for future paleo-denudation rate reconstructions but need to be better studied and constrained.

Abstract

Denudation is a key parameter controlling the evolution of the Earth's surface, the production of soils, the stability of relief or the long-term evolution of climate. Climate fluctuations conversely have a strong impact on denudation, but these complex feedback mechanisms are still under-constrained. To better predict future changes that will affect our habitat, and understand links between climate and denudation, precise quantification of paleo-denudation rates is required. In this work, we measure cosmogenic radionuclides (^{10}Be) in turbidites of a well-dated marine sedimentary core recovered in the Mozambique Channel to provide a 900 ka long near-continuous record of paleo-denudation rates over the 100 ka

climatic cycles. Neodymium isotopes and heavy mineral analysis were used to provide constraints on the provenance of terrigenous sediments exported from Madagascar to the studied site and show that temporal variations in sediment provenance are limited and decoupled from climatic cyclicity. Our ^{10}Be-based paleo-denudation rates are in the same order as modern rates, ranging from 17.4 ± 5.8 mm/ka to 73.9 ± 29.4 mm/ka (1 standard deviation), and do not show major variations through the Middle and Late Pleistocene. Importantly, we did not identify a systematic significant impact of glacial/interglacial cyclicity on denudation rates. Denudation of this subtropical island may instead have been controlled by variability of monsoon intensity associated with shifts in the Inter Tropical Convergence Zone, but this interpretation remains speculative at this stage as it cannot be recorded within the resolution of cosmogenic-derived denudation rates.

Plain Language Summary

Denudation, the collective action of physical erosion and chemical weathering, is a key parameter controlling the Earth's surface evolution. It is linked to climate by several complex feedback processes. Understanding if, how, and to what extent one controls the other is an active 35 year-long debate in the Earth Science community. In the actual context, understanding how our habitat will react to climate change becomes crucial and precise quantification of past denudation rates is necessary. We reconstruct denudation rates from sediments produced in south-western Madagascar and stored in the Mozambique Channel. Our record spans the last 900 ka, documenting several glacial/interglacial cycles. We also use two proxies to document the evolution of continental sediment sources to the Mozambique Channel. Our results show limited variations of sediment provenance, not following climatic cyclicity over the time considered. Most importantly, we show that the denudation of Madagascar remains constant, within the range of modern values, and completely uncorrelated to any climatic variability over the past 900 ka. We propose that denudation of this tropical island may be controlled by variations of the intensity of monsoons, but this remains a hypothesis as our method does not have the resolution to record such short variations.

Key words

Geomorphology; Paleo-denudation; Tropics; Turbidite; ^{10}Be; Sediment provenance

5.1. Introduction

Denudation, the combined effect of chemical weathering and physical erosion, is a key parameter controlling the evolution of the Earth's surface (Portenga and Bierman, 2011). It is controlled by climate through precipitation (e.g., Fuller et al., 2009; Moon et al., 2011), temperature and vegetation cover

(e.g., Acosta et al., 2015; Olen et al., 2016). Denudation, in turn, influences climate by controlling atmospheric CO_2 concentrations on geological timescales through silicate weathering (Berner et al., 1983) and burial of organic carbon (Galy et al., 2007). The relationship between weathering and atmospheric CO_2 has been extensively discussed in the literature as it is not straightforward and highly dependent on lithology (Hilton and West, 2020). Alternatively, land surface reactivity (i.e., exposure of fresh minerals to the surface by erosion) rather than weathering has been proposed to control long term (i.e., 10^0 Ma) climate (Caves Rugenstein et al., 2019). Tectonic uplift may also be a driver of denudation (e.g., Godard et al., 2014).

It has often been argued that denudation is a driver, if not a limiting factor, of climatic variations (e.g., West, 2012). Earth underwent a first-order global climate cooling over the Cenozoic (Zachos et al., 2001), culminating with the onset of the Quaternary glaciations *ca.* 2.56 Ma (Maslin et al., 1996). Understanding and quantifying the feedback processes that exist between climate and denudation, and the extent to which one drives the other has been a key objective, actively debated by Earth scientists over the past 35 years (Hay et al., 1988; Molnar and England, 1990; Zhang et al., 2001). This debate opposed arguments for an increase in erosion rates due to climate variability (Herman and Champagnac, 2016) to arguments for a steadiness of Quaternary erosion (Willenbring and Jerolmack, 2016). In the current context of global climate change, it is vital to predict how denudation may respond to rapid, high-amplitude climate changes. It is therefore essential to understand and quantify how continents erode, both today and under different past climatic conditions.

To resolve this debate, Late Cenozoic denudation rates have been estimated using various methods (e.g., sediment volumes, thermochronology, geochemical proxies) focusing mainly on orogenic settings. A twofold increase in sedimentation rates since 5 Ma has been suggested for both global marine (Hay et al., 1988) and continental alpine (Kuhlemann et al., 2002) basins. However, sediment budget reconstructions can be biased by the so-called Sadler effect (Sadler, 1981), lateral shifts of depocenter or stratal discontinuities (Métivier, 2002; Willenbring and Von Blanckenburg, 2010). Detailed sediment volume reconstructions in marine basins based on seismic profiles have yielded conflicting results (Clift, 2006), and the signal observed around the Alps could be influenced by the Messinian salinity crisis in the Mediterranean Sea. Geochemical proxies such as $^{10}Be/^{9}Be$ ratios (Willenbring and von Blanckenburg, 2010) showed constant weathering rates since the Late Miocene, although these results do not account for physical erosion and their integration time has been debated (von Blanckenburg and Bouchez, 2014). Reconstructions of glacial erosion (e.g., Hallet, 1996) suggested a greater effectiveness of glacial over fluvial erosion, implying an increase in erosion rates during glacial periods. However, subglacial storage of sediments and their release during deglaciation could delay the measured rates and lead to artificially higher apparent sediment fluxes in Holocene basins (Koppes and Hallet, 2006). Inversion of global thermochronological data showed an up to 4-fold increase in exhumation rates during the 0-2 Ma period when compared to the 4-6 Ma period (Herman et al., 2013), although it was suggested

that the spatial gradient in results was associated to the local geology of the sampled areas leading to a biased interpretation (Schildgen et al., 2018).

The methodological limitations mentioned above make it difficult to investigate the relationship between climate and denudation. Quantifying denudation rates without these biases is therefore key and the use of cosmogenic nuclides may prove crucial to better address the debate. Cosmogenic nuclides and in particular *in-situ* ^{10}Be measured in river sediments are powerful tools for reconstructing basin-averaged denudation rates (Brown et al., 1995; Malusà et al., 2024) with the advantages of being widely used and known (e.g., Granger et al., 1996; Portenga and Bierman, 2011), and unaffected by changes in depocenter or incomplete sediment preservation. *In-situ* cosmogenic nuclides in sedimentary records allow determination of paleo-denudation rates (e.g., Marshall et al., 2017; Puchol et al., 2017), an approach applied to a number of different archives such as cave sediments (e.g., Haeuselmann et al., 2007), lake deposits (e.g., Garcin et al., 2017), foreland fluvial deposits (Charreau et al., 2011) or turbidite records in marine sediment cores (e.g., Mariotti et al., 2021).

Many of these studies have focused on tectonically active (e.g., Gonzalez et al., 2016) or previously glaciated regions (e.g., Grischott et al., 2017; Madella et al., 2018, Mariotti et al., 2021). Over long time scales up to 10 Ma, paleo-denudation rates may have been influenced by geodynamic forcing (e.g., Lenard et al., 2020; Puchol et al., 2017). Over shorter Quaternary time scales, paleo-denudation rates were reconstructed in various geological settings (Bekaddour et al., 2014; Fisher et al., 2023; Fuller et al., 2009; Grischott et al., 2017; Hidy et al., 2014; Mariotti et al., 2021; Marshall et al., 2017; Schaller et al., 2002) but few records display sufficient continuity and resolution to reveal the impact of climate oscillations (Fisher et al., 2023; Mariotti et al., 2021; Marshall et al., 2017).

In the southern Central Andes, Fisher et al. (2023) showed synchrony between variations in denudation rates and Milankovitch-driven, 400-ka eccentricity cycles. In Oregon, Marshall et al. (2017) also proposed that climate modulates erosion rates over a glacial-interglacial cycle. Both studies were conducted in regions affected by glacial or periglacial processes. Conversely, the analysis of ^{10}Be in turbidites deposited in the Var submarine sedimentary system (France, Southern Alps) allowed Mariotti et al. (2021) to reconstruct a 75 ka record of paleo-denudation rates non-linearly responding to climatic forcings with rates estimated to be 2-7 times higher during the Last Glacial Maximum (LGM) than during previous less intense glacial stages. Such a non-linear response of denudation to climate change is plausibly controlled by the interplay between glacier velocity and basin topography. Glacial erosion rates were demonstrated to be proportional to the square of the basal ice-sliding velocity squared, resulting in a high sensitivity of erosion to small variations in topography (Herman et al., 2015) and strong influence of the basal valley shape (U-shaped or V-shaped) on glacial erosion (Brædstrup et al., 2016). This suggests that the erosional response to Quaternary climate change is not uniform.

Moreover, the theory of global acceleration of denudation during the more recent Quaternary period relies heavily on the hypothesis that landscape is everywhere in disequilibrium due to climate oscillations, and not only in glaciated regions (Godard et al., 2013; Molnar, 2004). The link between

Quaternary climatic oscillations and denudation in non-glaciated, tectonically quiescent areas is therefore key, but remains obscure.

The present work aims to fill this knowledge gap by focusing on the reconstruction of paleo-denudation rates of SW Madagascar to investigate the effect of the Quaternary climatic cyclicity on a subtropical island that remained unglaciated and tectonically quiescent throughout the Quaternary. We focus our analyses on the Pleistocene because the frequency of glacial/interglacial cycles has changed from ca. 41 ka to ca. 100 ka (Berends et al., 2021) between 1.2 and 0.7 Ma during a period named the Mid Pleistocene Transition (MPT).

The paleo-denudation rates determination for Madagascar are limited to two > 1 ka old river terrace samples (Cox et al., 2009), which showed no variation when compared to modern denudation rates (Brosens et al., 2023). The paleoclimate of Madagascar is expected to have been affected by variability at different frequencies. Paleoclimatic studies of Madagascar are concentrated in the Holocene, showing alternations of decadal to millennial wet and dry periods from speleothem analysis (e.g., Railsback et al., 2020; Scroxton et al., 2023; Voarintsoa et al., 2017; Wang et al., 2019). Studies conducted over longer timescales are located on the African continent. Over the Late Pleistocene, vegetation of SE Africa exhibited variability following the glacial/interglacial cyclicity (Dupont et al., 2011). A palynology study also suggested that temperatures may have varied by ~4°C between glacial and interglacial periods over the past 0.8 Ma (Chevalier et al., 2021). Finally, lake Malawi has been shown to display dramatic water level variations of up to ~400m over the past 1.3 Ma, with the MPT marking a transition from drier to wetter conditions (Lyons et al., 2015). As the evolution of vegetation cover and type, as well as global moisture, control to some extent the evolution of denudation rates (Schmid et al., 2018) one could expect variability in denudation rates of Madagascar which would follow variations in climate. However, no data supports such a hypothesis in tropical regions.

In this work, we measure cosmogenic-derived denudation rates in turbidites of a marine sedimentary piston core retrieved offshore western Madagascar. This sedimentary sequence spans several glacial cycles from ca. 900 ka to the present. These analyses were supplemented by the acquisition of new ^{10}Be-derived denudation rates for five modern river catchments in SW Madagascar. This was done in conjunction with neodymium isotopes and heavy mineral analyses of core and river samples to ensure the origin of sediments of the core and investigate the potential effect of changing sediment provenance and geology on calculated denudation rates.

5.2. Study Area

5.2.1. Physiography of Madagascar

Madagascar is a tropical to sub-tropical island located offshore southern Africa to the east of the Mozambique Channel (Latitude ranging from 11.9°S to 25.6°S). Three main topographic zones are

identified. A large central plateau with limited relief (mean elevation of ~1200 m) but with some high points (e.g., Mount Maromokotro, 2876 m) flanked by two zones of lower altitude (Figure 5.1A). The western transition from the central plateau down to the sea corresponds to a series of cuestas (ridges with gentle slopes), formed by differential erosion of hard and soft sedimentary layers (Delaunay, 2018). To the east, the great escarpment separates the high plateau from the narrow (50-190 km) coastal plain, extending for 1500 km from north to south and containing several small isolated basins (Wang et al., 2021). The drainage divide between the eastern and western watersheds is located only 50-100 km away from the eastern coast (Figure 5.1), reflecting the strong asymmetry of the relief, with much steeper slopes in the east than in the west. Major drainage basins drain towards the Mozambique Channel in the west, while rivers debouching into the open Indian Ocean are short and tend to extend westward by headward erosion and drainage capture (Figure 5.2). Two main sedimentary basins exist in the western part of the island, the Morondava basin to the south of Cap Saint-André and the Mahajanga basin to the north, spreading over~ 9000 km^2 and ~13,000 km^2, respectively (Figure 5.1A). The sediments analyzed in the marine core originate from catchments of the Morondava basin.

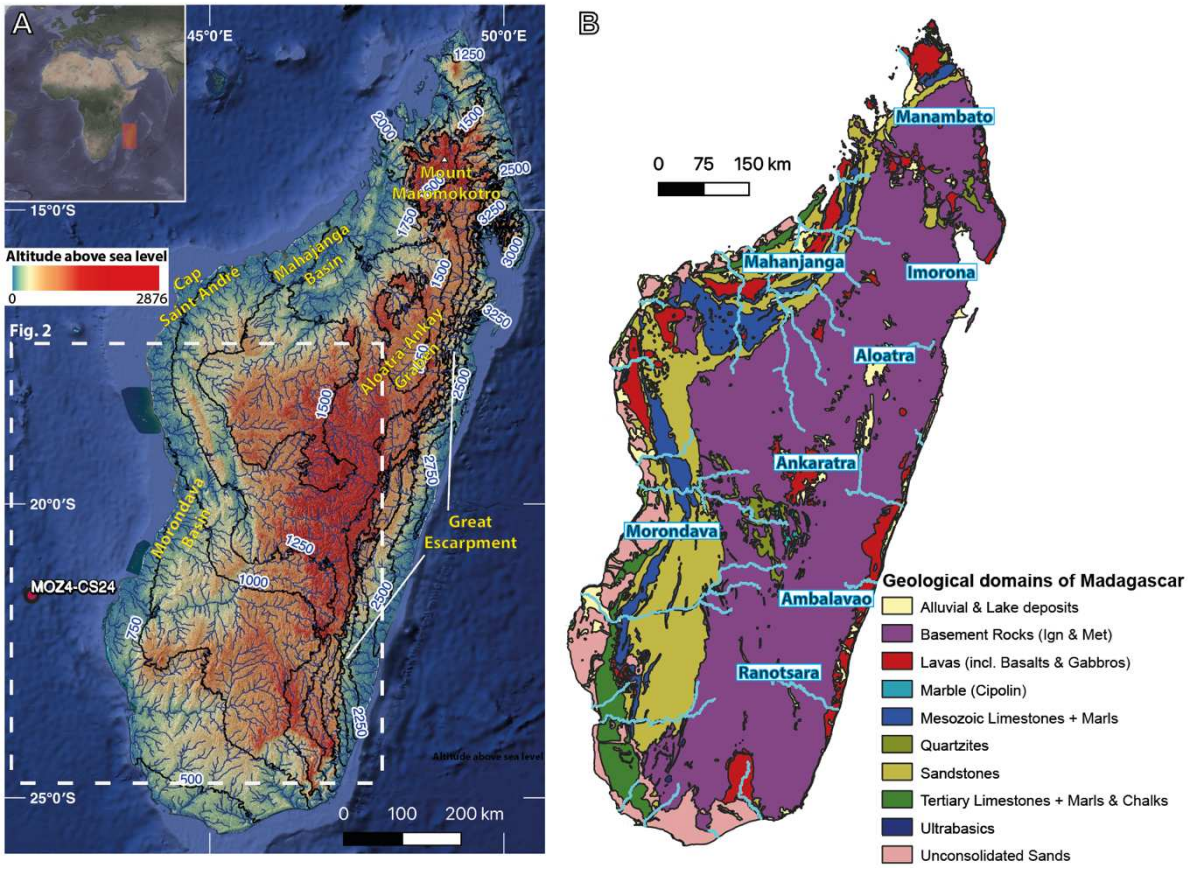

Figure 5.1: Location, topography and geology of the island of Madagascar. A/ Isohyets are from WorldClim2 model by Fick and Hijmans (2017). Red dot shows position of the studied core. White dotted square encompasses the zoom shown in Figure 2. Top left inset shows location of Madagascar. The Eastern Great Escarpment (see text) is located to the East of the main continental water divide shown in blue. B/ Geologic map simplified from Roig et al. (2012). The names of areas cited in the text are given in dark blue.

5.2.2. Geologic domains of Madagascar

The geology of Madagascar is characterized by two main regions: a widespread sedimentary zone in the western part and Mesoarchean to Neoproterozoic crystalline basement in the central and eastern parts (Boger et al., 2019). Mostly metamorphic basement rocks include granitoids, schists, mafic gneisses (Tucker et al., 2014), high-grade metasediments, (Archibald et al., 2015), amphibolites and dolomitic marbles (Cox et al., 1998; Tucker et al., 2011), and are intruded by Neoarchean granites (Paquette et al.,

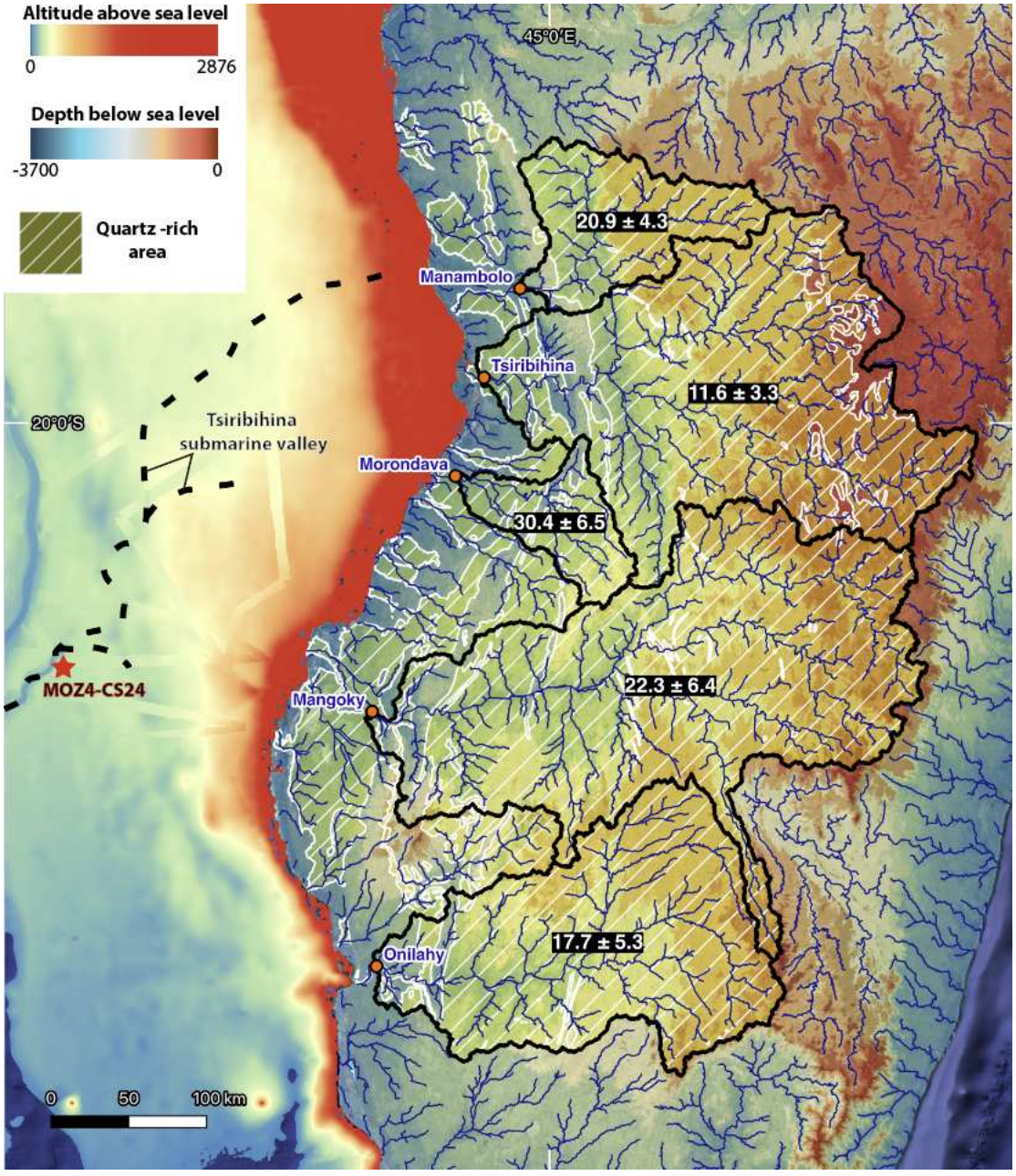

Figure 5.2: Catchments delivering sediments to the MOZ4-CS24 core. Red points indicate sites of the five fluvial samples analyzed for heavy minerals, εNd and ^{10}Be measurements were made. The names of the rivers are given in blue. Modern ^{10}Be-derived denudation rates (mm/ka) for each basin are outlined in black. The white dashed grey area shows location of Quartz-bearing lithologies used to calculate production rates (see text). MOZ4-CS24 core and Tsiribihina submarine valley are indicated by red star and black dashed line respectively. General bathymetry from GEBCO 2014 Grid (https://www.gebco.net). Higher precision bathymetry lines and location of the Tsiribihina submarine valley are from the PAMELA oceanic campaign (Jouet and Deville, 2015).

2003; Tucker et al., 2011) such as the Tonian plutonic suite of Imorona-Itsindro (Archibald et al., 2017) and the Ambalavao (Archibald et al., 2019) and Manambato suites (Thomas et al., 2009) (Figure 5.1B). The Morondava and Mahajanga basins in the west contain up to 10-km-thick Carboniferous to Neogene sedimentary successions (Besairie, 1972; Delaunay, 2018) (Figure 5.1B) including continental siliciclastic sediments and shallow-marine carbonate shelf deposits (Andriampenomanana et al., 2017). In the rest of the island, Cenozoic sediments fill small interior basins (e.g., Aloatra Lake and Ranotsara plains; Figure 5.1B) and a narrow strip of Quaternary deposits lines the eastern coast.

5.2.3. Tectonic activity of Madagascar

Although Madagascar is considered as tectonically dormant, over the past 15 Ma, large-wavelength uplift of 1-2 km was revealed by inverting 98 river profiles throughout the island (Roberts et al., 2012). Rates of general uplift, widespread throughout the island, reach 0.2 to 0.4 mm/a and are attributed to Neogene convective mantle upwelling below the island. However, widespread uplift may have remained active only until the end of the Miocene (Delaunay, 2018). The topography of central Madagascar, where the crust appears to be thinner, is held to be maintained by dynamic topography and upwelling of hot mantle material (Paul and Eakin, 2017; Pratt et al., 2017). Active uplift, very localized to the northern tip of Madagascar, was also revealed by the study of elevated marine terraces and linked to the Comoros hotspot (Stephenson et al., 2019). However, the large wavelength uplift of the island, supported by dynamic topography, does not create important relief or increased slopes and is thus considered to have little effect on denudation (Jiao et al., 2022). Volcanism as recent as Late Pleistocene is also recorded to the northwest and southwest of the Ankaratra volcanic complex (Figure 5.1) (Melluso et al., 2018; Rufer et al., 2014).

5.2.4. Climate

Madagascar is located at the southern limit of the modern Inter Tropical Convergence Zone (ITCZ) where converging winds and maximum precipitation are associated to the ascending branch of the Hadley circulation (e.g., Hu et al., 2007). These convective cells bring warm moist air into the upper troposphere and cold dry air down to mid latitudes, their lower part being the trade winds. This converging warm moist air leads to intense precipitation. The seasonal migration of the ITCZ drives a monsoon climate in Madagascar (e.g., Gadgil, 2018), especially in the southwest, with seasonal and spatial variability in precipitation marked by wet (December to February) and dry (March to November) seasons. In Tulear for instance (Figure 5.1A) wet and dry periods correspond respectively to up to ~ 200 mm/month and down to ~ 10 mm/month of precipitation. The combination of the trade winds bringing moisture from the East, and of the N/S orientation of the relief created by the Eastern Escarpment creates

an orographic effect leading to a marked decrease in precipitation gradient from East to West (Figure 5.1A). This results in Eastern precipitation rates of 120 mm/month to almost 500 mm/month.
Ecosystems thus vary significantly across the island. The eastern coastal plains and the northernmost parts of the island are covered by humid forests whereas the western and southwestern forests are mainly dry, spiny, or subhumid (e.g., Baena et al., 2007). The central plateau is characterized by a grassland-woodland mosaic and mangroves are found along the western and northwestern coasts (Antonelli et al., 2022). Because of such climatic conditions, much of Madagascar is covered by lateritic soils, up to 25-m-thick in the southern parts of the island (Paul et al., 2022).

5.2.5. Modern denudation rates of Madagascar

In Madagascar, various processes have been invoked to explain spatial variability in modern denudation rates. In the East, denudation rates of 3.8 mm/ka to 32.8 mm/ka were linked to scarp retreat (Wang et al., 2021). In the rest of the island, rates of 2.4 mm/ka to 51.1 mm/ka (Brosens et al., 2023) were found to be inversely proportional to altitude. One proposed mechanism is the presence of gullies, locally known as lavakas (Brosens et al., 2022) which may have increased in the last 1 ka due to anthropogenic forcings (settlements, deforestation and cattle grazing). It is proposed that a wetting climate and the decrease in vegetation associated to grazing led to increased runoff and decreased soil resistance causing increasing lavaka formation (Brosens et al., 2022). The physical mechanisms related to the formation of these lavakas and their impact on sediment generation however remain unclear. Values of ^{10}Be-derived denudation rates of the lavakas are of 3.2 ± 0.2 to 19.7 ± 1.2 mm/ka, integrating over 30 ka to 180 ka (Cox et al., 2009).

5.2.6. Sampling location and material used

To calculate ^{10}Be-derived paleo-denudation rates and paleo-provenance analysis, sand fractions were sampled on turbidites from the 26.42 m long MOZ4-CS24 sedimentary core at the Ifremer facility in Brest (France). This core was recovered by a CALYPSO piston corer on the RV “Pourquoi pas ?” in 2015 during the PAMELA-MOZ4 cruise (Jouet and Deville, 2015) which was part of the PAMELA (Passive Margins Exploration Laboratories) project. The core was retrieved ~150 km SW of Madagascar on net-depositional areas called terraces overhanging the axis of the Tsiribihina submarine canyon at 3090 m water depth (Figure 5.2). It consists of hemipelagic carbonated ooze intercalated with 99 turbiditic sand layers ranging in thickness from 0.5 to 19.5 cm (Figure 5.3A). It is ideally located, downstream of several submarine canyon confluences (Figure 5.2) and above the channel axis. This allows the recording of quartz-rich sediments ideally suited for cosmogenic-derived denudation reconstructions, from several large catchments of SW Madagascar (Figure 5.2). Seventeen turbidite

layers were sampled based on grain size, representativity and availability (typical weight of turbiditic samples ~35 g with relatively low Quartz concentrations Figure 5.3B, Table 5.1).

To compare paleo-denudation rates with modern denudation rates, and detrital Nd signatures in modern Malagasy rivers with core samples, ~ 2 kg of river sediments were sampled from active bars of the Mangoky, Tsiribihina, Onilahy, Manambolo and Morondava rivers (Figure 5.2, Table 5.2**Erreur ! Source du renvoi introuvable.**).

5.3. Methods

5.3.1. Chronostratigraphy of core MOZ4-CS24

The chronostratigraphy is based on the fluctuations of $^{18}O/^{16}O$ ($\partial^{18}O$ hereafter, expressed in ‰ vs. Vienna Pee-Dee Belemnite, VPDB, relative to NSB-19) measured in tests of the epibenthic foraminiferal species C*ibicidoides Wuellestorfi* and bio-stratigraphic analyses of calcareous nannofossil assemblages. These were studied in the hemipelagic intervals immediately surrounding the turbidite deposits, which were considered as instantaneous events (i.e., same age at base and top of a turbidite). The $\delta^{18}O$ measurements were analyzed at the Leibniz Laboratory for Radiometric Dating and Stable Isotope Research at Kiel University, Germany, using a Kiel IV carbonate preparation device connected to a ThermoScientific MAT 253 mass spectrometer. The precision of all different laboratory internal and international standards (NBS-19 and IAEA-603) is ± 0.09 ‰. The preliminary age model was constructed by correlating $\partial^{18}O$ variations to the LR04 benthic stack (Lisiecki and Raymo, 2005) with the program AnalySeries (Paillard et al., 1996), and then confirmed by calcareous nannofossil assemblages of stratigraphic significance (Figure 5.3C, Sup. Info. 5.1). Isotopic tie points and calcareous nannofossil data are presented in Sup. Info. 5.1Sup. Info. 5.2Sup. Info. 5.3.

5.3.2. Geochemical analysis

To assess any potential change in sedimentary source that may affect our paleo-denudation rate calculations, we use Nd isotopes.

Sediments reaching the Tsiribihina turbiditic system are provided by the Tsiribihina River as well as all continental basins considered in this study (Figure 5.2). The relative provenance of these sediments may evolve over time, thereby affecting the concentration of cosmogenic nuclides and calculations of paleo-denudation rates as these basins do not necessarily all erode at the same rate (this study and Brosens et al., 2023). To address this issue we used Nd isotopes, or more precisely, variations in the abundance of the radiogenic isotope ^{143}Nd, formed by the decay of ^{147}Sm, normalized to the abundance of the non-radiogenic isotope ^{144}Nd. Unlike stable isotope tracers, the abundances of the radiogenic isotope ^{143}Nd are not directly affected by weathering processes, making Nd isotopes a particularly robust tool for source tracing (e.g., Bayon et al., 2015; Garzanti et al., 2022b). Furthermore, given the very long half-

life of ^{147}Sm (~106 Ga), the $^{143}Nd/^{144}Nd$ ratios of the sediment sources can be viewed as essentially constant over the < 1 Ma time period covered by this study. Variations in Nd isotopic composition are

often expressed in εNd units, which represent the deviation, in parts per 10^4, of the measured $^{143}Nd/^{144}Nd$ ratio from the assumed value of a chondritic uniformed reservoir (CHUR, $^{143}Nd/^{144}Nd = 0.51263$

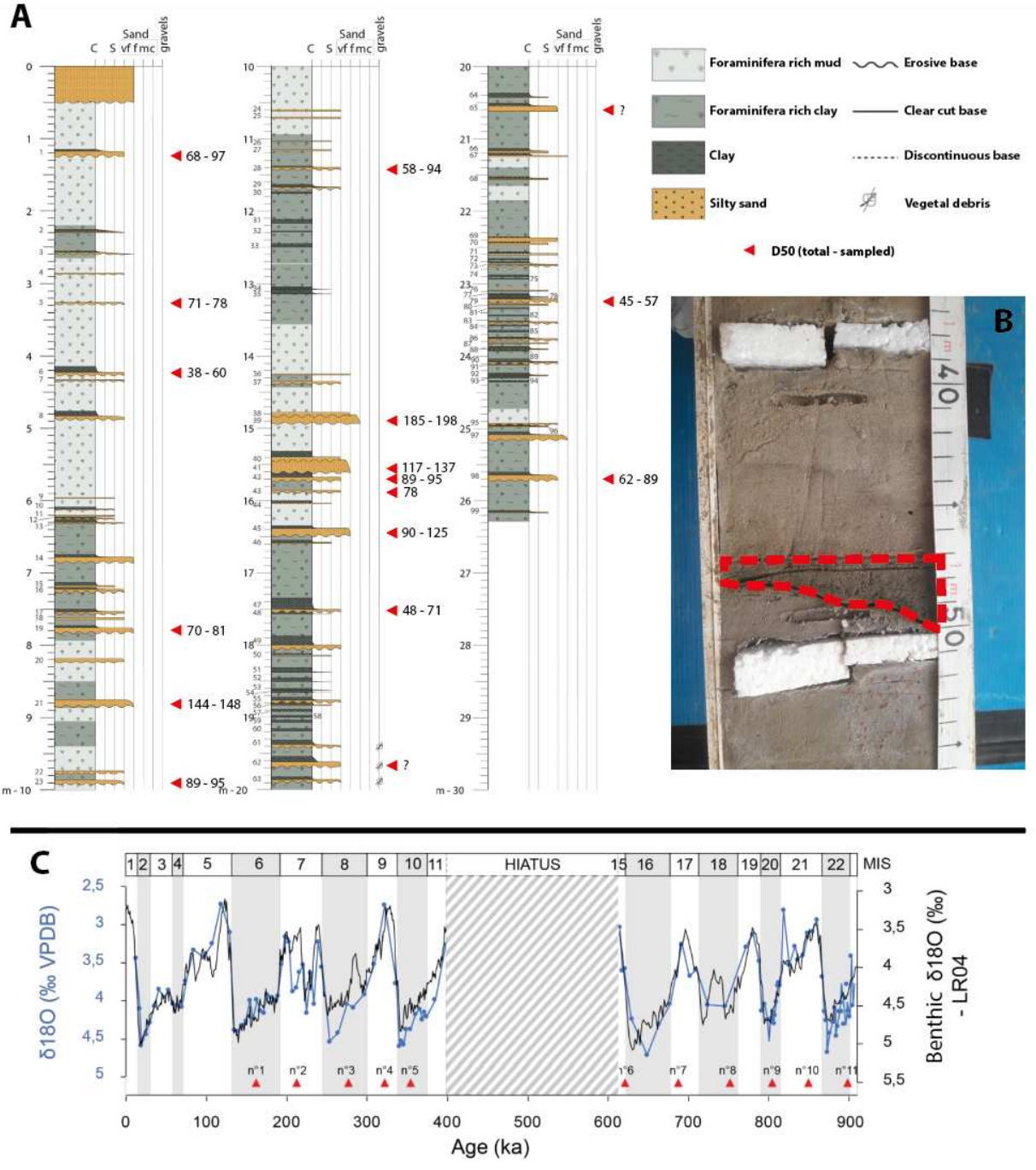

Figure 5.3 : Stratigraphy and age model of the MOZ4-CS24 core. A/ Log of the MOZ4-CS24 core with sampled intervals indicated by the triangles (adjacent numbers indicate median grain size of the turbidite bed and of specifically sampled portion; for two turbidites indicated by a question mark, the granulometry was not determined. B/ Photo of turbidite layer (indicated by red dashed line) before sampling. C/ Age model for core MOZ4-CS24. Blue and black lines are $\partial^{18}O$ measurements of benthic foraminifera from core MOZ4-CS24 (Sup Info 2 for raw data) and LR04 benthic stack (Lisiecki and Raymo, 2005c). Red triangles indicate calcareous nannofossil samples used for biostratigraphic control of the $\partial^{18}0$-derived age model.

Bouvier et al., 2008). Source regions with different Sm/Nd ratios will develop different $^{143}Nd/^{144}Nd$ ratios, and thus different εNd values, over time.

The Precambrian basement rocks of the central plateau in Madagascar, drained by the Manambolo and Mangoky rivers (Figure 5.1B) are characteristically associated with highly negative sediment εNd signatures of -17 to -24, respectively (Garzanti et al., 2022b). This range of values can be used to track significant changes in sediment sources to the studied underwater Tsiribihina valley terrigenous sedimentary record. Nd isotope data in Garzanti et al. (2022b) were obtained from the same 15-500 μm fraction analyzed for heavy minerals. Here, we determined εNd values using the same 50-250 μm fraction as used for ^{10}Be measurements, for 15 turbiditic samples and 5 river sand samples (Figure 5.2, Table 5.3). To assess any potential grain-size effects, we also measured the separate 50-100 μm and 100-250 μm size fractions in the five river sand samples and on turbidite samples whenever possible (3 samples were measured on the 50-100 μm fraction alone, 4 on the 100-250 μm fraction alone, and 8 were measured on both fractions, Table 5.3). Additional information on the geochemical treatment of the samples is given in the supplementary material.

We determined major and trace element compositions on bulk-sediment core samples and on separate size fractions of leached river-sand samples at the SARM (Service d'Analyse des Roches et des Minéraux, https://sarm.cnrs.fr/index.html/). We also determined abundances for selected major and trace elements in the detrital sediment fractions of core MOZ4-CS24 at the Pôle Spectrométrie Océan (Brest) using an Element XR ICPMS instrument (Sup. Info. 5.4).

5.3.3. Heavy minerals

Heavy minerals are used with the same objective as Nd isotopes, but they provide additional information regardiung transport mechanisms and processes.

As an additional approach to source tracing, we performed heavy-mineral analyses for the 17 sediment samples from MOZ4-CS24 core at the Laboratory for Provenance Studies (University of Milano-Bicocca, Italy). Quartered aliquots of each bulk sediment sample (ca. 3-4 g) were wet sieved with a standard 500 μm sieve in steel and with handmade tissue-net sieves with 15 μm mesh. Heavy minerals were separated from the 15-500 μm fraction by centrifuging in sodium polytungstate (density 2.90 g/cm^3) and recovered by partial freezing with liquid nitrogen. An appropriate amount (i.e., not too many to avoid overlap, not too few to avoid voids, see Garzanti and Andò, 2019) of the dense fraction was split carefully with a micro-riffle box and mounted with Canada balsam (n = 1.54) on a glass slide. Under a polarizing microscope, ≥ 200 transparent heavy minerals were point-counted at a suitable regular spacing to minimize overestimation of smaller grains (Garzanti and Andò, 2019). All uncertainly determined grains were checked and properly identified in a wide spectral range (140 - 4200 cm^{-1}) by an inVia^{TM} Renishaw Raman spectrometer equipped with a green laser 532 nm and a 50x LWD objective according to Andò and Garzanti (2014). Heavy-mineral concentration was calculated as the volume percentage of total (HMC) and transparent (tHMC) heavy minerals (Garzanti and Andò, 2007). The

ZTR index is the sum of zircon, tourmaline and rutile over total transparent heavy minerals (Hubert, 1962) and is classically used to estimate the "durability" (i.e., the extent of recycling; Garzanti, 2017) of the assemblage. The "Amphibole Colour Index" ACI and "Metasedimentary Minerals Index" MMI are used to estimate the average metamorphic grade of metaigneous and metasedimentary source rocks, respectively. They vary from 0 in detritus from low-grade rocks yielding exclusively blue/green amphibole and chloritoid, to 100 in detritus from high-grade rocks yielding exclusively brown hornblende and sillimanite (Table 5.4). The "Sillimanite Index" Sil.I., defined as the ratio between prismatic sillimanite and total (prismatic + fibrolitic) sillimanite grains, varies from 0 in detritus from upper amphibolite-facies metasediments to 100 in detritus from granulite-facies metasediments (Andò et al., 2014) (Table 5.4). Significant minerals are listed in order of abundance in section 5.4.2. The sediment contribution of each river of SW Madagascar is then calculated from these mineral abundances by forward mixing models following Garzanti et al. (2012).

5.3.4. Cosmogenic radionuclide denudation rates

Paleo-denudation rates in Madagascar were calculated following a method extensively described in previous studies (e.g., Charreau et al., 2021; Puchol et al., 2017). We measured the bulk ^{10}Be concentrations in quartz grains N_{total} in at/g of the sampled turbiditic layers from MOZ4-CS24 core. The basin-averaged denudation rate $\bar{\varepsilon}$ was then calculated from N_{total} by solving the following equation 1 (e.g., Charreau et al., 2011; Puchol et al., 2017):

$$N_{total} = e^{-\lambda t}\left[\sum_{j=1:3}\frac{\overline{P_j}}{\frac{\bar{\varepsilon}\,\rho_r}{\Lambda_j}} + N_{fp}\right] \qquad \text{Eq. 1}$$

where $\overline{P_j}$ is the overall paleo-production rate of ^{10}Be averaged over the drainage basin at the time of erosion, which accounts for all cosmogenic-production mechanisms (spallation, 'n', and slow and fast muons, 'μs' and 'μf', respectively, indicated by j = 1:3), ρ_r is the density of the denuded rocks (taken as 2.6 g/cm^3), λ the radioactive decay constant (^{10}Be half-life is 1.387 Ma, Korschinek et al., 2010), Λ_j the characteristic attenuation lengths of cosmogenic-production mechanisms (Λ_n = 160 g/cm^2, $\Lambda_{\mu s}$ = 1500 g/cm^2, and $\Lambda_{\mu f}$ = 4320 g/cm^2, Braucher et al., 2011), and t the time at which the sediments were buried (i.e. depositional age). N_{fp} is the number of ^{10}Be atoms (per g of quartz) accumulated by sediments during transport across the onshore watershed. To solve equation 1 and derive paleo-denudation rates from measured ^{10}Be concentrations, assumptions and corrections must be made including corrections for radioactive decay, cosmogenic accumulation during transport, sedimentation and re-exposure (Charreau et al., 2021, 2011; Puchol et al., 2017).

Firstly, we must assume paleo-production rates equivalent to modern basin-averaged cosmogenic ^{10}Be production rates. This assumption must consider the dependency of cosmogenic nuclide production rates on altitude (amount of atmosphere blocking the cosmic rays) and latitude (orientation and strength of the geo-magnetic field) (Dunai, 2000). Assuming a relative tectonic quiescence of Madagascar allowed us to consider that no significant change in the elevation of the drained watersheds had occurred since 900 ka, although drainage basin reorganizations may have taken place. This possibility was verified using εNd and Heavy Minerals (see above). The assumption of constant production rates over the past 1 Ma is thus considered acceptable and production rates of ^{10}Be were calculated using the Basinga ArcGIS toolbox (Charreau et al., 2019). Based on a 30 m Sentinel Digital Elevation Model (DEM, https://dataspace.copernicus.eu), this program calculates a production rate integrated over an entire drainage basin by determining a rate for each pixel of the DEM depending on its latitude and elevation. Secondly, because cosmogenic ^{10}Be concentrations are measured in quartz grains, we assumed that quartz-bearing lithologies were representative of basin geology. Only the areas of quartz-bearing lithologies (alluvial and lake deposits, basement rocks, quartzites, sandstones and unconsolidated sands, Figure 5.1B) were thus considered for production calculations (Figure 5.2). These lithologies are prevalent in the central high plateaus and in the western drainage basins, constituting ~85 % of the total drainage area considered in this study. Although these lithologies do not necessarily erode at the same rates, cosmogenic nuclides measured in river sands at the outlet of the drainage allows for the calculation of a basin-integrated mean denudation rate.

For paleo-denudation rate calculations (Table 5.1), we assumed that core turbiditic sediments were sourced from all considered basins. We used the production rate of the entire quartz-rich area shown in grey in Figure 5.2, corresponding to values of 4.798 at/g/a, 0.041 at/g/a and 0.015 at/g/a for neutrons, fast muons and slow muons, respectively. Modern denudation rates were calculated using the production rates of the area of quartz-bearing lithologies within each basin (results are given in Table 5.2). All production rates were corrected for topographic shielding using relief shadow modeling from (Codilean, 2006). Finally, we assumed that ^{10}Be production during transport until final deposition was negligible, as discussed below.

To solve equation 1 and assess the associated errors on paleo-denudation rates, we used a Monte Carlo simulation, as described in Puchol et al. (2017), which conservatively explores the range of each input parameter with 10^4 draws. The Monte Carlo simulation method was preferred to linear error propagations as it is better suited for estimating uncertainties on results of calculations implying several variables, themselves affected by individual uncertainties.

Each denudation rate data was associated to an integration time (or characteristic time) (Table 5.1**Erreur ! Source du renvoi introuvable.**). It corresponds to the time over which the denudation rate calculated is valid, in other words, the time taken by a quartz mineral to cross the subsurface depth where it accumulated cosmogenic nuclides (usually 60 cm). Denudation rates of 50 mm/ka will have an integration time of 12 ka, (60 cm / 0.005 cm/a, see Von Blanckenburg, 2005 for further explanation).

Further information on the geochemical extraction of cosmogenic nuclides, the granulometric fractions considered (50-100 µm, 100-250 µm and 50-250 µm), as well as on the blanks obtained are given in the supplementary information.

5.3.5. Comparison of calculated denudation rates with the climatic cycle ($\partial^{18}0$)

To investigate the covariance of denudation with climate, we first investigated how denudation rates measured during glacial and interglacial periods compared with each other. Furthermore, we compared our calculated denudation rates to the $\partial^{18}O$ values of the LR04 data from Lisiecki and Raymo (2005). Denudation rates are compared to the $\partial^{18}O$ values at the exact time of deposition but also to the values averaged over both uncertainties on ages and integration times associated with each denudation rate. For instance, for denudation rates of 50 mm/ka (i.e. integration time of 12 ka, see above and von Blanckenburg, 2005 for further explanation) measured at 150 ± 10 ka, $\partial^{18}O$ will be averaged from 140 to 172 ka. To refine this test, we randomly selected an age value within the uncertainty interval of the sediment ages and averaged the $\partial^{18}O$ over the characteristic time of the denudation rate associated with the turbidite age selected. If we take the same example as above of a denudation rate of 50 mm/ka measured at 150 ± 10 ka, we randomly selected an age within the uncertainty, for instance 143 ka, and integrated the $\partial^{18}O$ values over the integration time associated to the denudation rate (12 ka, see above), so from 143 ka to 155 ka. We did 100 000 iterations for each denudation point and calculated the best possible coefficient R^2 between the so averaged $\partial^{18}O$ and denudation rates.

For additional statistical analyses of our datasets, we used the IsoplotR calculator (http://isoplotr.es.ucl.ac.uk, Vermeesch, 2018), and more specifically the Mean Square of the Weighted Deviates (MSWD) to check the homogeneity of a given batch of values.

Table 5.1: Descriptive table of the MOZ4-CS24 turbiditic data. The core was drilled at 3090 depth below sea level, at 21°31'6.42"S, 45°51'40.475"E. Production rates of quartz-rich areas were used to calculate denudation rates (4.79824 at/g/a for neutrons, 0.014956 at/g/a for slow muons and 0.041427 at/g/a for fast muons). Ages correspond to the age model from the core + 6 ka (explanations provided in text). Corrected ^{10}Be values correspond to the Measured ^{10}Be values corrected for radioactive decay. Uncertainties are 1 sigma.

Core Section	Granulometric fraction	Batch	^{10}Be/^{9}Be	^{10}Be Counts	^{9}Be	Mass of Quartz	Measured ^{10}Be	Age	Corrected ^{10}Be	Denudation	Integration time	Denudation
	µm		10^{-15}		10^{19} at	g	10^{4} at/g	ka	10^{4} at/g	mm/ka	ka	t/km^2/a
S2 123-130	50-250	3_4	4.6 ± 0.9	40	3.0	0.8	14.2 ± 3.5	28	14.4 ± 3.5	24.9 ± 7.8	24.1	65.9 ± 20.6
S4 328-330	50-250	3_4	3.8 ± 0.5	64	3.0	0.9	10.4 ± 2.0	89	10.9 ± 2.1	32.2 ± 9.2	18.6	85.3 ± 24.3
S5 420-423	50-250	3_4	3.5 ± 0.6	51	3.0	0.4	19.9 ± 5.3	136	21.3 ± 5.7	17.4 ± 5.8	34.4	46.2 ± 15.5
S8 778-781	50-250	3_4	17.6 ± 0.9	413	3.0	4.2	11.9 ± 0.7	218	13.2 ± 0.8	25.5 ± 5.3	23.6	67.5 ± 14.3
S9 878-882	50-250	3_4	10.6 ± 0.7	275	3.0	2.6	11.3 ± 0.9	241	12.7 ±1.0	26.5 ± 5.9	22.6	70.2 ± 15.6
S10 991-992	50-250	3_4	8.4 ± 0.9	144	3.0	2.3	10.1 ±1.3	291	11.7 ±1.5	28.9 ± 6.8	20.7	76.7 ± 18.1
S12 1142-1143	50-250	3_4	4.7 ± 0.5	109	3.0	1.0	11.9 ±1.8	353	14.3 ± 2.1	24.0 ± 6.0	25.0	63.6 ± 15.8
S15 1488-1490	50-250	3_4	8.5 ± 3.2	11	3.0	5.3	4.4 ± 1.8	615	6.0 ±2.5	73.9 ± 29.4	8.1	195.8 ± 77.9
S16 1559-1562	50-100	1	17.0 ±0.9	392	3.1	3.4	11.7 ± 0.9	637	16.1 ± 1.3	20.9 ± 4.6	28.7	55.4 ± 12.2
S16 1559-1562	100-250	2	19.6 ± 1.0	425	3.1	8.01	6.7 ± 0.4	637	9.2 ± 0.6	36.7 ± 7.7	16.4	97.1 ± 20.4
S16 1570-1572	50-100	2	13.3 ± 0.9	252	3.1	4.7	7.3 ± 0.6	650	10.0 ± 0.8	33.7 ± 7.2	17.8	89.2 ± 19.2
S16 1587-1589	50-250	3_4	4.6 ± 0.5	118	3.0	1.7	6.6 ± 1.0	668	9.2 ± 1.4	37.3 ± 9.6	16.1	99.0 ± 25.4
S17 1647-1650	50-250	3_4	7.9 ± 0.5	239	3.0	2.6	8.4 ± 0.7	706	11.9 ± 1.1	28.3 ± 6.2	21.2	74.9 ± 16.5
S18 1752-1755	50-250	3_4	10.1 ± 0.6	252	3.0	4.9	5.7 ±0.5	781	8.4 ± 0.7	39.8 ± 8.6	15.1	105.5 ± 22.8
S21 1968-1970	50-250	3_4	6.9 ± 0.5	161	3.0	1.9	9.4 ± 1.0	810	14.1 ± 1.5	23.9 ± 5.4	25.1	63.4 ± 14.4
S21 2060-2062	50-100	1	17.0 ± 0.8	432	3.1	4.3	9.3 ± 0.7	818	14.0 ±1.1	24.0 ± 5.2	25.0	63.5 ± 13.7
S21 2060-2062	100-250	2	3.4 ± 0.4	77	3.1	0.33	11.3 ± 5.1	818	16.9 ± 7.6	28.8 ± 11.9	20.8	76.3 ± 31.5
S24 2322-2325	50-250	3_4	2.6 ± 0.3	79	3.0	0.6	8.5 ± 2.3	879	13.1 ± 3.5	28.0 ± 9.3	21.4	74.1 ± 24.6
S26 2568-2570	50-100	2	14.2 ± 1.0	205	3.1	5.2	7.2 ± 0.6	906	11.3 ± 1.0	29.9 ± 6.6	20.1	79.2 ± 17.6

Table 5.2: Location, production rates and size of drainage areas of the five modern-river sand samples, used for both ^{10}Be and εNd measurements

River	Sampling Site	Latitude	Longitude	Elevation	Neutronic production	Fast muonic production	Slow muonic production	Drainage
				m	at/g/a	10^{-2} at/g/a	10^{-2} at/g/a	10^3 km^2
Tsiribihina	Belon'i Tsiribihina	S 19° 42’ 36,6’’	E 044° 35’ 02,7’’	5	5.5	4.4	1.6	47.6
Mangoky	Tanambao	S 21° 50’ 01,9’’	E 043° 52’ 22,4’’	46	5.2	4.2	1.6	53.0
Onilahy	Ambohimahavelona	S 23° 27’ 10,1’’	E 043° 53’ 59,8’’	29	5.0	4.2	1.5	32.0
Manambolo	Bekopaka	S 19° 08’ 40,8’’	E 044° 48’ 49,2’’	46	4.3	4.1	1.5	11.6
Morondava	Upstream Bosimavo	S 20° 20’ 30,9’’	E 044° 24’ 07,1’’	18	3.5	3.9	1.3	6.2

River	Granulometric fraction	$^{10}Be/^{9}Be$	^{10}Be Counts	^{9}Be	Mass of Quartz	Measured 10Be	Denudation	Integration time	Denudation	Outflow
	µm	10^{-14}		10^{19} at	g	10^4 at/g	mm/ka	ka	t/km^2/a	10^5 t/a
Tsiribihina	50-250	8.7 ± 0.3	1246	2.9	7.4	34.1 ± 1.1	11.2 ± 2.3	53.5	29.7 ± 6.1	14.2 ± 2.9
Tsiribihina	100-700	21.6 ± 0.6	1651	3.0	20.1	31.8 ± 0.9	12.0 ± 2.4	50.1	31.8 ± 6.4	15.1 ± 3.1
Mangoky	50-250	10.6 ± 0.3	1230	3.0	18.3	17.1 ± 0.5	21.1 ± 4.4	28.4	55.9 ± 11.6	30.0 ± 6.1
Mangoky	100-700	9.2 ± 0.3	1255	3.0	17.8	15.3 ± 0.5	23.7 ± 4.9	25.4	62.7 ± 13.0	33.3 ± 6.9
Onilahy	50-250	5.9 ± 0.2	966	3.0	7.6	22.9 ± 0.8	15.1 ± 3.1	39.6	40.1 ± 8.2	12.8 ± 2.6
Onilahy	100-700	10.0 ± 0.5	833	3.0	21.7	13.6 ± 0.6	25.7 ± 5.4	23.3	68.1 ± 14.4	21.8 ± 4.6
Manambolo	100-700	6.8 ± 0.2	1225	3.0	13.8	14.5 ± 0.5	20.9 ± 4.3	28.8	55.3 ± 11.5	6.4 ± 1.3
Morondava	100-700	5.9 ± 0.4	595	3.0	21.1	8.3 ± 0.6	30.4 ± 6.5	19.8	80.5 ± 17.2	5.0 ± 1.1

Table 5.3: Values of $^{10}Be/^{9}Be$ ratios of blanks of batches prepared in old CRPG Be lab (batch 1) at CEREGE (batch 2) and at the new clean CRPG lab (batches 3 to 6).

	$^{10}Be/^{9}Be$ 10^{-16}	Total counts	^{9}Be 10^{19} at	^{9}Be Spike ppm
Batch 1	42.0 ± 5.1	74	3.1	2020 ± 6
Batch 2	22.0 ± 3.8	40	3.0	3025 ± 9
Batch 3_4	9.3 ± 1.9	25	3.0	2129 ± 13
	11.8 ± 2.6	25	3.0	
	5.7 ± 2.1	9	3.0	
	6.7 ± 2.1	11	3.0	
Batch 5_6	4.0 ± 1.4	8	3.0	2129 ± 13
	4.0 ± 1.4	9	3.0	
	1.7 ± 1.3	2	2.9	
	6.0 ± 1.8	13	3.7	

Table 5.4: Nd isotope measurements (εNd) for separate detrital fractions of core MOZ4-CS24 (first part and modern river sands (second part). Sampling sites are indicated in text and in Table 1 for core MOZ4-CS24 and in Table 2 for modern rivers. Data were normalized to CHUR value of $^{143}Nd/^{144}Nd = 0.51263$ (Bouvier et al. 2008).

Sample	Granulometry µm	$^{143}Nd/^{144}Nd$ ± (2se 10^{-6})	εNd ± 2se
S2_123-120	50-100	0.511791 ± 13	-16.2 ± 0.3
S2_123-120	100-250	0.511743 ± 14	-17.1 ± 0.4
S4_328-330	50-100	0.511765 ± 16	-16.7 ± 0.4
S4_328-330	100-250	0.511667 ± 14	-18.6 ± 0.4
S5_420-423	50-100	0.511808 ± 18	-15.8 ± 0.4
S5_420-423	100-250	0.511764 ± 14	-16.7 ± 0.3
S8_778-781	50-100	0.511802 ± 19	-16.0 ± 0.4
S9_878-882	50-100	0.511768 ± 12	-16.6 ± 0.3
S9_878-882	100-250	0.511751 ± 16	-16.9 ± 0.4
S12_1142-1143	100-250	0.511830 ± 16	-15.4 ± 0.4
S15_1488-1490	100-250	0.511818 ± 13	-15.6 ± 0.3
S16_1559-1562	50-100	0.511757 ± 14	-16.8 ± 0.3
S16_1559-1562	100-250	0.511785 ± 13	-16.3 ± 0.3
S16_1570-1572	50-100	0.511764 ± 18	-16.7 ± 0.4
S16_1587-1589	50-100	0.511792 ± 14	-16.1 ± 0.3
S16_1587-1589	100-250	0.511771 ± 11	-16.6 ± 0.3
S17_1647-1650	50-100	0.511736 ± 25	-17.2 ± 0.5
S17_1647-1650	100-250	0.511633 ± 23	-19.3 ± 0.5
S18_1752-1755	50-100	0.511702 ± 24	-17.9 ± 0.5
S21_2060-2062	100-250	0.511728 ±13	-17.4 ± 0.3
S24_2322-2325	100-250	0.511688 ± 18	-18.2 ± 0.4
S26_2568-2570	50-100	0.511776 ± 17	-16.5 ± 0.4

S26_2568-2570	100-250	0.511751 ± 14	-17.0 ± 0.3
Tsiribihina	50-100	0.511661 ± 8	-18.7 ± 0.3
Tsiribihina	100-250	0.511789 ± 8	-16.2 ± 0.3
Manambolo	50-100	0.511615 ± 9	-19.6 ± 0.3
Manambolo	100-250	0.511580 ± 6	-20.3 ± 0.2
Morondava	50-100	0.511811 ± 8	-15.8 ± 0.3
Morondava	100-250	0.511811 ± 8	-15.8 ± 0.3
Mangoky	50-100	0.511638 ± 9	-19.1 ± 0.3
Mangoky	100-250	0.511643 ± 8	-19.0 ± 0.3
Onilahy	50-100	0.511584 ± 6	-20.2 ± 0.2
Onilahy	100-250	0.511567 ± 6	-20.5 ± 0.2

5.4. Results

5.4.1. Age model of core MOZ4-CS24

The combined datasets indicate that the stratigraphic range of core MOZ4-CS24 extends from Holocene (11.6 ka) to Mid Pleistocene (905 ka), corresponding to Marine Isotope Stages (MIS) 1 to the MIS 22-23 boundary. The sedimentation is discontinuous with a ca. 200ka hiatus identified between MIS 11 and MIS 15 (from 421 ka to 599 ka). Further information is provided in supplementary information Sup. Info. 5.1Sup. Info. 5.2Sup. Info. 5.3).

5.4.2. Provenance analysis

Nd isotope data for turbidite samples range between εNd -15.6 ± 0.2 and -19.5 ± 0.2 (Table 5.3, Figure 5.4) with a weighted mean of -16.8 ± 0.15 (MSWD 5.4, p 2.6 10^{-15}). Samples analyzed in two different size fractions yield weighted mean εNd values of -16.3 ± 0.2 (MSWD 2.6, p 5.6 10^{-3}) for the finer 50-100 μm fraction, and -16.9 ± 0.2 (MSWD 2.7, p 2.2 10^{-3}) for the coarser 100-250 μm fraction. Finer and coarser fractions yield mean εNd values of -16.9 ± 0.3 (MSWD 8.8, p 4.2 10^{-7}) and -16.5 ± 0.3 (MSWD 0.65, p 0.63) above the hiatus and -16.2 ± 0.3 (MSWD 3.1, p 9 10^{-3}) and -17.49 ± 0.8 (MSWD 4.4, p 2 10^{-4}) below the hiatus, respectively.

The Nd isotopic composition of modern river sand samples ranges from -15.8 ± 0.3 to -20.5 ± 0.2 with a weighted mean εNd value of -18.6 ± 0.2 (MSWD 55, p 0). Finer and coarser fractions yield weighted mean values of -19.5 ± 0.3 (MSWD 6.5, p 2.2 10^{-4}) and -18.5 ± 0.2 (MSWD 78, p 0) respectively. With the exception of the Tsiribihina River which displays statistically different values (-18.7 ± 0.3 and -16.2 ± 0.3 for the fine and coarse fractions respectively), granulometry does not appear to significantly affect εNd compositions of modern river sands, consistently with findings of Bayon et al. (2015). Granulometric differences are instead significant for the turbidite samples (Table 5.3, Figure

5.4B). Note that for modern river sand samples, the uncertainty stemming from the single sampling of each river is probably much more important than the analytical uncertainty on each individual analysis.

The εNd values of the 100-250 μm fraction of 9 out of 12 the turbidite samples fall within the interval between the Mangoky (-19.1 ± 0.3) and the Tsiribihina (-16.2 ± 0.3) (Figure 5.4B), the two main rivers of the study area. One core sample, at 706 ka (S17, Table 5.1 Table 5.3), presents a more negative signature (-19.3 ± 0.5), closer to that of the Onilahy (-20.5 ± 2) or the Manambolo (-20.3 ± 0.2) rivers. Two turbidite samples at 353 ka and 615 ka (S12 and S15 respectively, Table 5.1 Table 5.3) present less negative signatures (-15.4 ± 0.4 and -15.6 ± 0.3 respectively), closer to that of the Morondava River (-15.8 ± 0.3).

The transparent heavy-mineral (tHM) assemblage of the studied turbidite samples from core MOZ04-CS24 represents between 1.0% and 3.4% of the bulk sediment and mostly consists of blue-green and subordinately green-brown amphibole (46-73%tHM, ACI 9-32), with minor garnet (1-19%tHM), epidote-group minerals (2-8%tHM), zircon (1-8%tHM), tourmaline (1-6%tHM), clinopyroxene (1-9%), prismatic sillimanite (≤ 7%tHM), apatite (1-6%tHM), and rarer titanite, anatase, rutile, hypersthene, kyanite, monazite, and staurolite (ZTR 5-16). Sporadically recorded minerals include enstatite, xenotime, topaz, vesuvianite, brookite, plus a few unidentified grains.

5.4.3. ^{10}Be concentrations and paleo-denudation rates

Measured $^{10}Be/^{9}Be$ ratios range from 2.6 ± 0.3 10^{-15} to 19.6 ± 1.0 10^{-15} with a mean of 6.5 ± 0.3 10^{-15} (Mean Square of the Weighted Deviates (MSWD) 63, p 0, calculated using http://isoplotr.es.ucl.ac.uk, Vermeesch, 2018) for turbidite samples and from 5.9 ± 0.2 10^{-14} to 21.6 ± 0.6 10^{-14} with a mean of 7.6 ± 0.2 10^{-14} (MSWD 43, p 0) for modern sands.

Accordingly, the measured concentrations of ^{10}Be in turbidite samples, corrected from blank values, but uncorrected for radioactive decay range from 4.4 ± 1.8 10^4 at/g at 615 ka to 19.9 ± 5.3 10^4 at/g at 136 ka (Table 5.1), with a mean of 8.0 ± 0.4 10^4 at/g (MSWD 7.2, p 0). For modern river sand samples, somewhat higher concentrations range from 8.3 ± 0.6 10^4 at/g for the Morondava river to 34.1 ± 1.1 10^4 at/g for the fine-grained Tsiribihina sample, with a mean of 16.5 ± 0.4 10^4 at/g (MSWD 130, p 0). The Onilahy is the only river to exhibit significant differences in ^{10}Be concentrations between the finer (50-250μm, 22.9 ± 0.8 at/g, **Erreur ! Source du renvoi introuvable.**) and coarser (100-700 μm, 13.6 ± 0.6 at/g, **Erreur ! Source du renvoi introuvable.**). Complete raw cosmogenic ^{10}Be dataset is given in Table 5.1**Erreur ! Source du renvoi introuvable.**.

Calculated paleo-denudation rates range from 20.9 ± 4.6 mm/ka at 637 ka to 73.9 ± 29.4 mm/ka at 615 ka (Figure 5.4A) with a weighted mean average of 27 ± 3 mm/ka (MSWD 0.81, p 0.7). Samples stratigraphically below the hiatus (i.e., during the MPT) yield mean denudation rates of 24.9 ± 4.7 mm/ka (MSWD 0.5, p 0.8), while samples above (i.e., after the MPT) yield mean denudation rates of 28.0 ± 3.9 mm/ka (MSWD 1.0, p 0.5).

Our modern denudation rates in main SW Madagascar catchments (Table 5.2Table 5.3, Figure 5.2) range from 11.2 ± 2.3 mm/ka for the Tsiribihina river to 30.4 ± 6.5 mm/ka for the Morondava river, with a weighted mean of 15.7 ± 2.4 mm/ka (MSWD 3, p 4 10^{-3}). The highest denudation rates thus characterize the smallest basin (Table 5.2Table 5.3). Weighted mean denudation rates are 14.8 ± 3.1 mm/ka (MSWD 2.2, p 0.091) for finer fractions (50-250 µm) and 17.1 ± 3.8 mm/ka (MSWD 4.3, p 0.0047) for coarser fractions (100-700 µm). Such a discrepancy is accounted for by the notably different values obtained for different fractions for the Onilahy river alone (15.1 ± 3.1 mm/ka and 25.7 ± 5.4 mm/ka for the finer and coarser fractions respectively, Table 5.3). It could be explained by fine grained aeolian deposits found in the more arid parts of the island (the southwestern-most areas), that could contaminate river sands leading to higher ^{10}Be concentrations in the finer fractions. Because we have no quantification of this aeolian input, we hereafter use the weighted mean value of the two fractions for the Onilahy river (17.7 ± 5.3 mm/ka, Figure 5.2). The Mangoky (21.1 ± 4.4 mm/ka and 23.7 ± 4.9 mm/ka for the finer and coarser fractions respectively, Table 5.3) and Tsiribihina (11.2 ± 2.3 mm/ka and 12.0 ± 2.4 mm/ka for the finer and coarser fractions respectively, Table 5.3) samples do not show any statistically relevant difference between size fractions.

5.4.4. Denudation rates vs. climate and ∂^{18}O variations

Glacial and interglacial paleo-denudation rates from MOZ4-CS24 core turbidites yield mean weighted values of 25.7 ± 3.8 mm/ka (n = 11) and 29 ± 5 mm/ka (n = 8), respectively, thus slightly higher during interglacial periods, although the two values are indistinguishable within uncertainties. Pre-hiatus (stratigraphically below) and post-hiatus (stratigraphically above) data, which likely represent syn- and post-MPT time intervals, yield weighted mean denudation rates of 28.0 ± 3.9 mm/ka (n = 7) and 24.9 ± 4.7 mm/ka (n = 12), respectively. These values are again indistinguishable within uncertainties, although syn-MPT denudation rates may have been slightly higher. During glacial periods weighted mean denudation rates are 27.1 ± 5.2 mm/ka (n = 6) and 24.0 ± 5.6 mm/ka (n = 5) for syn-MPT and post-MPT data, respectively. Weighted mean denudation rates during interglacial periods are 29.0 ± 6.0 mm/ka (n = 6) and 27.2 ± 9.1 mm/ka (n = 2) for syn-MPT and post-MPT data, respectively. Therefore, interglacial and glacial denudation are similar within 1 sigma during and after the MPT.

Figure 5.6A and 5.5B show no correlation between the instantaneous (i.e., at the time of deposition of the turbidite + 6ka, Table 5.1) or averaged ∂^{18}O compared to calculated denudation rates. Similarly, considering randomly selected ages, the best correlation between the so averaged ∂^{18}O and denudation rates is R^2 = 0.1508. This indicates no relation between denudation records and ∂^{18}O data (Figure 5.6). Overall, denudation rates in SW Madagascar remained stable during the past 900 ka. The lack of correlation with ∂^{18}O records of glacial/interglacial cycles may indicate that climate variability has not played a major role in controlling denudation on the island.

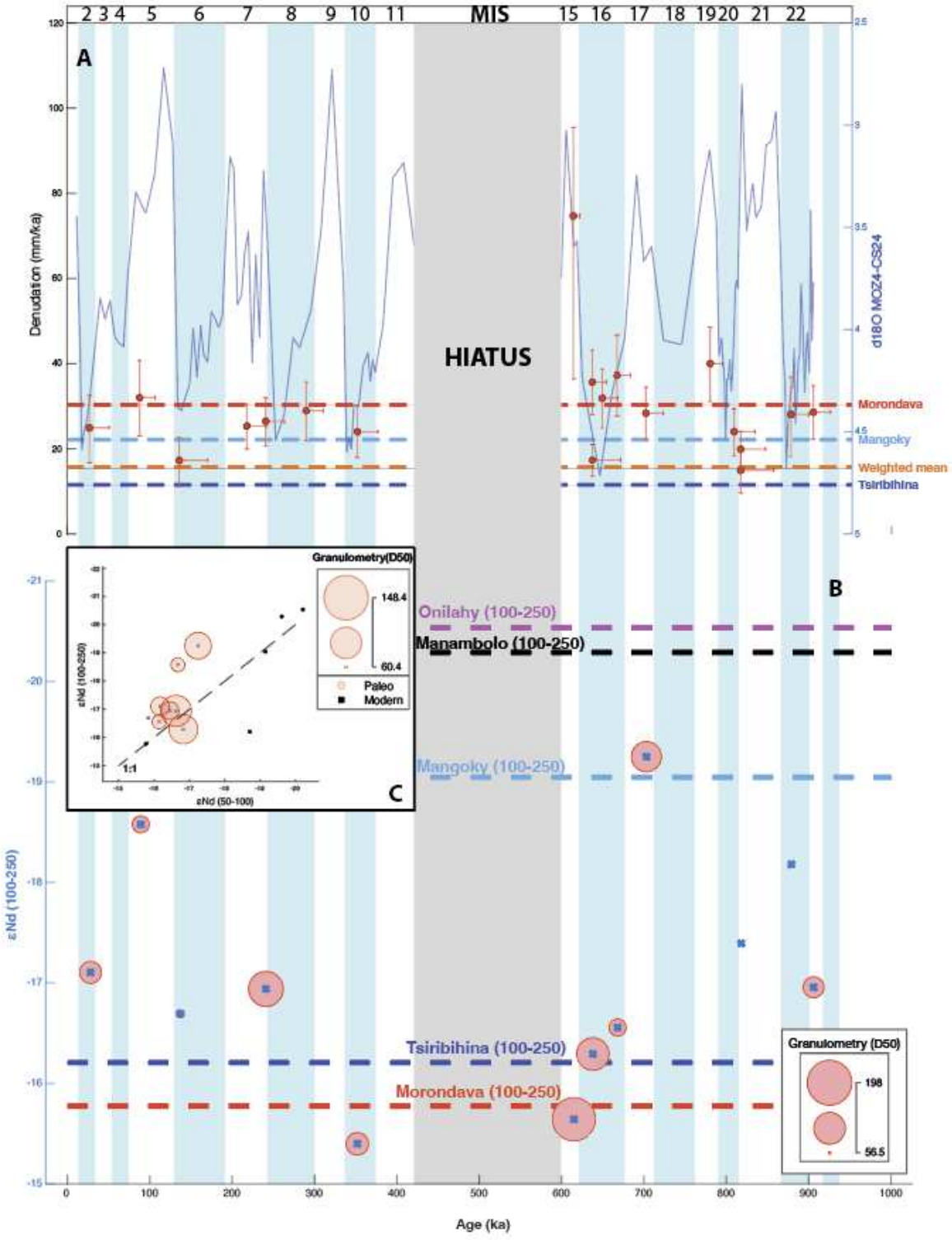

Figure 5.4: ^{10}Be derived denudation rates compared to climatic cyclicity and εNd data. In A/ and B/, light blue rectangles represent glacial periods and white areas interglacial periods. Dark grey area represents the hiatus between 400 and 600 ka. A/ Red points represent ^{10}Be-derived denudation rates of the MOZ4-CS24 core in mm/ka. Ages of these points have been shifted 6 ka to the right (explanation provided in text) and age uncertainty represents integration times associated with measured denudation rates (Table 1). Blue curve are benthic ∂^{18}O values from core MOZ4-CS24. Colored dashed lines are denudation rates for modern Mangoky, Tsiribihina and Morondava (highest rates measured for the latter) and weighted mean of all rivers. B/ εNd signatures through MOZ4-CS24 core, compared to signatures of modern rivers of Madagascar. εNd signatures of 100-250 µm sieved samples of core MOZ4-CS24 are shown by blue crosses. Diameter of red circle around each point is proportional to grain size of the sampled turbidite before sieving. Note the granulometry of point S21 at 818 ka was not measured. Dashed colored lines correspond to the signatures of modern rivers. C/ Comparison of εNd for 50 – 100 µm and 100 – 250 µm, when data was available for both fractions.

5.5. Discussion

5.5.1. Steadiness of denudation rates

Modern denudation rates from rivers of SW Madagascar are consistent with literature values (Brosens et al., 2023; Cox et al., 2009; Wang et al., 2021) which range from 2.4 ± 0.5 mm/ka to 53 ± 13.1 mm/ka with a weighted mean average of 8.7 ± 0.4 mm/ka (MSWD 5.1, p 0). Coastal areas dominated by detrital lithologies (Figure 5.1B), or the eastern great escarpment (weighted mean average of 20.0 ± 10.1 mm/ka) exhibit higher denudation rates. Denudation is lower in the central plateau highlands, dominated by crustal magmatic and metamorphic lithologies (Figure 5.1B) (weighted mean average of 7.5 ± 3.0 mm/ka) (Brosens et al., 2023). Calculated paleo-denudation rates remained nearly constant within uncertainties from 0 ka to ~400 ka and ~600 ka to ~900 ka, although higher than the average calculated

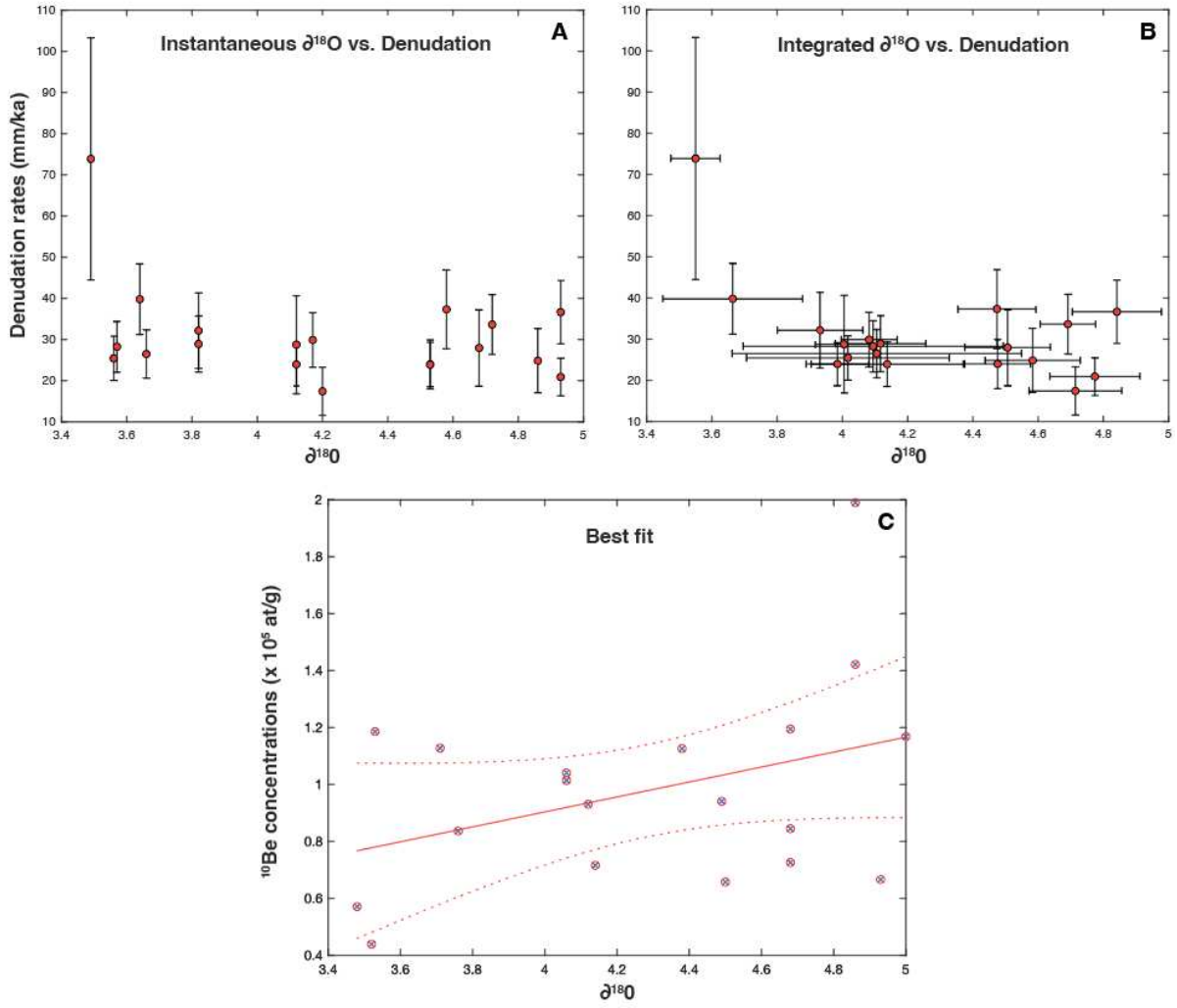

Figure 5.5: Comparison of ^{10}Be and $\partial^{18}O$. A/ $\partial^{18}O$ of the age of deposition of turbidites according to the core's age model versus ^{10}Be-derived denudation rates. B/ mean $\partial^{18}O$ integrated over the integration time associated with each ^{10}Be denudation rate versus ^{10}Be-derived denudation rates. C/ best possible fit between ^{10}Be concentrations and the range of values of $\partial^{18}O$ over each integration time.

denudation rates measured for modern-river catchments of SW Madagascar (15.7 ± 2.4 mm/ka) (Figure 5.4A). This suggests that denudation of SW Madagascar has remained relatively stable through Middle and Late Pleistocene. Consequently, this work suggests no strong impact of Quaternary climate oscillations on denudation rates in this tropical region. Before questioning the origin of this lack of impact, we will discuss whether the cosmogenic concentrations we measured accurately represent denudation rates of the catchments at the time of deposition or if they have been biased by other secondary processes.

5.5.2. Effect of sediment mixing and lateritic cover on cosmogenic nuclide concentrations

The denudation rates presented in this work show no significant variability over the considered period (i.e., 0 ka to ~400 ka and ~600 ka to ~900 ka). This section discusses the effect of thick lateritic soils on the cosmogenic nuclide concentrations and, by extension, on the denudation rates calculated. We are interested in understanding if the absence of high-amplitude variability in our paleo-denudation rate record is due to an absence of response of denudation to climatic cyclicity or if it is an artifact of regional soil processes creating artificially constant cosmogenic nuclide concentrations over the considered period (i.e., modern to Mid-Pleistocene).

In tropical regions, soils are generally thick, extensively weathered and homogenized by bioturbation (e.g., termites, ants, worms) in their upper 3-4 m (Braucher et al., 2000; Breemen and Buurman, 2002; von Blanckenburg et al., 2004). In the central plateau of SW Madagascar, lateritic soils, mostly (85 to 90 %) derived from the chemical weathering of metamorphic gneiss or schist bedrock, can attain maximum thicknesses of 25 m (Paul et al., 2022). The typical Malagasy lateritic cover, as described by Estrade et al. (2019), is composed in its uppermost part of a pedolith (20 to 70 % of the entire lateritic profile) where soil forming processes occur and where the fabric of the parent rock is lost. It overlies a saprolite (10 to 50 % of the profile) where over 20% of the weatherable minerals of the parent bedrock are typically altered. Below, the saprock (15 to 30 % of the profile) is distinguished from the saprolite by the amount of altered weatherable minerals (< 20 %) and is closer in texture and physical strength to the bedrock that it overlies. Organic material is typically concentrated in the pedolith where bioturbation preferentially occurs, although it is seldom spread throughout. Because bioturbation can affect the concentration of cosmogenic nuclides by mixing deep, low concentrated with shallow, high concentrated grains, cosmogenic depth profiles measured in tropical areas commonly present homogenized and constant concentrations in the upper 3-4 meters and classic exponential decrease with depth below that (Braucher et al., 2000). In the case of bioturbated soils, the time required to reach steady state is expected to be longer than when bioturbation is absent (Brown et al., 1995). We used equations (1) and (5) of Brown et al., (1995) to quantify this time delta for different values of denudation

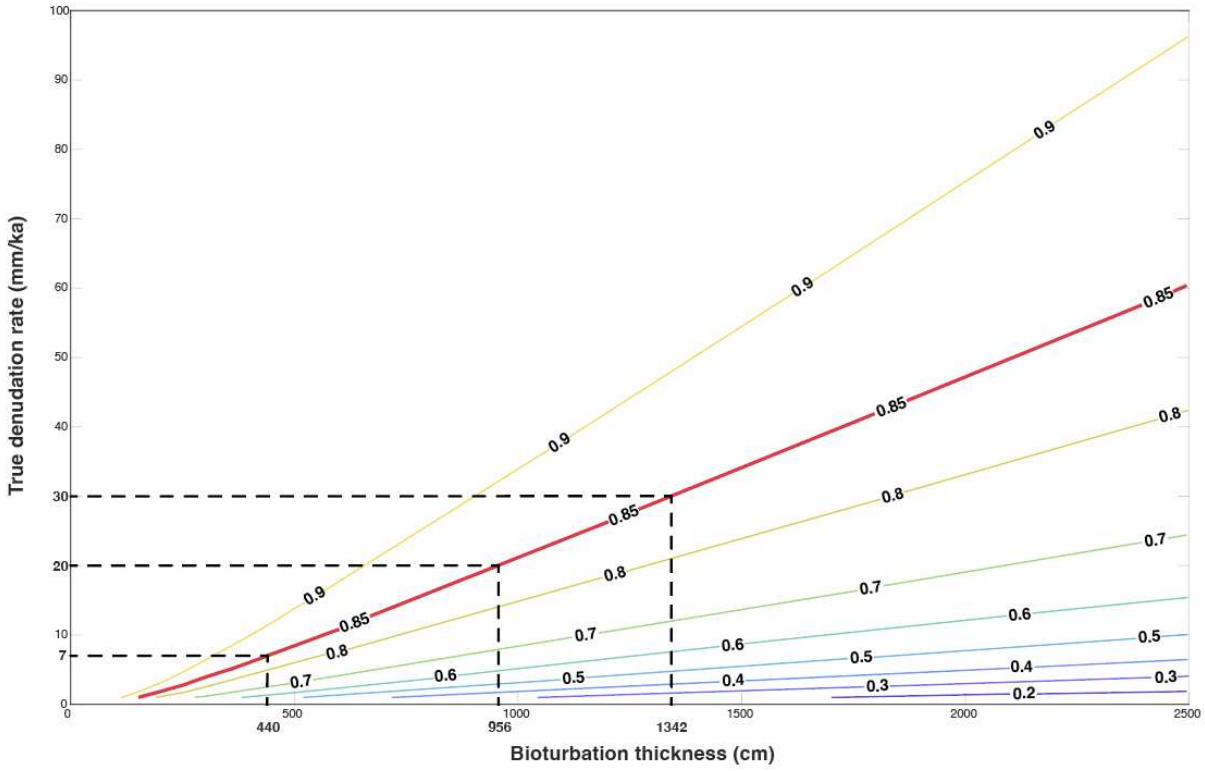

Figure 5.6: Variation in measured ^{10}Be ratio with or without bioturbation for different denudation rates and bioturbation thicknesses. Colored lines represent ratios of concentrations measured with bioturbation, relative to a case without bioturbation.

and bioturbation thicknesses (Sup. Info. 5.5). Our results show that denudation rates primarily control the time to reach steady state (i.e., the time to reach steady state is longer for lower denudation rates), while the thickness of the bioturbated interval appears less relevant.

The homogenized concentration throughout the bioturbated layer is generally similar to the concentration measured at the surface of a soil unaffected by bioturbation (Braucher et al., 2000; Brown et al., 1995; von Blanckenburg et al., 2004). The impact of bioturbation thus remains limited, unless the entire soil profile is removed in a single extreme event (von Blanckenburg et al., 2004). The significant time required to alter crystalline basement into lateritic soils (typically 50 to 100 ka/m, Breemen and Buurman, 2002) and the thicknesses of these soils in Madagascar (up to 25 m, Paul et al., 2022), makes it highly unlikely that such an event could have occurred in the past 900 ka, without the ^{10}Be denudation signal reacting.

However, Brown et al. (1995) suggested that very slow denudation and deep bioturbation might impact concentrations significantly, but without providing any quantification or calculations to support this suggestion. Following equations presented in Brown et al. (1995), we investigated this issue by comparing ^{10}Be cosmogenic surface concentrations with and without bioturbation for the range of values of denudation rates and bioturbation thicknesses expected in Madagascar (Figure 5.6). The lowest denudation rates determined in our study are 11.2 ± 2.3 mm/ka (Tsiribihina Basin, Table 5.3). However, small basins of the central plateau affected by lateritic soils have a notably lower mean value of 7 ± 0.6

mm/ka, and rates as low as 2.4 ± 0.5 mm/ka have been measured for extremely limited basins (Brosens et al., 2023; Paul et al., 2022). Our calculation and figure 6 indicate that for true denudation rates of 7 mm/ka, bioturbation thicknesses of 440 cm would be sufficient to affect calculated denudation rates beyond the inherent uncertainties within the measurements (~15%, Table 5.1). Estrade et al. (2019) found pedolith thicknesses of ~3 m with the exception of one borehole reaching a pedolith thickness of 7 m. However, as previously explained, only the upper part of the pedolith would be bioturbated (Braucher et al., 2000). Furthermore, our findings indicate that representative denudation rates for the island of Madagascar would be closer to values of 20 mm/ka (Table 5.3) or even 30 mm/ka for paleo-denudation rates (Table 5.1) than to 7 mm/ka. For such denudation rates, minimum bioturbation thicknesses of 956 cm and 1342 cm, respectively (determined graphically, Figure 5.6) would be needed to disrupt the ^{10}Be-derived denudation rates by over 15%. These thicknesses are unrealistic (Breemen and Buurman, 2002) and allow us to safely conclude that bioturbation should not be a major concern for the determination of ^{10}Be derived paleo denudation rates.

Intense weathering can also lead to the formation of ferricrust or ferruginous cap. This layer may act as a protective barrier, shielding less competent lower layers from erosion (e.g., Gagen et al., 2019). Modern denudation rates measured across the island (Brosens et al., 2023, and this study) show no clear correlation with laterite thicknesses reconstructed by Paul et al. (2022). It is unclear whether a ferricrust is present and widespread in Madagascar. While the slowest denudation rates (< 10 mm / ka) are found in the Central Highlands, they appear to be associated with a reduced rock erodibility of the basement lithologies, rather than increased thickness of the lateritic cover (Brosens et al., 2023).

Weathering itself may also result in biased ^{10}Be concentrations. If weathering occurs below the ^{10}Be attenuation length, the total denudation rate may be underestimated as cosmogenic nuclides are sensitive to near surface (i.e., 60 cm) mass removal (Dixon et al., 2009). This effect can be enhanced if the weathering is limited at the bedrock-regolith interface and not distributed throughout the entire regolith layer (Ott et al., 2022). Additionally, weathering close to the surface causes a longer residence time of non-soluble minerals (e.g., quartz), when compared to soluble minerals, leading to higher cosmogenic nuclide concentrations in the non-soluble minerals (Small et al., 1999). All these processes may result in a bias in calculated denudation rates that can be as high as 70% in a highly weathered region such as for instance Puerto Rico (Riebe and Granger, 2013).

Because weathering rates are closely related to temperature and precipitation (Riebe et al., 2003), it is highly unlikely that weathering in our studied region would be extreme, as SW Madagascar is subject to a semi-arid climate (Figure 5.1A). Assuming a granitic lithology and a Mean Annual Precipitation (MAP) of 1.5 m/a (mean value for Madagascar for the 1961-2021 period, theglobaleconomy.com), the denudation bias associated with weathering would be 26 ± 10 % (see equation 18 of Riebe and Granger, 2013). Given its semi-arid climate, the MAP for SW Madagascar would be closer to 1 mm/a. Using this value results in a denudation bias of 18 ± 8 %. This value, although

a crude estimate, shows that the possible underestimation of our calculated denudation rates is within the uncertainties affecting our data (Table 5.1Table 5.3).

Past weathering rates, however, may have been higher than in modern periods if Madagascar was affected by wetter, but not colder climates (wet vs. arid climate with only 4°C variations in temperature; Chevalier et al., 2021; Voarintsoa et al., 2017). However, these wetter conditions appear to be short-lived (centennial variations, Scroxton et al., 2019), with some studies finding more arid conditions in colder periods such as the Younger Dryas (Chase et al., 2015). While better constraints on the evolution of precipitation rates in Madagascar throughout the Pleistocene would allow for a more precise conclusion on the impact of weathering on paleo-denudation rates in this region, we remain confident that the bias on calculated denudation rates did not vary significantly (i.e., by a factor of 2 or greater) during the investigated period. This suggests that weathering is unlikely to be responsible for the near steadiness of our paleo-denudation rate.

Finally, as lateritic soils affected by more intense weathering are mainly concentrated on crustal domains, the lower denudation rates measured in these regions may be a result of both the lower erodibility of these lithologies and underestimated denudation rates due to weathering. This effect may also have evolved over time. In summary, although the presence of lateritic soils should be duly considered when measuring denudation rates in Madagascar, especially over long time periods, we are confident that their effect is limited on ^{10}Be-derived denudation rates. Weathering rates are however more difficult to constrain and may have evolved through time.

5.5.3. Duration of sediment transport duration from source to sink

Constraining the duration of transport from erosional to depositional environments essential to interpret the denudation rates calculated, especially in low relief, tectonically quiescent region such as Madagascar. A duration of transport exceeding the integration time of our data would be problematic as it may be associated to cosmogenic nuclide production during transport. Consequently, the measured cosmogenic concentration would be biased and would fail to truly reflect the denudation rates of the source area. Additionally, comparing paleo-denudation rates to precise climatic events requires a good estimate of the age of creation of the sediments considered. This concern is particularly true for turbidites that are remobilized distal sediments deposited in the deep ocean basin. An important issue is the length of transport duration of these continental sediments from the source to the final deposition as a turbidite deposit in the deep ocean basin. A significant lag time ($> 10^4$-10^5 years) between the depositional ages and the denudation time would greatly affect the calculation and interpretation of our ^{10}Be concentration record. Identifying the triggering mechanisms of turbidity currents at continental margins that influence said lag time can provide information on the connectivity of the river to the submarine canyons. Three main processes trigger turbidity currents (Piper and Normark, 2009): slope failure of clinoforms or canyon flanks (e.g., Clare et al., 2016), hyperpycnal flows (i.e., sediment-rich, flood-type river flows triggering turbidites, Mulder and Syvitski, 1995) and dilute river plumes with low sediment

concentrations (1 kg/m^3) (Parsons et al., 2001). Because none of the turbidites studied in this work present an inverse granulometric sorting, hyperpycnal flows were ruled out, although this interpretation could be challenged (e.g., Legros, 2002). Hage et al. (2019) maintained that turbidity currents can be initiated by river plumes with sediment densities as low as 0.07 kg/m^3 and in their global compilation of worldwide turbidity currents, Mulder and Syvitski (1995) show that the Morondava river has typical sediment densities of 3.7 kg/m^3. While this sediment value may evolve over time, it is two orders of magnitude above the minimum value of Hage et al. (2019). Turbidites of the submarine Tsiribihina canyon are thus considered to be triggered either by slope failure or dilute river plumes.

Given the erosive nature of turbidity currents, the sediments they carry may be subject to repeated erosion, transport and deposition on the canyon floor (e.g., Ruffell et al., 2024). This is particularly true for the coarse fraction meaning that the time needed to reach a deep depocenter can be significant. In core MOZ4-CS24, turbidite events appear to be more frequent during low sea-level stands, although there is no clear correlation between sea-level and turbidite occurrence. This suggests that turbidity currents, and associated sediment transport occur regularly over time, although the processes involved may change depending on sea-level (e.g., Mulder et al., 2003). As previously mentioned, a significant portion of the sediments transported by turbidity currents are remobilized, possibly smultiple times, and the inherent lag time between their erosion and their deposition should be considered when measuring ^{10}Be-derived denudation rates.

Unfortunately, few studies have dated turbidites accurately enough to constrain the lag time between continental erosion and deep-sea burial, especially in tropical low denudation settings. In Monterey Bay, Stevens et al. (2014) used Optically Simulated Luminescence (OSL) to date the timing of sediment entry into the canyon head and ^{14}C ages of benthic foraminifera to constrain the depositional age of hemipelagic sediments that bound the sand horizons. They demonstrated relatively rapid, decadal-to-millennial-scale lag time between the entry of sediment into the canyon and deposition in the deep-sea fan. Nakamura et al. (1990) dated organic fractions in 1 to 3 m deep turbidites recovered from Suruga Bay, yielding radiocarbon ages between 270 ± 80 to 2270 ± 90 a BP. These findings suggest rapid transport (< 2360 a) despite the lack of direct age constraints on the deposition of immediately succeeding and underlying hemipelagite deposits. However, these two studies were conducted in regions with significantly different geological settings from those found in Madagascar. Mignard (2017) investigated the source-to-sink transport time of turbidite deposits in the Ogooué deep-sea fan on the West African equatorial margin, using radiocarbon on both vegetal debris found within the turbidites and foraminiferal assemblages separated from neighboring hemipelagic sediment layers. She found lag times between the ages found in the turbidites and associated hemipelagic layers ranging between 0.01 to 14.33 ka, with a mean of 6.33 ka.

In summary, considering the various uncertainties involved, a realistic lag time between the depositional ages in the fan and the ages of continental sediment erosion is on the order of a few ka. This lag time is well within the integration times associated with our calculated denudation rates (mean

integration time of 21.3 ka, Table 5.1). Nevertheless, considering that the Ogooué catchment is a tectonically stable, low-relief region with a tropical climate, similar to Madagascar, we choose to shift our ages of 6 ka in the past to match the mean lag time measured by Mignard (2017), for a more accurate comparison of our data with climatic events of known age.

Another potential issue is the modification of the original cosmogenic signal by reworking and mixing of older sediments stored in the continental drainage basin and either depleted or enriched in cosmogenic nuclides. Because of the apparent absence of widespread terraces in the rivers considered in this work, storage and production of cosmogenic nuclides may occur mainly within the deltaic region. Accordingly, we calculated a production rate of 3.2 at/g/a in a small lowland basin, considered representative of the Mangoky Delta. At this rate, assuming an average sediment transport time similar to that determined for the Ogooué Basin (ca. 6 ka) and assuming that all production occurs onshore with instantaneous transfer to the sea, the total production in the floodplain (Nfp) would be of 1.9×10^4 at/g. This represents a maximum 30 % (for the sample at 614 ka) and an average of 16 % of the measured concentrations, an error well within the bounds of the other uncertainties involved. Additionally, because Mignard et al. (2017) dated vegetal debris, the time lag we assumed may account for both continental transport and potential storage along the continental margin. Because the drainage area considered for the Tsiribihina submarine valley (~ 140.10^3 km^2) is smaller than the area of the Ogooué catchment (~ 220.10^3 km^2) and is characterized by much higher relief and no large floodplain, a much shorter duration of onshore sediment transport than in the Ogooué catchment can be assumed. It is therefore most likely that storage on the continental margin accounted for a significant part of the lag time considered and that $1.9\ 10^4$ at/g of cosmogenic production over the floodplain (Nfp in equation 1) represents a conservative maximum value.

To better investigate the effect of potential storage and reworking of old sediments in the catchment, we examined the downstream evolution of ^{10}Be concentrations for the Mangoky River which shows decreasing concentrations downstream (Sup. Info. 5.6), suggesting possible reworking of ^{10}Be depleted sediments temporarily stored in the catchment. However, this possibility is challenged by the lack of correlation of ^{10}Be concentrations with catchment area (Sup. Info. 5.7). If we consider sediments with initial ^{10}Be concentrations similar to those measured by Brosens et al. (2023) in the plateau upstream (7.5×10^5at/g), then the thickness of the reworked alluvial sediments and the time of storage required to reduce the concentration measured downstream by a factor of 3 would be unrealistic, even in the case where the reworked alluvial sediments were generated during periods of higher denudation (Charreau et al., 2023, Sup. Info. 5.8). For instance, for a denudation of 90 mm/ka (3 times higher than the maximum value observed today), > 70% of the river sediments should originate from a 50 m thick and 500 ka old terrace to decrease the ^{10}Be concentration measured at the outlet by a factor of three (Sup. Info. 5.8). The observed decrease in concentration downstream is more likely due to a change in lithology. The upper reaches of SW Madagascar rivers drain crystalline basement, whereas the lower reaches drain sandstone formations more prone to erosion, and petrographic analyses show a sharp and

Table 5.5: Transparent heavy-mineral assemblages in studied Tsiribihina Valley samples. Estimated contribution of Mangoky river sediment for each sample is indicated in last column (the rest is inferred to have been supplied in subequal proportions from Tsiribihina and Manambolo rivers debouching north of submarine Tsiribihina Valley.

Sample	Age (ka)	HMC	tHMC	zircon	tourmaline	rutile	anatase	titanite	apatite	monazite	epidote	garnet	staurolite	kyanite	sillimanite	amphibole	clinopyroxene	hypersthene	other tHM	ZTR	ACI	MMI	Sil.I.	Est. Mangoky supply
S2 123-120	22	3.0	2.1	4	3	2	2	1	1	0	6	9	0	0	5	62	2	2	0	10	13	100	90	0.64
S4 328-330	83	3.3	2.1	7	1	0.4	3	2	3	0	7	11	0	2	7	52	4	0.4	0	8	16	90	100	0.80
S5 420-423	131	2.5	1.5	8	4	1	0.5	3	3	1	7	12	0	0.5	1	54	3	1	0	14	9	88	n.d.	0.77
S8 778-781	213	3.7	2.0	4	2	1	1	3	1	0	4	5	0	1	1	69	4	1	0.5	8	16	75	n.d.	0.39
S9878-882	236	1.9	1.0	6	4	0.4	0.4	3	2	3	5	19	0	0.4	5	46	4	1	1	11	32	96	100	0.98
S10 991-992	285	3.0	1.4	8	4	1	3	1	4	1	3	13	0	1	6	52	5	0.5	0	13	16	92	100	0.80
S12 1142-1143	347	5.2	2.6	7	5	1	1	2	2	1	8	5	0	0	1	62	3	1	0.5	13	15	n.d.	n.d.	0.53
S15 1488-1490	609	2.2	1.3	3	2	2	1	0.5	2	0.5	6	17	0.5	1	4	53	4	1	0	7	25	85	100	0.88
S16c 1559-1562	632	3.4	1.9	7	2	1	1	2	2	1	2	10	1	0	3	65	2	0	1	10	15	88	100	0.60
S16b 1570-1572	644	3.9	2.1	6	4	1	5	3	4	0..5	6	6	0	0	4	55	3	0.5	1	12	15	100	100	0.65
S16a 1587-1589	662	2.3	1.2	8	6	2	3	2	4	0.5	2	13	1	0.5	1	52	4	0	0	16	13	75	n.d.	0.79
S17 1647-1650	670	2.1	1.2	5	3	0.5	0.5	3	2	0	7	1	0	0.5	0.5	73	1	1	0.5	9	12	n.d.	n.d.	0.30
S18 1752-1755	775	4.0	2.4	2	2	0.5	2	3	5	0.5	3	9	1	0	4	62	2	1	0	5	14	90	100	0.62
S20 1968-1970	804	4.0	1.9	5	4	2	2	1	4	0	6	10	0.5	1	4	57	4	0	0	11	25	88	100	0.71
S21 2060-2062	812	7.4	3.4	5	4	0	0.5	1	6	0	4	5	0	0.5	4	59	9	1	0	9	28	94	100	0.50
S24 2322-2325	873	4.3	2.0	1	5	0.5	4	2	2	0.5	7	3	0	0	2	67	2	0.5	1	7	13	100	100	0.43
S26 2568-2570	900	4.7	3.0	1	3	0	1	2	2	0.5	2	9	0	1	1	71	4	0.5	0	5	24	70	n.d.	0.48

rapid enrichment in recycled quartz grains as the rivers leave the central plateau and cut through Mesozoic siliciclastic rocks. These observations, together with the limited extent of floodplains and fluvial terraces allow us to consider sediment reworking as a minor effect. We are therefore confident that our concentrations truly represent denudation rates and not post-erosion production.

5.5.4. Source evolution and impact of geology

In calculating paleo-denudation rates, we assumed that paleo-drainage basins were similar to modern ones and used the modern cosmogenic production rates in equation 1. This assumption must be discussed based on our rock source analysis. Because the two methods used to reconstruct the source evolution of sediments generated in SW Madagascar (i.e., heavy minerals and εNd) yielded conflicting results, we discuss below possible causes for these discrepancies and how they may affect our results and interpretation. These rock source data also provide information on the possible influence of geology on denudation rates.

Heavy mineral assemblages in turbidites document extensive mixing in various proportions of detritus supplied by the Tsiribihina or Manambolo Rivers debouching to the north of the Tsiribihina submarine canyon, with detritus largely supplied by the Mangoky River debouching to the south. Contributions from other smaller rivers or more distant mouths (e.g., Morondava, Finerenana, Onilahy Figure 5.2) are considered minor from the heavy mineral point of view. This could be due to the limited areas of their basins, with crystalline lithologies present only in their uppermost parts. The major contribution of the Mangoky River is explained by the predominantly northward littoral sand drift along the coasts of SW Madagascar, as indicated by the numerous deltaic spits in the region, although counter-transport locally prevails with smaller spits oriented southward in response to wave diffraction (Anthony, 2015). The Mangoky Canyon, which joins the Tsiribihina submarine valley upstream of the MOZ4-CS24 core site (Figure 5.2), is located in an area where the continental shelf is narrower, leading to likely connection of the river to the canyon during sea level high stands.

The sediment contribution of the Mangoky versus the Tsiribihina, Manambolo and other rivers was calculated using forward mixing models (Garzanti et al., 2012) based on integrated bulk petrography and heavy mineral data from modern river sands of Garzanti et al. (2022a). The results of these calculations are more accurate when end-member compositional signatures are defined by a broad set of parameters that do not display marked grain-size-dependent compositional variability and are both precisely determined and sufficiently distinct (Resentini et al., 2017). This is the case for SW Madagascar, where amphibole dominates the tHM suite of the Tsiribihina and Manambolo sands, in contrast to southern rivers where garnet is invariably abundant. Predominant Mangoky River contribution is thus indicated for samples characterized by higher garnet/amphibole ratios, more sillimanite, staurolite, apatite, zircon, and monazite. Sample S9, dated at 236 ka, in which xenotime was detected, appears to be almost entirely of Mangoky origin. Samples S4, S5, S10, S15, S16a, and S20 are

also mostly (75-90%) derived from the Mangoky River, whereas samples S8, S17, and S24 appear to be mainly (~60-70%) supplied by the Tsiribihina and Manambolo Rivers (Table 5.5). Similarly, our ^{10}Be denudation data from the same modern river sands, with integration times of the order of 10 ka, suggest significantly larger sediment fluxes for the Mangoky (weighted mean of 3.1 ± 0.9 Mt/a) than for the Tsiribihina and Onilahy Rivers, which have the same weighted mean outflow (1.5 ± 0.4 Mt/a).

Garzanti et al. (2022b) found εNd signatures of -18 and -24 from the 15-500 μm fraction of sands of the Tsiribihina and Mangoky Rivers, respectively, the two largest catchments in our study area. For the Tsiribihina River, our result for the finer grained fraction is comparable to that of Garzanti et al. (2022b), although the εNd values (-18.7 ± 0.3 and -16.2 ± 0.3) of the two fractions we analyzed (50-100 μm and 100-250 μm, respectively), differ significantly. In contrast, our results for the Mangoky River are much less negative, -19.1 ± 0.3 and -19.0 ± 0.3 for the two size fractions respectively, than the value of Garzanti et al. (2022b). Unlike for the Tsiribihina River, the two size fractions of the Mangoky River, agree within uncertainty, which is also true or nearly true for the other rivers we analyzed (Table 5.4). This apparent insensitivity of Nd isotopes to sediment grain size has been observed in sediments from most studied global rivers (Bayon et al., 2015). In the core samples, we found that in half of the cases where results for two size fractions are available, the εNd values of these fractions agree within uncertainty. However, for other samples (S2, S4, S5, S17, Table 5.4), the finer fraction is about 1 to 2 εNd units less negative (Figure 5.4C). As shown by Garçon et al. (2013), grain size sorting has little effect on the Nd isotopic composition of river sediments. Instead, the small differences in εNd existing between the size fractions of some of the marine core samples may indicate that they were derived from sources of different average lithological composition. The slightly higher εNd of the finer fractions may imply that they originate from sources containing a greater proportion of younger and/or more mafic material than the coarser fractions. To facilitate comparisons between the different samples, and considering that different minerals (such as monazite) may control the Nd budget, and that most are ultradense and consequently strongly concentrated in the finest tail of the size distribution (Garzanti et al., 2024) (Sup. Info. 5.4), we chose to base the remainder of this discussion on the 100-250 μm fraction only.

We consider that over the past 900 ka, changes in lithologies drained by the studied rivers can be viewed as negligible. This may not be true for source regions affected by glacial processes with a high amplitude glacial-interglacial cyclicity, as the weathering processes operating under these two regimes may differentially impact varying lithologies. However, this is unlikely to be a problem in our study area, which was never affected by glacial processes. Hence, we consider the εNd values of the studied rivers as end members in the provenance analysis of MOZ4-CS24 core turbidites. Figure 5.4B suggests that the turbidite sands were mainly derived from the Tsiribihina River, assuming that the εNd value of the 100-250 μm fraction is indeed representative of the sediments from this river. However, this interpretation is inconsistent with both modern ^{10}Be and heavy mineral assemblages which

collectively suggest that the sediments were mainly derived from the Mangoky catchment (Table 5.3Table 5.5).

Siliciclastic rocks exposed near the coast are expected to have a much less negative εNd signature than Mesoarchean to Neoproterozoic crystalline lithologies exposed on the central plateau. This is confirmed by the more radiogenic Nd isotope composition of sediments from the Morondava River, whose small basin is largely confined to the coastal plain. The εNd values of the MOZ4-CS24 turbidites may therefore reflect a dominant sediment contribution from the coastal region, dominated by detrital lithologies, rather than a North-South signature. However, it is unrealistic to assume that sediments would originate only from the lower sedimentary coastal areas. Although denudation rates are lower on the crustal high central plateaus (e.g., 7.5 ± 3.0 mm/ka, Brosens et al., 2023), this vast region represents over half of the drainage area considered in this study. Should sediments be derived almost exclusively from the coastal areas, the production rate of cosmogenic nuclides would be closer to that of the Morondava Basin (P_n = 3.5 at/g/a, P_{fm} = 0.04 at/g/a and P_{sm} = 0.01 at /g/a), implying a maximum increase in rates of 26% compared to the rates measured with production rates calculated over

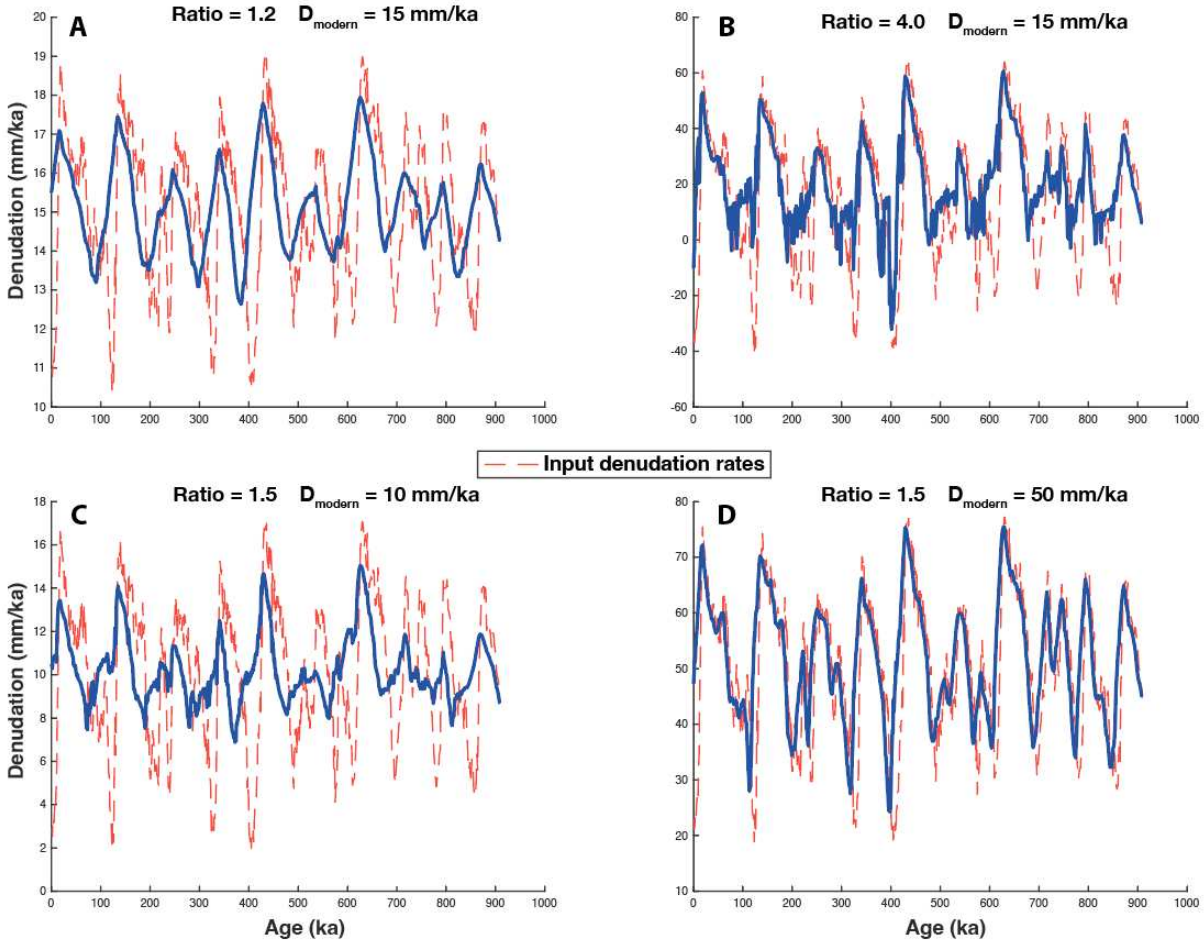

Figure 5.7: Sensitivity test of ^{10}Be-derived denudation rates to variations in "true" denudation rates. In each of the graphs, red dotted line represents D_{input} and the plain blue line D_{output}. For each graph, fixed amplitudes of variations and original modern value of denudation are given by the ratios D_{input}/D_{modern} and D_{modern}. Note that denudation rates are negative for graph B. This is an artefact of the model, because we fix the amplitude (1.5) for low denudation rates (15 mm/ka).

the entire quartz-rich area (P_n = 4.8 at/g/a, P_{fm} = 0.04 at/g/a, P_{sm} = 0.01 at/g/a). This potential bias in the calculated denudation rates remains within uncertainties of our data.

The causes of the observed discrepancy between provenance estimates derived from Nd isotope compositions and heavy minerals remain elusive. One possibility could be a mineralogical effect, although previous studies of Nd isotopes in river sediments suggest that this is unlikely (Garçon et al., 2013). Another possibility is that the river sediment samples we analyzed are not representative of the average Nd isotopic composition of the corresponding rivers. For the Mangoky Basin, the very large discrepancy between the εNd value we obtained (-19) and that of (Garzanti et al., 2022b) (-24) suggests that the Nd budget of this river's sediment load may be quite heterogeneous. Whatever the cause of this apparent contradiction, both provenance tracers show no correlation or covariation between their stratigraphic trends in the MOZ4-CS24 core and calculated denudation rates. Our data show neither major provenance changes nor steady trends in sediments delivered to the submarine Tsiribihina Canyon over the past 900 ka, and no systematic control of denudation or relationship with glacial/interglacial cycles.

5.5.5. Why are denudation rates not impacted by climate in Madagascar ?

Our previous data analysis and discussion indicate that (1) the *in-situ* ^{10}Be cosmogenic concentration measured in the MOZ4-CS24 core turbidites truly reflects paleo-denudation rate in SW Madagascar at the time of deposition, (2) that these rates were near-steady from 0 ka to ~400 ka and ~600 ka to ~900 ka and consequently, (3) that the MPT and the Middle to Late Pleistocene glacial cycles did not significantly affect the denudation processes in SW Madagascar. These results are in contradiction with other regions previously investigated. In Alaska for instance, a tectonic/erosion imbalance created by more extensive ice cover after the MPT is suggested (Gulick et al., 2015). In the Alps, the MPT would be responsible for valley over-deepening and a large part of the dramatic relief observed today (Valla et al., 2011). This latter finding is supported by cosmogenic nuclide dating of cave sediments in the Aare Valley, showing a tenfold increase in incision rates at the MPT (Haeuselmann et al., 2007). In mid-latitude, mid-elevation regions, affected only by periglacial and not glacial processes, the MPT has also been shown to have influenced denudation rates (Del Vecchio et al., 2022). Our results show that in low latitude regions unaffected by glacial or periglacial processes, denudation rates did not change after the MPT. The effect of the MPT on denudation rates would thus be strongly related to glacial processes and glacial topography at mid to high latitudes, and would not have had the global effect suggested by Peter Molnar (2004). However, this important result could be challenged by the lack in our dataset, of denudation rates clearly predating the MPT transition (>1.2 Ma).

An important question to address is whether the resolution of the cosmogenic nuclide data can capture the climatic forcing. If the integration time associated with ^{10}Be derived denudation rates is too long, the ^{10}Be-derived denudation rates could average over several climatic cycles, thus smoothing the climate-driven variability. We used the approach of Schaller and Ehlers, (2006) to test this smoothing

effect by calculating apparent ^{10}Be denudation rates versus time, and using as input "hypothetical" denudation rates whose fluctuations vary in perfect synchrony with the climate variability. We use the ∂^{18}O data of the LR04 stack as a climatic proxy to construct this synthetic denudation curve D_{input}, considering different amplitudes around the mean (1.2 and 2) and different mean denudation rates (5, 15 and 30 mm/ka) (Figure 5.7). The integration times of ^{10}Be, which are inversely related to D_{input}, are used to calculate the apparent denudation, D_{output}, that is recorded by this cosmogenic nuclide (Figure 5.7, D_{input} in red, D_{output} in blue). This modeling shows that for denudation rates of 15 mm/ka, which is the weighted mean of the modern rivers of SW Madagascar (Table 5.3), ^{10}Be is able to accurately record the main trend in these variations, although minima and maxima are smoothed, this effect being more pronounced when the amplitude of the signal is larger (Figure 5.7C, D). It is also worth noting that the effect of this smoothing is significantly enhanced for denudation rates close to 5 mm/ka, with the minimum excursion becoming almost invisible. On the contrary, higher rates of 30 mm/ka reproduce the amplitude of the initial forcing much better (Figure 5.7E, F). In all cases we also observe a temporal delay of the maximum and minimum peaks, which can reach several thousand years (Figure 5.7). This reasoning implies that, given the range of modern denudation rates we measure (~15 mm/ka), the ^{10}Be proxy is capable of capturing climate-related cyclicity in denudation rates with variations as small as 1.2 times the modern values. This reinforces the strength of our main conclusion: the climatic cyclicity did significantly influence denudation in SW Madagascar over the past 900 ka. If this forcing existed, it was probably characterized by a variability of less than 20% around the denudation mean.

Such a limited effect of climate cyclicity on denudation rates in Madagascar may be explained by the lower amplitudes of temperature and precipitation changes that characterize subtropical regions of the Southern Hemisphere (Chevalier et al., 2021). Although glacial periods are generally considered to be drier than interglacial periods (e.g., Litt et al., 2014; Scheff et al., 2017), this was not necessarily the case for subtropical Africa (McGee, 2020). However, it was proposed that the 100 ka cyclicity associated with glacial/interglacial periods would have affected southern subtropical Africa (Castañeda et al., 2016; Dupont et al., 2011; Johnson et al., 2016), although this effect is not evident in our paleo-denudation rate record.

In tropical regions, monsoonal processes drive spatial and seasonal variations in precipitation and temperature, and are thus the primary driver of sediment production and transport (e.g., Andermann et al., 2012; Lupker et al., 2012; Marc et al., 2019), an effect that must have been important in the past. For instance, variations in erosion and sediment transport to the Indus fan, driven by changing monsoon intensities have been documented on millennial to multimillennial timescales (Clift and Jonell, 2021). Modeling of the African monsoon has shown that precession (i.e. 20 ka cyclicity) and obliquity (i.e., 40 ka cyclicity) control over its temporal variability (Tuenter et al., 2003). Overall, variations in monsoon intensity are often proposed to be in phase with precessional cyclicity (Kutzbach et al., 2008). This shorter-frequency forcing on the SE African climate was also outlined by the study of different proxies (Caley et al., 2018; Daniau et al., 2023).

In Madagascar, a stable isotope study of speleothems over the past 150 ka (Voarintsoa et al., 2017) suggested that the ITCZ, which partly drives the monsoons (Gadgil, 2018), shifted southward several times during the Holocene, causing an alternation of wet and dry climates. Migrations of the ITCZ in the southern tropics are complex and not well understood (Burns et al., 2022). Because SW Madagascar is semi-arid (Fig. 1A), a southward shift of the ITCZ, and thus monsoon intensity, may have affected precipitation patterns in this region. These shifts may have modulated the denudation rates of the island, and similar shifts have likely occurred in the past, although there are no data to support such a scenario. However, due to the short time scale (10^3 a) of such shifts (Voarintsoa et al., 2017), it is possible that they were buffered by the sedimentary system before reaching the deep sea (Castelltort and Van Den Driessche, 2003). Furthermore, these shorter timescale climatic variations (23 and 41 ka periods) would be difficult to observe in cosmogenic-derived denudation rates, which have an order of magnitude higher integration durations (10^4 a).

5.6. Conclusion and perspectives

This study sheds new light on the evolution of denudation rates in the subtropics from modern times to the Mid Pleistocene. We find paleo-denudation rates ranging from 17.4 ± 5.8 mm/ka to 73.9 ± 29.4 mm/ka. These compare well with modern denudation rates of SW Madagascar ranging from 11.2 ± 2.3 mm/ka to 30.4 ± 6.5 mm/ka. No systematic change in denudation rates was observed in SW Madagascar over the past 900 ka, in relation neither with the MPT nor glacial/interglacial cycles. Our study suggests that this interpretation does not reflect a lack of resolution, either in terms of denudation rates or of sample age. However, the resolution of the applied method would be insufficient to capture higher-frequency climatic changes controlled by changes in monsoon intensity associated with shifts in the ITCZ, a mechanism that most certainly drove Madagascar's past climate. Understanding the control of monsoon on denudation is limited not only by these methodological issues, but also by the lack of paleoclimatic data for subtropical regions documenting the past evolution of the monsoon. Such a gap in the global data is of concern and future paleoclimatic reconstructions should focus on the tropics and the Southern Hemisphere to better understand planetary climate systems. Although the effect of weathering on our data should be small, it is difficult to constrain and additional work such as regolith profiles and immobile element measurements are needed to fully understand its effect.

Finally, we emphasize that measuring denudation rates from turbidites represents a huge potential source of information especially for turbidites deposited near major rivers, opening the door to global compilations of paleo-denudation rates. Turbidites may contain significant reworking from slope destabilization and seafloor erosion, and the selection of well-resolved, river-connected canyons may help avoiding some of the inherent uncertainties. In any case, more quantitative data are needed to better constrain the duration of storage on the continental shelf and hence the duration of submarine transport.

Acknowledgements

This study received input from detailed analysis realised in the framework of the PAMELA project led by IFREMER and TotalEnergies in collaboration with IFP Energies nouvelles, Université de Bretagne Occidentale, Université de Rennes 1, Sorbonne Université and CNRS. We thank the captain and crew of the PAMELA-MOZ4 cruise aboard R/V Pourquoi pas? and the technical staff of IFREMER for their help in data acquisition. We particularly thank Léa Faubert for the contribution on the study of the MOZ4-CS24 core during her undergraduate degree. We thank Laëtitia Leanni and Régis Braucher for the help provided during sample treatment in CEREGE. Sample analytical procedures (^{10}Be, Nd, elemental compositions) were financed by the ANR funded PANTERA project (AAPG2021, PI: Julien Charreau).

We thank Amy East and Chris Mark for editorial handling, and Dr. Yanyan Wang and an anonymous reviewer for their comments and suggestions which helped improve the structure, readability and overall quality of this manuscript significantly.

This is contribution number 2869 of CRPG.

Availability Statement

All data presented in this paper is available at (Large, 2024) as an excel document. Every sheet corresponds to a table present either in the main text, or in the supplementary material of this article. This data is under a CC BY 4.0 License. If used, copied, or modified, appropriate credit must be given. The numerical dataset and processed multibeam bathymetry collected during the oceanographic cruises PAMELA-MOZ4 (Jouet and Deville, 2015, doi:10.18142/236) are stored at SISMER data repository (http://en.data.ifremer.fr/). Sediment core collected offshore Madagascar are curated at CREAM, the IFREMER core repository in Plouzané (France). Core data related to this article can be requested at: MOZ4-CS24 http://igsn.org/bfbgx-128009 . Access to these data is however restricted and must be accepted by the partners of the PAMELA project.

Supplementary Information

Age model of the MOZ4-CS24 core

MIS 5, 6, 9 and 10 where easily identifiable by correlation of the benthic $\partial^{18}O$ record of core MOZ4-CS24 and the LR04 benthic stack. Correlations were fixed to glacial and interglacial transitions using the *Analyseries* software (Paillard et al., 1996). Nannofossil-based biostratigraphic analyses confirmed the $\partial^{18}O$-based age model from MIS1 to 10 and constrained the age model for the bottom half of the core by introducing a hiatus from Mis 11 to MIS 15. MIS 9 to MIS 11 were validated from samples 4 and 5 (Fig. 3C), by the presence of a *Gephyrocapsa caribbeanica* acme zone and the absence of *Pseudoemiliania lacunosa.* The presence in sample 6 of *P. lacunosa*, together with a mixed dominance of *G. carribeanica* and small *Gephyrocapsa*, as well as the absence *Reticulofenestra asanoi* and *Helicosphaera sellii*, allows to constrain the stratigraphic range of the hiatus. Stratigraphy was done after (Di Stefano et al., 2023; Giraudeau et al., 1998)

Sample	Depth (cm)	Observations	Period
1	548	Small *Gephyrocapsa*; presence of *E. huxleyi*	MIS 6 - 8
2	768		
3	970	Transition from small *Gephyrocapsa* / *G. carribbeanica*; absence of *E. huxleyi* and *P. lacunosa*	Transition MIS 8/9
4	1045	Acme *Gephyrocapsa carribbeanica*; absence of *P. lacunosa*	MIS 9 - 11
5	1185		
6	1470	Transition from acme *G. carribbeanica* / *small Gephyrocapsa*; presence of *P. lacunosa*; absence of *R. asanoi* and *H. sellii*. Reworked	MIS15 - 16
7	1548	Acme Small *Gephyrocapsa*; presence of *P. lacunosa*; absence of *R. asanoi* and *H. sellii*. Less reworked than above	MIS 15 - 23
8	1637		
9	1900	Acme Small Gephyrocapsa; presence of P. lacunosa; absence of R. asanoi and H. sellii	MIS 15 - 23
10	2135		
11	2495		

Sup. Info. 5.1: Calcareous nannofossil stratigraphy (after Di Stefano et al., 2023: Giraudeau et al., 1998). Location of samples on the core are given in figure 3C.

Sup. Info. 5.2 : Benthic $\partial^{18}O$ values (‰ VPDB) of core MOZ4-CS24 and associated position on the core and age.

Top (cm)	65	85	95	105	125	145	165	185	205	225	245	265	290	305	323	345	365	385	405	425	445	465	488
∂18O (‰ VPDB)	3.444	4.097	4.588	4.509	4.437	4.291	4.07	3.845	3.949	3.859	4.035	4.064	4.083	3.738	3.327	3.432	3.238	2.72	3.086	4.382	4.395	4.332	4.27
Age (ka)	11.6	15.8	18.0	20.1	24.4	28.6	34.2	40.1	46.1	52.1	57.8	62.5	68.4	73.5	83.4	95.4	106.3	117.2	128.2	134.3	138.8	143.3	148.5

Top (cm)	508	528	548	565	585	605	625	645	665	685	706	726	746	768	785	805	826	845	865	887	907	927	946
∂18O (‰ VPDB)	3.991	4.234	3.979	4.127	4.159	3.912	3.945	3.991	3.933	3.511	3.154	3.215	3.879	3.831	3.622	3.52	4.162	3.632	4.036	3.223	3.554	4.542	4.417
Age (ka)	153.0	157.5	162.0	165.9	170.4	174.9	179.4	183.9	188.4	192.9	197.6	202.1	206.6	211.6	215.4	219.9	224.6	228.9	233.4	238.3	242.8	252.8	263.3

Top (cm)	966	980	1005	1025	1045	1066	1085	1105	1124	1145	1185	1224	1264	1285	1304	1325	1345	1364	1385	1405	1449	1470	1505
∂18O (‰ VPDB)	4.04	4.089	3.905	3.51	2.728	3.765	4.603	4.528	4.584	4.367	4.372	4.177	4.111	4.252	4.148	4.21	3.978	3.257	3.185	3.587	3.746	3.019	3.595
Age (ka)	274.3	282.0	295.7	308.1	321.3	335.1	339.2	342.1	344.8	347.8	353.5	359.1	364.9	367.9	370.6	373.6	383.3	395.2	408.3	420.8	599.3	605.3	614.5

Top (cm)	1520	1535	1564	1584	1605	1625	1637	1650	1665	1685	1725	1745	1765	1785	1824	1868	1886	1907	1926	1949	1972	1992	2012
∂18O (‰ VPDB)	3.565	4.243	4.715	4.311	4.044	3.245	3.666	3.594	4.053	4.073	3.294	3.119	3.471	4.127	4.042	4.254	4.531	4.245	4.241	4.144	4.302	4.192	4.009
Age (ka)	618.4	624.9	646.2	660.9	676.3	690.8	699.4	708.78	723.4	745.4	771.4	779.4	787.4	790.7	793.8	797.3	798.8	800.4	802.0	803.8	805.6	807.2	808.9

Top (cm)	2032	2049	2070	2090	2110	2135	2148	2170	2190	2210	2230	2250	2278	2297	2311	2336	2368	2385	2400	2415	2431	2450	2465
∂18O (‰ VPDB)	3.8	3.76	3.799	2.8	3.519	3.282	3.45	3.4	3.097	3.08	2.933	3.683	4.136	4.262	4.683	4.422	4.283	4.283	4.094	4.46	4.339	4.142	4.125
Age (ka)	810.5	811.8	813.5	818.3	824.2	831.6	835.5	842.0	847.9	853.8	859.7	865.7	868.8	870.8	872.3	874.9	878.3	880.1	881.7	883.3	885.0	887.0	888.6

Top (cm)	2479	2498	2521	2535	2551	2575	2590	2605	2620
∂18O (‰ VPDB)	3.777	3.957	4.307	4.14	4.017	4.214	3.414	4.055	3.767
Age (ka)	890.1	892.1	894.6	896.1	897.8	900.3	901.9	903.5	905.1

Sup. Info. 5.3: Correlation pointers : benthic $\partial^{18}O$ from MOZ4-CS24 aligned to LR04.

MOZ4-CS24 depth (cm)	MOZ4-CS24 age LR04 (ky)
75.4	13.8
150.1	29.7
241.5	57
299.9	70.8
410.1	131
678	191.3
910	243.5
1012.1	299.7
1068.7	336.9
1330.9	374.4
1405.3	421
1449.1	599.7
1529.8	621
1606.3	677.3
1654.9	712.3
1699.1	761
1770	789.5
2075.3	813.9
2250.7	865.9
2580.9	900.9

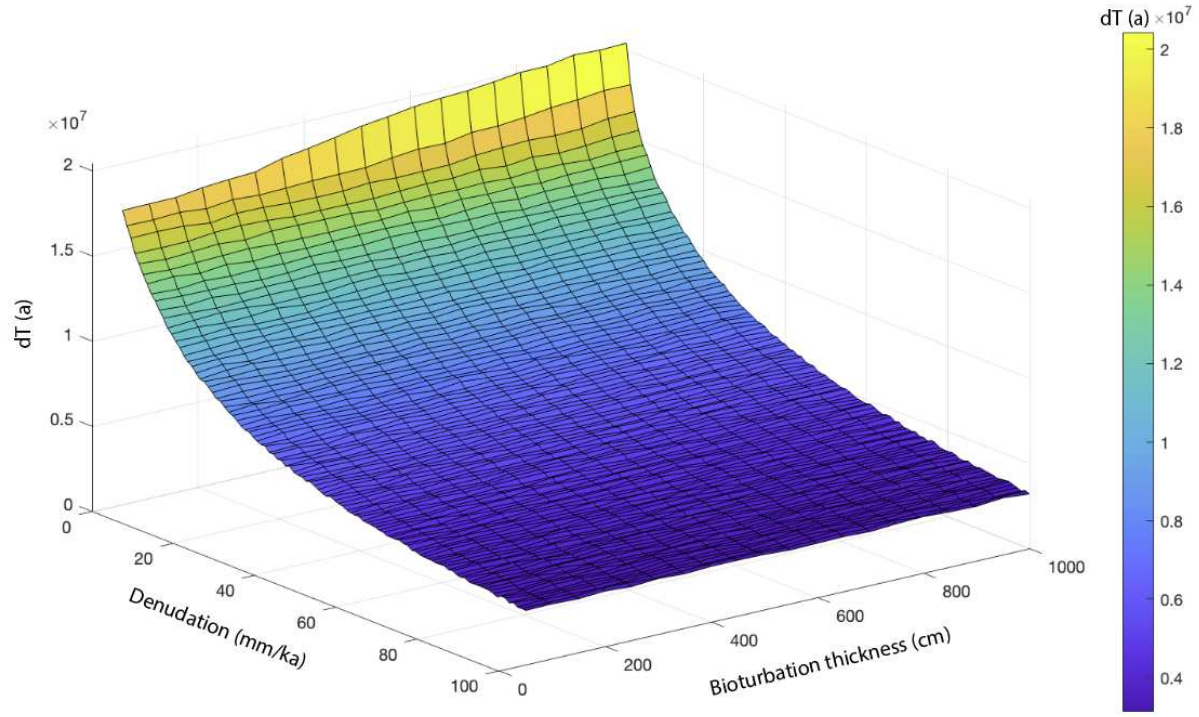

Sup. Info. 5.4: Time differences (dT) to reach steady state in conditions with and without bioturbation depending on denudation (mm/ka) and bioturbation thickness (cm). See text for further details

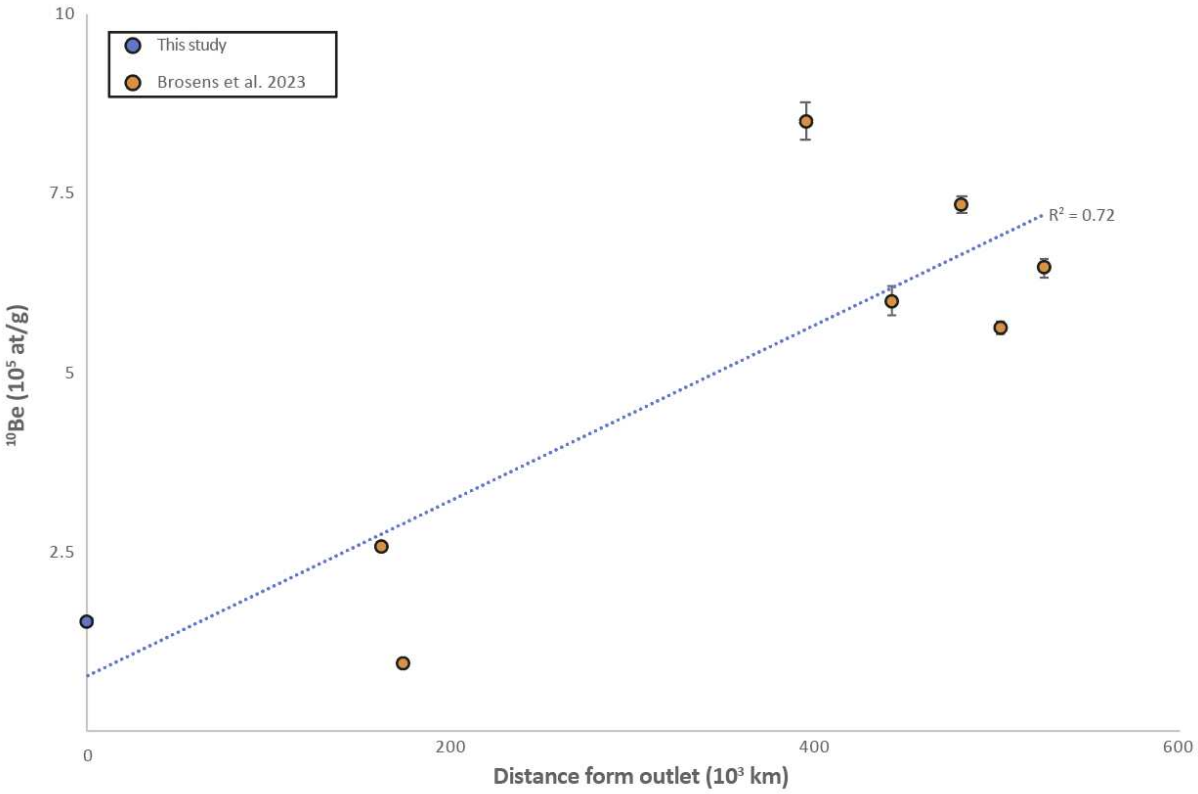

Sup. Info. 5.5: ^{10}Be oncentration of the Mangoky river Madagascar as a function of distance from the downstream most sampling point. Blue point is from this study (Table 3). The 100-700 µm was used. Orange points correspond to data from Brosens et al., 2023. The data points are, from downstream to upstream : 2011-11; 2011-12; 2011-08; MDG-1199B1; 2011-07; 2011-26; 2011-25.

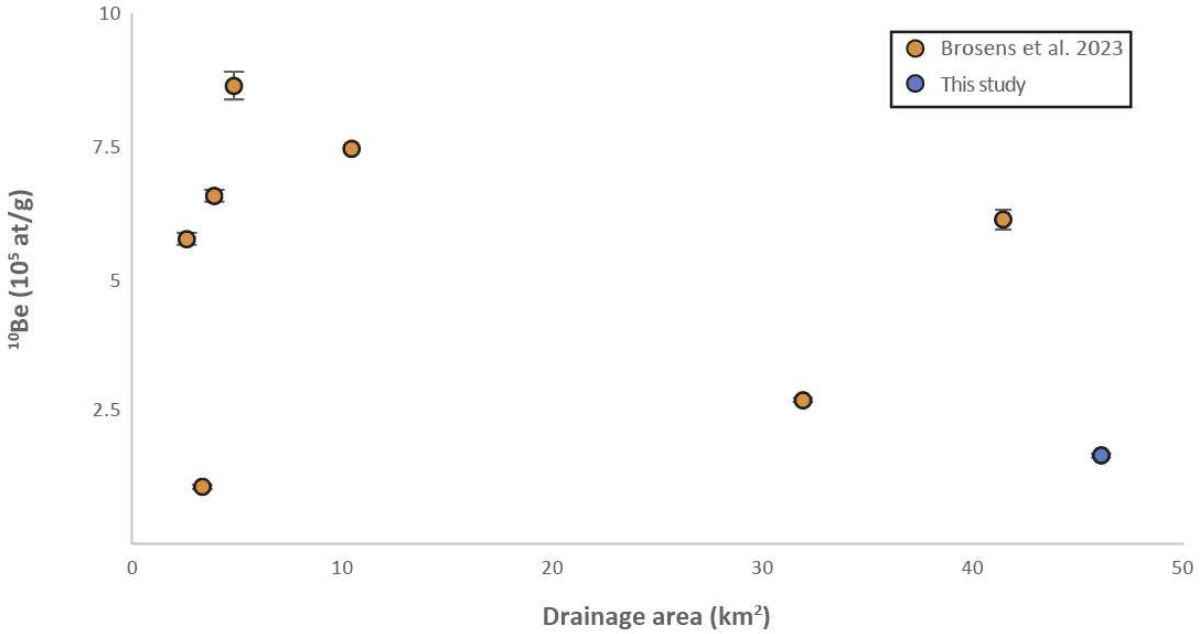

Sup. Info. 5.6: ^{10}Be concentrations as a function of drainage area. The data points are the same as in Sup. Info. 5.5.

Sup. Info. 5.7: Major and Trace elements of Malagasy rivers measured by the SARM (https://sarm.cnrs.fr/index.html/)

River	Granulometry	As	Ba	Be	Bi	Cd	Co	Cr	Cs	Cu	Ga	Ge	Hf	In	Mo	Nb	Ni	Pb	Rb	Sb	Sc	Sn	Sr
	µm	µg/g	µg/g	µg/g	µg/g	µg/g	µg/g	µg/g	µg/g	µg/g	µg/g	µg/g	µg/g	µg/g	µg/g	µg/g	µg/g	µg/g	µg/g	µg/g	µg/g	µg/g	µg/g
Tsiribihina	100-250	< L.D.	883	0.62	< L.D.	0.05	0.25	2.83	0.57	< L.D.	6.84	0.71	7.8	< L.D.	< L.D.	0.48	< L.D.	13.99	63.7	< L.D.	< L.D.	< L.D.	260
Manambolo	50-100	< L.D.	1619	0.97	< L.D.	0.58	0.29	3.54	0.65	< L.D.	11.23	0.79	108.1	< L.D.	< L.D.	1.36	< L.D.	23.55	107.5	0.17	< L.D.	< L.D.	362
Manambolo	100-250	< L.D.	1260	0.67	< L.D.	0.21	0.25	2.54	0.42	< L.D.	8.05	0.71	32.3	< L.D.	< L.D.	1.11	< L.D.	18.73	81.3	0.20	< L.D.	< L.D.	276
Morondava	50-100	< L.D.	911	0.56	< L.D.	0.51	0.56	10.35	0.58	< L.D.	6.46	0.61	122.0	< L.D.	< L.D.	4.71	< L.D.	15.65	69.1	0.20	1.32	< L.D.	191
Morondava	100-250	< L.D.	771	0.28	< L.D.	< L.D.	0.20	4.39	0.44	< L.D.	4.27	0.58	5.4	< L.D.	< L.D.	0.57	< L.D.	12.32	57.5	0.18	< L.D.	< L.D.	132
Mangoky	50-100	< L.D.	1162	1.16	< L.D.	1.08	0.35	9.72	0.94	< L.D.	11.04	0.85	213.8	< L.D.	< L.D.	7.63	< L.D.	24.67	118.2	0.19	2.18	0.63	292
Mangoky	100-250	< L.D.	833	0.57	< L.D.	0.12	0.26	5.54	0.84	4.24	6.87	0.70	24.5	< L.D.	< L.D.	2.27	< L.D.	18.32	97.9	0.19	< L.D.	< L.D.	189
Onilahy	100-250	< L.D.	533	0.47	< L.D.	0.12	0.24	4.84	0.33	< L.D.	5.67	0.71	18.6	< L.D.	< L.D.	1.72	< L.D.	10.62	45.7	0.17	< L.D.	< L.D.	181

River	Granulometry	Ta	Th	U	V	W	Y	Zn	Zr	La	Ce	Pr	Nd	Sm	Eu	Gd	Tb	Dy	Ho	Er	Tm	Yb	Lu
	µm	µg/g	µg/g	µg/g	µg/g	µg/g	µg/g	µg/g	µg/g	µg/g	µg/g	µg/g	µg/g	µg/g	µg/g	µg/g	µg/g	µg/g	µg/g	µg/g	µg/g	µg/g	µg/g
Tsiribihina	100-250	0.14	1.30	0.62	< L.D.	< L.D.	2.59	< L.D.	342	3.76	6.07	0.77	2.75	0.49	0.31	0.42	0.06	0.42	0.10	0.31	0.06	0.46	0.08
Manambolo	50-100	0.14	2.64	3.18	3.19	< L.D.	13.91	< L.D.	4729	2.90	4.71	0.60	2.19	0.53	0.35	0.70	0.17	1.56	0.50	2.02	0.42	4.03	0.72
Manambolo	100-250	0.13	1.33	0.94	2.47	< L.D.	4.82	< L.D.	1436	3.12	5.22	0.62	2.16	0.44	0.30	0.39	0.07	0.61	0.17	0.63	0.13	1.19	0.20
Morondava	50-100	0.46	2.57	4.48	8.49	< L.D.	20.97	< L.D.	5431	3.52	6.31	0.77	2.95	0.82	0.52	1.12	0.28	2.44	0.72	2.68	0.53	4.85	0.79
Morondava	100-250	0.05	0.67	0.37	1.94	< L.D.	2.00	< L.D.	207	3.56	5.75	0.72	2.70	0.48	0.32	0.36	0.05	0.34	0.07	0.23	0.04	0.29	0.05
Mangoky	50-100	0.74	7.81	9.76	12.32	< L.D.	29.58	< L.D.	8863	7.60	12.96	1.49	5.36	1.33	0.87	1.66	0.38	3.51	1.04	3.93	0.80	7.45	1.27
Mangoky	100-250	0.22	1.48	1.38	4.25	< L.D.	4.89	< L.D.	1033	6.09	9.36	1.09	3.86	0.71	0.56	0.59	0.10	0.72	0.18	0.60	0.12	0.99	0.16
Onilahy	100-250	0.16	1.41	0.91	5.20	< L.D.	3.89	< L.D.	785	5.69	8.44	0.91	3.16	0.54	0.51	0.45	0.08	0.56	0.14	0.48	0.09	0.75	0.12

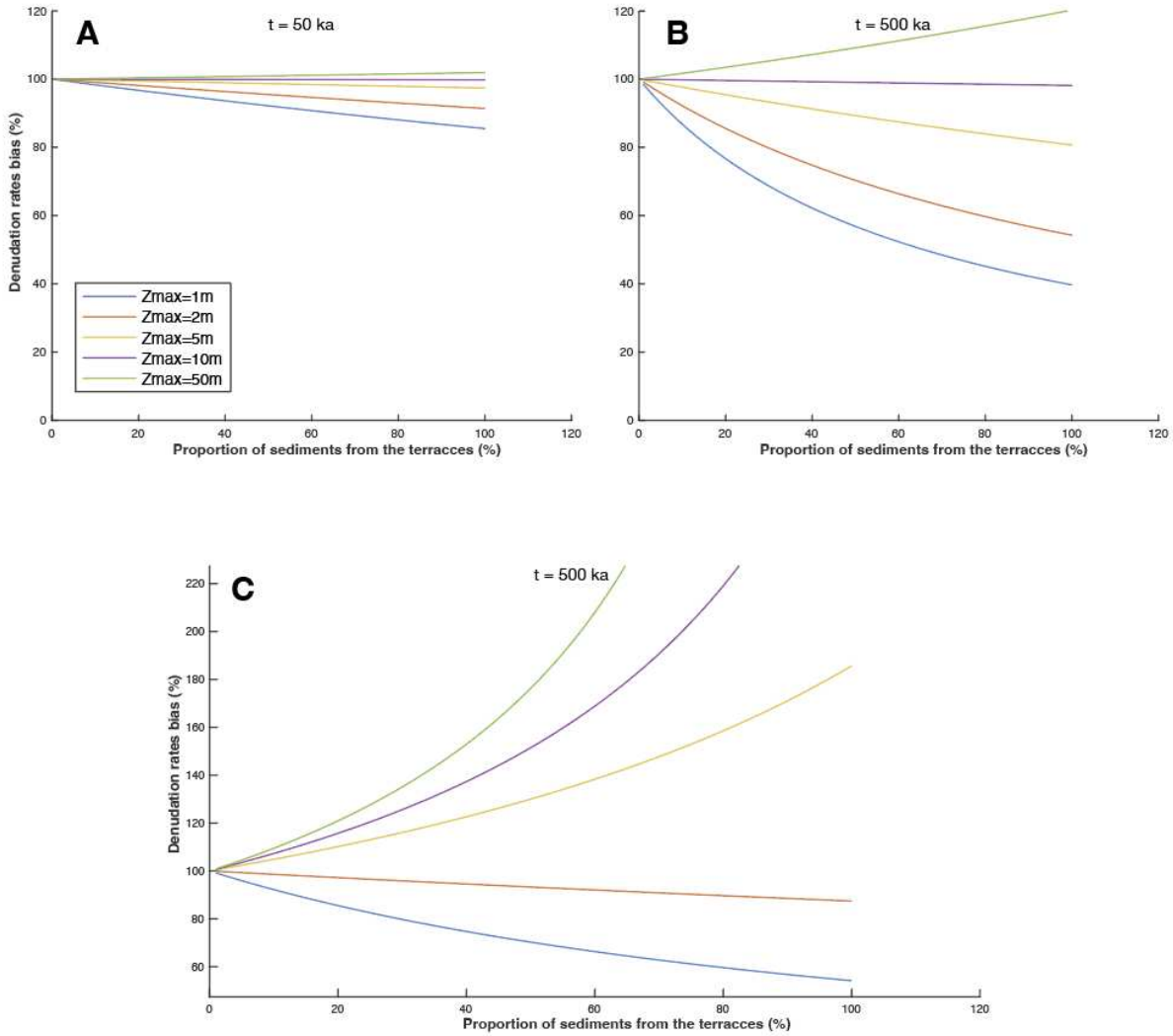

Sup. Info. 5.8: Tests of denudation rate bias by the addition of stored material within the river with depleted ^{10}Be concentrations. For all graphs, the true denudation rate is fixed at 6 mm/ka. For each graph, the different colors of the lines represent different thicknesses of the terraces. A/ Bias in the case of addition of different percentages of sediment stored in a terrace of different thicknesses for 50 ka. B/ Same as in A/ but with a storage within the terrace of 500 ka. C/ Addition of sediments to the sample from a terrace with an itintial concentration of 5 x 10^4 at/g (i.e., stronger denudation rates), stored for 500 ka.

Chapter 6. Landscape steady state in an anorogenic tropical region?

Authors

Etienne Large[1], Alexis Derycke[1], Julien Charreau[1], Pierre-Henri Blard[1], Alfred Andriamamonjy[2], Amos Fety Michel Rakotondrazafy[2]

[1]CNRS/Université de Lorraine, UMR 7358 CRPG, 54500 Vandoeuvre-lès-Nancy, France

[2]Université d'Antananarivo/Département des Sciences de La Terre, 101 Antananarivo, Madagascar

Abstract

It has been hypothesized that the global cooling of the Earth's climate during the Cenozoic, along with the initiation of the Quaternary glacial/interglacial climate, has provoked extensive landscape disequilibrium, leading to a global increase in denudation rates. For this hypothesis to be validated, all regions must have had experienced disequilibrium-associated high denudation rates, but most studies working on testing this hypothesis were done in mid-to-high latitudes, mostly in orogenic regions, and tropical anorogenic regions remain largely understudied. The objective of this work is to question the steadiness of the landscape in an anorogenic and tropical region. To this aim we bring constrains on long-term denudation rates of Madagascar, an anorogenic (epeirogenic) tropical island, and compare these denudation rates to the Late Mesozoic to Cenozoic uplift of this island. We present 9 new ^{10}Be denudation rates to complete an existing dataset of 104 samples allowing a good general view of the spatial distribution of recent (10-100ka) denudation rates. We also derive long-term (10-100Ma) denudation rates from 270 previously published Apatite Fission Track and Helium on Apatite time-temperature inversion models that have mapped the thermochronological history of the island. Finally, we compare these results to uplift data that exist for the Meso-Cenozoic in Madagascar. We conclude that the island appears to be in a sub-steady state, with denudation/uplift ratios comprised between 0.3 ± 0.1 and 1.6 ± 0.4 with a mean of 1 ± 0.2. A Neogene increase of both uplift and denudation rates is consistent with this conclusion. Before Neogene, rates of uplift and denudation remain low and overall constant since at least the Cretaceous.

6.1. Introduction

The effect of Cenozoic cooling on continental erosion has been a long lasting research subject in the past 20 years (Herman et al., 2013; Willenbring and Jerolmack, 2016; Willenbring and von Blanckenburg, 2010) following the pioneering work of Zhang et al. (2001) and Molnar (2004). The latter qualitatively hypothesized that high frequency oscillations in climate (during the Quaternary) denied the landscape the chance to reach equilibrium leading to increasing erosion with increased amplitude of the forcing. Godard et al. (2013) indeed showed with a landscape evolution model that an oscillating climatic forcing could lead to a peak in erosion rates and that the frequency of the changes associated to this peak, or even its existence, was in a large part controlled by erodibility and diffusion coefficient. However, if the late Cenozoic increase in denudation is global, then all landscapes must have had difficulty to adapt and reach a steady-state, especially since the cyclic change in climatic settings is itself considered global (Zachos et al., 2001). Geomorphic evidence for landscape disequilibrium during the Quaternary have been observed in many regions (Beeson et al., 2017; Jagoe et al., 2021; Kim et al., 2016; Moumeni et al., 2024; Yaaqoub and Essaifi, 2023). However, most of these observations have been made in orogenic settings, and the state of equilibrium of the landscape in anorogenic and unglaciated regions of the tropics, a cornerstone of Molnar's hypothesis to support a global acceleration of denudation, has been poorly investigated.

In this work, we reconstruct Meso-Cenozoic variations in denudation rates of Madagascar (Figure 6.1A), an ancient, tectonically quiescent shield (Mesoarchean to Neoproterozoic, Boger et al., 2019) located in the tropics, between 12°S and 25°S and unglaciated during the Cenozoic. A both spatially and temporally widespread set of data already exists, allowing a reconstruction of denudation rates, either via exhumation rates calculated using Low Temperature Thermochronological (LTT) data (Emmel et al., 2012, 2008, 2006b, 2006a, 2004; Giese et al., 2012; Jöns et al., 2009; Schreurs et al., 2010; Seward et al., 2004; Stephenson et al., 2021), or by measuring in situ ^{10}Be cosmogenic nuclides in river sediments (Brosens et al., 2023; Cox et al., 2009; Wang et al., 2021).

To complete the existing ^{10}Be dataset, we collected and analyzed for *in-situ* cosmogenic ^{10}Be, 9 new modern river sands of SW Madagascar, an area lacking detailed data. Short term (10^3-10^4 a) ^{10}Be basin-averaged denudation rates were then calculated over the drainage area based on these new concentrations and the 104 previously published ^{10}Be values, using the same procedure and parametrization to homogenize the different dataset.

For longer time scales (10^6-10^7 a), denudation rates were estimated from the previously published LTT data. Rigorously, LTT data allows measuring exhumation, and not denudation, but we consider these two terms to correspond to a single process acting in two opposite directions.

For the sake of clarity and simplicity, ^{10}Be-derived basin averaged denudation rates will be named ^{10}Be-denudation while denudation rates inverted from LTT data will be called LTT-denudation. ^{10}Be-denudation rates represent basin averaged values while LLT-denudation are calculated locally. Also,

because the LTT-denudation rates are long term values integrated over several Ma, whereas the ^{10}Be-denudation rates are short-term values integrated over 10 ka to 100 ka (depending on the integration time, Sup. Info. 6.2), denudation rates will be expressed in m/Ma and in mm/ka, respectively, so the different rates can be easily compared (i.e., 10m/Ma = 10mm/ka).

The state of equilibrium of the island is tested by comparing both short-term ^{10}Be-denudation, and long-term LLT-denudation rates data to uplift rates derived from planation surface mapping and modelling (Delaunay, 2018; Jiao et al., 2022), river profile inversion (Roberts et al., 2012) or marine terrace mapping (Stephenson et al., 2019).

In a future version of this work, we will revise and use a uniformed inversion model on the existing thermochronological dataset to reconstruct a unified spatial distribution of long-term (>10^6 a) denudation across the island.

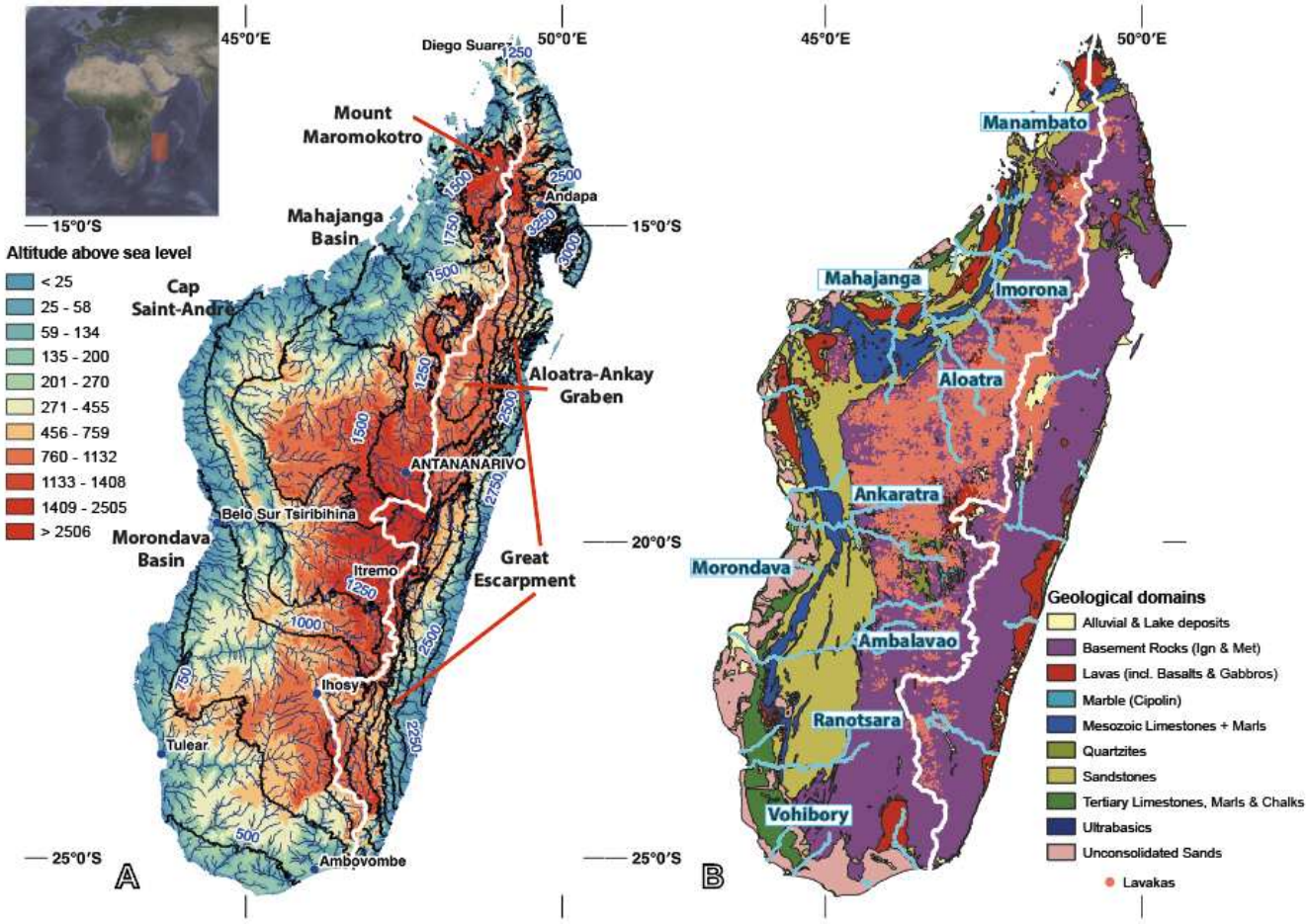

Figure 6.1: Topography and geology of Madagascar. In both maps, the white line gives the E/W water divide of Madagascar. A/ Topography of Madagascar. Altitudes are given by the legend to the left. Top left inset gives global location of the island. City names are given in black. Important geographical areas are also given. Black lines represent 250 mm/a isohyets. B/ Simplified geological map of Madagascar adapted from Roig et al. (2012). Important areas are named in blue. Major rivers are in blue. Lavakas are shown by orange dots.

6.2. Geodynamic history and geological setting of Madagascar

Until the Early Jurassic initiation of the Karoo rifting phase, Madagascar was part of Gondwana (Reeves, 2000; Seton et al., 2012; Storey et al., 2001). The full separation between Africa and Madagascar/India/Antarctica is believed to have initiated in Early to Mid-Jurassic. During Jurassic and Early Cretaceous, Madagascar, still attached to India and Antarctica, migrated southwards relatively to Africa along a right-lateral fracture zone that would correspond to the present-day Davie ridge (Reeves, 2014), reaching latitudes as high as 50°S (Bunce and Molnar, 1977; Seton et al., 2012), until Antarctica detached from the Madagascar/India block in Early Cretaceous. Between India and Madagascar, a low-rate left-lateral strike-slip motion initiated in the Turonian (Thompson et al., 2019), probably initiated after the inversion of the Davie ridge (Delaunay, 2018; Reeves, 2014). The emplacement of the Madagascar Large Igneous Province (LIP) (Bardintzeff et al., 2010; Storey et al., 1995) finally led to complete opening of the Mascarene basin and separation of India and Madagascar (Delaunay, 2018; Seton et al., 2012). Madagascar is supposed to be in its present position since that time (i.e., ~88 Ma, Delaunay 2018)

In the Oligocene, a second phase of volcanism initiated (Delaunay, 2018), with a northern province believed to be related to the Comoros hotspot (Emerick and Duncan, 1982), consistent with Late Neogene propagation of the East African Rift System (EARS), (Stamps et al., 2021). This is confirmed by recently published K-Ar ages which state in favor of a global geodynamic context, rather than a regional hotspot history for the Comoros islands (Rougeau et al., 2025). This is also confirmed by chemical consistency between the Comoros and Northern Madagascar volcanism (Rusquet et al., 2025), indicating that the Comoros islands do in fact link Madagascar to the EARS volcanism (Thinon et al., 2023). This context is associated to extensional dynamics on the high plateaus (Aloatra-Ankay Graben, Figure 6.1A, e.g., Kusky et al., 2010) and to a contemporaneous central volcanic province (Cucciniello et al., 2024). Several phases of doming and tilting are also recorded on the island during the Cenozoic, and associated to mantle dynamics (Delaunay, 2018; Roberts et al., 2012; Stephenson et al., 2021).

The seismo-tectonic context of Madagascar shows low seismicity (≤ 5.3M) and focal mechanisms showing mostly normal faulting, associated to sub-volcanic activity in the central part of the island and uplift related extensional dynamics of the higher plateaus (Rakotondraibe et al., 2020).

This geodynamic history of Madagascar led to two main geological regions (Figure 6.1B). In the western part of the island, sedimentary lithologies are found in the Morondava and Mahajanga basins, containing up to 10-km-thick successions of continental siliciclastic sediments and shallow-marine carbonate shelf deposits (Andriampenomanana et al., 2017) of Carboniferous to Neogene age (Besairie, 1972; Delaunay, 2018). In central and eastern Madagascar, mostly metamorphic Mesoarchean to Neoproterozoic crystalline basement (Boger et al., 2019) includes granitoides, schists, mafic gneisses (Tucker et al., 2014), high-grade metasediments, (Archibald et al., 2015), amphibolites and dolomitic marbles (Cox et

al., 1998; Tucker et al., 2011), and is intruded by Neoarchean granites (Paquette et al., 2003; Tucker et al., 2011).

6.3. ^{10}Be denudation rates

6.3.1. Material and methods

Both central and eastern parts of Madagascar have been intensively sampled for *in-situ* ^{10}Be analyses with a total of 99 studied basins ((Brosens et al., 2023; Cox et al., 2009; Wang et al., 2021). In SW Madagascar only 5 large catchment areas were studied by Large et al., (2025) (Chapter 5). To complement this dataset and provide more detail in the SW part of the island we have collected 9 new fine to coarse modern river sand samples from active river bars for ^{10}Be measurements. These 9 new samples were treated and analyzed for ^{10}Be following the same methods described in Large et al., (2025) (Chapter 5).

^{10}Be-denudation rates were calculated based on these 9 new and 104 previously measured ^{10}Be concentrations and following the method published in Brown et al. (1995) and extensively republished (e.g., Lupker et al., 2012; Schaller et al., 2001; Von Blanckenburg, 2005). For each sampling point (both previously published and new), the associated drainage areas were constrained using QGIS toolboxes. Production rates of ^{10}Be for each basin were calculated using the QGIS-based BASINGA toolbox (Charreau et al., 2019), considering only the quartz-bearing lithologies (i.e., magmatic and metamorphic basement, sandstones and quartzites, Figure 6.1B) contained within each individual basin. All denudation rates were then recalculated using these updated production rates and following a conservative MonteCarlo type simulation in order to account for all uncertainties (Puchol et al., 2017) and obtain homogeneity within the data. The updated and new denudation rates obtained can be found in the supplementary information of this work.

6.3.2. Results

Our 9 new ^{10}Be-denudation rates range from 4 ± 0.8 mm/ka for the Andiolava catchment (sample 20, tributary of the larger Tsiribihina catchment, Sup. Info. 6.2), to 24.3 ± 5.1 mm/ka for the Fiheranana catchment (sample 17, Sup. Info. 6.2), with a weighted mean of 7.1 ± 1.2 mm/ka. The four blanks made with these samples have ^{10}Be/^{9}Be ratios ranging from 1.7 ± 1.3 10^{-16} to 6.0 ± 1.8 10 10^{-16} (Sup. Info. 6.2).

Our recalculations of the previously published ^{10}Be concentrations (Brosens et al., 2023) with the new production rates modify the ^{10}Be-denudation rates by a mean of 19%, a value that decreases to 17% when two samples (MDG-1013B1 and 2006-31, Sup. Info. 6.1) showing 100% differences are removed.

Overall measured ^{10}Be concentrations for Madagascar river sands range from 4.6 ± 0.1 10^4 at/g to 190.8 ± 2.8 10^4 at/g, with a weighted mean of 13.8 ± 0.8 10^4 at/g (MSWD 670, p 0, calculated using http://isoplotr.es.ucl.ac.uk , Vermeesch, 2018). In SW Madagascar, denudation rates range from 4.0 ± 0.8 mm/ka for the small, high elevation Andiolava catchment (sample 20, area of 752 km^2, averaged altitude of 1027 m, Sup. Info. 6.2) draining the central plateaus into the larger Onilahy catchment, to 30.1 ± 6.4 mm/ka for the larger coastal Morondava drainage (sample 10, area of 6213 km^2, averaged altitude of 299 m, Sup. Info. 6.2), with a weighted mean of 8.3 ± 1.1 mm/ka (MSWD 8.2, p 3.5). In the central and eastern parts, lowest and highest calculated ^{10}Be-denudation rates both come from small drainages, the former from a high elevation drainage (sample 2006-5, 2.8 ± 0.6 mm/ka, area of 4km^2, averaged altitude of 1502 m, Sup. Info. 6.1, Brosens et al., 2023) in northern central Madagascar, draining into the Ikopa river, the latter from a lower elevation drainage (sample 2006-23, 49.2 ± 10.2 mm/ka, area of 9 km^2, averaged altitude of 519 m, Sup. Info. 6.1, Brosens et al., 2023) in eastern Madagascar, draining into the Vohitra river. Weighted mean value of the complete dataset is 8.5 ± 0.4 mm/ka (MSWD 6.9, p 0). In terms of weighted means these two datasets are thus consistent and both show relatively high spatial variations of denudation rates in Madagascar. Three data points that had already been measured by Brosens et al. (2023) were reanalyzed in CRPG, from different sampling

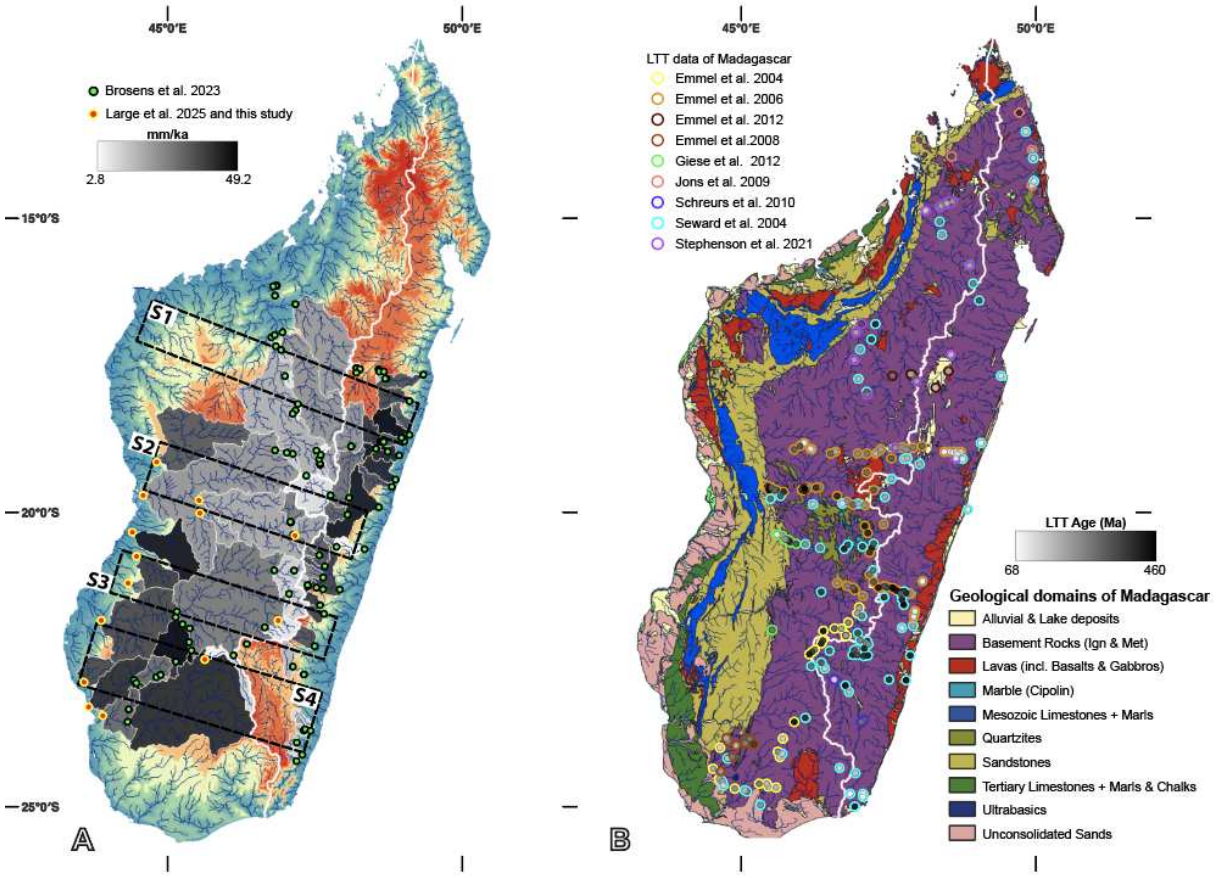

Figure 6.2: Spatial distribution of data and modern ^{10}Be-derived denudation of Madagascar. The blue line is the E/W water divide of Madagascar. A/ Denudation rates of all drainages studied in Madagascar given in mm/ka. Green points are from Brosens et al. (2023) and red and yellow points are from this study and Large et al. 2025. B/ Position of swath profiles shown in Fig.3. Data points are the same as in A/.

campaigns but from the same localities. These samples are all consistent with one another. Sampling was done in the same location, at a decade interval, for samples 20 and 2011-9 (Sup. Info. 6.1 and Sup. Info. 6.2, 4.0 ± 0.8 mm/ka and 4.3 ± 0.9 mm/ka respectively), samples 22 and 2011-7 (Sup. Info. 6.1 and Sup. Info. 6.2, 6.9 ± 1.5 mm/ka and 6.2 ± 1.3 mm/ka respectively) and samples 24 and 2006-29 (Sup. Info. 6.1 and Sup. Info. 6.2, 10.4 ± 2.1 mm/ka and 10.7 ± 2.2 mm/ka respectively).

6.4. Low-Temperature-Thermochronology

6.4.1. Methods

Low-temperature thermochronology (LTT) is typically employed to ascertain the time-temperature history of the subsurface (< 5 km depth) and to infer the nature of exhumation and burial events, considering a stable geothermal gradient. Apatite Fission Track (AFT) analysis is based on spontaneous nuclear fission of ^{238}U in apatite grains (e.g., Donelick et al., 2005; Laslett et al., 1987; Price and Walker, 1963; Tagami and O'Sullivan, 2005), which damages the mineral lattice, creating a fission track (FT) (e.g. Donelick et al., 2005; Tagami and O'Sullivan, 2005) that is annealed or shortened in time with increasing temperature (Partial Annealing Zone, PAZ, e.g., Carlson et al., 1999; Green et al., 1986, 1985). The number of FT, and their length distribution, provides insight both on the time since the mineral passed the PAZ, and on the time the mineral spent within the PAZ, respectively. Helium (He) is produced within mineral matrices by the radioactive decay of ^{238}U, ^{235}U, ^{232}Th and ^{147}Sm and is diffused out of the mineral lattice above a certain temperature range known as the Partial Retention Zone (PRZ) (Farley, 2000; Shuster et al., 2006). Apatite mineral is commonly used as its PAZ and PRZ are well studied and FT annealing and He diffusion models exist (Flowers et al., 2009; Gautheron et al., 2009; Ketcham et al., 2007) and are currently used to interpret LTT results.

A widespread thermochronological dataset is available on Madagascar and was measured to reconstruct a long-term (i.e., 10^7-10^8 a) exhumation and geodynamic history of the island (Emmel et al., 2012, 2008, 2006b, 2004; Giese et al., 2012; Jöns et al., 2009; Schreurs et al., 2010; Seward et al., 2004; Stephenson et al., 2021). In this work, we first rely on associated time-temperature (T(t)) reconstructions to reconstruct Meso-Cenozoic denudation rates across the island. Based on the geodynamic history of Madagascar and on the results of these LTT studies, we identify geologically relevant periods (i.e., known regional geodynamic periods reported in the literature and in the LTT studies). For each period and all published T(t) reconstructions, we extract the initial and final temperatures which we then use to determine a mean cooling rate (°C/Ma). The estimation of LLT-denudation rates is then obtained by converting cooling rates to exhumation rates considering a stable geothermal gradient of 30°C/km (Macgregor, 2020), a surface temperature of 15°C (Randriamarolaza et al., 2022).

We acknowledge that this method may present limitations as (i) initial and final temperatures of each period were determined graphically inducing a potential uncertainty, and (ii) T(t) reconstructions were

obtained using different inversion models leading to possible discrepancies. To account for the temperature uncertainties, we apply to each LTT- denudation rate an error equal to 20% of the rate calculated. Different inversion models may lead to different results, but the relative T(t) paths should not vary significantly from one model to the other. The variability inherent to the use of different inversion processes, should thus be minimized by the usage of relative, and not absolute temperature variations from individual T(t) histories at least for a first-order comparison.

To refine these estimates of LTT- denudation rates, the next step of this work, before final submission in a peer-reviewed journal, will be to invert the complete thermochronological raw dataset thanks to a generalized inversion process currently developed by Kerry Gallagher. This work is under progress, and we do not have results yet. However, we present below the method that will be used.

To avoid the discrepancies and biases potentially arising from comparing denudation data derived from various thermochronological inversion models and softwares (MonteTracks/QTQt/HeFty), we perform a global inversion using all available raw data based on a newly spatialized aspect of the QTQt software (Gallagher, 2012). This update consists in a conventional QTQt inversion for each sample but with an additional stage where, at each iteration, all sample predicted T(t) paths are spatially compared and aggregated accordingly. This additional step allows QTQt to cluster spatially relevant samples with similar time-temperature histories. This approach allows building a statistically robust 2D map of clustered samples inverted together and characterized by single T(t) histories. For each clustered area, we then extract predicted initial and final temperatures of each period using the expected T(t) path. To assert the precision of these temperatures, we also report the min and max temperatures that include 68% (1s) of the predicted T(t) paths. The extracted temperatures of these periods are used to determine a mean cooling rate (°C/Ma). The estimation of past denudation rates is then obtained by converting cooling rates to exhumation rates based on same assumptions given above (i.e., thermal gradient, surface temperature and consistency of exhumation and denudation).

6.4.2. Material and results

The complete LTT dataset is compiled in Sup. Info. 6.4 and mapped in Figure 6.2B. To shorten the present text and simplify its readability, the original hypotheses and discussions put forth by the authors of the studies have been omitted and only their main conclusion are reported below. Seward et al., (2004), did an extensive AFT study of the Precambrian crustal basement of Madagascar. Their T(t) paths inversions (Monte Trax, Gallagher, 1995) indicated a first homogenous Paleozoic cooling followed by a heterogenous Meso-Cenozoic thermal history with EW and NS dichotomies that the authors relate to differential east and west margin histories and a NS segmentation related to the Ranotsara/Bongolava Shear zone, respectively. Similarly, Emmel et al. (2004) reconstructed T(t) paths from AFT data (using

Monte Trax Gallagher, 1995) of south central crustal Madagascar, and along a vertical profile ranging from 860 m to 1870 m, and found two cooling steps at ~300 Ma, interpreted as orogenic processes occurring within Gondwana, and ~50 Ma, that they associate with reheating during more recent volcanic processes. Emmel et al. (2006) presented additional AFT data of the central crustal domains of Madagascar (using Monte Trax, Gallagher, 1995) showing little to no exhumation along the eastern margin since Triassic times, although some samples were reset due to a thermal overprint associated to the Madagascar India/Seychelles break-up during the Cretaceous. They associate the Ankay-Aloatra graben initiation to this period (Figure 6.1A). Emmel et al. (2008), added 8 new AFT data (inverted with HeFTy, Ketcham, 2005), to reconstruct the history of the Vohibory domain (SW Madagascar, Figure 6.1B), which they found to have uplifted in the Jurassic, due to isostatic compensation of the carbonate platform being put in place to the west. Emmel et al. (2012) measured (U-Th)/He on 4 samples of the two previous publications and on 2 new samples and added 7 new AFT data points in the Aloatra-Ankay region (Figure 6.1A, and Figure 6.2B). The inversion of their dataset (HeFTy, Ketcham, 2005) showed only a Carboniferous to Permian cooling interpreted as limited erosion (0.7-2 km) since the Permo-Triassic for most samples, located in central and W Madagascar. An acceleration of cooling during the Cenozoic was however found for samples located on the Aloatra-Ankay (Figure 6.1A) rift shoulders and along the eastern coast. Exhumation related to an Oligocene opening was invoked to explain the former, while the latter was associated to faulting of the Graben, and Cenozoic magmatic or tectonic events. In 2009, Jöns et al. inverted AFT data (using HeFTy, Ketcham, 2005) of the N Madgascar Bemarivo Belt (e.g., Thomas et al., 2009), finding no relation between the Bemarivo belt exhumation and the Madgascar India/Seychelles separation, but a Cenozoic cooling from 60°C, which lasted 20 Ma and is suggested to be associated to volcanism and fault activity. Giese et al. (2012) sampled the edge of the central plateau in SW Madagascar along two NW-SE and E-W profiles for AFT analysis (using HeFTy, Ketcham, 2005), showing Eocene cooling that they related to exhumation produced by a stress field reorganization due to India/Eurasia collision, leading to a reactivation of NE-SW oriented faults. Finally, Stephenson et al. (2021) sampled the edge of the central plateau in northern Madagascar along two N-S and E-W profiles. Their AFT dataset (using QTQt, Gallagher, 2012) suggests a recent cooling interpreted as 0.5 to 1.6 km of exhumation associated with uplift occurring after ~30 Ma.

Based on these datasets and on the geodynamic history of Madagascar, we define three relevant geodynamic time periods: i) a large period spanning from 250 Ma to 100 Ma, encompassing Gondwana break-up, Africa-Madagascar/India/Antarctica separation and Madagascar/India-Antarctica separation; ii) the Cretaceous separation between India and Madagascar and the Meso-Cenozoic stability period from 100 Ma to 35 Ma; iii) a 35-0 Ma period, corresponding to the Neogene recorded cooling/exhumation acceleration (Stephenson et al., 2021).

Mean LLT-denudation rates from the compilation of all datasets are of 4.6 m/Ma, 7.5 m/Ma and 25.2 m/Ma for the 250-100 Ma, 100-35 Ma and 35-0 Ma periods respectively. Individual means of each study vary from -4.1 m/Ma to 46.7 m/Ma, -1.1 m/Ma to 12.8 m/Ma and 10.3 m/Ma to 42.9 m/Ma, for the 250-

100Ma, 100-35Ma and 35-0Ma periods, respectively. It should be noted however that the higher means of 46.7 m/Ma and 42.9 m/Ma are from the inversion of a single sample of the Bemarivo Belt (Jöns et al., 2009), and using Titanite Fission Tracks (TFT), a method with much higher closure temperatures but far less constrained. If we discard these two means, then the highest means for the 250-100Ma and 35-0Ma periods are 10.2 m/Ma and 40.7 m/Ma, respectively. This general trend of increasing LLT-denudation in the more recent period (35-0 Ma), is confirmed if we calculate the individual means of each published datasets, although it is less evident in the inversions of Emmel et al. (2012) and Jöns et al. (2009) (Sup. Info. 6.4).

6.5. Discussion

6.5.1. Spatial distribution of recent denudation (10-100ka) derived from cosmogenic nuclides

In Madagascar, ^{10}Be-denudation rates of the high central plateaus are generally low, while coastal areas seem to be eroding significantly faster (Figure 6.2A, Sup. Info. 6.1 and Sup. Info. 6.2). This is true for both eastern and western coastal regions, although the explanation for this spatial variability probably varies between these two regions. In the eastern part of the island, the sharp relief created by the Great Eastern Escarpment (Figure 6.1A), associated with higher humidity and precipitation, due to trade winds and an orographic effect, lead to higher denudation rates than in the neighboring central plateaus (Wang et al., 2021).

In W Madagascar however, the absence of scarp and the semi-arid to arid climate compels to find another explanation for the spatial distribution of ^{10}Be-denudation. The crustal rocks of the central plateaus (Figure 6.1B), mostly metamorphic and ranging from granitoids to dolomitic marbles (Archibald et al., 2015; Cox et al., 1998; Tucker et al., 2014), are probably much more difficult to erode than the sediments, present in the Morondava and Mahajunga basins (Figure 6.1). A lithological effect could explain the distribution of ^{10}Be-denudation, consistent with figure 3, where for each profile ^{10}Be-denudation tend to drop East of the sedimentary area. This is particularly true for small rivers draining only sedimentary lithologies, but less for very large rivers draining both crustal and sedimentary lithologies, such as the Tsiribihina and Morondava rivers in swath profile 2 (S2, Figure 6.3, Sup. Info. 6.2). It is notable that in this second profile, which is located in between the Morondava and Mahajunga basins, and where the sedimentary units are scarce, the larger SW rivers (Tsiribihina, Manambolo) yield notably slower ^{10}Be-denudation rates than for other SW large rivers, further to the south, and where sedimentary units are much more widespread (Figure 6.3).

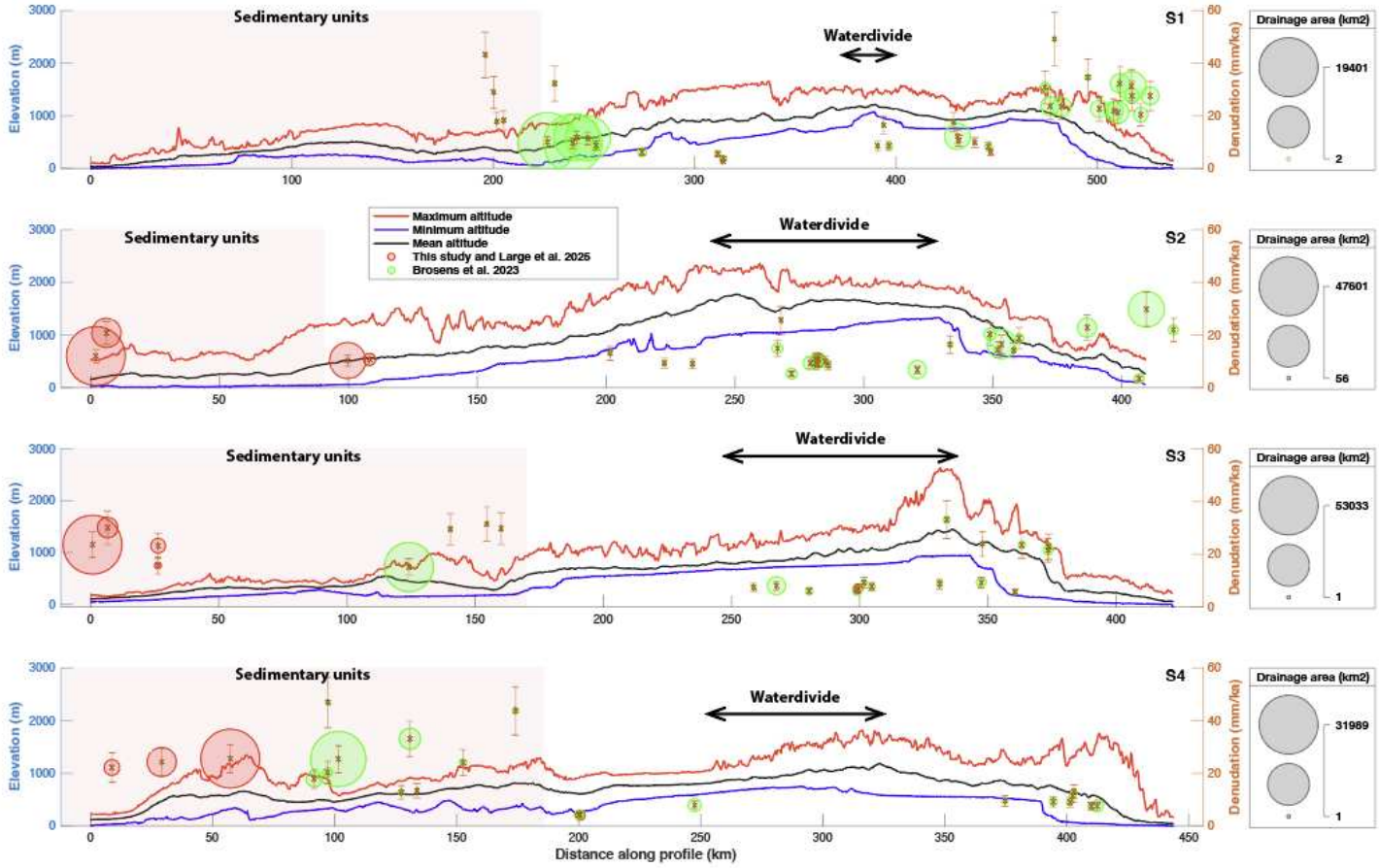

Figure 6.3: Denudation rates of Madagascar, projected along swath profiles presented in Fig.2. Position of the water divide throughout every swath profile is shown by the double verging arrow. Extension of the western sedimentary units is shown by the light red rectangle for each profile. Data presented in green is from Brosens et al. 2023 and data presented in red is from this study and Large et al. 2025. The size of each circle around each data point represents the drainage areas. Legend for the sizes of drainage are given to the right of each profile.

Lavakas, erosional gullies that form in the lateritic soils of the high central plateau (Figure 6.1B), have been suspected to have contributed to a possible recent (i.e., past 1ka) increase in denudation (Broothaerts et al., 2022; Brosens et al., 2022). This increase would have followed a growth in the number of active lavakas, caused by rising pressure on the landscape due to anthropogenic forcings such as cattle and deforestation. Although the resolution of cosmogenic nuclides (i.e., integration times, ranging from 12.2 ka to 211.3 ka, see Sup. Info. 6.1Sup. Info. 6.2, and Large et al., 2025, Chapter 5 for further explanation) does not allow to resolve the evolution of denudation over such short time scales, the spatial distribution of the ^{10}Be-denudation shows no correlation whatsoever with the spatial distribution of lavakas and the fastest eroding drainages of Madagascar are located in NE and SW Madagascar (Figure 6.2A), areas where no lavakas have been reported (Figure 6.1B). This result implies that, although an increase in lavakas in the past 1ka may have led to increased denudation, the presence of lavakas do not control the evolution and distribution of denudation over longer timescales (i.e., 10-100ka), and lavakas cannot be considered as the only, or even the main, parameter controlling ^{10}Be-denudation in Madagascar.

Finally, Large et al., (2025) (Chapter 5) have shown that these values of ^{10}Be-denudation remain constant since the Late Pleistocene, with very little to no effect of Quaternary climatic cycles on denudation in this tropical island. This spatial distribution of ^{10}Be-denudation may thus very well have been constant throughout the Quaternary.

6.5.2. Denudation history across the island

To reconstruct the denudation history across Madagascar we classified all denudation data in groups, spatially consistent with geology, topography, ^{10}Be results and LTT pre-existing spatial classifications (Figure 6.4). Five zones are thus created, the Northern, Eastern and Central areas are similar for both datasets, although the northernmost part of the island lacks ^{10}Be data. However, due to spatial discrepancies in the distribution of the ^{10}Be and LTT datasets, the Coastal and Southern areas record only ^{10}Be-denudation and LTT-denudation, respectively. For each group, we take the mean ^{10}Be-denudation of every drainage, weighted by their areas, and the means of LTT-denudation of all data within said group, to which we apply a 20% error.

The different zones are compiled and presented in Figure 6.4. For the 0-35 Ma period, where both ^{10}Be-denudation and LTT-denudation are available, the Northern, Eastern and Central areas yield denudation rates of 10.6 ± 2.2 mm/ka and 28.0 ± 5.6 m/Ma, 23.2 ± 4.9 mm/ka and 21.9 ± 4.4 m/Ma, and 12.8 ± 2.6 mm/ka and 22.8 ± 4.6 m/Ma, respectively. The Coastal and Southern areas yield denudation rates of 25.9 ± 5.5 mm/ka, and 32.6 ± 6.5 m/Ma, respectively. In the Northern, Central, Southern and Eastern parts of the island, mean LTT-denudation rates for the 250-100Ma, 100-35Ma and 35-0Ma are of 8.9 ± 1.8 m/Ma (n=23), 3.4 ± 0.7 m/Ma (n=22) and 28.0 ± 5.6 m/Ma (n=24); 1.7 ± 0.3 m/Ma (n=38), 7 ± 1.4 m/Ma (n=44), and 22.8 ± 4.6 m/Ma (n=48), 6.1 ± 1.2 m/Ma (n=12), 5.6 ± 1,1 m/Ma (n=18) and 32.6 ± 6.5 m/Ma (n=19) and finally 1.5 ± 0.3 m/Ma (n=3), 21.7 ± 4.3 m/Ma (n=9) and 21.9 ± 4.4 m/Ma (n=10), respectively.

All zones demonstrate a similar history, marked by an increase in denudation during the Cenozoic compared to the Mesozoic. However, the Eastern area stands out for its earlier (Upper Cretaceous, ~100 Ma) and more consistent changes visible both in ^{10}Be-denudation and LTT-denudation of 23.2 ± 4.9 mm/ka, and 21.7 ± 4.3 m/Ma and 21.9 ± 4.4 m/Ma, for the 100-35 Ma and 35-0 Ma periods, respectively (Figure 6.4). This observation agrees well with the onset of escarpment-related high denudation rates after the separation between Madagascar and India and the emplacement of the Madagascar LIP (Bardintzeff et al., 2010; Delaunay, 2018; Seton et al., 2012; Storey et al., 1995). These findings confirm observations of scarp retreat as the main (and only) long-term control over denudation rates in E Madagascar (Wang et al., 2021).

Apart from the Eastern area, the denudation acceleration appears to have initiated at ~35 Ma and recently ceased as ^{10}Be-denudation rates are somewhat lower than the LTT-denudation. In the North, the explanation for such a decrease could be the spatial distribution of data. The LTT-denudation may record the rapid (10-100 mm/ka), very localized uplift in the northern tip of the island (Stephenson et al., 2019), while a lack of ^{10}Be records in that area make them blind to it. In Upper Cretaceous to Eocene periods, LTT-denudation rates are slightly lower (3.4 ± 0.7 m/Ma) than in the pre-Cretaceous (8.9 ± 1.8 m/Ma). The initiation of doming in the Central area, and drainage reorganization associated to westward tilting

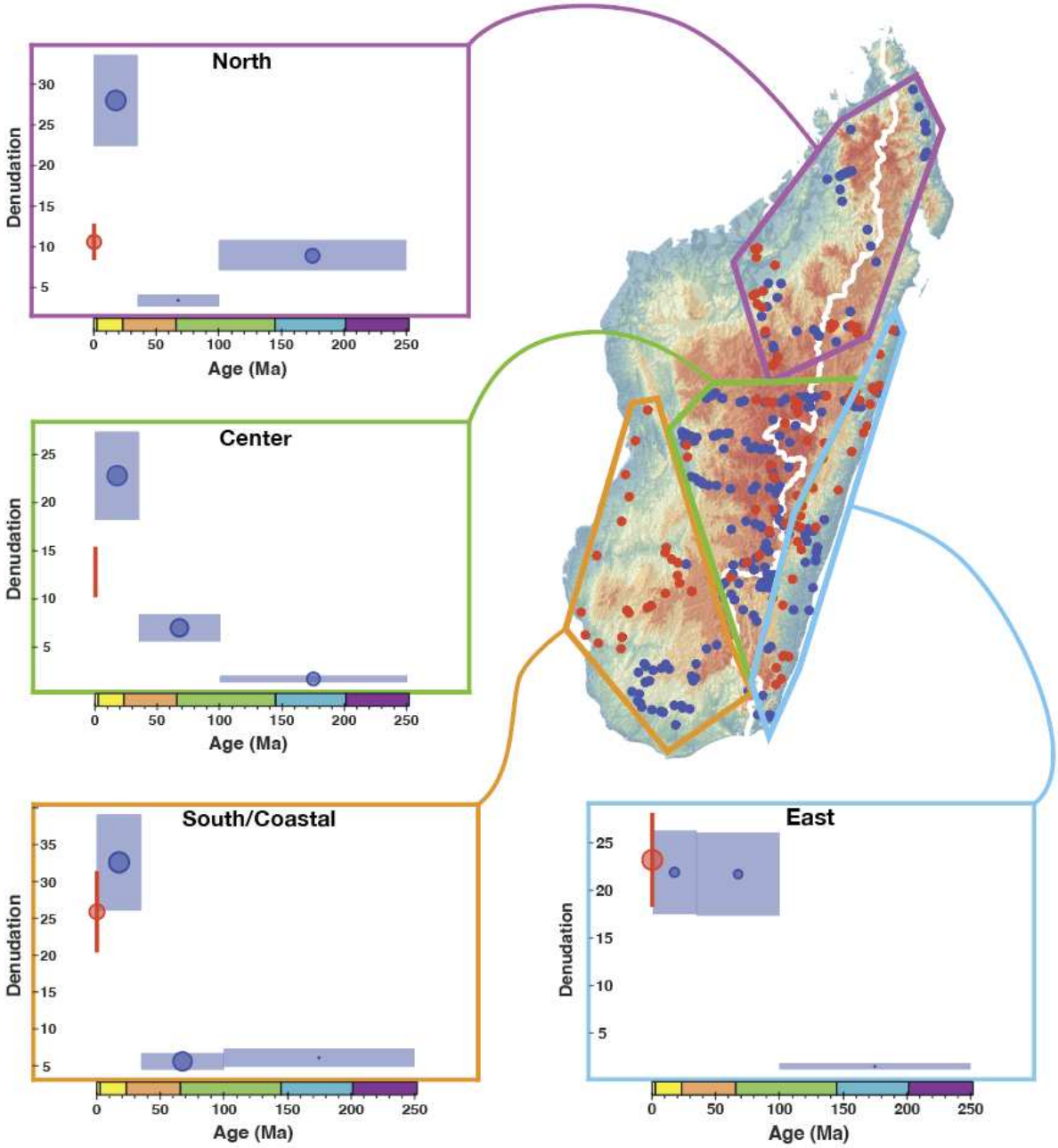

Figure 6.4 : Evolution of denudation rates with time for the different areas of Madagascar. Blue points correspond to LTT-derived denudation rates, red points to ^{10}Be-derived denudation rates. For each colored inset, blue and red points correspond to calculated mean denudation of all data points located within the associated polygons on the map, weighted by the size of their respective drainages. Size of each circle is proportional to the number of data points taken to calculate the means. Under each inset, colored bars give ages of different geological eras with, from left to right, Quaternary, Neogene, Paleogene, Cretaceous, Jurassic and Triassic.

of the island after Madagascar/India separation (Delaunay, 2018) may explain the increase in denudation from 1.7 ± 0.3 m/Ma in the 250-100 Ma range to 7 ± 1.4 m/Ma in the post-Cretaceous. Uplift due to continued doming of Madagascar since the Oligocene (Delaunay, 2018; Roberts et al., 2012) explains the high LTT-denudation rates in the more recent 35-0 Ma period (22.8 ± 4.6 m/Ma), while the Quaternary period, associated to the end of widespread doming, records lower denudation (12.8 ± 2.6 mm/ka). The Coastal and Southern areas are in good agreement with one another, with similar rates of denudation within errors, the small difference being easily explained by different processes being recorded, an increased erodibility in the Coastal area (Large et al., 2025) (Chapter 5), and doming-related uplift in the Southern area (Delaunay, 2018). In older times, denudation of the Southern region shows no visible variation from Triassic to Paleogene (6.1 ± 1.2 m/Ma to 5.6 ± 1.1 m/Ma).

6.5.3. Temporal and spatial distribution of uplift

To study the uplift history of Madagascar, Delaunay (2018) mapped planation surfaces across the island using both field campaigns and SIG tools such as shading, curvature, swath profiles, Altitude/Relief ratio, or the Topographic Position Index (Weiss, 2001). These surfaces were dated using their geometric relationship with previously dated layers (i.e., capped or incised) or by previously published absolute ages (e.g., ^{40}Ar-^{39}Ar, Cucciniello et al., 2024). By comparing their different altitudes and ages, and based on the successive pediment formation hypothesis of Guillocheau et al. (2018), where successive phases of uplift lead to the creation of successive planation surfaces, the lowest being the youngest, Delaunay (2018) was able to reconstruct periods of uplift across the island and their spatial distribution. These surfaces are presented in Figure 6.5 and described below.

Of the oldest of the 9 surfaces, S_1, dated from the Lower Jurassic (Dixey, 1960), only little remnants exist at high altitudes (i.e., 1500-2800 m), possibly inherited from Gondwana break-up. At 150-420m below this first surface, in the central plateaus and in the northernmost areas lies surface S_2 of Lower Cretaceous age (~113-100 Ma, mean altitude of 1581 m). It is associated with the inversion of the Davie ridge and the continentalization of the Morondava basin. S_{3a} (94-80 Ma, mean altitude of 1462 m), 50-200m below S_2 is a stripped etchplain (i.e. planation surface formed under tropical warm and humid weathering conditions; Guillocheau et al., 2018; Migoń, 2004), continuous in central Madagascar, but highly degraded in the southern part of the island. S_{3B} (80 – 66 Ma, mean altitude of 1110 m), 0-500m below S_{3a}, is well preserved in the Antananarivo plain. These two surfaces are associated with Madagascar LIP-related uplift. A seaward-tilted pediplain (i.e., 100 km-scale flat erosional surfaces; Guillocheau et al., 2018), preserved along the high axial plateau corresponds to S_4 (41-29 Ma, 150-200 m below S_3, mean altitude of 946 m) and is associated to the initiation of flexural uplift and westward tilting of the margin. In between surfaces S_3 and S_4, a transgression related to the Early Eocene Climatic Optimum (EECO, Zachos et al., 2001) led to carbonate platform growth in W Madagascar. S_{5a} (23-12 Ma, 100-200 m below S_4, mean altitude of 816 m) and S_{5b} (12-5 Ma, 150-200 m below S_4, mean altitude

of 600 m) constitute the edges of the central plateau all around Madagascar and record an acceleration of uplift, the paroxysm of which being recorded by the former. These surfaces are contemporaneous with the second phase of intense Neogene volcanism in Madagascar. Finally, surface S_6 (3.6-0 Ma, mean altitude of 358 m) is widespread and well developed along all coastal plains of the island and located 200-350m below S_4, and the lowest and youngest Quaternary surface (S_7, 300-400 m below S_6, mean altitude of 62 m) corresponds to river incisions, coastal dunes, and alluvial infilling. These two surfaces correspond to lowering of base-level, related to eustatic drops and maintaining of Madagascar in an elevated position.

From these surfaces, two main phases of uplift are deducted in Madagascar. A first phase in Late Cretaceous, associated with Madagascar/India break-up and the Madagascar LIP, and a second, Late Paleogene to Neogene uplift. This latter more recent phase of uplift is consistent with large-wavelength uplift of up to 1-2 km over the past 15 Ma, revealed by the inversion of 98 river profiles throughout the island (Roberts et al., 2012), reaching rates of 200 to 400 m/Ma, and attributed to Neogene convective mantle upwelling below the island. These rates of uplift, only one order of magnitude below some of the fastest uplifting areas on Earth such as Taiwan (e.g., Hsu et al., 2018) or the Himalaya range (e.g.,

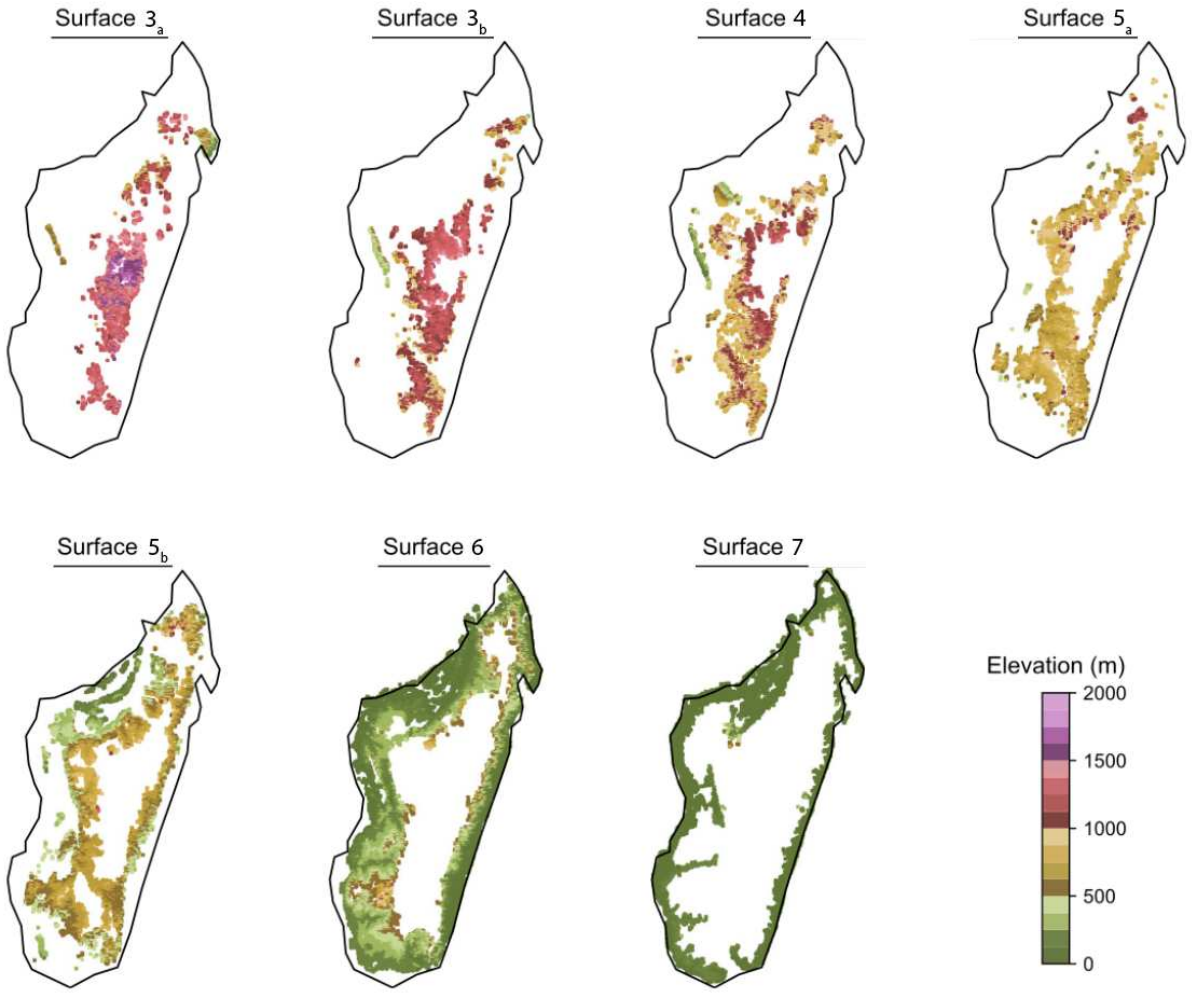

Figure 6.5 : Location of the different planation surfaces mapped by Delaunay (2018). Surfaces S1 and S2 are not presented as only remnants remain and they are not spatially continuous. Figure modified from Jiao et al. (2022).

Grandin et al., 2012), must have been relatively short-lived (i.e., 10^5-10^6 a), as they would have accounted for 3 to 6 km of uplift in Madagascar, had they persisted throughout the Late Cenozoic. Mapping of marine coral reef terraces in northern Madagascar (Battistini, 1972; Stephenson et al., 2019) showed recent (i.e., 100 ka) and very localized uplift ranging from ~19 mm/ka to ~80 mm/ka since the past 125 ka, also associated to dynamic topography and mantle processes showing a continuity in the processes controlling uplift in Madagascar.

In 2022, Jiao et al. used Delaunay's results to create a Landscape Evolution Model and better constrain periods of uplift and erosion on the island. Of the 9 surfaces mapped by Delaunay, Jiao et al. used 7 (S_{3a} to S_7, Figure 6.5) corresponding to periods 90-84 Ma, 84-66 Ma, 34-11 Ma, 11-5 Ma, 5-3 Ma, 3-2.6 Ma and 2.6-0 Ma. By mapping and extrapolating the vertical offsets between successive planation surfaces, they obtain maps of cumulated uplift for these periods. Their results show uplift throughout the island before ~85 Ma, with more rapid rates of up to ~60 m/Ma recorded in N Madagascar. These values are however affected by strong uncertainties as the initial topography (surfaces S_1 and S_2 of Delaunay, 2018) is not well constrained. After this episode, rates are low (< 10 m/Ma) until ~60 Ma, when uplift is no longer recorded, consistent with the EECO (Zachos et al., 2001) and the deposition of the carbonate platforms in the West (Delaunay, 2018). In the Oligocene, slow uplift of 10 m/Ma is recorded throughout the island. Later, uplift of up to 200 m/Ma is recorded in the Mid-Miocene in the North, and in Late Miocene in the Central and Southern parts of Madagascar, peaking throughout the island in the Pliocene, consistent with river profile inversions (Roberts et al., 2012). Their model also enables erosion recording, which they find to follow trends of uplift. However, important sediment volume loss through chemical alteration may be unaccounted for, possibly responsible for some disagreements between uplift and erosion, a conclusion shared by Brosens et al. (2023).

6.5.4. Implication for Meso-Cenozoic landscape equilibrium

To obtain values of uplift rates comparable to our calculated rates of denudation, we use values of vertical offset between the planation surfaces mapped by Delaunay (2018) and modelled by Jiao et al. (2022). Using ArcGIS Pro, we calculate cumulated uplift by adding the values of these extrapolated vertical offset maps between planation surfaces 3a and 4, and between surfaces 4 and sea level (Figure 6.5), corresponding to 90-66 Ma and 34-0 Ma periods, respectively. Resulting cumulated uplift maps are shown in Figure 6.6. We then extract from these maps the mean values of uplift of each area considered in section 5.2 (Figure 6.4Figure 6.6), using the statistics tool on ArcGIS Pro (Sup. Info. 6.5) and divide the cumulated uplift by the time (i.e., 24 Ma for the 90-66 Ma period, and 34 Ma for the 34-0 Ma period) to obtain uplift rates in m/Ma.

These uplift rates are then compared to our LTT-denudation rates data (Figure 6.7). Because Jiao et al., (2022) only have data for the 90-66 Ma and 34-0 Ma periods, and our LTT-denudation rates span periods

of 100-35 Ma and 35-0 Ma, discrepancies may arise between these two datasets. However, for the analysis of LTT data, the 100-35 Ma period was chosen for its uniformity, in terms of both geodynamic and LTT exhumation histories. This uniformity is very well represented by the compilation of uplift rates adapted from Jiao et al. (2022). Figure 6.6 shows that the 90-66 Ma period corresponds to a very stable uplift with very low uplift (i.e., ~200 m in 24 Ma), except in the northern part of the island (i.e., > 600 m in 24 Ma). Only few T(t) paths (Emmel et al., 2012) show higher exhumation in the 100-80 Ma period, followed by a longer period of stability with no exhumation recorded until 35 Ma, which could lead to an underestimation of denudation rates, when compared to uplift rates. Nevertheless, we remain confident that comparing these different time periods should not alter our conclusions.

Figure 6.7A shows the comparison of uplift rates with LTT-denudation rates for the 4 areas and the two time periods considered (Sup. Info. 6.5 and Sup. Info. 6.6). In the 90-66 Ma period, the northern, southern, and central areas show LTT-denudation rates that are about two times lower than the uplift

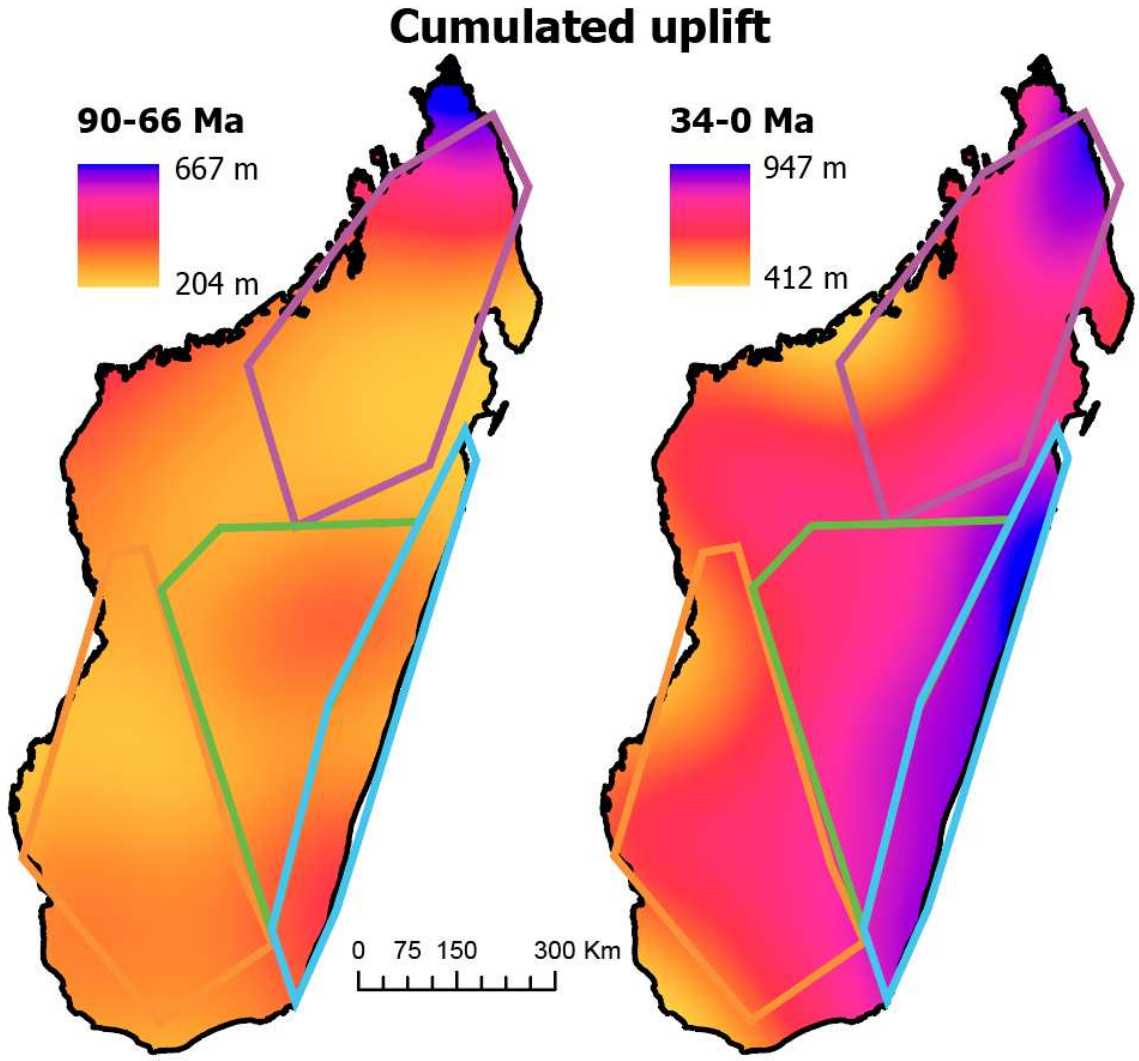

Figure 6.6 : Cumulated uplift maps for the 90-60 Ma and 35-0 Ma periods, calculated from the extrapolation of the offsets of the planation surfaces of Delaunay (2018), modelled by Jiao et al., (2022). Areas on each map correspond to the areas of figure 4 and to the zones of extraction of data presented in figure 7.

rates of the same period, leading to ratios between LTT-denudation and uplift of 0.3 ± 0.1 to 0.6 ± 0.1 (Figure 6.7B). This small discrepancy could be in part explained by the difference in temporal periods considered for the uplift and LTT-denudation rates. Moreover, in the north, where the ratio is the lowest, uplift is concentrated in the northernmost tip of the island (Figure 6.6), an area where the density in LTT data, and thus the resolution is low. For the same period, the eastern area is the only one to yield a ratio LTT-denudation/Uplift above 1 (1.6 ± 0.4). This is easily explained by the denudation of this area controlled by scarp retreat and not uplift (Wang et al., 2021), as already presented in section 6.5.2 of this work.

In the more recent 34-0 Ma period, both LTT-denudation rates and uplift rates increase (Figure 6.7A), with LTT-denudation increasing more, as shown by the LTT-denudation/Uplift ratios ranging from 0.9 ± 0.2 for the eastern area, to almost 1.7 ± 0.4 for the southern area (Figure 6.7B). In the South, this high ratio could be explained by the concentration of uplift further to the East with a tilting towards the West of the island (Delaunay, 2018). This situation would create low uplift rates in SW Madagascar, whereas the strong asymmetry of the drainage networks, leads to the largest catchments, with a potentially high erosive power, flowing towards the West and leading to higher denudation rates.

Omitting the exceptions described above, all regions yield ratios comprised between 0.5 ± 0.1 (90-66 Ma southern region) and 1.3 ± 0.3 (34-0 Ma northern region), showing a somewhat good consistency between uplift and denudation in Madagascar for this period. Moreover, the combined increase in LTT-denudation and uplift between the 90-66 Ma and 34-0 Ma periods (Figure 6.7B) is consistent with a tectonic control over denudation in Madagascar and a sub-steady state between these two processes.

Our study thus confirms an increase of denudation rates during the Cenozoic, generalized all over Madagascar during the most recent of the periods (35-0 Ma) with regard to pre-Oligocene rates which

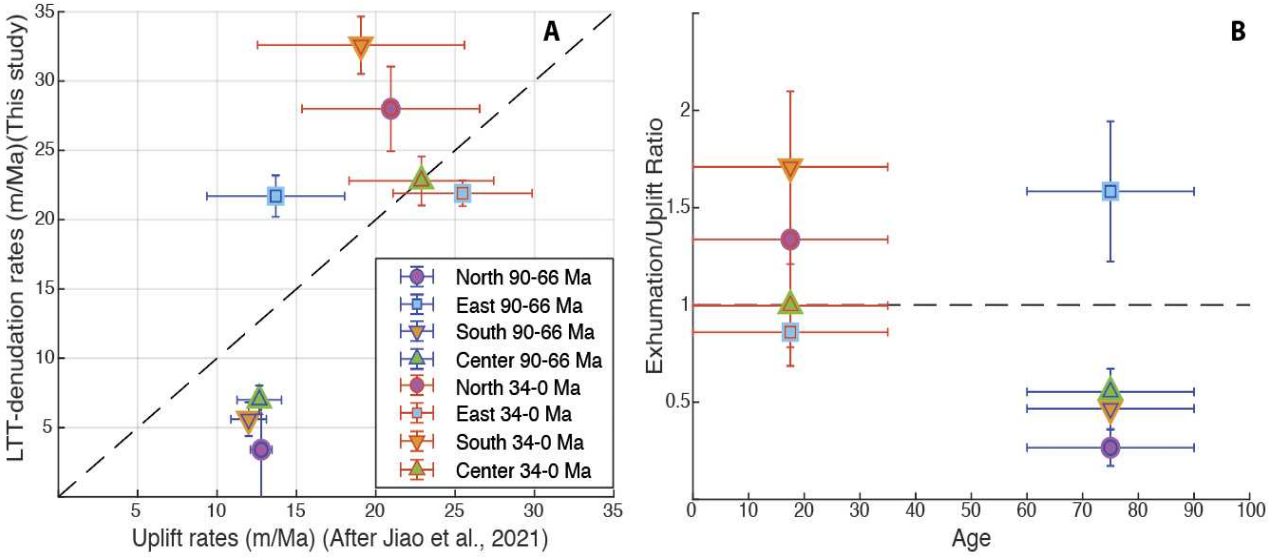

Figure 6.7 : Comparisons of LTT-denudation and uplift. Color coding corresponds to the areas presented in figures 4 and 6. Blue outlines are 90-66 Ma period, Red outlines are 34-0 Ma period. Legend shown in A/ is valid for both insets. A/ Uplift rates for each region plotted against corresponding LTT-denudation rates. The dotted line is the 1:1 ratio. B/ Values of LTT-denudation/Uplift ratios for all regions and the two time spans considered. Dotted line shows ratio of 1.

are up to one order of magnitude lower (Sup. Info. 6.5). Denudation rates remain within a narrow range from 2.8 ± 0.6 mm/ka (^{10}Be, sample 2006-5) to 49.2 ± 10.2 mm/ka (^{10}Be, sample 2006-23, Sup. Info. 6.1), showing a somewhat long-term consistency of denudation in Madagascar. These observation are consistent with predictions of the model from Jiao et al. (2022) showing good agreement between uplift and denudation, the latter being in appearance, unaffected by climatic variations. Our work and results confirm this observation, showing a relative state of equilibrium between denudation and uplift over the Cenozoic. This state is long-lived as uplift and denudation appear to be agreeing with one another at least since the Cenozoic separation of the island from Gondwana (~100 Ma). These low rates of denudation, associated with slow, unlocalized, epeirogenic rather than orogenic type uplift, would be accountable for the modern topography of the island. Climatic variations, however, may have been responsible for much more short-lived (i.e., 10^3-10^4 a) variations in denudation, to which our methods are blind (Large et al., 2025) (Chapter 5). Overall, ^{10}Be-denudation rates are generally in good agreement with the long term LTT-denudation, and the tectonic activity of the island explains well the spatial distribution and temporal trends of said denudation.

6.6. Conclusions

The main take home messages from this work are:

- ^{10}Be data from Madagascar show that, although precipitation and relief seem to control recent denudation rates in the eastern part of the island, in the SW, lithology is the main control of the evolution of denudation rates. This method yields rates of denudation that remain however low, with an order of magnitude of variability (2.8 ± 0.6mm/ka to 49.2 ± 10.2mm/ka).
- Our results show that on the scale of 10-100ka, the presence of lavakas is uncorrelated to denudation of Madagascar.
- Long-term (10-100Ma) denudation rates are within the range of recent (10-100ka) values.
- Late Cenozoic denudation is within range of some of the fastest eroding modern basins of Madagascar, whereas Mesozoic to Early Cenozoic denudation rates are comparable with the slowest denudating modern basins of the island. This evolution of denudation is linked to a likewise evolution of uplift on the island.
- Cenozoic denudation of Eastern Madagascar is controlled by a scarp-retreat mechanism, developed after Madagascar isolation.
- Denudation rates and uplift rates are consistent with one another throughout the Cenozoic, with a late Paleogene increase in both uplift and denudation rates.
- During the Cenozoic, the denudation rates/Uplift rates ratios of the different areas of the island are comprised between 0.3 and 1.7, with a mean ratio of 1, showing an overall equilibrium

between Cenozoic uplift and denudation in Madagascar, and allowing us to conclude to a sub-steady state on the island.

- Our work confirms that denudation of Madagascar follows the uplift of the island and that a possible late Cenozoic increase in denudation rates would have been created more possibly by mantle processes than by climatic forcing. From these results, Molnar's hypothesis seems unlikely to be complete.

Supplementary Information

Sup. Info. 6.1: All data compiled in Brosens et al. 2023 and recalculated in this work.

River	Sample	Longitude	Latitude	Drainage area	Quartz bearing area	Average altitude	Source
		DD	DD	km^2	km^2	m	
Mazy	2004-2A	46.8227	-18.9452	133	133	1327	Cox et al. (2009)
Onibe in Tana	2004-6A	47.1251	-19.0045	210	67	1636	Cox et al. (2009)
Ikopa in Tana	2004-9A	47.5259	-18.95	1593	305	1452	Cox et al. (2009)
Valley stream	2005-3B	48.2078	-17.5496	4	4	872	Cox et al. (2009)
Morarano	2005-6	48.264	-17.5648	184	183	930	Cox et al. (2009)
Imamba	2005-7	48.2027	-17.6273	7	7	807	Cox et al. (2009)
Ikalariana	2006-1	47.0222	-18.9853	148	148	1463	Brosens et al. (2023)
Sisaony trib.	2006-2	47.5874	-19.1913	317	317	1515	Brosens et al. (2023)
Sisaony	2006-3	47.5866	-19.1689	483	163	1503	Brosens et al. (2023)
unnamed	2006-5	47.1691	-18.2666	4	4	1502	Brosens et al. (2023)
Mamokomita	2006-6	46.989	-17.6818	367	367	1002	Brosens et al. (2023)
Betsiboka	2006-7	46.9484	-16.9383	11798	11182	996	Brosens et al. (2023)
Kamoro	2006-8	47.169	-16.4623	11197	11140	732	Brosens et al. (2023)
Ampijiroa res.	2006-9	46.8225	-16.317	64	64	163	Brosens et al. (2023)
Ampijiroa res. 1	2006-10	46.8539	-16.146	14	3	79	Brosens et al. (2023)
Ambilivily res.2	2006-11	46.8387	-16.1489	7	4	54	Brosens et al. (2023)
Ikopa	2006-12	46.7608	-17.0246	19401	15538	1151	Brosens et al. (2023)
Androtroa	2006-13	46.8163	-16.9862	26	26	150	Brosens et al. (2023)
Amboromalandy	2006-14	46.7923	-16.1603	2	2	36	Brosens et al. (2023)
Ikopa	2006-15	46.8368	-17.177	19234	18420	1159	Brosens et al. (2023)
Andriantoany	2006-16	46.9256	-17.2405	420	420	632	Brosens et al. (2023)
Manankazo	2006-17	47.2109	-18.1582	132	132	1573	Brosens et al. (2023)
Andranobe	2006-18	47.1239	-18.3231	129	122	1396	Brosens et al. (2023)
Mangoro	2006-19A	48.1147	-18.8788	3684	3682	1026	Brosens et al. (2023)
Sahantandra	2006-21	48.5368	-18.919	487	475	985	Brosens et al. (2023)
Vohitra dam Andekaleka	2006-22	48.6122	-18.7938	1884	1387	965	Brosens et al. (2023)
Vohitra trib.	2006-23	48.6362	-18.8065	9	9	519	Brosens et al. (2023)
Vohitra	2006-24	48.6652	-18.7997	1928	35	947	Brosens et al. (2023)
Namorona	2006-25	47.3933	-21.2411	508	503	1217	Brosens et al. (2023)
Anivorano	2006-26	47.6368	-21.3073	30	11	484	Brosens et al. (2023)
Tsaratandro	2006-27	47.5265	-21.2773	80	80	976	Brosens et al. (2023)
Namorona	2006-28	47.3741	-21.2351	393	393	1255	Brosens et al. (2023)
Mania	2006-29	47.1646	-20.3942	2507	2507	1491	Brosens et al. (2023)
Manandona trib.	2006-30	47.091	-20.1711	56	56	1808	Brosens et al. (2023)
Manandona	2006-31	47.0826	-20.1578	1482	1054	1699	Brosens et al. (2023)

Vohitra-Rianila	2011-01	49.0164	-18.7903	4737	1968	703	Brosens et al. (2023)
Rianila	2011-02	48.9816	-18.7237	2032	1918	639	Brosens et al. (2023)
Sakanila	2011-03	48.8687	-19.4418	1687	1495	437	Brosens et al. (2023)
Manampotsy	2011-04	48.8055	-19.5641	1231	1209	553	Brosens et al. (2023)
Iaroka	2011-05	48.9318	-19.0324	1120	985	396	Brosens et al. (2023)
Farimbona	2011-06	48.7364	-18.9669	120	120	449	Brosens et al. (2023)
Mananantana	2011-07	46.8817	-21.8297	1199	1199	1141	Brosens et al. (2023)
Zomandao	2011-08	46.6495	-21.9531	575	575	1268	Brosens et al. (2023)
Ihazofotsy	2011-09	45.6282	-22.4989	752	752	1027	Brosens et al. (2023)
Menamaty	2011-10	45.4037	-22.3454	208	207	861	Brosens et al. (2023)
Mangoky	2011-11	45.1561	-21.6855	36860	28171	897	Brosens et al. (2023)
Malio at Ilaza	2011-12	45.1345	-21.7817	4015	3645	568	Brosens et al. (2023)
Malio trib.	2011-13	45.2539	-21.9003	27	26	420	Brosens et al. (2023)
Iloto	2011-14	45.3742	-21.9698	16	16	452	Brosens et al. (2023)
Mamolaky	2011-15	45.3641	-22.2052	1	0	651	Brosens et al. (2023)
Malio	2011-16	45.1404	-22.5351	347	347	854	Brosens et al. (2023)
Sakondry	2011-17	44.3389	-23.3464	736	381	397	Brosens et al. (2023)
Onilahy	2011-18	44.3201	-23.5584	28215	27285	713	Brosens et al. (2023)
Fiheranana	2011-19	44.4281	-22.8475	2252	1821	688	Brosens et al. (2023)
Tegninday	2011-20	44.4677	-22.8995	74	39	477	Brosens et al. (2023)
Maninday	2011-21	44.8082	-22.7992	239	238	822	Brosens et al. (2023)
Dry canyon	2011-22	44.8798	-22.761	1	1	822	Brosens et al. (2023)
Ihosy	2011-23	46.1177	-22.4286	1473	1473	1106	Brosens et al. (2023)
Fandramana	2011-24	46.3435	-22.2358	112	110	932	Brosens et al. (2023)
Manovoriaka	2011-25	47.0607	-21.3848	467	466	1297	Brosens et al. (2023)
Androhibe	2011-26	47.1466	-20.989	315	312	1387	Brosens et al. (2023)
Andragorona trib.	RL-1	48.5811	-17.5716	14	14	883	Brosens et al. (2023)
Andragorona trib.	RL-2	48.5946	-17.6055	19	19	1004	Brosens et al. (2023)
Maintimbato	RF-1	48.7086	-17.7245	7	7	1130	Brosens et al. (2023)
Sahatritry	RF-2	48.6941	-17.7267	224	221	1051	Brosens et al. (2023)
Lovoka trib.	RF-3	48.6709	-17.6074	10	10	1388	Brosens et al. (2023)
Manampanihy trib.	MDG-1653D2	47.1884	-24.2253	209	202	932	Wang et al. (2021)
Isandra	MDG-1631B1	47.1919	-23.9111	409	409	943	Wang et al. (2021)
Mamandro trib.	MDG-1609A1	47.3116	-23.7053	279	279	226	Wang et al. (2021)
Mamandro trib.	MDG-1586D1	47.3339	-23.6826	236	236	314	Wang et al. (2021)
Mamandro	MDG-1610A1	47.4265	-23.7105	1239	720	249	Wang et al. (2021)
Manampotrana	MDG-1460C1	47.3126	-22.754	107	106	353	Wang et al. (2021)
Matatana	MDG-1405A1	47.495	-22.273	1266	1266	537	Wang et al. (2021)
Ionilahy	MDG-1318A2	47.6543	-21.7243	673	672	577	Wang et al. (2021)
Faraony headw.	MDG-1287B2	47.5865	-21.5769	591	583	823	Wang et al. (2021)
Andriambe trib.	MDG-1654A2	47.2848	-24.1175	316	315	428	Wang et al. (2021)
Manampatrana	MDG-1459B1	47.1243	-22.62	1323	1323	791	Wang et al. (2021)
Matsiatra	MDG-1199B1	46.8098	-20.9842	4776	3987	1254	Wang et al. (2021)

Mananjary	MDG-1234D1	47.9218	-21.3105	4999	2439	769	Wang et al. (2021)
Mananjary W	MDG-1204C1	47.6389	-21.1058	696	693	1012	Wang et al. (2021)
Mananjary N	MDG-1176C1	47.6684	-20.9148	1872	1494	1017	Wang et al. (2021)
Maintinandry	MDG-1147D1	47.5741	-20.7258	376	376	1266	Wang et al. (2021)
Sakaleona	MDG-1122C1	47.8663	-20.5848	312	312	1021	Wang et al. (2021)
Sakaleona	MDG-1152B1	48.3422	-20.6254	1221	606	728	Wang et al. (2021)
Sandranamba	MDG-1038C1	48.0527	-20.0395	1092	1092	1059	Wang et al. (2021)
Onive	MDG-1011B1	47.7647	-19.7094	4387	3426	1700	Wang et al. (2021)
Mania	MDG-1089D1	47.1344	-20.3795	2608	103	1495	Wang et al. (2021)
Sisaony	MDG-Antana2	47.5721	-19.0952	1369	144	1455	Wang et al. (2021)
Ikopa	MDG-Antana1	47.5972	-19.0239	1286	1286	1479	Wang et al. (2021)
Mangoro	MDG-1013B1	48.0804	-19.7526	11556	6728	1305	Wang et al. (2021)
Mangoro	MDG-1042A1	48.5845	-19.9129	17538	4863	1108	Wang et al. (2021)
Vohitra	MDG-0848C1	48.9692	-18.7325	2634	703	769	Wang et al. (2021)
Rongaronga	MDG-0849A2	49.1042	-18.6832	1061	1056	433	Wang et al. (2021)
Ivondro	MDG-0754A2	49.105	-18.1096	1687	1674	869	Wang et al. (2021)
Onibe	MDG-0657C1	49.3404	-17.6594	1956	1712	754	Wang et al. (2021)

Sup. Info 6.1, followed

Sample	Neutronic production	Fast muonic production	Slow muonic production	10Be concentration	Denudation	Integration time	Denudation	Outflow
	at/g/a	10^{-2} at/g/a	10^{-2} at/g/a	10^{4} at/g	mm/ka	ka	t/km^2/a	t/a
2004-2A	7.13	4.81	1.95	37.1 ± 1.4	13.1 ± 2.7	45.7	34.8 ± 7.1	4627 ± 941
2004-6A	7.83	4.93	2.05	58.6 ± 1.8	9.1 ± 1.9	66.1	24 ± 4.9	5048 ± 1039
2004-9A	7.78	4.92	2.04	100.1 ± 2.3	5.3 ± 1.1	113.5	14 ± 2.9	22325 ± 4575
2005-3B	5.06	4.38	1.63	41.1 ± 1.3	8.6 ± 1.8	69.8	22.8 ± 4.7	91 ± 19
2005-6	5.28	4.43	1.67	42.9 ± 1.2	8.6 ± 1.7	70.2	22.7 ± 4.6	4170 ± 848
2005-7	4.83	4.32	1.58	20.5 ± 0.6	16.5 ± 3.4	36.4	43.7 ± 8.9	306 ± 62
2006-1	7.85	4.94	2.06	57.4 ± 1.1	9.3 ± 1.9	64.5	24.7 ± 5	3649 ± 739
2006-2	8.14	4.98	2.09	65.8 ±1.5	8.4 ± 1.7	71.4	22.3 ± 4.5	7059 ± 1428
2006-3	8.07	4.97	2.09	55.1 ± 0.9	9.9 ± 2	60.6	26.2 ± 5.3	12671 ± 2539
2006-5	8	4.98	2.09	190.8 ± 2.8	2.8 ± 0.6	211.3	7.5 ± 1.5	30 ± 6
2006-6	5.62	4.5	1.72	62.4 ± 1.1	6.2 ± 1.3	96.5	16.5 ± 3.4	6049 ± 1237
2006-7	5.64	4.47	1.71	33.1 ± 0.8	11.8 ± 2.4	50.9	31.2 ± 6.4	368547 ± 75322
2006-8	4.64	4.23	1.53	28.3 ± 0.7	11.5 ± 2.3	52.4	30.4 ± 6	340012 ± 67735
2006-9	2.99	3.76	1.21	11.8 ± 0.3	18.3 ± 3.7	32.8	48.5 ± 9.8	3104 ± 627
2006-10	2.77	3.68	1.15	11.4 ± 0.3	17.8 ± 3.6	33.7	47.2 ± 9.5	661 ± 133
2006-11	2.75	3.67	1.15	6.9 ± 0.2	29 ± 6	20.7	77 ± 16	539 ± 112
2006-12	6.23	4.6	1.8	42.2 ± 0.8	10.1 ± 2.1	59.2	26.9 ± 5.5	521345 ± 106871
2006-13	2.98	3.75	1.2	6.7 ± 0.2	32.3 ± 6.7	18.6	85.7 ± 17.7	2228 ± 460
2006-14	2.72	3.66	1.14	4.6 ± 0.1	43.2 ± 8.7	13.9	114.3 ± 23.2	229 ± 46
2006-15	6.27	4.6	1.81	44.7 ± 0.9	9.6 ± 2	62.5	25.5 ± 5.2	489532 ± 100547
2006-16	4.3	4.16	1.48	34.3 ± 0.8	8.8 ± 1.8	67.9	23.4 ± 4.7	9835 ± 1994
2006-17	8.39	5.04	2.15	147.7 ± 2.7	3.8 ± 0.8	156.2	10.2 ± 2.1	1344 ± 272
2006-18	7.45	4.87	2.01	91 ± 1.5	5.6 ± 1.1	107.3	14.8 ± 3	1911 ± 393
2006-19A	5.73	4.51	1.73	32.5 ± 0.8	12.2 ± 2.5	49.1	32.4 ± 6.6	106529 ± 21666
2006-21	5.57	4.48	1.7	12.5 ± 0.3	30.8 ± 6.2	19.5	81.6 ± 16.5	39763 ± 8035
2006-22	5.5	4.46	1.69	16.1 ± 0.4	23.7 ± 5	25.3	62.9 ± 13.1	118473 ± 24727
2006-23	3.96	4.06	1.4	5.7 ± 0.2	49.2 ± 10.2	12.2	130.4 ± 27.1	1174 ± 244
2006-24	4.89	4.29	1.57	14.5 ± 0.4	23.5 ± 4.8	25.6	62.2 ± 12.7	119970 ± 24482
2006-25	6.98	4.72	1.88	14.5 ± 1.2	33.1 ± 7.2	18.1	87.6 ± 19.1	44521 ± 9712
2006-26	4	4.02	1.37	49.6 ± 0.4	5.7 ± 1.1	105.6	15.1 ± 3	452 ± 91
2006-27	5.8	4.47	1.69	16.7 ± 0.3	23.9 ± 4.7	25.1	63.4 ± 12.6	5068 ± 1006
2006-28	7.02	4.73	1.89	54.9 ± 1	8.7 ± 1.8	68.9	23.1 ± 4.6	9068 ± 1825
2006-29	8.14	4.95	2.07	51.6 ± 0.9	10.7 ± 2.2	55.9	28.4 ± 5.9	71257 ± 14688
2006-30	10.07	5.28	2.34	26.3 ± 0.6	25.7 ± 5.3	23.4	68.1 ± 14	3745 ± 768
2006-31	9.15	5.14	2.23	41.2 ± 1	14.9 ± 3	40.2	39.5 ± 8	58552 ±11801
2011-01	4.69	4.23	1.53	10.5 ± 0.3	31.3 ± 6.4	19.1	83.1 ± 17.1	393429 ± 80850
2011-02	4.47	4.17	1.49	9.7 ± 0.2	32.3 ± 6.5	18.6	85.5 ± 17.3	173754 ± 35230
2011-03	3.94	4.02	1.38	10.1 ± 0.3	27.6 ± 5.6	21.8	73.1 ± 14.9	103322 ± 21053

2011-04	4.15	4.09	1.43	13.3 ± 0.3	22 ± 4.4	27.3	58.3 ± 11.7	69726 ± 14013
2011-05	3.69	3.95	1.33	9.5 ± 0.2	27.6 ± 5.6	21.7	73.2 ± 14.9	81996 ± 16666
2011-06	3.77	4	1.36	7.7 ± 0.2	34.6 ± 7	17.4	91.6 ± 18.6	10992 ± 2228
2011-07	6.65	4.62	1.81	73.4 ± 1.2	6.2 ± 1.3	97.1	16.4 ± 3.3	19626 ± 3990
2011-08	7.52	4.75	1.92	85.1 ± 2.6	6 ± 1.2	100.1	15.9 ± 3.2	9135 ± 1856
2011-09	6.15	4.52	1.73	97.8 ± 1.8	4.3 ± 0.9	138.8	11.5 ± 2.3	8589 ± 1740
2011-10	5.5	4.37	1.62	8.7 ± 0.3	43.8 ± 9.1	13.7	116 ± 24	24129 ± 4991
2011-11	5.62	4.38	1.64	25.8 ± 0.4	15.1 ± 3.1	39.8	40 ± 8.2	1473489 ± 3007770
2011-12	4.43	4.1	1.43	9.4 ± 0.2	33.1 ± 6.7	18.1	87.6 ± 17.7	351837 ± 70989
2011-13	3.92	3.98	1.35	9.4 ± 0.2	29.5 ± 6	20.3	78.2 ± 16	2112 ± 433
2011-14	4.01	4	1.36	9 ±0.2	31.5 ± 6.5	19	83.6 ± 17.1	1337 ± 274
2011-15	4.67	4.18	1.48	11 ± 0.2	29.7 ± 6.1	20.2	78.7 ± 16.3	79 ± 16
2011-16	5.48	4.36	1.61	15.7 ± 0.3	24.1 ± 4.9	24.9	64 ± 12.9	22197 ± 4474
2011-17	4.03	3.97	1.34	14 ± 0.5	20.3 ± 4.2	29.5	53.9 ± 11.1	39653 ± 8149
2011-18	5.08	4.22	1.52	13.9 ± 0.2	25.4 ± 5.2	23.6	67.3 ± 13.7	1898127 ± 386523
2011-19	4.94	4.22	1.52	19.2 ± 0.4	17.9 ± 3.6	33.6	47.4 ± 9.6	106665 ± 21723
2011-20	4.15	4.02	1.37	6.2 ± 0.2	47 ± 9.6	12.8	124.7 ± 25.3	9224 ± 1873
2011-21	5.39	4.34	1.59	29.1 ± 0.4	12.8 ± 2.6	46.8	34 ± 6.9	8118 ± 1659
2011-22	5.34	4.33	1.59	27.5 ± 0.5	13.4 ± 2.7	44.6	35.6 ± 7.2	36 ± 7
2011-23	6.64	4.58	1.79	57.2 ± 0.9	7.9 ± 1.6	75.5	21.1 ± 4.3	30972 ± 6295
2011-24	5.75	4.43	1.67	53 ± 0.8	7.5 ± 1.5	80.2	19.8 ± 4	2220 ± 450
2011-25	7.34	4.77	1.93	64.7 ± 1.3	7.7 ± 1.6	77.8	20.4 ± 4.2	9542 ± 1975
2011-26	7.66	4.86	1.99	56.3 ± 0.9	9.2 ± 1.9	65	24.4 ± 5	7700 ± 1578
RL-1	5.11	4.39	1.63	20 ± 0.7	17.7 ± 3.7	33.8	47 ± 9.8	282 ± 59
RL-2	5.59	4.5	1.72	36.4 ± 0.7	10.6 ± 2.2	56.6	28.1 ± 5.8	197 ± 40
RF-1	6.14	4.62	1.81	67.5 ± 1.5	6.3 ± 1.3	96	16.6 ± 3.4	99 ± 20
RF-2	5.79	4.55	1.75	47.6 ± 1.2	8.4 ± 1.7	71.4	22.3 ± 4.5	4990 ± 1013
RF-3	7.36	4.87	2	51.3 ± 1	9.9 ± 2	60.9	26.1 ± 5.3	261 ± 53
MDG-1653D2	6.37	4.45	1.69	33.4 ± 1.4	13 ± 2.6	46	34.6 ± 7	7223 ± 1466
MDG-1631B1	6.24	4.45	1.69	46.3 ± 1.6	9.2 ± 1.9	64.9	24.5 ± 5	9990 ± 2054
MDG-1609A1	3.58	3.8	1.24	28.2 ± 1	9 ± 1.9	66.5	23.9 ± 4.9	6651 ± 1373
MDG-1586D1	3.88	3.88	1.29	24.1 ± 0.8	11.4 ± 2.3	52.7	30.2 ± 6.2	7056 ± 1439
MDG-1610A1	3.65	3.82	1.25	34.1 ± 1.2	7.6 ± 1.5	79.4	20 ± 4.1	24826 ± 5034
MDG-1460C1	3.79	3.91	1.3	28.3 ± 1.1	9.5 ± 2	63.3	25.1 ± 5.2	2686 ± 555
MDG-1405A1	4.42	4.07	1.42	14.5 ± 0.8	21.5 ± 4.5	28	56.9 ± 11.9	71935 ± 15085
MDG-1318A2	4.48	4.11	1.44	13.7 ± 0.6	22.9 ± 4.8	26.2	60.8 ± 12.7	40918 ± 8570
MDG-1287B2	5.27	4.33	1.6	15.6 ± 0.8	23.5 ± 4.9	25.6	62.2 ± 12.9	36759 ± 7623
MDG-1654A2	4.34	3.98	1.36	40.3 ± 1.2	7.5 ± 1.5	79.6	20 ± 4.1	6309 ± 1282
MDG-1459B1	5.33	4.29	1.58	39.9 ± 1.3	9.2 ± 1.9	64.9	24.5 ± 5.1	31822 ± 6654
MDG-1199B1	7.06	4.72	1.89	60.1 ± 2.1	8 ± 1.6	74.7	21.3 ± 4.3	101709 ± 20741
MDG-1234D1	5.16	4.3	1.58	15.8 ± 0.9	22.8 ± 4.8	26.3	60.4 ± 12.7	301756 ± 63414
MDG-1204C1	5.97	4.5	1.72	28.6 ± 1.3	14.4 ± 2.9	41.8	38 ± 7.8	26481 ± 5439
MDG-1176C1	5.95	4.5	1.73	20.2 ± 1.1	20.3 ± 4.2	29.6	53.7 ± 11.1	100508 ± 20730

MDG-1147D1	7.06	4.74	1.9	29.4 ±0.8	16.4 ± 3.3	36.6	43.4 ± 8.8	16322 ± 3320
MDG-1122C1	5.95	4.51	1.73	29.1 ± 1.2	14.1 ± 2.9	42.6	37.3 ± 7.7	11640 ± 2417
MDG-1152B1	4.83	4.24	1.53	95.9 ± 3.3	3.5 ± 0.7	170.7	9.3 ± 1.9	11372 ± 2365
MDG-1038C1	6.11	4.55	1.76	22.5 ± 1.5	18.8 ± 4.1	31.9	49.8 ± 10.7	53551 ± 11460
MDG-1011B1	9	5.11	2.21	89.7 ± 4.4	6.8 ± 1.4	88.3	18 ± 3.7	78983 ± 16178
MDG-1089D1	8.17	4.95	2.08	59.7 ± 2.5	9.3 ± 1.9	64.6	24.6 ± 5.1	64193 ± 13319
MDG-Antana2	7.91	4.94	2.06	60.7 ± 1.8	8.8 ± 1.8	68	23.4 ± 4.7	14603 ± 2937
MDG-Antana1	7.92	4.94	2.06	48.9 ± 1.5	11 ± 2.2	54.5	29.2 ± 5.9	37321 ± 7604
MDG-1013B1	6.99	4.73	1.91	28.9 ± 1.5	16.5 ± 3.5	36.3	43.8 ± 9.2	506700 ± 106054
MDG-1042A1	6.16	4.55	1.77	14.2 ± 0.9	29.8 ± 6.4	20.1	79 ± 16.9	1386224 ± 296681
MDG-0848C1	3.36	3.85	1.27	11.3 ± 0.6	21.3 ± 4.5	28.1	56.5 ± 12	148885 ± 31506
MDG-0849A2	3.81	3.98	1.36	13.3 ± 0.9	20.4 ± 4.2	29.5	54 ± 11.2	57275 ± 11929
MDG-0754A2	5.16	4.38	1.63	15.8 ± 0.7	22.7 ± 4.7	26.4	60.3 ± 12.5	101660 ± 21135
MDG-0657C1	4.79	4.28	1.56	15.3 ± 0.7	21.9 ± 4.6	27.4	58 ± 12.2	113393 ± 23822

Sup. Info. 6.2: *Data presented in Large et al. 2025 (Chapter 5) (in grey), and new data from this work. Ratios of the blanks are given at the end. Spike values were of 2123 ± 13ppm of ^{9}Be.*

River	Sample	Latitude	Longitude	Altitude	Basin averaged altitude	Drainage area	Quartz bearing area	Neutronic production	Fast muonic production	Slow muonic production
		DD	DD	m	m	km^2	km^2	at/g/a	10^{-2} at/g/a	10^{-2} at/g/a
Tsiribihina	8	-19.7103	44.584	5	868	47601	41550	5.53	4.36	1.64
Mangoky	14	-21.8352	43.8728	46	770	53033	49000	5.22	4.24	1.55
Onilahy	18	-23.4545	43.9004	29	688	31989	29823	4.99	4.19	1.51
Manambolo	9	-19.1447	44.8137	46	590	11618	10968	4.31	4.12	1.46
Morondava	10	-20.3368	44.4019	18	299	6213	5390	3.5	3.87	1.28
Fiheranana	17	-23.3058	43.6592	10	614	7723	3811	4.65	4.13	1.46
Mania (Tsiribihina trib.)	5	-19.7955	45.5325	73	1220	17810	16295	6.94	4.69	1.88
Manambolo (Tsiribihina trib.)	6	-20.0118	45.5472	92	714	1864	1848	4.74	4.23	1.53
Maharivo	11	-20.746	44.4713	104	339	3082	2086	3.62	3.91	1.3
Lampaolo	12	-21.2016	44.3282	201	310	520	205	3.57	3.88	1.29
Manombo	16	-22.8839	43.5803	59	204	2142	1028	3.44	3.79	1.23
Andiolava (Onilahy trib.)	20	-22.4996	45.6292	908	1027	752	752	6.15	4.52	1.73
Mananantanana (Mangoky trib.)	22	-21.8364	46.8764	940	1144	1175	1175	6.66	4.62	1.81
Mania (Tsiribihina trib.)	24	-20.3932	47.163	1184	1491	2511	2510	8.14	4.95	2.07

Sample	^{10}Be/^{9}Be	^{10}Be counts	Mass of quartz	^{9}Be	Measured ^{10}Be	Denudation	Integration time	Denudation	Outflow
	10^{-14}		g	10^{19} at	10^{4} at/g	mm/ka	ka	t/km^2/a	10^{4} t/a
8	21.6 ± 0.60	1651	20.1	3	31.8 ± 0.9	12.0 ± 2.5	50,0	31.8 ± 6.6	151.5 ± 31.2
14	9.2 ± 0.28	1255	17.8	3	15.3 ± 0.5	23.6 ± 4.9	25.4	62.6 ± 12.9	331.7 ± 68.4
18	10 ± 0.45	833	21.7	3	13.6 ± 0.6	25.6 ± 5.2	23.4	67.9 ± 13.8	217.3 ± 44.1
9	6.8 ± 0.22	1225	13.8	3	14.5 ± 0.5	20.8 ± 4.3	28.9	55.0 ± 11.4	63.9 ± 13.3
10	5.9 ± 0.40	595	21.1	3	8.3 ± 0.6	30.1 ± 6.4	19.9	79.7 ± 17.0	49.5 ± 10.6
17	9.9 ± 0.41	787	21.6	3	13.5 ± 0.6	24.3 ± 5.1	24.7	64.3 ± 13.4	49.7 ± 10.4
5	30.7 ± 0.87	2281	19.5	2.9	46.1 ± 1.3	10.3 ± 2.1	58.3	27.3 ± 5.5	48.5 ± 9.8
6	17.2 ±0.56	1301	16.2	2.9	31.1 ± 1	10.7 ± 2.2	56.3	28.2 ± 5.8	5.3 ± 1.1
11	5.8 ± 0.21	995	15.1	2.9	11.1 ± 0.4	23.2 ± 4.7	25.8	61.5 ± 12.5	19 ± 3.8
12	9.3 ± 0.36	1008	16.7	2.9	16.2 ± 0.6	15.7 ± 3.3	38.3	41.5 ± 8.7	2.2 ± 0.5
16	6.7 ± 1.00	75	17.1	2.9	11.3 ± 1.7	22.2 ± 5.6	27.1	58.7 ± 14.9	12.6 ± 3.2
20	61.0 ± 1.33	3143	16.8	2.9	105.9 ± 2.3	4.0 ± 0.8	150.7	10.6 ± 2.2	0.8 ± 0.2
22	41.2 ± 3.45	146	18.1	2.9	66.1 ± 5.5	6.9 ± 1.5	86.8	18.3 ± 4.0	2.2 ± 0.5
24	36.3 ± 0.99	2016	19.8	2.9	53.3 ± 1.5	10.4 ± 2.1	57.9	27.5 ±5.6	6.9 ± 1.4

	$^{10}Be/^{9}Be$ 10^{-16}	^{10}Be counts	^{9}Be 10^{19} at
Batch 6_7	4.0 ± 1.4	8	3.0
	4.0 ± 1.4	9	3.0
	1.7 ± 1.3	2	2.9
	6.0 ± 1.8	13	3.7

4

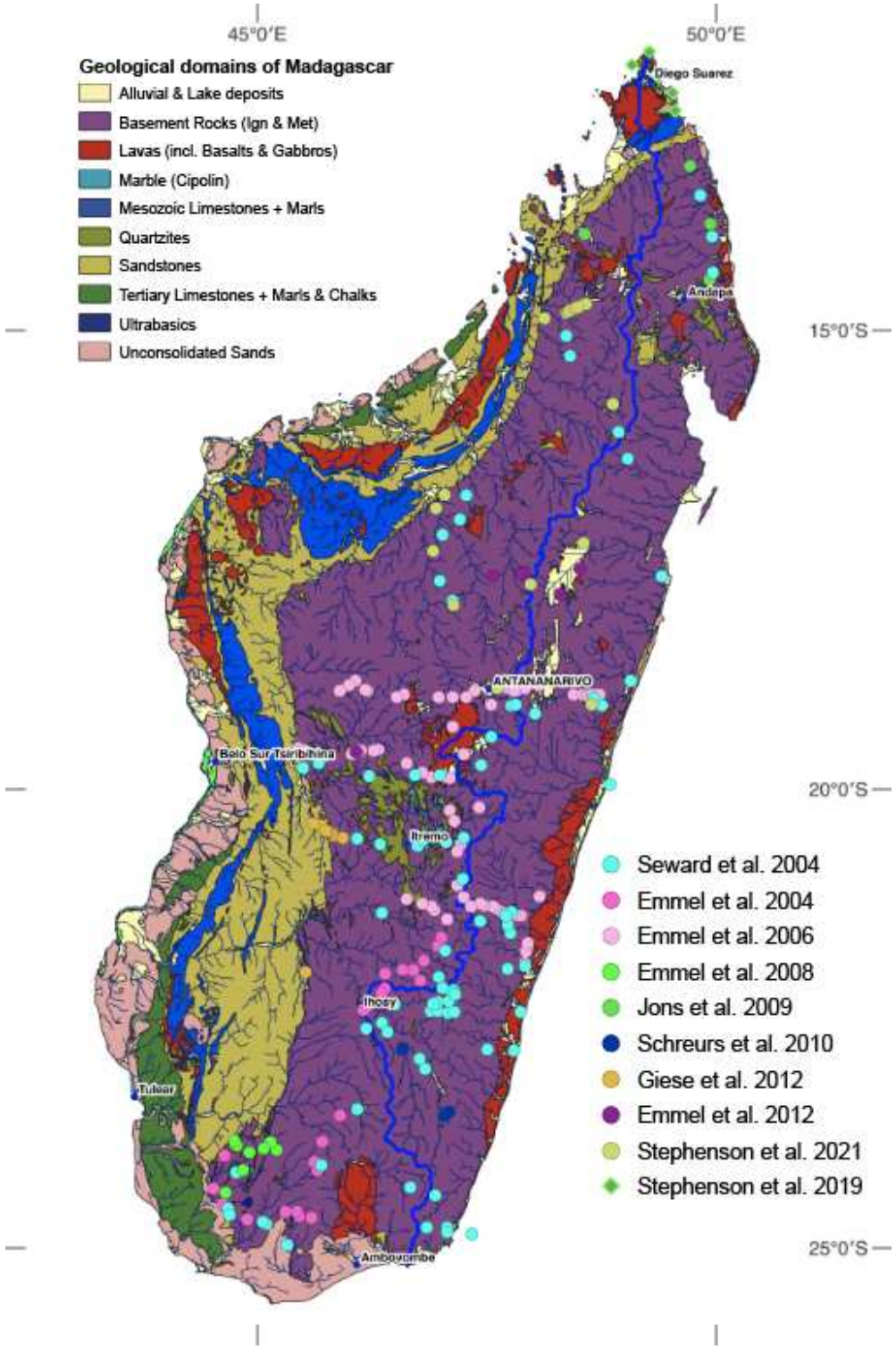

Sup. Info. 6.3: Location of thermochronological samples used in this work. Stephenson et al. 2019 is the location of dated marine terraces. Legend for geological domains is the same as in figure 1B. Blue continuous line is the main EW drainage divide of Madagascar

Sup. Info. 6.4: Thermochronology-derived denudation rates for every thermochronological study of Madagascar using AFT.

Sample	DT 250-100	DT 100-35	DT 35-0	Denudation 250-100 (m/Ma)	Denudation 100-35 (m/Ma)	Denudation 35-0 (m/Ma)
Seward et al. 2004						
South of RSZ (Section D-D')						
M101	-20	20	45	-4.4	10.3	42.9
M28	70	-20	45	15.6	-10.3	42.9
M99		10	35		5.1	33.3
M98	60	-10	45	13.3	-5.1	42.9
M97	50	10	35	11.1	5.1	33.3
M37	40	20	35	8.9	10.3	33.3
M81	30	5	60	6.7	2.6	57.1
M74		40	15		20.5	14.3
M85		50	15		25.6	14.3
M94			15			14.3
			Area mean	**8.5**	**7.1**	**32.9**
NE of RSZ (Section C-C')						
M64	-30	40	35	-6.7	20.5	33.3
M115	10	30	15	2.2	15.4	14.3
M185	10	40	25	2.2	20.5	23.8
M184	10	20	15	2.2	10.3	14.3
			Area mean	**0**	**16.7**	**21.4**
Vertical profile						
M103	10	15	20	2.2	7.7	19
M104	0	15	20	0	7.7	19
M106	10	20	15	2.2	10.3	14.3
M105	-10	20	25	-2.2	10.3	23.8
M107	-10	25	20	-2.2	12.8	19
M110	10	0	25	2.2	0	23.8
M112	10	10	15	2.2	5.1	14.3
M114	20	10	25	4.4	5.1	23.8
			Area mean	**0.7**	**10.5**	**20.2**
Northern regions						
Section A-A'						
M147	0	0	35	0	0	33.3
M148	-20	30	25	-4.4	15.4	23.8
M145	30	-20	55	6.7	-10.3	52.4
M149	40	20	25	8.9	10.3	23.8
M151	30	20	35	6.7	10.3	33.3
M152	20	0	25	4.4	0	23.8
M130		10	15		5.1	14.3
M131	60	0	35	13.3	0	33.3
M132	60	-10	45	13.3	-5.1	42.9
M133		50	45		25.6	42.9
M139		80	15		41	14.3
M134		70	25		35.9	23.8
M138		70	25		35.9	23.8
M137		50	45		25.6	42.9
			Area mean	**6.1**	**13.6**	**30.6**
Section B-B'						
M125	-30	10	45	-6.7	5.1	42.9
M126	-10	0	35	-2.2	0	33.3
M124	50	10	35	11.1	5.1	33.3
M121		-10	45		-5.1	42.9
M119	10	10	25	2.2	5.1	23.8
M128	70	-10	35	15.6	-5.1	33.3
			Area mean	**4**	**0.9**	**34.9**

			Article mean	**4.2**	**9.4**	**28.8**
Emmel et al. 2004						
North of the BRSZ/ZFSZ						
BE050	-40	0	45	-8.9	0	42.9
BE163-6	10	-10	55	2.2	-5.1	52.4
BE163-13	10	-20	55	2.2	-10.3	52.4
			Area mean	**-1.5**	**-5.1**	**49.2**
Within the BRSZ/ZFSZ						
BE062	-30	-10	45	-6.7	-5.1	42.9
BE065	-20	10	25	-4.4	5.1	23.8
			Area mean	-5.6	0	33.4
South of the BRSZ/ZFSZ						
BE075	-10	10	15	-2.2	5.1	14.3
BE083		0	45		0	42.9
BE090		0	45		0	42.9
BE094		0	55		0	52.4
			Area mean	**-2.2**	**1.3**	**38.1**
			Article mean	**-3**	**-1.1**	**40.8**
Emmel et al. 2006						
Miandrivazo area						
BE030	-20	20	15	-4.4	10.3	14.3
BE037	-10	20	15	-2.2	10.3	14.3
BE038	-20	10	15	-4.4	5.1	14.3
			Area mean	**-3.7**	**8.6**	**14.3**
Domain 3						
BE013	50	30	5	11.1	15.4	4.8
BE014	60	-10	35	13.3	-5.1	33.3
BE016	-10	30	5	-2.2	15.4	4.8
			Area mean	**7.4**	**8.6**	**14.3**
Ambohiby area						
BE110	10	30	15	2.2	15.4	14.3
BE109			5			4.8
			Area mean	**2.2**	**15.4**	**9.6**
Northern profile						
BE114		20	15		10.3	14.3
BE115		10	5		5.1	4.8
BE117			10			9.5
BE119		15	10		7.7	9.5
BE120			5			4.8
			Area mean		**7.7**	**8.6**
			Article mean	**1.9**	**9**	**11.4**
Emmel et al. 2008						
BE184	40	0	45	8.9	0	42.9
BE185	20	0	25	4.4	0	23.8
BE193	-10	30	15	-2.2	15.4	14.3
BE196	40	20	25	8.9	10.3	23.8
BE203-2	20	10	35	4.4	5.1	33.3
			Article mean	**4.9**	**6.2**	**27.6**
Emmel et al. 2012						
BE021	30	0	5	6.7	0	4.8
BE065	50	10	5	11.1	5.1	4.8
BE107		20	15		10.3	14.3
BE122		50	5		25.6	4.8

BE128	20	0	35	4.4	0	33.3
BE129		40	5		20.5	4.8
BE130		40	5		20.5	4.8
BE136	30	0	25	6.7	0	23.8
BE151	100	0	5	22.2	0	4.8
			Article mean	**10.2**	**9.1**	**11.1**
Jöns et al. 2009						
MD73-2-03	210	0	45	46.7	0	42.9
Giese et al_2012						
Malaimbandy area						
Central Domain						
JG52	0	-10	55	0	-5.1	52.4
JG50	0	0	45	0	0	42.9
JG49	-40	20	25	-8.9	10.3	23.8
JG47	-40	20	25	-8.9	10.3	23.8
			Area mean	**-4.5**	**3.9**	**35.7**
Eastern Domain						
JG40	-30	40	15	-6.7	20.5	14.3
Ilotro area						
JG68	-10	-20	35	-2.2	-10.3	33.3
JG69	-10	-20	25	-2.2	-10.3	23.8
			Area mean	**-2.2**	**-10.3**	**28.6**
			Article mean	**-4.1**	**2.2**	**30.6**
Stephenson et al. 2021						
Central Transect						
2	30	0	35	6.7	0	33.3
3	20	20	15	4.4	10.3	14.3
4	60	10	15	13.3	5.1	14.3
5	20	20	25	4.4	10.3	23.8
			Area mean	**7.2**	**6.4**	**21.4**
Northern Transect						
7b	30	-10	45	6.7	-5.1	42.9
11	20	0	45	4.4	0	42.9
13	30	20	15	6.7	10.3	14.3
16	60	10	5	13.3	5.1	4.8
			Area mean	**7.8**	**2.6**	**26.2**
			Article mean	**7.5**	**4.5**	**23.8**
Joint invers modelling						
2	40	-10	25	8.9	-5.1	23.8
3	40	-5	20	8.9	-2.6	19
4	90	0	15	20	0	14.3
7a	50	0	25	11.1	0	23.8
7b	-20	30	35	-4.4	15.4	33.3
8	50	10	45	11.1	5.1	42.9
10	10	10	45	2.2	5.1	42.9
16	50	10	15	11.1	5.1	14.3
			Article mean	**8.6**	**2.9**	**26.8**

	Minimum uplift	Maximum uplift	Mean uplift	Median	Mean uplift rate
	m	m			m/Ma
90-66 Ma					
North	226	611	307 ± 87	268	12.8 ± 3.6
East	231	393	329 ± 36	328	13.7 ± 1.5
South-West	241	338	288 ± 29	291	12 ± 1.2
Center	251	357	304 ± 25	300	12.7 ± 1
34-0 Ma					
North	458	916	712 ± 104	726	21 ± 3.1
East	787	943	866 ± 31	864	25.5 ± 0.9
South-West	494	788	648 ± 70	653	19.1 ± 2.1
Center	607	911	778 ± 60	785	22.9 ± 1.8

Sup. Info. 6.5: Statistics of uplift calculated from the extrapolated uplift maps of Jiao et al. (2022), using ArcGIS Pro. Uncertainties are the standard deviation for each calculated mean.

Area	LTT-denudation 250-100 m/Ma	LTT-denudation 100-35 m/Ma	LTT-denudation 35-0 m/Ma
North	8.9 ± 1.8	3.4 ± 0.7	28 ± 5.6
East	1.5 ± 0.3	21.7 ± 4.3	21.9 ± 4.4
South	6.1 ± 1.2	5.6 ± 1.1	32.6 ± 6.5
Central	1.7 ± 0.3	7 ± 1.4	22.8 ± 4.6

Sup. Info. 6.6 : Mean LTT-denudation rates for the four areas considered and the three time periods. All uncertainties are 20% of the values.

Conclusions and Perspectives

Extracting conclusions from a PhD manuscript is no easy task, but it is mine in this section.

A first important result of this work is that it successfully proves that turbidites are important archives, not only for studying continental processes of the past, but also to constrain transport durations of sediments from source to sink and understand the processes and triggers of this transport. Our work suggests that turbidity currents mobilize sediments that were transported or stored for up to 12.9 ± 0.2 ka (Figure c.1). This value is bound to be highly variable from one region to the other, and additional studies are needed to better constrain and understand these wonderful archives.

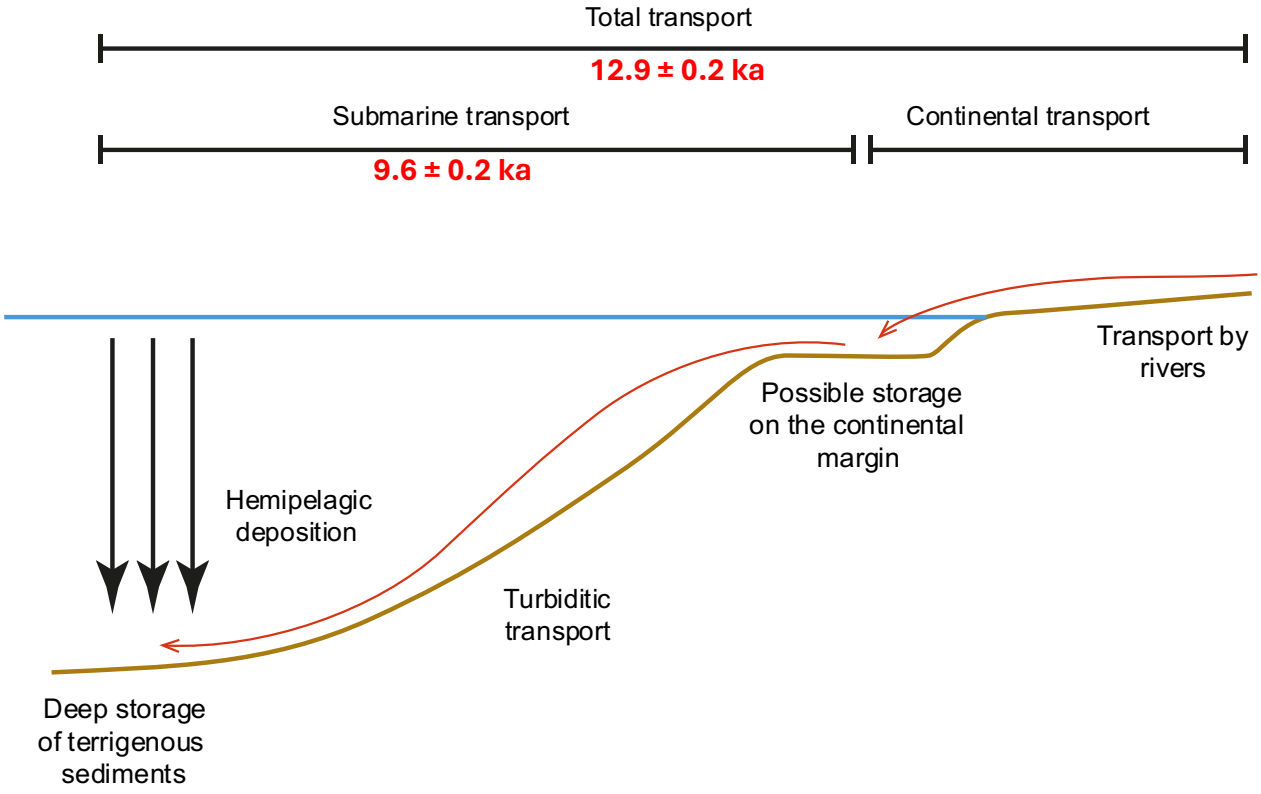

Figure c.1: Summary of transport times found from our high-resolution dating of turbidites.

The effect of the Quaternary climatic cycles is less straightforward to resolve, and I do not have the pretention of solving on my own this long-lasting question. However, this work has successively shown that denudation rates of tropical regions may very well be the Achilles' heel to Molnar's theory of increased global denudation due to the Quaternary climate cyclic instabilities. In fact, this PhD very clearly demonstrates that Quaternary denudation rates of Tropical regions are not controlled by the Quaternary climatic cycles (Figure c.2). In Gabon, denudation rates have remained near constant over the past 3.5 Ma years. The MPT however, appears to have affected the paleo-denudation rates of this tropical catchment. Although our record contains some hiatuses, Pliocene values are indistinguishable

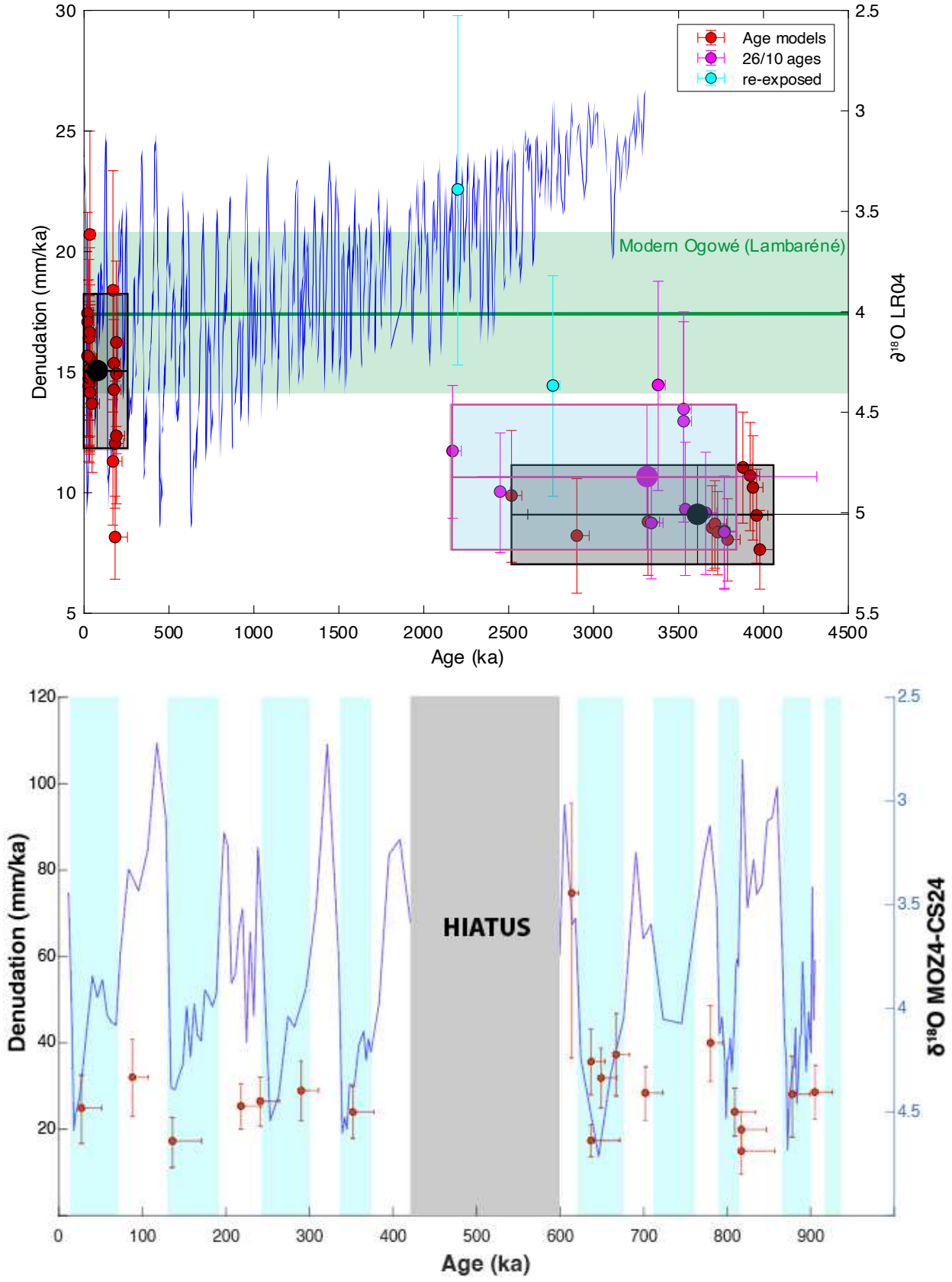

Figure c.2: Paleo-denudation records of SW Madgascar (bottom) and Gabon (top) showing constant denudation rates in these two regions over the Plio-Pliostocene, with a possible effect of the MPT in Gabon.

from values measured in the modern catchment of the Ogowé river. This allows us to safely postulate that no major variation in denudation occurred in this region over the Quaternary.

In Madagascar, denudation rates were steady throughout the past 900 ka, with no visible effect of the MPT. This higher resolution dataset allows capturing the effect, or rather the absence of effect, of glacial/interglacial cyclicity on denudation rates. These two datasets are interestingly complimentary, as they allow to safely postulate that **neither the initiation of the Quaternary climatic cyclicity, nor the cyclicity itself, affect denudation rates of non-glacial, tectonically quiescent and slowly eroding Tropical regions.**

These results imply that, although a Late Cenozoic increase in denudation rates may have occurred in some regions, provoked by the initiation of the Quaternary climatic cycles, this increase was far from being global. Two possible interpretations thus arise, (i) the effect of Quaternary climate on denudation was spatially heterogeneous or (ii) the Quaternary cyclicity of climate itself was spatially heterogeneous, especially on continental, Tropical regions. These hypotheses bring us to the limits of this work, as our data does not allow us to favor one or the other conclusion.

We suggest that in these tropical regions, very short climatic variations over scales of < 1 ka, may control the evolution of denudation rates. It is more than possible that the proximity of the ITCZ and the monsoonal type of climate controls denudation on much shorter timescales than the ones investigated in this work. This hypothesis remains at this point, purely speculative since both paleo-denudation rate and paleoclimatic data at sufficient resolutions are lacking in these regions. The Tropics remain understudied, making them crucial areas to understand the Earth system as a whole.

Although short-lived (i.e., < 1 ka) have yet to be resolved, the control of denudation over larger timescales was also investigated in this work. Our new analysis of previously published work has allowed us to reconstruct the Cenozoic denudation of this Tropical Island. We have successfully shown that Madagascar has experienced variations in denudation by only one order of magnitude over 100 Ma, this amplitude being consistent with modern spatial variability of denudation rates. We propose that Cenozoic paleo-denudation rates of Madagascar are controlled by large-wavelength mantle plume-related tectonics. Our knowledge of this island, from new and previously published data, allows us to consider that Madagascar has been in a landscape steady state over Meso-Cenozoic times, with denudation rate variations closely following the evolution of uplift. More importantly, uplift and denudation rates remain within the same order of magnitude over the past 100 Ma, allowing us to suggest that the relief of Madagascar is inherited from the Late Mesozoic. These results bring new constraints to erosion mechanisms of slowly eroding, tectonically quiescent regions, and show that tectonics can control long term denudation rates, even in anorogenic settings.

Future work should concentrate on better constraining the age of sediments transported by turbidity currents, as well as the triggers that lead to their initiation, and the processes involved in the consequent flow. To do so, I believe the key is to combine different dating methods (e.g., ^{14}C, OSL, $^{26}Al/^{10}Be$, …) with a thorough sedimentary analysis of the deposit itself. This should be done in different settings to

test the effect of bathymetry, topography, lithology, tectonics, climate and denudation on these deposits. Turbidites are archives recording sediments at all resolutions and scales, and in all climatic and tectonic settings. The lack of constraint on the processes controlling them and the sediments they carry is the only wall left that we must break to open the way for global analysis of continental processes using them.

Tropical regions must be further studied. We have shown that they do not erode following the Quaternary climate, but we have only scratched the surface to begin to understand these regions. Precise paleoclimatic recordings are crucial. High resolution geomorphological mapping along with collection of data on land to allow the quantification of the geomorphic processes controlling these landscapes is of the upmost importance.

References

Acosta, V.T., Schildgen, T.F., Clarke, B.A., Scherler, D., Bookhagen, B., Wittmann, H., Von Blanckenburg, F., Strecker, M.R., 2015. Effect of vegetation cover on millennial-scale landscape denudation rates in East Africa. Lithosphere 7, 408–420. https://doi.org/10.1130/L402.1

Al-Hajri, Y., White, N., Fishwick, S., 2009. Scales of transient convective support beneath Africa. Geology 37, 883–886. https://doi.org/10.1130/G25703A.1

Andermann, C., Bonnet, S., Crave, A., Davy, P., Longuevergne, L., Gloaguen, R., 2012. Sediment transfer and the hydrological cycle of Himalayan rivers in Nepal. Comptes Rendus Géoscience 344, 627–635. https://doi.org/10.1016/j.crte.2012.10.009

Andò, S., Garzanti, E., 2014. Raman spectroscopy in heavy-mineral studies. Geol. Soc. Lond. Spec. Publ. 386, 395–412. https://doi.org/10.1144/SP386.2

Andò, S., Morton, A., Garzanti, E., 2014. Metamorphic grade of source rocks revealed by chemical fingerprints of detrital amphibole and garnet. Geol. Soc. Lond. Spec. Publ. 386, 351–371. https://doi.org/10.1144/SP386.5

Andriampenomanana, F., Nyblade, A.A., Wysession, M.E., Durrheim, R.J., Tilmann, F., Julià, J., Pratt, M.J., Rambolamanana, G., Aleqabi, G., Shore, P.J., Rakotondraibe, T., 2017. The structure of the crust and uppermost mantle beneath Madagascar. Geophys. J. Int. 210, 1525–1544. https://doi.org/10.1093/gji/ggx243

Anthony, E.J., 2015. Wave influence in the construction, shaping and destruction of river deltas: A review. Mar. Geol. 361, 53–78. https://doi.org/10.1016/j.margeo.2014.12.004

Antonelli, A., Smith, R.J., Perrigo, A.L., Crottini, A., Hackel, J., Testo, W., Farooq, H., Torres Jiménez, M.F., Andela, N., Andermann, T., Andriamanohera, A.M., Andriambololonera, S., Bachman, S.P., Bacon, C.D., Baker, W.J., Belluardo, F., Birkinshaw, C., Borrell, J.S., Cable, S., Canales, N.A., Carrillo, J.D., Clegg, R., Clubbe, C., Cooke, R.S.C., Damasco, G., Dhanda, S., Edler, D., Faurby, S., De Lima Ferreira, P., Fisher, B.L., Forest, F., Gardiner, L.M., Goodman, S.M., Grace, O.M., Guedes, T.B., Henniges, M.C., Hill, R., Lehmann, C.E.R., Lowry, P.P., Marline, L., Matos-Maraví, P., Moat, J., Neves, B., Nogueira, M.G.C., Onstein, R.E., Papadopulos, A.S.T., Perez-Escobar, O.A., Phelps, L.N., Phillipson, P.B., Pironon, S., Przelomska, N.A.S., Rabarimanarivo, M., Rabehevitra, D., Raharimampionona, J., Rajaonah, M.T., Rajaonary, F., Rajaovelona, L.R., Rakotoarinivo, M., Rakotoarisoa, A.A., Rakotoarisoa, S.E., Rakotomalala, H.N., Rakotonasolo, F., Ralaiveloarisoa, B.A., Ramirez-Herranz, M., Randriamamonjy, J.E.N., Randriamboavonjy, T., Randrianasolo, V., Rasolohery, A., Ratsifandrihamanana, A.N., Ravololomanana, N., Razafiniary, V., Razanajatovo, H., Razanatsoa, E., Rivers, M., Sayol, F., Silvestro, D., Vorontsova, M.S., Walker, K., Walker, B.E., Wilkin, P., Williams, J., Ziegler, T., Zizka, A., Ralimanana, H., 2022. Madagascar's extraordinary biodiversity: Evolution, distribution, and use. Science 378, eabf0869. https://doi.org/10.1126/science.abf0869

Archibald, D.B., Collins, A.S., Foden, J.D., Payne, J.L., Holden, P., Razakamanana, T., 2019. Late syn- to post-collisional magmatism in Madagascar: The genesis of the Ambalavao and Maevarano Suites. Geosci. Front. 10, 2063–2084. https://doi.org/10.1016/j.gsf.2018.07.007

Archibald, D.B., Collins, A.S., Foden, J.D., Payne, J.L., Taylor, R., Holden, P., Razakamanana, T., Clark, C., 2015. Towards unravelling the Mozambique Ocean conundrum using a triumvirate of zircon isotopic proxies on the Ambatolampy Group, central Madagascar. Tectonophysics 662, 167–182. https://doi.org/10.1016/j.tecto.2015.02.018

Archibald, D.B., Collins, A.S., Foden, J.D., Razakamanana, T., 2017. Tonian Arc Magmatism in Central Madagascar: The Petrogenesis of the Imorona-Itsindro Suite. J. Geol. 125, 271–297. https://doi.org/10.1086/691185

Arnold, J.R., 1961. Nuclear Effects of Cosmic Rays in Meteorites. Annu. Rev. Nucl. Sci. 11, 349–370. https://doi.org/10.1146/annurev.ns.11.120161.002025

Baena, S., Beentje, H., Cameron, A., Lowry, P., Moat, J., Rabehevitra, D., Rahantamalala, J., Rakotoarisoa, S., Randriarimalala, Z.L., Rasolohery, A., 2007. Atlas of the Vegetation of Madagascar.

Balco, G., Stone, J.O.H., 2005. Measuring middle Pleistocene erosion rates with cosmic-ray-produced nuclides in buried alluvial sediment, Fisher Valley, southeastern Utah. Earth Surf. Process. Landf. 30, 1051–1067. https://doi.org/10.1002/esp.1262

Barbarand, J., Carter, A., Wood, I., Hurford, T., 2003. Compositional and structural control of fission-track annealing in apatite. Chem. Geol. 198, 107–137. https://doi.org/10.1016/S0009-2541(02)00424-2

Bardintzeff, J.-M., Liégeois, J.-P., Bonin, B., Bellon, H., Rasamimanana, G., 2010. Madagascar volcanic provinces linked to the Gondwana break-up: Geochemical and isotopic evidences for contrasting mantle sources. Gondwana Res. 18, 295–314. https://doi.org/10.1016/j.gr.2009.11.010

Barfod, D.N., Fitton, J.G., 2014. Pleistocene volcanism on São Tomé, Gulf of Guinea, West Africa. Quat. Geochronol. 21, 77–89. https://doi.org/10.1016/j.quageo.2012.11.006

Battistini, R., 1972. L'hypothèse de l'absence de hauts stationnements marins quaternaires: Essai d'application à Madagascar et au sud-ouest de l'océan Indien. Quaternaire 9, 75–81.

Bayon, G., Toucanne, S., Skonieczny, C., André, L., Bermell, S., Cheron, S., Dennielou, B., Etoubleau, J., Freslon, N., Gauchery, T., Germain, Y., Jorry, S.J., Ménot, G., Monin, L., Ponzevera, E., Rouget, M.-L., Tachikawa, K., Barrat, J.A., 2015. Rare earth elements and neodymium isotopes in world river sediments revisited. Geochim. Cosmochim. Acta 170, 17–38. https://doi.org/10.1016/j.gca.2015.08.001

Beeson, H.W., McCoy, S.W., Keen-Zebert, A., 2017. Geometric disequilibrium of river basins produces long-lived transient landscapes. Earth Planet. Sci. Lett. 475, 34–43. https://doi.org/10.1016/j.epsl.2017.07.010

Bekaddour, T., Schlunegger, F., Vogel, H., Delunel, R., Norton, K.P., Akçar, N., Kubik, P., 2014a. Paleo erosion rates and climate shifts recorded by Quaternary cut-and-fill sequences in the Pisco valley, central Peru. Earth Planet. Sci. Lett. 390, 103–115. https://doi.org/10.1016/j.epsl.2013.12.048

Bekaddour, T., Schlunegger, F., Vogel, H., Delunel, R., Norton, K.P., Akçar, N., Kubik, P., 2014b. Paleo erosion rates and climate shifts recorded by Quaternary cut-and-fill sequences in the Pisco valley, central Peru. Earth Planet. Sci. Lett. 390, 103–115. https://doi.org/10.1016/j.epsl.2013.12.048

Berends, C.J., Köhler, P., Lourens, L.J., Wal, R.S.W., 2021. On the Cause of the Mid-Pleistocene Transition. Rev. Geophys. 59. https://doi.org/10.1029/2020RG000727

Berner, R.A., Lasaga, A.C., Garrels, R.M., 1983. The carbonate-silicate geochemical cycle and its effect on atmospheric carbon dioxide over the past 100 million years. Am. J. Sci. 283, 641–683. https://doi.org/10.2475/ajs.283.7.641

Besairie, H., 1972. Géologie de Madagascar. I. Les terrains sédimentaires.

Binks, R.M., Fairhead, J.D., 1992. A plate tectonic setting for Mesozoic rifts of West and Central Africa. Tectonophysics 213, 141–151. https://doi.org/10.1016/0040-1951(92)90255-5

Blard, P.-H., Lupker, M., Rousseau, M., 2019a. Paired-cosmogenic nuclide paleoaltimetry. Earth Planet. Sci. Lett. 515, 271–282. https://doi.org/10.1016/j.epsl.2019.03.005

Blard, P.-H., Lupker, M., Rousseau, M., Tesson, J., 2019b. Two MATLAB programs for computing paleo-elevations and burial ages from paired-cosmogenic nuclides. MethodsX 6, 1547–1556. https://doi.org/10.1016/j.mex.2019.05.017

Boger, S.D., Maas, R., Pastuhov, M., Macey, P.H., Hirdes, W., Schulte, B., Fanning, C.M., Ferreira, C.A.M., Jenett, T., Dallwig, R., 2019. The tectonic domains of southern and western Madagascar. Precambrian Res. 327, 144–175. https://doi.org/10.1016/j.precamres.2019.03.005

Borchers, B., Marrero, S., Balco, G., Caffee, M., Goehring, B., Lifton, N., Nishiizumi, K., Phillips, F., Schaefer, J., Stone, J., 2016. Geological calibration of spallation production rates in the CRONUS-Earth project. Quat. Geochronol. 31, 188–198. https://doi.org/10.1016/j.quageo.2015.01.009

Bouma, A., 1964. Turbidites, in: Developments in Sedimentology. Elsevier, pp. 247–256.

Bouvier, A., Vervoort, J.D., Patchett, P.J., 2008. The Lu–Hf and Sm–Nd isotopic composition of CHUR: Constraints from unequilibrated chondrites and implications for the bulk composition of terrestrial planets. Earth Planet. Sci. Lett. 273, 48–57. https://doi.org/10.1016/j.epsl.2008.06.010

Brædstrup, C.F., Egholm, D.L., Ugelvig, S.V., Pedersen, V.K., 2016. Basal shear stress under alpine glaciers: insights from experiments using the iSOSIA and Elmer/Ice models. Earth Surf. Dyn. 4, 159–174. https://doi.org/10.5194/esurf-4-159-2016

Braucher, R., Bourlès, D.L., Brown, E.T., Colin, F., Muller, J.-P., Braun, J.-J., Delaune, M., Edou Minko, A., Lescouet, C., Raisbeck, G.M., Yiou, F., 2000. Application of in situ-produced cosmogenic 10Be and 26Al to the study of lateritic soil development in tropical forest: theory and examples from Cameroon and Gabon. Chem. Geol. 170, 95–111. https://doi.org/10.1016/S0009-2541(99)00243-0

Braucher, R., Guillou, V., Bourlès, D.L., Arnold, M., Aumaître, G., Keddadouche, K., Nottoli, E., 2015. Preparation of ASTER in-house 10Be/9Be standard solutions. Nucl. Instrum. Methods Phys. Res. Sect. B Beam Interact. Mater. At. 361, 335–340. https://doi.org/10.1016/j.nimb.2015.06.012

Braucher, R., Merchel, S., Borgomano, J., Bourlès, D.L., 2011. Production of cosmogenic radionuclides at great depth: A multi element approach. Earth Planet. Sci. Lett. 309, 1–9. https://doi.org/10.1016/j.epsl.2011.06.036

Breemen, N. van, Buurman, P., 2002. Soil formation, 2nd ed. ed. Kluwer Academic Publishers, Dordrecht.

Bronk Ramsey, C., 2009. Bayesian Analysis of Radiocarbon Dates. Radiocarbon 51, 337–360. https://doi.org/10.1017/S0033822200033865

Broothaerts, N., Razanamahandry, V.F., Brosens, L., Campforts, B., Jacobs, L., Razafimbelo, T., Rafolisy, T., Verstraeten, G., Bouillon, S., Govers, G., 2022. Vegetation changes and sediment dynamics in the Lake Alaotra region, central Madagascar. The Holocene 095968362211453. https://doi.org/10.1177/09596836221145376

Brosens, L., Broothaerts, N., Campforts, B., Jacobs, L., Razanamahandry, V.F., Van Moerbeke, Q., Bouillon, S., Razafimbelo, T., Rafolisy, T., Govers, G., 2022. Under pressure: Rapid lavaka erosion and floodplain sedimentation in central Madagascar. Sci. Total Environ. 806, 150483. https://doi.org/10.1016/j.scitotenv.2021.150483

Brosens, L., Cox, R., Campforts, B., Jacobs, L., Vanacker, V., Bierman, P., Razanamahandry, V.F., Rakotondrazafy, A.F.M., Razafimbelo, T., Rafolisy, T., Govers, G., 2023. The slow downwearing of Madagascar: Inferring patterns and controls on long-term basin-averaged erosion rates from *in situ* ^{10}Be at the catchment and regional level. Earth Surf. Process. Landf. esp.5586. https://doi.org/10.1002/esp.5586

Brown, E.T., Edmond, J.M., Raisbeck, G.M., Yiou, F., Kurz, M.D., Brook, E.J., 1991. Examination of surface exposure ages of Antarctic moraines using in situ produced 10Be and 26Al. Geochim. Cosmochim. Acta 55, 2269–2283. https://doi.org/10.1016/0016-7037(91)90103-C

Brown, E.T., Stallard, R.F., Larsen, M.C., Raisbeck, G.M., Yiou, F., 1995. Denudation rates determined from the accumulation of in situ-produced 10Be in the luquillo experimental forest, Puerto Rico. Earth Planet. Sci. Lett. 129, 193–202. https://doi.org/10.1016/0012-821X(94)00249-X

Brown, L., 1984. Applications of accelerator mass spectrometry. Annu. Rev. Earth Planet. Sci. Vol 12 P 39 12, 39.

Bunce, E.T., Molnar, P., 1977. Seismic reflection profiling and basement topography in the Somali Basin: Possible fracture zones between Madagascar and Africa. J. Geophys. Res. 82, 5305–5311. https://doi.org/10.1029/JB082i033p05305

Burns, S.J., McGee, D., Scroxton, N., Kinsley, C.W., Godfrey, L.R., Faina, P., Ranivoharimanana, L., 2022. Southern Hemisphere controls on ITCZ variability in southwest Madagascar over the past 117,000 years. Quat. Sci. Rev. 276, 107317. https://doi.org/10.1016/j.quascirev.2021.107317

Burton, M.R., Sawyer, G.M., Granieri, D., 2013. Deep Carbon Emissions from Volcanoes. Rev. Mineral. Geochem. 75, 323–354. https://doi.org/10.2138/rmg.2013.75.11

Caley, T., Extier, T., Collins, J.A., Schefuß, E., Dupont, L., Malaizé, B., Rossignol, L., Souron, A., McClymont, E.L., Jimenez-Espejo, F.J., García-Comas, C., Eynaud, F., Martinez, P., Roche, D.M., Jorry, S.J., Charlier, K., Wary, M., Gourves, P.-Y., Billy, I., Giraudeau, J., 2018. A two-million-year-long hydroclimatic context for hominin evolution in southeastern Africa. Nature 560, 76–79. https://doi.org/10.1038/s41586-018-0309-6

Calvin, K., Dasgupta, D., Krinner, G., Mukherji, A., Thorne, P.W., Trisos, C., Romero, J., Aldunce, P., Barrett, K., Blanco, G., Cheung, W.W.L., Connors, S., Denton, F., Diongue-Niang, A.,

Dodman, D., Garschagen, M., Geden, O., Hayward, B., Jones, C., Jotzo, F., Krug, T., Lasco, R., Lee, Y.-Y., Masson-Delmotte, V., Meinshausen, M., Mintenbeck, K., Mokssit, A., Otto, F.E.L., Pathak, M., Pirani, A., Poloczanska, E., Pörtner, H.-O., Revi, A., Roberts, D.C., Roy, J., Ruane, A.C., Skea, J., Shukla, P.R., Slade, R., Slangen, A., Sokona, Y., Sörensson, A.A., Tignor, M., Van Vuuren, D., Wei, Y.-M., Winkler, H., Zhai, P., Zommers, Z., Hourcade, J.-C., Johnson, F.X., Pachauri, S., Simpson, N.P., Singh, C., Thomas, A., Totin, E., Arias, P., Bustamante, M., Elgizouli, I., Flato, G., Howden, M., Méndez-Vallejo, C., Pereira, J.J., Pichs-Madruga, R., Rose, S.K., Saheb, Y., Sánchez Rodríguez, R., Ürge-Vorsatz, D., Xiao, C., Yassaa, N., Alegría, A., Armour, K., Bednar-Friedl, B., Blok, K., Cissé, G., Dentener, F., Eriksen, S., Fischer, E., Garner, G., Guivarch, C., Haasnoot, M., Hansen, G., Hauser, M., Hawkins, E., Hermans, T., Kopp, R., Leprince-Ringuet, N., Lewis, J., Ley, D., Ludden, C., Niamir, L., Nicholls, Z., Some, S., Szopa, S., Trewin, B., Van Der Wijst, K.-I., Winter, G., Witting, M., Birt, A., Ha, M., Romero, J., Kim, J., Haites, E.F., Jung, Y., Stavins, R., Birt, A., Ha, M., Orendain, D.J.A., Ignon, L., Park, S., Park, Y., Reisinger, A., Cammaramo, D., Fischlin, A., Fuglestvedt, J.S., Hansen, G., Ludden, C., Masson-Delmotte, V., Matthews, J.B.R., Mintenbeck, K., Pirani, A., Poloczanska, E., Leprince-Ringuet, N., Péan, C., 2023. IPCC, 2023: Climate Change 2023: Synthesis Report. Contribution of Working Groups I, II and III to the Sixth Assessment Report of the Intergovernmental Panel on Climate Change [Core Writing Team, H. Lee and J. Romero (eds.)]. IPCC, Geneva, Switzerland. Intergovernmental Panel on Climate Change (IPCC). https://doi.org/10.59327/IPCC/AR6-9789291691647

Carlson, P., De Angelis, A., 2011. Nationalism and internationalism in science: the case of the discovery of cosmic rays. Eur. Phys. J. H 35, 309–329. https://doi.org/10.1140/epjh/e2011-10033-6

Carlson, W.D., 1990. Mechanisms and kinetics of apatite fission-track annealing. Am. Mineral. 75, 1120–1139.

Carlson, W.D., Donelick, R.A., Ketcham, R.A., 1999. Variability of apatite fission-track annealing kinetics; I, Experimental results. Am. Mineral. 84, 1213–1223. https://doi.org/10.2138/am-1999-0901

Castañeda, I.S., Caley, T., Dupont, L., Kim, J.-H., Malaizé, B., Schouten, S., 2016. Middle to Late Pleistocene vegetation and climate change in subtropical southern East Africa. Earth Planet. Sci. Lett. 450, 306–316. https://doi.org/10.1016/j.epsl.2016.06.049

Castelltort, S., Van Den Driessche, J., 2003. How plausible are high-frequency sediment supply-driven cycles in the stratigraphic record? Sediment. Geol. 157, 3–13. https://doi.org/10.1016/S0037-0738(03)00066-6

Caves Rugenstein, J.K., Ibarra, D.E., von Blanckenburg, F., 2019. Neogene cooling driven by land surface reactivity rather than increased weathering fluxes. Nature 571, 99–102. https://doi.org/10.1038/s41586-019-1332-y

Charreau, J., Blard, P., Zumaque, J., Martin, L.C.P., Delobel, T., Szafran, L., 2019. Basinga: A cell-by-cell GIS toolbox for computing basin average scaling factors, cosmogenic production rates and denudation rates. Earth Surf. Process. Landf. 44, 2349–2365. https://doi.org/10.1002/esp.4649

Charreau, J., Blard, P.-H., Lavé, J., Dominguez, S., Li, W.S., 2023. Unsteady topography in the eastern Tianshan due to imbalance between denudation and crustal thickening. Tectonophysics 848, 229702. https://doi.org/10.1016/j.tecto.2022.229702

Charreau, J., Blard, P.-H., Puchol, N., Avouac, J.-P., Lallier-Vergès, E., Bourlès, D., Braucher, R., Gallaud, A., Finkel, R., Jolivet, M., Chen, Y., Roy, P., 2011. Paleo-erosion rates in Central Asia since 9Ma: A transient increase at the onset of Quaternary glaciations? Earth Planet. Sci. Lett. 304, 85–92. https://doi.org/10.1016/j.epsl.2011.01.018

Charreau, J., Lavé, J., France-Lanord, C., Puchol, N., Blard, P., Pik, R., Gajurel, A.P., ASTER Team, 2021. A 6 Ma record of palaeodenudation in the central Himalayas from in situ cosmogenic ^{10}Be in the Surai section. Basin Res. 33, 1218–1239. https://doi.org/10.1111/bre.12511

Chase, B.M., Boom, A., Carr, A.S., Carré, M., Chevalier, M., Meadows, M.E., Pedro, J.B., Stager, J.C., Reimer, P.J., 2015. Evolving southwest African response to abrupt deglacial North Atlantic climate change events. Quat. Sci. Rev. 121, 132–136. https://doi.org/10.1016/j.quascirev.2015.05.023

Chevalier, M., Chase, B.M., Quick, L.J., Dupont, L.M., Johnson, T.C., 2020. Temperature change in subtropical southeastern Africa during the past 790,000 yr. Geology 49, 71–75. https://doi.org/10.1130/G47841.1

Clare, M.A., Hughes Clarke, J.E., Talling, P.J., Cartigny, M.J.B., Pratomo, D.G., 2016. Preconditioning and triggering of offshore slope failures and turbidity currents revealed by most detailed monitoring yet at a fjord-head delta. Earth Planet. Sci. Lett. 450, 208–220. https://doi.org/10.1016/j.epsl.2016.06.021

Clift, P., Vannucchi, P., 2004. Controls on tectonic accretion versus erosion in subduction zones: Implications for the origin and recycling of the continental crust. Rev. Geophys. 42, 2003RG000127. https://doi.org/10.1029/2003RG000127

Clift, P.D., 2006. Controls on the erosion of Cenozoic Asia and the flux of clastic sediment to the ocean. Earth Planet. Sci. Lett. 241, 571–580. https://doi.org/10.1016/j.epsl.2005.11.028

Clift, P.D., Jonell, T.N., 2021. Monsoon controls on sediment generation and transport: Mass budget and provenance constraints from the Indus River catchment, delta and submarine fan over tectonic and multimillennial timescales. Earth-Sci. Rev. 220, 103682. https://doi.org/10.1016/j.earscirev.2021.103682

Codilean, A.T., 2006. Calculation of the cosmogenic nuclide production topographic shielding scaling factor for large areas using DEMs. Earth Surf. Process. Landf. 31, 785–794. https://doi.org/10.1002/esp.1336

Corbett, L.B., Bierman, P.R., Rood, D.H., 2016. An approach for optimizing in situ cosmogenic 10Be sample preparation. Quat. Geochronol. 33, 24–34. https://doi.org/10.1016/j.quageo.2016.02.001

Corbett, L.B., Bierman, P.R., Woodruff, T.E., Caffee, M.W., 2019. A homogeneous liquid reference material for monitoring the quality and reproducibility of in situ cosmogenic 10Be and 26Al analyses. Nucl. Instrum. Methods Phys. Res. Sect. B Beam Interact. Mater. At. 456, 180–185. https://doi.org/10.1016/j.nimb.2019.05.051

Corrigan, J.D., 1993. Apatite fission-track analysis of Oligocene strata in South Texas, U.S.A.: Testing annealing models. Chem. Geol. 104, 227–249. https://doi.org/10.1016/0009-2541(93)90153-A

Cox, R., Armstrong, R.A., Ashwal, L.D., 1998. Sedimentology, geochronology and provenance of the Proterozoic Itremo Group, central Madagascar, and implications for pre-Gondwana palaeogeography. J. Geol. Soc. 155, 1009–1024. https://doi.org/10.1144/gsjgs.155.6.1009

Cox, R., Bierman, P., Jungers, M.C., Rakotondrazafy, A.F.M., 2009. Erosion Rates and Sediment Sources in Madagascar Inferred from ^{10} Be Analysis of Lavaka, Slope, and River Sediment. J. Geol. 117, 363–376. https://doi.org/10.1086/598945

Cucciniello, C., Le Roex, A.P., De' Gennaro, R., Jourdan, F., Grifa, C., Morra, V., Melluso, L., 2024. Geochemistry of Cenozoic mafic potassic and sodic volcanic rocks in southwestern Madagascar: Long-lived lithospheric mantle heterogeneities in an extensional tectonic setting. Lithos 482–483, 107735. https://doi.org/10.1016/j.lithos.2024.107735

Cyr, A.J., Granger, D.E., 2008. Dynamic equilibrium among erosion, river incision, and coastal uplift in the northern and central Apennines, Italy. Geology 36, 103. https://doi.org/10.1130/G24003A.1

Dahlen, F.A., Suppe, J., 1988. Mechanics, growth, and erosion of mountain belts, in: Geological Society of America Special Papers. Geological Society of America, pp. 161–178. https://doi.org/10.1130/SPE218-p161

Daniau, A.-L., Loutre, M.-F., Swingedouw, D., Laepple, T., Bassinot, F., Malaizé, B., Kageyama, M., Charlier, K., Carfantan, H., 2023. Precession and obliquity forcing of the South African monsoon revealed by sub-tropical fires. Quat. Sci. Rev. 310, 108128. https://doi.org/10.1016/j.quascirev.2023.108128

Del Vecchio, J., DiBiase, R., Corbett, L., Bierman, P.R., Caffee, M., Ivory, S.J., 2022. Increased erosion rates following the onset of Pleistocene periglaciation at Bear Meadows, Pennsylvania, USA. Geophys. Res. Lett. 49, e2021GL096739.

Delaunay, A., 2018. Les mouvements verticaux de Madagascar (90 - 0 Ma) : une analyse couplée des formes du relief et de l'enregistrement sédimentaire des marges ouest malgaches. Rennes 1.

Delmelle, P., Maters, E., Oppenheimer, C., 2015. Volcanic Influences on the Carbon, Sulfur, and Halogen Biogeochemical Cycles, in: The Encyclopedia of Volcanoes. Elsevier, pp. 881–893. https://doi.org/10.1016/B978-0-12-385938-9.00050-X

Di Stefano, A., Baldassini, N., Raffi, I., Fornaciari, E., Incarbona, A., Negri, A., Bonomo, S., Villa, G., Di Stefano, E., Rio, D., 2023. Neogene-Quaternary Mediterranean calcareous nannofossil biozonation and biochronology: A review. Stratigraphy 20.

Division Plans De DMI-SHOM, 2010. MOCOSED 2010 cruise,Pourquoi pas ? R/V. https://doi.org/10.17600/10030110

Dixey, B.F., 1960. THE GEOLOGY AND GEOMORPHOLOGY OF MADAGASCAR, AND A COMPARISON WITH EASTERN AFRICA. Q. J. Geol. Soc. Lond. 116, 255–268. https://doi.org/10.1144/gsjgs.116.1.0255

Dixon, J.L., Heimsath, A.M., Amundson, R., 2009. The critical role of climate and saprolite weathering in landscape evolution. Earth Surf. Process. Landf. 34, 1507–1521. https://doi.org/10.1002/esp.1836

Donelick, R.A., O'Sullivan, P.B., Ketcham, R.A., 2005. Apatite Fission-Track Analysis. Rev. Mineral. Geochem. 58, 49–94. https://doi.org/10.2138/rmg.2005.58.3

Dunai, T.J., 2010. Cosmogenic nuclides: principles, concepts and applications in the earth surface sciences. Cambridge University Press.

Dunai, T.J., 2000. Scaling factors for production rates of in situ produced cosmogenic nuclides: a critical reevaluation. Earth Planet. Sci. Lett. 176, 157–169. https://doi.org/10.1016/S0012-821X(99)00310-6

Dupont, L.M., Caley, T., Kim, J.-H., Castañeda, I., Malaizé, B., Giraudeau, J., 2011. Glacial-interglacial vegetation dynamics in South Eastern Africa coupled to sea surface temperature variations in the Western Indian Ocean. Clim. Past 7, 1209–1224. https://doi.org/10.5194/cp-7-1209-2011

Dupré, S., Bertotti, G., Cloetingh, S., 2007. Tectonic history along the South Gabon Basin: Anomalous early post-rift subsidence. Mar. Pet. Geol. 24, 151–172. https://doi.org/10.1016/j.marpetgeo.2006.11.003

Emerick, C.M., Duncan, R.A., 1982. Age progressive volcanism in the Comores Archipelago, western Indian Ocean and implications for Somali plate tectonics. Earth Planet. Sci. Lett. 60, 415–428. https://doi.org/10.1016/0012-821X(82)90077-2

Emmel, B., Boger, S.D., Jacobs, J., Daszinnies, M.C., 2012. Maturity of central Madagascar's landscape — Low-temperature thermochronological constraints. Gondwana Res. 21, 704–713. https://doi.org/10.1016/j.gr.2011.05.018

Emmel, B., Geiger, M., Jacobs, J., 2006a. Detrital apatite fission-track ages in Middle Jurassic strata at the rifted margin of W Madagascar—indicator for a protracted resedimentation history. Sediment. Geol. 186, 27–38. https://doi.org/10.1016/j.sedgeo.2005.09.022

Emmel, B., Jacobs, J., Kastowski, M., Graser, G., 2006b. Phanerozoic upper crustal tectono-thermal development of basement rocks from central Madagascar: An integrated fission-track and structural study. Tectonophysics 412, 61–86. https://doi.org/10.1016/j.tecto.2005.09.008

Emmel, B., Jacobs, J., Razakamanana, T., 2004. Titanite and apatite fission track analyses on basement rocks of central-southern Madagascar: constraints on exhumation and denudation rates along the eastern rift shoulder of the Morondava basin. J. Afr. Earth Sci. 38, 343–361. https://doi.org/10.1016/j.jafrearsci.2003.10.009

Emmel, B., Jöns, N., Kröner, A., Jacobs, J., Wartho, J. -A., Schenk, V., Razakamanana, T., Austegard, A., 2008. From Closure of the Mozambique Ocean to Gondwana Breakup: New Evidence from Geochronological Data of the Vohibory Terrane, Southwest Madagascar. J. Geol. 116, 21–38. https://doi.org/10.1086/524121

Eshel, G., Levy, G.J., Mingelgrin, U., Singer, M.J., 2004. Critical Evaluation of the Use of Laser Diffraction for Particle-Size Distribution Analysis. Soil Sci. Soc. Am. J. 68, 736–743. https://doi.org/10.2136/sssaj2004.7360

Estrade, G., Marquis, E., Smith, M., Goodenough, K., Nason, P., 2019. REE concentration processes in ion adsorption deposits: Evidence from the Ambohimirahavavy alkaline complex in Madagascar. Ore Geol. Rev. 112, 103027. https://doi.org/10.1016/j.oregeorev.2019.103027

Farley, K.A., 2000. Helium diffusion from apatite: General behavior as illustrated by Durango fluorapatite. J. Geophys. Res. Solid Earth 105, 2903–2914. https://doi.org/10.1029/1999JB900348

Fisher, G.B., Luna, L.V., Amidon, W.H., Burbank, D.W., De Boer, B., Stap, L.B., Bookhagen, B., Godard, V., Oskin, M.E., Alonso, R.N., Tuenter, E., Lourens, L.J., 2023a. Milankovitch-paced erosion in the southern Central Andes. Nat. Commun. 14, 424. https://doi.org/10.1038/s41467-023-36022-0

Fisher, G.B., Luna, L. V., Amidon, W.H., Burbank, D.W., de Boer, B., Stap, L.B., Bookhagen, B., Godard, V., Oskin, M.E., Alonso, R.N., Tuenter, E., Lourens, L.J., 2023b. Milankovitch-paced erosion in the southern Central Andes. Nat. Commun. 14. https://doi.org/10.1038/s41467-023-36022-0

Fitzgerald, P.G., Malusà, M.G., 2019. Concept of the Exhumed Partial Annealing (Retention) Zone and Age-Elevation Profiles in Thermochronology, in: Malusà, M.G., Fitzgerald, P.G. (Eds.), Fission-Track Thermochronology and Its Application to Geology, Springer Textbooks in Earth Sciences, Geography and Environment. Springer International Publishing, Cham, pp. 165–189. https://doi.org/10.1007/978-3-319-89421-8_9

Flowers, R.M., Ketcham, R.A., Shuster, D.L., Farley, K.A., 2009. Apatite (U–Th)/He thermochronometry using a radiation damage accumulation and annealing model. Geochim. Cosmochim. Acta 73, 2347–2365. https://doi.org/10.1016/j.gca.2009.01.015

Fuller, T.K., Perg, L.A., Willenbring, J.K., Lepper, K., 2009a. Field evidence for climate-driven changes in sediment supply leading to strath terrace formation. Geology 37, 467–470. https://doi.org/10.1130/G25487A.1

Fuller, T.K., Perg, L.A., Willenbring, J.K., Lepper, K., 2009b. Field evidence for climate-driven changes in sediment supply leading to strath terrace formation. Geology 37, 467–470. https://doi.org/10.1130/G25487A.1

Gadgil, S., 2018. The monsoon system: Land–sea breeze or the ITCZ? J. Earth Syst. Sci. 127, 1. https://doi.org/10.1007/s12040-017-0916-x

Gagen, E.J., Levett, A., Paz, A., Gastauer, M., Caldeira, C.F., Valadares, R.B.D.S., Bitencourt, J.A.P., Alves, R., Oliveira, G., Siqueira, J.O., Vasconcelos, P.M., Southam, G., 2019. Biogeochemical processes in canga ecosystems: Armoring of iron ore against erosion and importance in iron duricrust restoration in Brazil. Ore Geol. Rev. 107, 573–586. https://doi.org/10.1016/j.oregeorev.2019.03.013

Gallagher, K., 2012. Transdimensional inverse thermal history modeling for quantitative thermochronology. J. Geophys. Res. Solid Earth 117, 2011JB008825. https://doi.org/10.1029/2011JB008825

Gallagher, K., 1995. Evolving temperature histories from apatite fission-track data. Earth Planet. Sci. Lett. 136, 421–435. https://doi.org/10.1016/0012-821X(95)00197-K

Galvez, M.E., Pubellier, M., 2019. How Do Subduction Zones Regulate the Carbon Cycle? ETH Zurich, p. 37 p. https://doi.org/10.3929/ETHZ-B-000389115

Galy, V., France-Lanord, C., Beyssac, O., Faure, P., Kudrass, H., Palhol, F., 2007. Efficient organic carbon burial in the Bengal fan sustained by the Himalayan erosional system. Nature 450, 407–410. https://doi.org/10.1038/nature06273

Garcin, Y., Schildgen, T.F., Torres Acosta, V., Melnick, D., Guillemoteau, J., Willenbring, J., Strecker, M.R., 2017. Short-lived increase in erosion during the African Humid Period: Evidence from the northern Kenya Rift. Earth Planet. Sci. Lett. 459, 58–69. https://doi.org/10.1016/j.epsl.2016.11.017

Garçon, M., Chauvel, C., France-Lanord, C., Huyghe, P., Lavé, J., 2013. Continental sedimentary processes decouple Nd and Hf isotopes. Geochim. Cosmochim. Acta 121, 177–195. https://doi.org/10.1016/j.gca.2013.07.027

Garzanti, E., 2017. The Maturity Myth In Sedimentology and Provenance Analysis. J. Sediment. Res. 87, 353–365. https://doi.org/10.2110/jsr.2017.17

Garzanti, E., Andò, S., 2019. Heavy Minerals for Junior Woodchucks. Minerals 9, 148. https://doi.org/10.3390/min9030148

Garzanti, E., Andò, S., 2007. Chapter 20 Heavy Mineral Concentration in Modern Sands: Implications for Provenance Interpretation, in: Developments in Sedimentology. Elsevier, pp. 517–545. https://doi.org/10.1016/S0070-4571(07)58020-9

Garzanti, E., Bayon, G., Barbarano, M., Resentini, A., Vezzoli, G., Pastore, G., Levacher, M., Adeaga, O., 2024. Anatomy of Niger and Benue river sediments from clay to granule: grain-size dependence and provenance budgets. J. Sediment. Res. https://doi.org/10.2110/jsr.2024.024

Garzanti, E., Bayon, G., Dinis, P., Vermeesch, P., Pastore, G., Resentini, A., Barbarano, M., Ncube, L., Van Niekerk, H.J., 2022a. The Segmented Zambezi Sedimentary System from Source to Sink: 2. Geochemistry, Clay Minerals, and Detrital Geochronology. J. Geol. 130, 171–208. https://doi.org/10.1086/719166

Garzanti, E., Bayon, G., Vermeesch, P., Barbarano, M., Pastore, G., Resentini, A., Dennielou, B., Jouet, G., 2022b. The Zambezi deep-sea fan: mineralogical, REE, Zr/Hf, Nd-isotope, and zircon-age variability in feldspar-rich passive-margin turbidites. J. Sediment. Res. 92, 1022–1043. https://doi.org/10.2110/jsr.2022.033

Garzanti, E., Resentini, A., Vezzoli, G., Andò, S., Malusà, M., Padoan, M., 2012. Forward compositional modelling of Alpine orogenic sediments. Sediment. Geol. 280, 149–164. https://doi.org/10.1016/j.sedgeo.2012.03.012

Gautheron, C., Tassan-Got, L., Barbarand, J., Pagel, M., 2009. Effect of alpha-damage annealing on apatite (U–Th)/He thermochronology. Chem. Geol. 266, 157–170. https://doi.org/10.1016/j.chemgeo.2009.06.001

Gerin, C., Gautheron, C., Oliviero, E., Bachelet, C., Mbongo Djimbi, D., Seydoux-Guillaume, A.-M., Tassan-Got, L., Sarda, P., Roques, J., Garrido, F., 2017. Influence of vacancy damage on He diffusion in apatite, investigated at atomic to mineralogical scales. Geochim. Cosmochim. Acta 197, 87–103. https://doi.org/10.1016/j.gca.2016.10.018

Giese, J., Seward, D., Schreurs, G., 2012. Low-temperature evolution of the Morondava rift basin shoulder in western Madagascar: An apatite fission track study. Tectonics 31, 2011TC002921. https://doi.org/10.1029/2011TC002921

Giraudeau, J., Christensen, B.A., Hermelin, O., Lange, C.B., Motoyama, I., Party, S.S., 1998. 19. BIOSTRATIGRAPHIC AGE MODELS AND SEDIMENTATION RATES ALONG THE SOUTHWEST AFRICAN MARGIN1, in: Proceedings Ocean Drilling Program, Initial Reports. pp. 543–546.

Gleadow, A.J.W., Duddy, I.R., Green, P.F., Hegarty, K.A., 1986. Fission track lengths in the apatite annealing zone and the interpretation of mixed ages. Earth Planet. Sci. Lett. 78, 245–254. https://doi.org/10.1016/0012-821X(86)90065-8

Godard, V., Bourles, D.L., Spinabella, F., Burbank, D.W., Bookhagen, B., Fisher, G.B., Moulin, A., Leanni, L., 2014. Dominance of tectonics over climate in Himalayan denudation. Geology 42, 243–246. https://doi.org/10.1130/G35342.1

Godard, V., Tucker, G.E., Burch Fisher, G., Burbank, D.W., Bookhagen, B., 2013. Frequency-dependent landscape response to climatic forcing. Geophys. Res. Lett. 40, 859–863. https://doi.org/10.1002/grl.50253

Goldstein, S.L., Hemming, S.R., 2003. Long-lived Isotopic Tracers in Oceanography, Paleoceanography, and Ice-sheet Dynamics, in: Treatise on Geochemistry. Elsevier, pp. 453–489. https://doi.org/10.1016/B0-08-043751-6/06179-X

Gonzalez, V.S., Bierman, P.R., Nichols, K.K., Rood, D.H., 2016. Long-term erosion rates of Panamanian drainage basins determined using in situ 10 Be. Geomorphology 275, 1–15. https://doi.org/10.1016/j.geomorph.2016.04.025

Grandin, R., Doin, M.-P., Bollinger, L., Pinel-Puyssegur, B., Ducret, G., Jolivet, R., Sapkota, S.N., 2012. Long-term growth of the Himalaya inferred from interseismic InSAR measurement. Geology 40, 1059–1062. https://doi.org/10.1130/G33154.1

Granger, D.E., 2006. A review of burial dating methods using ^{26}Al and ^{10}Be, in: In Situ-Produced Cosmogenic Nuclides and Quantification of Geological Processes. Geological Society of America. https://doi.org/10.1130/2006.2415(01)

Granger, D.E., Kirchner, J.W., Finkel, R., 1996. Spatially Averaged Long-Term Erosion Rates Measured from in Situ-Produced Cosmogenic Nuclides in Alluvial Sediment. J. Geol. 104, 249–257. https://doi.org/10.1086/629823

Granger, D.E., Muzikar, P.F., 2001. Dating sediment burial with in situ-produced cosmogenic nuclides: theory, techniques, and limitations. Earth Planet. Sci. Lett. 188, 269–281. https://doi.org/10.1016/S0012-821X(01)00309-0

Green, P.F., Duddy, I.R., Gleadow, A.J.W., Tingate, P.R., Laslett, G.M., 1986. Thermal annealing of fission tracks in apatite. Chem. Geol. Isot. Geosci. Sect. 59, 237–253. https://doi.org/10.1016/0168-9622(86)90074-6

Green, P.F., Duddy, I.R., Gleadow, A.J.W., Tingate, P.R., Laslett, G.M., 1985. Fission-track annealing in apatite: Track length measurements and the form of the Arrhenius plot. Nucl. Tracks Radiat. Meas. 1982 10, 323–328. https://doi.org/10.1016/0735-245X(85)90121-8

Grin, E., Schaller, M., Ehlers, T.A., 2018. Spatial distribution of cosmogenic 10Be derived denudation rates between the Western Tian Shan and Northern Pamir, Tajikistan. Geomorphology 321, 1–15. https://doi.org/10.1016/j.geomorph.2018.08.007

Grischott, R., Kober, F., Lupker, M., Hippe, K., Ivy-Ochs, S., Hajdas, I., Salcher, B., Christl, M., 2017. Constant denudation rates in a high alpine catchment for the last 6 kyrs: Alpine ^{10} Be denudation rates over 6 kyr. Earth Surf. Process. Landf. 42, 1065–1077. https://doi.org/10.1002/esp.4070

Grischott, Reto, Kober, F., Lupker, M., Reitner, J.M., Drescher-Schneider, R., Hajdas, I., Christl, M., Willett, S.D., 2017a. Millennial scale variability of denudation rates for the last 15 kyr inferred from the detrital ^{10} Be record of Lake Stappitz in the Hohe Tauern massif, Austrian Alps. The Holocene 27, 1914–1927. https://doi.org/10.1177/0959683617708451

Grischott, Reto, Kober, F., Lupker, M., Reitner, J.M., Drescher-schneider, R., Hajdas, I., Christl, M., Willett, S.D., 2017b. Millennial scale variability of denudation rates for the last 15 kyr inferred from the detrital 10 Be record of Lake Stappitz in the Hohe Tauern massif , Austrian Alps. The Holocene 27, 1914–1927. https://doi.org/10.1177/0959683617708451

Guillocheau, F., Chelalou, R., Linol, B., Dauteuil, O., Robin, C., Mvondo, F., Callec, Y., Colin, J.-P., 2015. Cenozoic Landscape Evolution in and Around the Congo Basin: Constraints from Sediments and Planation Surfaces, in: De Wit, M.J., Guillocheau, François, De Wit, M.C.J. (Eds.), Geology and Resource Potential of the Congo Basin. Springer Berlin Heidelberg, Berlin, Heidelberg, pp. 271–313. https://doi.org/10.1007/978-3-642-29482-2_14

Guillocheau, F., Simon, B., Baby, G., Bessin, P., Robin, C., Dauteuil, O., 2018. Planation surfaces as a record of mantle dynamics: The case example of Africa. Gondwana Res. 53, 82–98. https://doi.org/10.1016/j.gr.2017.05.015

Gulick, S.P., Jaeger, J.M., Mix, A.C., Asahi, H., Bahlburg, H., Belanger, C.L., Berbel, G.B., Childress, L., Cowan, E., Drab, L., 2015. Mid-Pleistocene climate transition drives net mass loss from rapidly uplifting St. Elias Mountains, Alaska. Proc. Natl. Acad. Sci. 112, 15042–15047.

Gutiérrez-Pastor, J., Nelson, C.H., Goldfinger, C., Escutia, C., 2013. Sedimentology of seismo-turbidites off the Cascadia and northern California active tectonic continental margins, northwest Pacific Ocean. Mar. Geol. 336, 99–119. https://doi.org/10.1016/j.margeo.2012.11.010

Haeuselmann, P., Granger, D.E., Jeannin, P.-Y., Lauritzen, S.-E., 2007. Abrupt glacial valley incision at 0.8 Ma dated from cave deposits in Switzerland. Geology 35, 143. https://doi.org/10.1130/G23094A

Hage, S., Cartigny, M.J.B., Sumner, E.J., Clare, M.A., Hughes Clarke, J.E., Talling, P.J., Lintern, D.G., Simmons, S.M., Silva Jacinto, R., Vellinga, A.J., Allin, J.R., Azpiroz-Zabala, M., Gales, J.A., Hizzett, J.L., Hunt, J.E., Mozzato, A., Parsons, D.R., Pope, E.L., Stacey, C.D., Symons, W.O., Vardy, M.E., Watts, C., 2019. Direct Monitoring Reveals Initiation of Turbidity Currents From Extremely Dilute River Plumes. Geophys. Res. Lett. 46, 11310–11320. https://doi.org/10.1029/2019GL084526

Hallet, B., 1996. Glacial quarrying: a simple theoretical model. Ann. Glaciol. 22, 1–8. https://doi.org/10.3189/1996AoG22-1-1-8

Hampel, W., Takagi, J., Sakamoto, K., Tanaka, S., 1975. Measurement of muon-induced^{26} Al in terrestrial silicate rock. J. Geophys. Res. 80, 3757–3760. https://doi.org/10.1029/JB080i026p03757

Haug, G.H., Tiedemann, R., 1998. Effect of the formation of the Isthmus of Panama on Atlantic Ocean thermohaline circulation. Nature 393, 673–676. https://doi.org/10.1038/31447

Hay, W.W., 1996. Tectonics and climate. Geol. Rundsch. 85, 409–437. https://doi.org/10.1007/BF02369000

Hay, W.W., Sloan, J.L., Wold, C.N., 1988. Mass/age distribution and composition of sediments on the ocean floor and the global rate of sediment subduction. J. Geophys. Res. Solid Earth 93, 14933–14940. https://doi.org/10.1029/JB093iB12p14933

Heaton, T.J., Köhler, P., Butzin, M., Bard, E., Reimer, R.W., Austin, W.E.N., Bronk Ramsey, C., Grootes, P.M., Hughen, K.A., Kromer, B., Reimer, P.J., Adkins, J., Burke, A., Cook, M.S., Olsen, J., Skinner, L.C., 2020. Marine20—The Marine Radiocarbon Age Calibration Curve (0–55,000 cal BP). Radiocarbon 62, 779–820. https://doi.org/10.1017/RDC.2020.68

Herman, F., Beyssac, O., Brughelli, M., Lane, S.N., Leprince, S., Adatte, T., Lin, J.Y.Y., Avouac, J.-P., Cox, S.C., 2015. Erosion by an Alpine glacier. Science 350, 193–195. https://doi.org/10.1126/science.aab2386

Herman, F., Champagnac, J., 2016. Plio-Pleistocene increase of erosion rates in mountain belts in response to climate change. Terra Nova 28, 2–10. https://doi.org/10.1111/ter.12186

Herman, F., Seward, D., Valla, P.G., Carter, A., Kohn, B., Willett, S.D., Ehlers, T.A., 2013. Worldwide acceleration of mountain erosion under a cooling climate. Nature 504, 423–426. https://doi.org/10.1038/nature12877

Hess, V.F., 1912. Über Beobachtungen der durchdringenden Strahlung bei sieben Freiballonfahrten. Z Phys 13, 1084.

Hidy, A.J., Gosse, J.C., Blum, M.D., Gibling, M.R., 2014a. Glacial–interglacial variation in denudation rates from interior Texas, USA, established with cosmogenic nuclides. Earth Planet. Sci. Lett. 390, 209–221. https://doi.org/10.1016/j.epsl.2014.01.011

Hidy, A.J., Gosse, J.C., Blum, M.D., Gibling, M.R., 2014b. Glacial–interglacial variation in denudation rates from interior Texas, USA, established with cosmogenic nuclides. Earth Planet. Sci. Lett. 390, 209–221. https://doi.org/10.1016/j.epsl.2014.01.011

Hilton, R.G., West, A.J., 2020. Mountains, erosion and the carbon cycle. Nat. Rev. Earth Environ. 1, 284–299. https://doi.org/10.1038/s43017-020-0058-6

Honda, M., Shedlovsky, J.P., Arnold, J.R., 1961. Radioactive species produced by cosmic rays in iron meteorites. Geochim. Cosmochim. Acta 22, 133–154. https://doi.org/10.1016/0016-7037(61)90112-0

Hsu, Y.-J., Lai, Y.-R., You, R.-J., Chen, H.-Y., Teng, L.S., Tsai, Y.-C., Tang, C.-H., Su, H.-H., 2018. Detecting rock uplift across southern Taiwan mountain belt by integrated GPS and leveling data. Tectonophysics 744, 275–284. https://doi.org/10.1016/j.tecto.2018.07.012

Hu, Y., Li, D., Liu, J., 2007. Abrupt seasonal variation of the ITCZ and the Hadley circulation. Geophys. Res. Lett. 34, L18814. https://doi.org/10.1029/2007GL030950

Hubert, J.F., 1962. A Zircon-Tourmaline-Rutile Maturity Index and the Interdependence of the Composition of Heavy Mineral Assemblages with the Gross Composition and Texture of Sandstones. SEPM J. Sediment. Res. Vol. 32. https://doi.org/10.1306/74D70CE5-2B21-11D7-8648000102C1865D

Hunt, A.L., Larsen, J., Bierman, P.R., Petrucci, G.A., 2008. Investigation of Factors That Affect the Sensitivity of Accelerator Mass Spectrometry for Cosmogenic^{10} Be and^{26} Al Isotope Analysis. Anal. Chem. 80, 1656–1663. https://doi.org/10.1021/ac701742p

Jagoe, L., Sagripanti, L., Colavitto, B., Folguera, A., 2021. Landscape evolution in the Guañacos fold and thrust belt (37° S): Insights from geomorphological and morphometric analysis. J. South Am. Earth Sci. 111, 103484. https://doi.org/10.1016/j.jsames.2021.103484

Jiao, R., Braun, J., Delaunay, A., Robin, C., Guillocheau, F., 2022. Linking uplift, erosion, and sedimentation using landscape evolution models: Madagascar since the Late Cretaceous. Earth Surf. Process. Landf. esp.5482. https://doi.org/10.1002/esp.5482

Johnson, T.C., Werne, J.P., Brown, E.T., Abbott, A., Berke, M., Steinman, B.A., Halbur, J., Contreras, S., Grosshuesch, S., Deino, A., Scholz, C.A., Lyons, R.P., Schouten, S., Damsté, J.S.S., 2016. A progressively wetter climate in southern East Africa over the past 1.3 million years. Nature 537, 220–224. https://doi.org/10.1038/nature19065

Jöns, N., Emmel, B., Schenk, V., Razakamanana, T., 2009. From orogenesis to passive margin—the cooling history of the Bemarivo Belt (N Madagascar), a multi-thermochronometer approach. Gondwana Res. 16, 72–81. https://doi.org/10.1016/j.gr.2009.02.006

Jouet, G., Deville, E., 2015. PAMELA-MOZ04 cruise,Pourquoi pas ? R/V. https://doi.org/10.17600/15000700

Jull, A.J.T., Scott, E.M., Bierman, P., 2015. The CRONUS-Earth inter-comparison for cosmogenic isotope analysis. Quat. Geochronol. 26, 3–10. https://doi.org/10.1016/j.quageo.2013.09.003
Kapannusch, R., Scherler, D., King, G., Wittmann, H., 2020. Glacial influence on late Pleistocene 10Be-derived paleo-erosion rates in the north-western Himalaya, India. Earth Planet. Sci. Lett. 547, 116441. https://doi.org/10.1016/j.epsl.2020.116441
Kennett, J.P., Stott, L.D., 1991. Abrupt deep-sea warming, palaeoceanographic changes and benthic extinctions at the end of the Palaeocene. Nature 353, 225–229. https://doi.org/10.1038/353225a0
Ketcham, R.A., 2005. Forward and Inverse Modeling of Low-Temperature Thermochronometry Data. Rev. Mineral. Geochem. 58, 275–314. https://doi.org/10.2138/rmg.2005.58.11
Ketcham, R.A., Carter, A., Donelick, R.A., Barbarand, J., Hurford, A.J., 2007. Improved modeling of fission-track annealing in apatite. Am. Mineral. 92, 799–810. https://doi.org/10.2138/am.2007.2281
Ketcham, R.A., Donelick, R.A., Carlson, W.D., 1999. Variability of apatite fission-track annealing kinetics: III. Extrapolation to geological time scales. Am. Mineral. 84, 1235–1255.
Kim, D.-E., Seong, Y.B., Byun, J., Weber, J., Min, K., 2016. Geomorphic disequilibrium in the Eastern Korean Peninsula: Possible evidence for reactivation of a rift-flank margin. Geomorphology 254, 130–145. https://doi.org/10.1016/j.geomorph.2015.11.022
Klein, J., Giegengack, R., Middleton, R., Sharma, P., Underwood, J.R., Weeks, R.A., 1986. Revealing Histories of Exposure Using *In Situ* Produced^{26} Al and^{10} Be in Libyan Desert Glass. Radiocarbon 28, 547–555. https://doi.org/10.1017/S0033822200007700
Koch, P.L., Zachos, J.C., Gingerich, P.D., 1992. Correlation between isotope records in marine and continental carbon reservoirs near the Palaeocene/Eocene boundary. Nature 358, 319–322. https://doi.org/10.1038/358319a0
Kohl, C.P., Nishiizumi, K., 1992. Chemical isolation of quartz for measurement of in-situ -produced cosmogenic nuclides. Geochim. Cosmochim. Acta 56, 3583–3587. https://doi.org/10.1016/0016-7037(92)90401-4
Konert, M., Vandenberghe, J., 1997. Comparison of laser grain size analysis with pipette and sieve analysis: a solution for the underestimation of the clay fraction. Sedimentology 44, 523–535. https://doi.org/10.1046/j.1365-3091.1997.d01-38.x
Koppes, M., Hallet, B., 2006. Erosion rates during rapid deglaciation in Icy Bay, Alaska. J. Geophys. Res. 111, F02023. https://doi.org/10.1029/2005JF000349
Korschinek, G., Bergmaier, A., Faestermann, T., Gerstmann, U.C., Knie, K., Rugel, G., Wallner, A., Dillmann, I., Dollinger, G., Von Gostomski, Ch.L., Kossert, K., Maiti, M., Poutivtsev, M., Remmert, A., 2010. A new value for the half-life of 10Be by Heavy-Ion Elastic Recoil Detection and liquid scintillation counting. Nucl. Instrum. Methods Phys. Res. Sect. B Beam Interact. Mater. At. 268, 187–191. https://doi.org/10.1016/j.nimb.2009.09.020
Kottek, M., Grieser, J., Beck, C., Rudolf, B., Rubel, F., 2006. World Map of the Köppen-Geiger climate classification updated. Meteorol. Z. 15, 259–263. https://doi.org/10.1127/0941-2948/2006/0130
Kuhlemann, J., Frisch, W., Székely, B., Dunkl, I., Kàzmer, M., 2002. Post-collisional sediment budget history of the Alps: tectonic versus climatic control. Int. J. Earth Sci. 91, 818–837. https://doi.org/10.1007/s00531-002-0266-y
Kusky, T.M., Toraman, E., Raharimahefa, T., Rasoazanamparany, C., 2010. Active tectonics of the Alaotra–Ankay Graben System, Madagascar: Possible extension of Somalian–African diffusive plate boundary? Gondwana Res. 18, 274–294. https://doi.org/10.1016/j.gr.2010.02.003
Kutzbach, J.E., Liu, X., Liu, Z., Chen, G., 2008. Simulation of the evolutionary response of global summer monsoons to orbital forcing over the past 280,000 years. Clim. Dyn. 30, 567–579. https://doi.org/10.1007/s00382-007-0308-z
Lal, D., 1991. Cosmic ray labeling of erosion surfaces: in situ nuclide production rates and erosion models. Earth Planet. Sci. Lett. 104, 424–439. https://doi.org/10.1016/0012-821X(91)90220-C
Lal, D., Arnold, J.R., 1985. Tracing quartz through the environment. J. Earth Syst. Sci. 94, 1–5. https://doi.org/10.1007/BF02863403
Large, E., 2024. Large et al. Near steady denudation rates during the late Pleistocene in the tropics. https://doi.org/10.17632/VD3X5TV4HW.1

Large, E., Charreau, J., Blard, P., Bayon, G., Garzanti, E., Dennielou, B., Jouet, G., Vazquez Riveiros, N., Giraudeau, J., Reisberg, L., Shcumacher, A., Andriamamonjy, A., Rakotondrazafy, A.F.M., 2025. Near Steady Late Pleistocene Tropical Denudation Rates in SW Madagascar. J. Geophys. Res. Earth Surf. 130, e2024JF008147. https://doi.org/10.1029/2024JF008147

Laslett, G.M., Green, P.F., Duddy, I.R., Gleadow, A.J.W., 1987. Thermal annealing of fission tracks in apatite 2. A quantitative analysis. Chem. Geol. Isot. Geosci. Sect. 65, 1–13. https://doi.org/10.1016/0168-9622(87)90057-1

Legros, F., 2002. Can Dispersive Pressure Cause Inverse Grading in Grain Flows? J. Sediment. Res. 72, 166–170. https://doi.org/10.1306/041301720166

Lenard, S.J.P., Lavé, J., France-Lanord, C., Aumaître, G., Bourlès, D.L., Keddadouche, K., 2020. Steady erosion rates in the Himalayas through late Cenozoic climatic changes. Nat. Geosci. 13, 448–452. https://doi.org/10.1038/s41561-020-0585-2

Libby, W.F., Johnson, F., 1955. Radiocarbon dating. University of Chicago Press Chicago.

Lippold, J., Fohlmeister, J., Wacker, L., Kucera, M., Kromer, B., Grützner, J., 2024. Contrasting paired benthic and planktonic foraminifera radiocarbon ages from Bermuda Rise ODP Site 1063 during Heinrich Stadials 1 and 2. Radiocarbon 66, 816–823. https://doi.org/10.1017/RDC.2024.78

Lisiecki, L.E., Raymo, M.E., 2005. A Pliocene-Pleistocene stack of 57 globally distributed benthic δ^{18}O records. Paleoceanography 20, 2004PA001071. https://doi.org/10.1029/2004PA001071

Litt, T., Pickarski, N., Heumann, G., Stockhecke, M., Tzedakis, P.C., 2014. A 600,000 year long continental pollen record from Lake Van, eastern Anatolia (Turkey). Quat. Sci. Rev. 104, 30–41. https://doi.org/10.1016/j.quascirev.2014.03.017

Lupker, M., Blard, P.-H., Lavé, J., France-Lanord, C., Leanni, L., Puchol, N., Charreau, J., Bourlès, D., 2012. 10Be-derived Himalayan denudation rates and sediment budgets in the Ganga basin. Earth Planet. Sci. Lett. 333–334, 146–156. https://doi.org/10.1016/j.epsl.2012.04.020

Lyons, R.P., Scholz, C.A., Cohen, A.S., King, J.W., Brown, E.T., Ivory, S.J., Johnson, T.C., Deino, A.L., Reinthal, P.N., McGlue, M.M., Blome, M.W., 2015. Continuous 1.3-million-year record of East African hydroclimate, and implications for patterns of evolution and biodiversity. Proc. Natl. Acad. Sci. 112, 15568–15573. https://doi.org/10.1073/pnas.1512864112

Macgregor, D.S., 2020. Regional variations in geothermal gradient and heat flow across the African plate. J. Afr. Earth Sci. 171, 103950. https://doi.org/10.1016/j.jafrearsci.2020.103950

Madella, A., Delunel, R., Akçar, N., Schlunegger, F., Christl, M., 2018. 10Be-inferred paleo-denudation rates imply that the mid-Miocene western central Andes eroded as slowly as today. Sci. Rep. 8, 2299. https://doi.org/10.1038/s41598-018-20681-x

Malamud, B.D., Turcotte, D.L., Guzzetti, F., Reichenbach, P., 2004. Landslides, earthquakes, and erosion. Earth Planet. Sci. Lett. 229, 45–59. https://doi.org/10.1016/j.epsl.2004.10.018

Malusà, M.G., Resentini, A., Wittmann, H., 2024. Impact of river capture on erosion rates and offshore sedimentation revealed by geological and in situ 10Be cosmogenic data (Corsica, western Mediterranean). Earth Planet. Sci. Lett. 637, 118728. https://doi.org/10.1016/j.epsl.2024.118728

Mandal, S.K., Scherler, D., Wittmann, H., 2021. Tectonic Accretion Controls Erosional Cyclicity in the Himalaya. AGU Adv. 2, e2021AV000487. https://doi.org/10.1029/2021AV000487

Marc, O., Behling, R., Andermann, C., Turowski, J.M., Illien, L., Roessner, S., Hovius, N., 2019. Long-term erosion of the Nepal Himalayas by bedrock landsliding: the role of monsoons, earthquakes and giant landslides. Earth Surf. Dyn. 7, 107–128. https://doi.org/10.5194/esurf-7-107-2019

Mariotti, A., Blard, P.-H., Charreau, J., Toucanne, S., Jorry, S.J., Molliex, S., Bourlès, D.L., Aumaître, G., Keddadouche, K., 2021a. Nonlinear forcing of climate on mountain denudation during glaciations. Nat. Geosci. 14, 16–22. https://doi.org/10.1038/s41561-020-00672-2

Mariotti, A., Blard, P.H., Charreau, J., Toucanne, S., Jorry, S.J., Molliex, S., Bourlès, D.L., Aumaître, G., Keddadouche, K., 2021b. Nonlinear forcing of climate on mountain denudation during glaciations. Nat. Geosci. 14, 16–22. https://doi.org/10.1038/s41561-020-00672-2

Marshall, J.A., Roering, J.J., Gavin, D.G., Granger, D.E., 2017a. Late quaternary climatic controls on erosion rates and geomorphic processes in western Oregon, USA. Bull. Geol. Soc. Am. 129, 715–731. https://doi.org/10.1130/B31509.1

Marshall, J.A., Roering, J.J., Gavin, D.G., Granger, D.E., 2017b. Late Quaternary climatic controls on erosion rates and geomorphic processes in western Oregon, USA. Geol. Soc. Am. Bull. 129, 715–731. https://doi.org/10.1130/B31509.1

Maslin, M.A., Haug, G.H., Sarnthein, M., Tiedemann, R., 1996. The progressive intensification of northern hemisphere glaciation as seen from the North Pacific. Geol. Rundsch. 85, 452–465. https://doi.org/10.1007/BF02369002

Mason, C.C., Romans, B.W., 2018. Climate-driven unsteady denudation and sediment flux in a high-relief unglaciated catchment–fan using 26Al and 10Be: Panamint Valley, California. Earth Planet. Sci. Lett. 492, 130–143. https://doi.org/10.1016/j.epsl.2018.03.056

Mbina Mounguengui, M., Lang, J., Guiraud, M., Jocktane, O., 2002. Sedimentary dynamics and structural geology of pre-rift deposits of the interior basin of Gabon. J. Afr. Earth Sci. 35, 315–329. https://doi.org/10.1016/S0899-5362(02)00035-0

McGee, D., 2020. Glacial–Interglacial Precipitation Changes. Annu. Rev. Mar. Sci. 12, 525–557. https://doi.org/10.1146/annurev-marine-010419-010859

Melluso, L., Tucker, R.D., Cucciniello, C., Le Roex, A.P., Morra, V., Zanetti, A., Rakotoson, R.L., 2018. The magmatic evolution and genesis of the Quaternary basanite-trachyphonolite suite of Itasy (Madagascar) as inferred by geochemistry, Sr-Nd-Pb isotopes and trace element distribution in coexisting phases. Lithos 310–311, 50–64. https://doi.org/10.1016/j.lithos.2018.04.003

Merchel, S., Beutner, S., Opel, T., Rugel, G., Scharf, A., Tiessen, C., Weiß, S., Wetterich, S., 2019. Attempts to understand potential deficiencies in chemical procedures for AMS. Nucl. Instrum. Methods Phys. Res. Sect. B Beam Interact. Mater. At. 456, 186–192. https://doi.org/10.1016/j.nimb.2019.05.005

Merchel, S., Bremser, W., 2004. First international 26Al interlaboratory comparison – Part I. Nucl. Instrum. Methods Phys. Res. Sect. B Beam Interact. Mater. At. 223–224, 393–400. https://doi.org/10.1016/j.nimb.2004.04.076

Métivier, F., 2002. On the use of sedimentation rates in deciphering global change. Geophys. Res. Lett. 29. https://doi.org/10.1029/2002GL015261

Meyers, J.B., Rosendahl, B.R., Harrison, C.G.A., Ding, Z.-D., 1998. Deep-imaging seismic and gravity results from the offshore Cameroon Volcanic Line, and speculation of African hotlines. Tectonophysics 284, 31–63. https://doi.org/10.1016/S0040-1951(97)00173-X

Mignard, S., 2017. Transport et accumulation de matière organique dans le système turbiditique de l'Ogooué (Gabon). Université de Bordeaux.

Mignard, S., Mulder, T., Martinez, P., Garlan, T., 2019. The Ogooue Fan (offshore Gabon): a modern example of deep-sea fan on a complex slope profile. Solid Earth 10, 851–869. https://doi.org/10.5194/se-10-851-2019

Mignard, S.L.-A., Mulder, T., Martinez, P., Charlier, K., Rossignol, L., Garlan, T., 2017. Deep-sea terrigenous organic carbon transfer and accumulation: Impact of sea-level variations and sedimentation processes off the Ogooue River (Gabon). Mar. Pet. Geol. 85, 35–53. https://doi.org/10.1016/j.marpetgeo.2017.04.009

Migoń, P., 2004. Etching, etchplain and etchplanation. Encycl. Geomorphol. Lond.

Mollenhauer, G., Grotheer, H., Gentz, T., Bonk, E., Hefter, J., 2021. Standard operation procedures and performance of the MICADAS radiocarbon laboratory at Alfred Wegener Institute (AWI), Germany. Nucl. Instrum. Methods Phys. Res. Sect. B Beam Interact. Mater. At. 496, 45–51. https://doi.org/10.1016/j.nimb.2021.03.016

Molnar, P., 2004. Late Cenozoic increase in accumulation rates of terrestrial sediment: How might climate change have affected erosion rates? Annu. Rev. Earth Planet. Sci. 32, 67–89. https://doi.org/10.1146/annurev.earth.32.091003.143456

Molnar, P., England, P., 1990. Late Cenozoic uplift of mountain ranges and global climate change: chicken or egg? Nature 346, 29–34. https://doi.org/10.1038/346029a0

Moon, S., Page Chamberlain, C., Blisniuk, K., Levine, N., Rood, D.H., Hilley, G.E., 2011. Climatic control of denudation in the deglaciated landscape of the Washington Cascades. Nat. Geosci. 4, 469–473. https://doi.org/10.1038/ngeo1159

Moumeni, M., Delchiaro, M., Seta, M.D., Nozaem, R., Ballato, P., Leonard, J.S., Clementucci, R., Rouhi, J., 2024. Interplay between tectonics and surface processes in the evolution of mountain

ranges: Insights from landscape dynamics, uplift, and active deformation of Talesh Mountains (NW Iranian Plateau margin). Geomorphology 448, 109029. https://doi.org/10.1016/j.geomorph.2023.109029
Mulder, T., Syvitski, J.P.M., 1995. Turbidity Currents Generated at River Mouths during Exceptional Discharges to the World Oceans. J. Geol. 103, 285–299. https://doi.org/10.1086/629747
Mulder, T., Syvitski, J.P.M., Migeon, S., Faugères, J.-C., Savoye, B., 2003. Marine hyperpycnal flows: initiation, behavior and related deposits. A review. Mar. Pet. Geol. 20, 861–882. https://doi.org/10.1016/j.marpetgeo.2003.01.003
Nakamura, T., Shiki, T., Nakai, N., 1990. Variations in 14C ages of various organic fractions in a turbidite sediment core from Suruga Trough. Geochem. J. 24, 47–56. https://doi.org/10.2343/geochemj.24.47
Nishiizumi, K., Kohl, C.P., Arnold, J.R., Klein, J., Fink, D., Middleton, R., 1991. Cosmic ray produced 10Be and 26Al in Antarctic rocks: exposure and erosion history. Earth Planet. Sci. Lett. 104, 440–454. https://doi.org/10.1016/0012-821X(91)90221-3
Nkono, C., Féménias, O., Demaiffe, D., 2014. Geodynamic model for the development of the Cameroon Hot Line (Equatorial Africa). J. Afr. Earth Sci. 100, 626–633. https://doi.org/10.1016/j.jafrearsci.2014.08.008
Norton, K.P., Schlunegger, F., 2017. Lack of a weathering signal with increased Cenozoic erosion? Terra Nova 29, 265–272. https://doi.org/10.1111/ter.12278
Olen, S.M., Bookhagen, B., Strecker, M.R., 2016. Role of climate and vegetation density in modulating denudation rates in the Himalaya. Earth Planet. Sci. Lett. 445, 57–67. https://doi.org/10.1016/j.epsl.2016.03.047
Oskin, M.E., Longinotti, N.E., Peryam, T.C., Dorsey, R.J., DeBoer, C.J., Housen, B.A., Blisniuk, K.D., 2017. Steady ^{10} Be-derived paleoerosion rates across the Plio-Pleistocene climate transition, Fish Creek-Vallecito basin, California: PALEOEROSION RATES FROM 4 MA TO 1 MA. J. Geophys. Res. Earth Surf. 122, 1653–1677. https://doi.org/10.1002/2016JF004113
Ott, R.F., Gallen, S.F., Granger, D.E., 2022. Cosmogenic nuclide weathering biases: corrections and potential for denudation and weathering rate measurements. Geochronology 4, 455–470. https://doi.org/10.5194/gchron-4-455-2022
Paillard, D., Labeyrie, L.D., Yiou, P., 1996. AnalySeries 1.0: a Macintosh software for the analysis of geophysical time-series. Eos 77, 379.
Paquette, J.-L., Moine, B., Rakotondrazafy, M.A.F., 2003. ID-TIMS using the step-wise dissolution technique versus ion microprobe U–Pb dating of metamict Archean zircons from NE Madagascar. Precambrian Res. 121, 73–84. https://doi.org/10.1016/S0301-9268(02)00200-0
Parsons, J.D., Bush, J.W.M., Syvitski, J.P.M., 2001. Hyperpycnal plume formation from riverine outflows with small sediment concentrations. Sedimentology 48, 465–478. https://doi.org/10.1046/j.1365-3091.2001.00384.x
Paul, J.D., Eakin, C.M., 2017. Mantle upwelling beneath Madagascar: evidence from receiver function analysis and shear wave splitting. J. Seismol. 21, 825–836. https://doi.org/10.1007/s10950-016-9637-x
Paul, J.D., Radimilahy, A., Randrianalijaona, R., Mulyakova, T., 2022. Lateritic processes in Madagascar and the link with agricultural and socioeconomic conditions. J. Afr. Earth Sci. 196, 104681. https://doi.org/10.1016/j.jafrearsci.2022.104681
Pingel, H., Schildgen, T., Strecker, M.R., Wittmann, H., 2019. Pliocene–Pleistocene orographic control on denudation in northwest Argentina. Geology 47, 359–362. https://doi.org/10.1130/G45800.1
Piper, D.J.W., Normark, W.R., 2009. Processes That Initiate Turbidity Currents and Their Influence on Turbidites: A Marine Geology Perspective. J. Sediment. Res. 79, 347–362. https://doi.org/10.2110/jsr.2009.046
Portenga, E.W., Bierman, P.R., 2011. Understanding Earth's eroding surface with 10Be. GSA Today 21, 4–10. https://doi.org/10.1130/G111A.1
Pratt, M.J., Wysession, M.E., Aleqabi, G., Wiens, D.A., Nyblade, A.A., Shore, P., Rambolamanana, G., Andriampenomanana, F., Rakotondraibe, T., Tucker, R.D., Barruol, G., Rindraharisaona, E., 2017. Shear velocity structure of the crust and upper mantle of Madagascar derived from surface wave tomography. Earth Planet. Sci. Lett. 458, 405–417. https://doi.org/10.1016/j.epsl.2016.10.041

Price, P.B., Walker, R.M., 1963. Fossil tracks of charged particles in mica and the age of minerals. J. Geophys. Res. 68, 4847–4862. https://doi.org/10.1029/JZ068i016p04847

Puchol, N., Charreau, J., Blard, P.-H., Lavé, J., Dominguez, S., Pik, R., Saint-Carlier, D., ASTER Team, 2017. Limited impact of Quaternary glaciations on denudation rates in Central Asia. Geol. Soc. Am. Bull. 129, 479–499. https://doi.org/10.1130/B31475.1

Railsback, L.B., Dupont, L.A., Liang, F., Brook, G.A., Burney, D.A., Cheng, H., Edwards, R.L., 2020. Relationships between climate change, human environmental impact, and megafaunal extinction inferred from a 4000-year multi-proxy record from a stalagmite from northwestern Madagascar. Quat. Sci. Rev. 234, 106244. https://doi.org/10.1016/j.quascirev.2020.106244

Rakotondraibe, T., Nyblade, A.A., Wysession, M.E., Durrheim, R.J., Rambolamanana, G., Aleqabi, G.I., Shore, P.J., Pratt, M.J., Andriampenomanana, F., Rümpker, G., Rindraharisaona, E., 2020. Seismicity and seismotectonics of Madagascar revealed by the 2011–2013 deployment of the island-wide MACOMO broadband seismic array. Tectonophysics 790, 228547. https://doi.org/10.1016/j.tecto.2020.228547

Randriamarolaza, L.Y.A., Aguilar, E., Skrynyk, O., Vicente-Serrano, S.M., Domínguez-Castro, F., 2022. Indices for daily temperature and precipitation in Madagascar, based on quality-controlled and homogenized data, 1950–2018. Int. J. Climatol. 42, 265–288. https://doi.org/10.1002/joc.7243

Raymo, M.E., Ruddiman, W.F., 1992. Tectonic forcing of late Cenozoic climate. Nature 359, 117–122. https://doi.org/10.1038/359117a0

Reeves, C., 2014. The position of Madagascar within Gondwana and its movements during Gondwana dispersal. J. Afr. Earth Sci. 94, 45–57. https://doi.org/10.1016/j.jafrearsci.2013.07.011

Reeves, C., 2000. The geophysical mapping of Mesozoic dyke swarms in southern Africa and their origin in the disruption of Gondwana. J. Afr. Earth Sci. 30, 499–513. https://doi.org/10.1016/S0899-5362(00)00035-X

Refsnider, K.A., 2010. Dramatic increase in late Cenozoic alpine erosion rates recorded by cave sediment in the southern Rocky Mountains. Earth Planet. Sci. Lett. 297, 505–511. https://doi.org/10.1016/j.epsl.2010.07.002

Regard, V., Carretier, S., Moquet, J.-S., Choy, S., Blard, P.-H., Bogning, S., Mbonda, A.P., Mambela, E., Paiz, M.C., Séranne, M., Charreau, J., Rouby, D., Bouchez, J., Gaillardet, J., Braun, J.-J., Denèle, Y., 2025. Contrasting physical erosion rates in cratonic catchments: The Ogooué and Mbei rivers, Western Central Africa. Gondwana Res. 138, 192–209. https://doi.org/10.1016/j.gr.2024.10.013

Reimer, P.J., Austin, W.E.N., Bard, E., Bayliss, A., Blackwell, P.G., Bronk Ramsey, C., Butzin, M., Cheng, H., Edwards, R.L., Friedrich, M., Grootes, P.M., Guilderson, T.P., Hajdas, I., Heaton, T.J., Hogg, A.G., Hughen, K.A., Kromer, B., Manning, S.W., Muscheler, R., Palmer, J.G., Pearson, C., Van Der Plicht, J., Reimer, R.W., Richards, D.A., Scott, E.M., Southon, J.R., Turney, C.S.M., Wacker, L., Adolphi, F., Büntgen, U., Capano, M., Fahrni, S.M., Fogtmann-Schulz, A., Friedrich, R., Köhler, P., Kudsk, S., Miyake, F., Olsen, J., Reinig, F., Sakamoto, M., Sookdeo, A., Talamo, S., 2020. The IntCal20 Northern Hemisphere Radiocarbon Age Calibration Curve (0–55 cal kBP). Radiocarbon 62, 725–757. https://doi.org/10.1017/RDC.2020.41

Resentini, A., Goren, L., Castelltort, S., Garzanti, E., 2017. Partitioning sediment flux by provenance and tracing erosion patterns in Taiwan. J. Geophys. Res. Earth Surf. 122, 1430–1454. https://doi.org/10.1002/2016JF004026

Riebe, C.S., Granger, D.E., 2013. Quantifying effects of deep and near-surface chemical erosion on cosmogenic nuclides in soils, saprolite, and sediment. Earth Surf. Process. Landf. 38, 523–533. https://doi.org/10.1002/esp.3339

Riebe, C.S., Kirchner, J.W., Finkel, R.C., 2003. Long-term rates of chemical weathering and physical erosion from cosmogenic nuclides and geochemical mass balance. Geochim. Cosmochim. Acta 67, 4411–4427. https://doi.org/10.1016/S0016-7037(03)00382-X

Roberts, G.G., Paul, J.D., White, N., Winterbourne, J., 2012. Temporal and spatial evolution of dynamic support from river profiles: A framework for Madagascar: DYNAMIC SUPPORT OF MADAGASCAR. Geochem. Geophys. Geosystems 13, n/a-n/a. https://doi.org/10.1029/2012GC004040

Rosenblum, S., 1958. Magnetic susceptibilities of minerals in the Frantz Isodynamic magnetic separator1. Am. Mineral. 43, 170–173.

Rougeau, S., Quidelleur, X., Famin, V., Michon, L., Nauret, F., Rusquet, A., Di Muro, A., 2025. Reconstruction of the volcanic history of Grande Comore and volcano-tectonic implications for the Comoros Archipelago. Comptes Rendus Géoscience 357, 125–144. https://doi.org/10.5802/crgeos.292

Rufer, D., Preusser, F., Schreurs, G., Gnos, E., Berger, A., 2014. Late Quaternary history of the Vakinankaratra volcanic field (central Madagascar): insights from luminescence dating of phreatomagmatic eruption deposits. Bull. Volcanol. 76, 817. https://doi.org/10.1007/s00445-014-0817-7

Ruffell, S.C., Talling, P.J., Baker, M.L., Pope, E.L., Heijnen, M.S., Jacinto, R.S., Cartigny, M.J.B., Simmons, S.M., Clare, M.A., Heerema, C.J., McGhee, C., Hage, S., Hasenhündl, M., Parsons, D.R., 2024. Time-lapse surveys reveal patterns and processes of erosion by exceptionally powerful turbidity currents that flush submarine canyons: A case study of the Congo Canyon. Geomorphology 463, 109350. https://doi.org/10.1016/j.geomorph.2024.109350

Rusquet, A., Famin, V., Michon, L., Quidelleur, X., Nauret, F., Danišík, M., Ruffet, G., Berthod, C., Revillon, S., Bachèlery, P., Thinon, I., Lemoine, A., Leroy, S., Zaragosi, S., Thivet, S., Bernard, J., Gourbet, L., Médard, E., Toulier, A., 2025. Phases of Magmatism and Tectonics Along the Madagascar-Comoros Volcanic Chain, and Synchronous Changes in the Kinematics of the Lwandle and Somalia Plates. J. Geophys. Res. Solid Earth 130, e2024JB029488. https://doi.org/10.1029/2024JB029488

Sadler, P.M., 1981. Sediment Accumulation Rates and the Completeness of Stratigraphic Sections. J. Geol. 89, 569–584. https://doi.org/10.1086/628623

Schaller, M., Blanckenburg, F. von, Hovius, N., Veldkamp, A., van den Berg, M.W., Kubik, P.W., 2004. Paleoerosion Rates from Cosmogenic ^{10}Be in a 1.3 Ma Terrace Sequence: Response of the River Meuse to Changes in Climate and Rock Uplift. J. Geol. 112, 127–144. https://doi.org/10.1086/381654

Schaller, M., Ehlers, T.A., 2006. Limits to quantifying climate driven changes in denudation rates with cosmogenic radionuclides. Earth Planet. Sci. Lett. 248, 153–167. https://doi.org/10.1016/j.epsl.2006.05.027

Schaller, M., Ehlers, T.A., Stor, T., Torrent, J., Lobato, L., Christl, M., Vockenhuber, C., 2016. Spatial and temporal variations in denudation rates derived from cosmogenic nuclides in four European fluvial terrace sequences. Geomorphology 274, 180–192. https://doi.org/10.1016/j.geomorph.2016.08.018

Schaller, M., Von Blanckenburg, F., Hovius, N., Kubik, P.W., 2001. Large-scale erosion rates from in situ-produced cosmogenic nuclides in European river sediments. Earth Planet. Sci. Lett. 188, 441–458. https://doi.org/10.1016/S0012-821X(01)00320-X

Schaller, M, von Blanckenburg, F., Veldkamp, A., Tebbens, L.A., Hovius, N., Kubik, P.W., 2002. A 30 000 yr record of erosion rates from cosmogenic 10Be in Middle European river terraces. Earth Planet. Sci. Lett. 204, 307–320.

Schaller, M., von Blanckenburg, F., Veldkamp, A., Tebbens, L.A., Hovius, N., Kubik, P.W., 2002. A 30 000 yr record of erosion rates from cosmogenic 10Be in Middle European river terraces. Earth Planet. Sci. Lett. 204, 307–320. https://doi.org/10.1016/S0012-821X(02)00951-2

Scheff, J., Seager, R., Liu, H., Coats, S., 2017. Are Glacials Dry? Consequences for Paleoclimatology and for Greenhouse Warming. J. Clim. 30, 6593–6609. https://doi.org/10.1175/JCLI-D-16-0854.1

Schildgen, T.F., Van Der Beek, P.A., Sinclair, H.D., Thiede, R.C., 2018. Spatial correlation bias in late-Cenozoic erosion histories derived from thermochronology. Nature 559, 89–93. https://doi.org/10.1038/s41586-018-0260-6

Schmid, M., Ehlers, T.A., Werner, C., Hickler, T., Fuentes-Espoz, J.-P., 2018. Effect of changing vegetation and precipitation on denudation – Part 2: Predicted landscape response to transient climate and vegetation cover over millennial to million-year timescales. Earth Surf. Dyn. 6, 859–881. https://doi.org/10.5194/esurf-6-859-2018

Schreurs, G., Giese, J., Berger, A., Gnos, E., 2010. A new perspective on the significance of the Ranotsara shear zone in Madagascar. Int. J. Earth Sci. 99, 1827–1847. https://doi.org/10.1007/s00531-009-0490-9

Scroxton, N., Burns, S.J., McGee, D., Godfrey, L.R., Ranivoharimanana, L., Faina, P., Tiger, B.H., 2023. Hydroclimate variability in the Madagascar and Southeast African summer monsoons at the Mid- to Late-Holocene transition. Quat. Sci. Rev. 300, 107874. https://doi.org/10.1016/j.quascirev.2022.107874

Scroxton, N., Burns, S.J., McGee, D., Hardt, B., Godfrey, L.R., Ranivoharimanana, L., Faina, P., 2019. Competing Temperature and Atmospheric Circulation Effects on Southwest Madagascan Rainfall During the Last Deglaciation. Paleoceanogr. Paleoclimatology 34, 275–286. https://doi.org/10.1029/2018PA003466

Séranne, M., Anka, Z., 2005. South Atlantic continental margins of Africa: A comparison of the tectonic vs climate interplay on the evolution of equatorial west Africa and SW Africa margins. J. Afr. Earth Sci. 43, 283–300. https://doi.org/10.1016/j.jafrearsci.2005.07.010

Seranne, M., Bruguier, O., Moussavou, M., 2008. U-Pb single zircon grain dating of Present fluvial and Cenozoic aeolian sediments from Gabon: consequences on sediment provenance, reworking, and erosion processes on the equatorial West African margin. Bull. Société Géologique Fr. 179, 29–40. https://doi.org/10.2113/gssgfbull.179.1.29

Seton, M., Müller, R.D., Zahirovic, S., Gaina, C., Torsvik, T., Shephard, G., Talsma, A., Gurnis, M., Turner, M., Maus, S., Chandler, M., 2012. Global continental and ocean basin reconstructions since 200Ma. Earth-Sci. Rev. 113, 212–270. https://doi.org/10.1016/j.earscirev.2012.03.002

Seward, D., Grujic, D., Schreurs, G., 2004. An insight into the breakup of Gondwana: Identifying events through low-temperature thermochronology from the basement rocks of Madagascar. Tectonics 23, 2003TC001556. https://doi.org/10.1029/2003TC001556

Shiki, T., Kumon, F., Inouchi, Y., Kontani, Y., Sakamoto, T., Tateishi, M., Matsubara, H., Fukuyama, K., 2000. Sedimentary features of the seismo-turbidites, Lake Biwa, Japan. Sediment. Geol. 135, 37–50. https://doi.org/10.1016/S0037-0738(00)00061-0

Shuster, D.L., Flowers, R.M., Farley, K.A., 2006. The influence of natural radiation damage on helium diffusion kinetics in apatite. Earth Planet. Sci. Lett. 249, 148–161. https://doi.org/10.1016/j.epsl.2006.07.028

Siddall, M., Rohling, E.J., Thompson, W.G., Waelbroeck, C., 2008. Marine isotope stage 3 sea level fluctuations: Data synthesis and new outlook. Rev. Geophys. 46, 2007RG000226. https://doi.org/10.1029/2007RG000226

Small, E.E., Anderson, R.S., Hancock, G.S., 1999. Estimates of the rate of regolith production using and from an alpine hillslope. Geomorphology 27, 131–150. https://doi.org/10.1016/S0169-555X(98)00094-4

Soulet, G., Maestrati, P., Gofas, S., Bayon, G., Dewilde, F., Labonne, M., Dennielou, B., Ferraton, F., Siani, G., 2023. Marine reservoir ages for coastal West Africa. Geochronology 5, 345–359. https://doi.org/10.5194/gchron-5-345-2023

Stamps, D.S., Kreemer, C., Fernandes, R., Rajaonarison, T.A., Rambolamanana, G., 2021. Redefining East African Rift System kinematics. Geology 49, 150–155. https://doi.org/10.1130/G47985.1

Stephenson, S.N., White, N.J., Carter, A., Seward, D., Ball, P.W., Klöcking, M., 2021. Cenozoic Dynamic Topography of Madagascar. Geochem. Geophys. Geosystems 22, e2020GC009624. https://doi.org/10.1029/2020GC009624

Stephenson, S.N., White, N.J., Li, T., Robinson, L.F., 2019. Disentangling interglacial sea level and global dynamic topography: Analysis of Madagascar. Earth Planet. Sci. Lett. 519, 61–69. https://doi.org/10.1016/j.epsl.2019.04.029

Stevens, T., Paull, C.K., Ussler, W., McGann, M., Buylaert, J.-P., Lundsten, E., 2014. The timing of sediment transport down Monterey Submarine Canyon, offshore California. Geol. Soc. Am. Bull. 126, 103–121. https://doi.org/10.1130/B30931.1

Stone, J.O., 2000. Air pressure and cosmogenic isotope production. J. Geophys. Res. Solid Earth 105, 23753–23759. https://doi.org/10.1029/2000JB900181

Storey, B.C., Leat, P.T., Ferris, J.K., 2001. The location of mantle-plume centers during the initial stages of Gondwana breakup, in: Mantle Plumes: Their Identification through Time. Geological Society of America. https://doi.org/10.1130/0-8137-2352-3.71

Storey, M., Mahoney, J.J., Saunders, A.D., Duncan, R.A., Kelley, S.P., Coffin, M.F., 1995. Timing of Hot Spot—Related Volcanism and the Breakup of Madagascar and India. Science 267, 852–855. https://doi.org/10.1126/science.267.5199.852

Tagami, T., O'Sullivan, P.B., 2005. Fundamentals of Fission-Track Thermochronology. Rev. Mineral. Geochem. 58, 19–47. https://doi.org/10.2138/rmg.2005.58.2

Tanaka, S., Sakamoto, K., Takagi, J., Tsuchimoto, M., 1968. Search for aluminum 26 induced by cosmic-ray muons in terrestrial rock. J. Geophys. Res. 73, 3303–3309. https://doi.org/10.1029/JB073i010p03303

Thiéblemont, D., Bouton, P., Préat, A., Goujou, J.-C., Tegyey, M., Weber, F., Ebang Obiang, M., Joron, J.L., Treuil, M., 2014. Transition from alkaline to calc-alkaline volcanism during evolution of the Paleoproterozoic Francevillian basin of eastern Gabon (Western Central Africa). J. Afr. Earth Sci. 99, 215–227. https://doi.org/10.1016/j.jafrearsci.2013.12.007

Thiéblemont, D., Callec, Y., Fernandez-Alonso, M., Chène, F., 2018. A Geological and Isotopic Framework of Precambrian Terrains in Western Central Africa: An Introduction, in: Siegesmund, S., Basei, M.A.S., Oyhantçabal, P., Oriolo, S. (Eds.), Geology of Southwest Gondwana, Regional Geology Reviews. Springer International Publishing, Cham, pp. 107–132. https://doi.org/10.1007/978-3-319-68920-3_5

Thiéblemont, P., Castaing, C., Billa, M., Bouton, P., Préat, A., 2009. Notice explicative de la carte géologique et des ressources minerales de la Republique Gabonaise. BRGM-Minist. Mines Hydrocarb. Libr.

Thinon, I., Lemoine, A., Leroy, S., Paquet, F., Berthod, C., Zaragosi, S., Famin, V., Feuillet, N., Boymond, P., Masquelet, C., Mercury, N., Rusquet, A., Scalabrin, C., Van Der Woerd, J., Bernard, J., Bignon, J., Clouard, V., Doubre, C., Jacques, E., Jorry, S.J., Rolandone, F., Chamot-Rooke, N., Delescluse, M., Franke, D., Watremez, L., Bachèlery, P., Michon, L., Sauter, D., Bujan, S., Canva, A., Dassie, E., Roche, V., Ali, S., Sitti Allaouia, A.H., Deplus, C., Rad, S., Sadeski, L., 2023. Volcanism and tectonics unveiled in the Comoros Archipelago between Africa and Madagascar. Comptes Rendus Géoscience 354, 7–34. https://doi.org/10.5802/crgeos.159

Thomas, R.J., De Waele, B., Schofield, D.I., Goodenough, K.M., Horstwood, M., Tucker, R., Bauer, W., Annells, R., Howard, K., Walsh, G., Rabarimanana, M., Rafahatelo, J.M., Ralison, A.V., Randriamananjara, T., 2009a. Geological evolution of the Neoproterozoic Bemarivo Belt, northern Madagascar. Precambrian Res. 172, 279–300. https://doi.org/10.1016/j.precamres.2009.04.008

Thomas, R.J., De Waele, B., Schofield, D.I., Goodenough, K.M., Horstwood, M., Tucker, R., Bauer, W., Annells, R., Howard, K., Walsh, G., Rabarimanana, M., Rafahatelo, J.M., Ralison, A.V., Randriamananjara, T., 2009b. Geological evolution of the Neoproterozoic Bemarivo Belt, northern Madagascar. Precambrian Res. 172, 279–300. https://doi.org/10.1016/j.precamres.2009.04.008

Thompson, J.O., Moulin, M., Aslanian, D., De Clarens, P., Guillocheau, F., 2019. New starting point for the Indian Ocean: Second phase of breakup for Gondwana. Earth-Sci. Rev. 191, 26–56. https://doi.org/10.1016/j.earscirev.2019.01.018

Tucker, R.D., Roig, J.Y., Macey, P.H., Delor, C., Amelin, Y., Armstrong, R.A., Rabarimanana, M.H., Ralison, A.V., 2011. A new geological framework for south-central Madagascar, and its relevance to the "out-of-Africa" hypothesis. Precambrian Res. 185, 109–130. https://doi.org/10.1016/j.precamres.2010.12.008

Tucker, R.D., Roig, J.Y., Moine, B., Delor, C., Peters, S.G., 2014. A geological synthesis of the Precambrian shield in Madagascar. J. Afr. Earth Sci. 94, 9–30. https://doi.org/10.1016/j.jafrearsci.2014.02.001

Tuenter, E., Weber, S.L., Hilgen, F.J., Lourens, L.J., 2003. The response of the African summer monsoon to remote and local forcing due to precession and obliquity. Glob. Planet. Change 36, 219–235. https://doi.org/10.1016/S0921-8181(02)00196-0

Val, P., Hoke, G.D., Fosdick, J.C., Wittmann, H., 2016. Reconciling tectonic shortening, sedimentation and spatial patterns of erosion from 10Be paleo-erosion rates in the Argentine Precordillera. Earth Planet. Sci. Lett. 450, 173–185. https://doi.org/10.1016/j.epsl.2016.06.015

Valla, P.G., Shuster, D.L., Van Der Beek, P.A., 2011. Significant increase in relief of the European Alps during mid-Pleistocene glaciations. Nat. Geosci. 4, 688–692.
Vandekerkhove, E., Van Daele, M., Praet, N., Cnudde, V., Haeussler, P.J., De Batist, M., 2020. Flood-triggered versus earthquake-triggered turbidites: A sedimentological study in clastic lake sediments (Eklutna Lake, Alaska). Sedimentology 67, 364–389. https://doi.org/10.1111/sed.12646
Vermeesch, P., 2018. IsoplotR: A free and open toolbox for geochronology. Geosci. Front. 9, 1479–1493. https://doi.org/10.1016/j.gsf.2018.04.001
Voarintsoa, N.R.G., Railsback, L.B., Brook, G.A., Wang, L., Kathayat, G., Cheng, H., Li, X., Edwards, R.L., Rakotondrazafy, A.F.M., Madison Razanatseheno, M.O., 2017. Three distinct Holocene intervals of stalagmite deposition and nondeposition revealed in NW Madagascar, and their paleoclimate implications. Clim. Past 13, 1771–1790. https://doi.org/10.5194/cp-13-1771-2017
von Blanckenburg, F., 2005. The control mechanisms of erosion and weathering at basin scale from cosmogenic nuclides in river sediment. Earth Planet. Sci. Lett. 237, 462–479. https://doi.org/10.1016/j.epsl.2005.06.030
von Blanckenburg, F., Bouchez, J., 2014. River fluxes to the sea from the ocean's 10Be/9Be ratio. Earth Planet. Sci. Lett. 387, 34–43. http://dx.doi.org/10.1016/j.epsl.2013.11.004
von Blanckenburg, F., Hewawasam, T., Kubik, P.W., 2004. Cosmogenic nuclide evidence for low weathering and denudation in the wet, tropical highlands of Sri Lanka. J. Geophys. Res. Earth Surf. 109, 2003JF000049. https://doi.org/10.1029/2003JF000049
Wang, L., Brook, G.A., Burney, D.A., Voarintsoa, N.R.G., Liang, F., Cheng, H., Edwards, R.L., 2019. The African Humid Period, rapid climate change events, the timing of human colonization, and megafaunal extinctions in Madagascar during the Holocene: Evidence from a 2m Anjohibe Cave stalagmite. Quat. Sci. Rev. 210, 136–153. https://doi.org/10.1016/j.quascirev.2019.02.004
Wang, Y., Willett, S.D., Wu, D., Haghipour, N., Christl, M., 2021. Retreat of the Great Escarpment of Madagascar From Geomorphic Analysis and Cosmogenic. Geochem. Geophys. Geosystems 25 p. https://doi.org/10.3929/ETHZ-B-000519815
Weber, F., Gauthier-Lafaye, F., Whitechurch, H., Ulrich, M., El Albani, A., 2016. The 2-Ga Eburnean Orogeny in Gabon and the opening of the Francevillian intracratonic basins: A review. Comptes Rendus Geosci. 348, 572–586. https://doi.org/10.1016/j.crte.2016.07.003
Weiss, A., 2001. Topographic position and landforms analysis. Presented at the Poster presentation, ESRI user conference, San Diego, CA.
West, A.J., 2012. Thickness of the chemical weathering zone and implications for erosional and climatic drivers of weathering and for carbon-cycle feedbacks. Geology 40, 811–814. https://doi.org/10.1130/G33041.1
Wilhelm, B., Arnaud, F., Sabatier, P., Magand, O., Chapron, E., Courp, T., Tachikawa, K., Fanget, B., Malet, E., Pignol, C., Bard, E., Delannoy, J.J., 2013. Palaeoflood activity and climate change over the last 1400 years recorded by lake sediments in the north-west European Alps. J. Quat. Sci. 28, 189–199. https://doi.org/10.1002/jqs.2609
Willenbring, J.K., Jerolmack, D.J., 2016. The null hypothesis: globally steady rates of erosion, weathering fluxes and shelf sediment accumulation during Late Cenozoic mountain uplift and glaciation. Terra Nova 28, 11–18. https://doi.org/10.1111/ter.12185
Willenbring, J.K., von Blanckenburg, F., 2010. Long-term stability of global erosion rates and weathering during late-Cenozoic cooling. Nature 465, 211–214. https://doi.org/10.1038/nature09044
Willett, S.D., Hovius, N., Brandon, M.T., Fisher, D.M. (Eds.), 2006. Contents, in: Tectonics, Climate, and Landscape Evolution. Geological Society of America, p. 0.
Wittmann, H., Von Blanckenburg, F., Maurice, L., Guyot, J.L., Kubik, P.W., 2011. Recycling of Amazon floodplain sediment quantified by cosmogenic 26Al and 10Be. Geology 39, 467–470. https://doi.org/10.1130/G31829.1
Yaaqoub, A., Essaifi, A., 2023. Drainage rearrangement and landscape evolution: Insights from the Moroccan Massif Central. Geomorphology 437, 108811. https://doi.org/10.1016/j.geomorph.2023.108811
Yiou, F., Raisbeck, G.M., Klein, J., Middleton, R., 1984. 26Al/10Be in terrestrial impact glasses. J. Non-Cryst. Solids 67, 503–509. https://doi.org/10.1016/0022-3093(84)90172-8

Zachos, J., Pagani, M., Sloan, L., Thomas, E., Billups, K., 2001. Trends, Rhythms, and Aberrations in Global Climate 65 Ma to Present. Science 292, 686–693. https://doi.org/10.1126/science.1059412

Zhang, P., Molnar, P., Downs, W.R., 2001. Increased sedimentation rates and grain sizes 2–4 Myr ago due to the influence of climate change on erosion rates. Nature 410, 891–897. https://doi.org/10.1038/35073504

Zhang, X., Scholz, C.A., Hecky, R.E., Wood, D.A., Zal, H.J., Ebinger, C.J., 2014. Climatic control of the late Quaternary turbidite sedimentology of Lake Kivu, East Africa: Implications for deep mixing and geologic hazards. Geology 42, 811–814. https://doi.org/10.1130/G35818.1